

Research on

Engineering

Structures

Materials

M

R

E

S

P-ISSN: 2148-9807 E-ISSN: 2149-4088

www.jresm.org

Volume
8

Issue
3

September
2022



Research Group

The International Journal of **Research on Engineering Structures and Materials (RESM)** is a peer-reviewed open access journal (p-ISSN: 2148-9807; o-ISSN: 2149-4088) published by MIM Research Group. It is published in February, June, September, and December.

The main objective of RESM is to provide an International academic platform for researchers to share scientific results related to all aspects of mechanical, civil and material engineering areas.

RESM aims the publication of original research articles, reviews, short communications technical reports, and letters to the editor on the latest developments in the related fields.

All expenditures for the publication of the manuscripts are most kindly reimbursed by *MIM Research Group*. Thus, authors do not need to pay for publishing their studies in the journal.

The scope of the journal covers (but not limited to) behavior of structures, machines and mechanical systems, vibration, impact loadings and structural dynamics, mechanics of materials (elasticity, plasticity, fracture mechanics), material science (structure and properties of concrete, metals, ceramics, composites, plastics, wood, etc.), nano-materials performances of new and existing buildings and other structural systems, design of buildings and other structural systems, seismic behavior of buildings and other structural systems, repair and strengthening of structural systems, case studies and failure of structural systems, safety and reliability in structural and material engineering, use of new and innovative materials and techniques in energy systems and mechanical aspects of biological systems (biomechanics and biomimetics).

The topics covered in JRESM include:

- Structural Engineering
- Mechanical Engineering
- Material Engineering
- Earthquake Engineering
- Nano-technology
- Energy Systems
- Biomechanics and Biomimetics

Abstracting and Indexing

Please visit <http://www.jresm.org> for more information.

Graphics and Design

Yunus Demirtaş

ydemirtas@iresm.net



**RESEARCH on
ENGINEERING STRUCTURES &
MATERIALS**



RESEARCH on ENGINEERING STRUCTURES & MATERIALS

Editorial Board

Editor in Chief		
Hayri Baytan Özmen	Usak University	Turkey
Editor (Energy, Thermodynamics)		
Canan Kandilli	Usak University	Turkey
Editor (Physics, Fluid Dynamics)		
Antonio F. Miguel	University of Evora	Portugal
Editor (Earthquake Eng., Structural Eng.)		
Michele Barbato	University of California Davis	USA
Editor (Mechanics, Biosystems, Meta-materials)		
Alp Karakoç	Aalto University	Finland
Editor (Applied Mechanics, Manufacturing, Design)		
Faris Tarlochan	Qatar University	Qatar
Editor (Civil Engineering)		
Mehmet Palancı	Arel University	Turkey

Editorial Office

Publishing Assistant		
Yunus Demirtaş	Eskişehir Technical University	Turkey
Yusuf Öztürk	MIM Resarch Group	Turkey
Language Editors		
Gaye Kuru	Usak University	Turkey
Mete Çal	Niğde Ömer Halisdemir University	Turkey

Editorial Board Members

Farid Abed-Meraim	Arts et Metiers ParisTech	France
P. Anbazhagan	Indian Institute of Science	India
Raffaele Barretta	University of Naples Federico II	Italy
R.S. Beniwal	Council of Scientific and Industrial Research	India
Antonio Caggiano	University of Buenos Aires	Argentina
Noel Challamel	University of South Brittany	France
Abdulkadir Çevik	Gaziantep University	Turkey
J. Paulo Davim	University of Aveiro	Portugal
Hom Nath Dhakal	University of Portsmouth	UK
Ali Faghidian	Islamic Azad University	Iran
S. Amir M. Ghannadpour	Shahid Beheshti University	Iran
Ali Goodarzi	Harvard University	USA
Jian Jiang	National Institute of Standards and Technology	USA
Ramazan Karakuzu	Dokuz Eylül University	Turkey
Arkadiusz Kwiecien	Cracow University of Technology	Poland
Stefano Lenci	Universita Politecnica delle Marche	Italy
Silva Lozančić	University of Osijek	Croatia
Fabio Mazza	University of Calabria	Italia
Yuan Meini	North University of China	China
Stergios A. Mitoulis	University of Surrey	UK
Vinayagam Mohanavel	Anna University	India
Ehsan Noroozinejad Farsangi	Kerman Graduate University of Technology	Iran
Alaa M. Rashad	Shaqra University	Saudi Arabia
Mohammad Mehdi Rashidi	University of Tongji	China
Pier Paolo Rossi	University of Catania	Italy
Neritan Shkodrani	Polythecnic University of Tirana	Albania
Y.B. Yang	National Taiwan University	Taiwan

Advisory Board Members

Yaser Açıkbaz	Usak University	Turkey
Mehmet Ada	Usak University	Turkey
Mohammad Afrazi	Tarbiat Modares University	Iran
Ayse Bilge Aksoy	Celal Bayar University	Turkey
Ali Özhan Akyüz	Burdur Mehmet Akif Ersoy University	Turkey
Mohammad Al Biajawi	Universiti Malaysia Pahang	Malaysia
Gabriel Arce	Louisiana State University	USA
E. Arunraj	Karunya Institute of Technology and Sciences	India
K. Ashwini	Jawaharlal Nehru Technological University Hyderabad	India
Olumoyewa Atoyebi	Landmark University	Nigeria
Samuel Awe	Automotive Components Floby AB	Sweden
Ameer Baiee	University of Babylon	Iraq
Ajay Sudhir Bale	CMR University	India
Megha Bhatt	SV National Institute of Technology	India
Tanik Bayram Cayci	Pamukkale University	Turkey
Noé Cheung	Universidade Estadual de Campinas	Brazil
Chella Giftha Christopher	National Engineering College	India
Hüseyin Coşkun	Usak University	Turkey
Daniel Cruze	Hindustan Institute of Technology and Science	India
Ali İhsan Çelik	Kayseri University	Turkey
Ahmet Demir	Bolu University	Turkey
Cengiz Görkem Dengiz	Ondokuz Mayıs University	Turkey
Marwan Effendy	Universitas Muhammadiyah Surakarta	Indonesia
Halil Murat Enginsoy	Çanakkale Onsekiz Mart University	Turkey
Ali Erçetin	Bingöl University	Turkey
S. Ali Faghidian	Islamic Azad University	Iran

Advisory Board Members

Christopher Fapohunda	Federal University Oye-Ekiti	Nigeria
Abdullah Fettahoglu	Usak University	Turkey
Mehmet Cemal Genes	Eastern Mediterranean University	North Cyprus
Vahidreza Gharehbaghi	University of Southern Queensland	Australia
Anjeza Gjini	Polytechnic University of Tirana	Albania
Layachi Guelmine	University Of Bordj Bou Arreridj	Algeria
Kadir Günaydın	GE Aviation	Turkey
Orhan Gülcan	General Electric Aviation	USA
Marijana Hadzima-Nyarko	University of Osijek	Croatia
Dulce Franco Henriques	Instituto Politécnico de Lisboa	Portugal
Qing Hong	Midwestern University	USA
Ercan Isik	Bitlis Eren University	Turkey
Khairul Nizar Ismail	Universiti Malaysia Perlis	Malaysia
Berrin Ikizler	Ege University	Turkey
Saifulnizan Jamian	Universiti Tun Hussein Onn Malaysia	Malaysia
Joel Shelton Joseph	RGM College of Engineering and Technology	India
Arunkumar K.	-	India
Nikhil R. Kadam	Birla Institute of Technology and Science	India
Abdulhalim Karasin	Dicle University	Turkey
Hemant B. Kaushik	Indian Institute of Technology Guwahati	India
Mehmet Kaya	Yozgat Bozok University	Turkey
Zafer Kaya	Dumlupınar University	Turkey
Sedat Kömürcü	Istanbul Technical University	Turkey
B. Radha Krishnan	College of Engineering and Technology	India
Karthik Krishnasamy	Vel Tech Rangarajan Dr Sagunthala R&D Institute of Science and Technology	India
Nitin Kumar	University of California Davis	USA
Manjunatha Kuruba	B.M.S College of Engineering	India

Advisory Board Members

Ravichandran M.	K.Ramakrishnan College of Engineering	India
Lomesh Mahajan	Dr. Babasaheb Ambedkar Technological University	India
Waqas Ahmed Mahar	University of Liege	Belgium
Emrah Meral	Osmaniye Korkut Ata University	Turkey
Sedat Metlek	Mehmet Akif Ersoy University	Turkey
Masoomeh Mirrashid	Semnan University	Iran
Mustafa K. A. Mohammed	Dijlah University College	Iraq
Berker Nacak	Usak University	Turkey
Samson Olalekan Odeyemi	Kwara State University	Nigeria
Mehmet Orhan	Pamukkale University	Turkey
Alp Özdemir	Eskişehir Technical University	Turkey
Yasin Onuralp Özkılıç	Necmettin Erbakan University	Turkey
Partheeban Pachaivannan	Chennai Institute of Technology	India
Moslem Paidar	Islamic Azad University	Iran
Chitaranjan Pany	Vikram Sarabhi Space Center	India
Vikas Patel	National Council for Cement and Building Materials	India
Lalit Pawar	Veermata Jijabai Technological Institute	India
Amin Moslemi Petrudi	Tehran University	Iran
Josphat Phiri	Aalto University	Finland
B.Prabakaran	Hindustan Institute of Technology and Science	India
K. Venkatesh Raja	Sona College of Technology	India
Badrinarayan Rath	Wollega University	Ethiopia
Pier Paola Rossi	University of Catania	Italy
Francesca Russo	Istituto per la Tecnologia delle Membrane CNR-ITM	Italy
Abbasali Sadeghi	Islamic Azad University	Iran
S. Reza Salimbahrami	Semnan University	Iran

Advisory Board Members

M.Helen Santhi	Vellore Institute of Technology	India
Sudesh Singh	Sharda University	India
Rianti Dewi Sulamet-Ariobimo	Universitas Trisakti	Indonesia
Hamide Tekeli	Suleyman Demirel University	Turkey
Serdar Tez	Pamukkale University	Turkey
Tugce Tezel	Akdeniz University	Turkey
Subash Thanappan	Ambo University	Ethiopia
Fatma Coskun Topuz	Yuzuncu Yil University	Turkey
Prem Kumar V.	-	India
Suiwen Wu	University of Nevada	USA
Jhair Yacila	Pontifical Catholic University of Peru	Peru
Omid Aminoroayai Yamani	K. N. Toosi University of Technology	USA

In This Issue

Research Article

- 431 **KR Yellu Kumar, Adnan Qayoum, Shahid Saleem, Fasil Qayoom Mir**
Effect of blowing ratio on adiabatic effectiveness for effusion cooling in gas turbine combustor liners

Research Article

- 447 **Bisma Ali, Adnan Qayoum, Shahid Saleem, Fasil Qayoom Mir**
Synthesis and characterization of high-quality multi layered graphene by electrochemical exfoliation of graphite

Research Article

- 463 **Nitin Kumar, Michele Barbato, Erika L. Rengifo-López, Fabio Matta**
Capabilities and limitations of existing finite element simplified micro-modeling techniques for unreinforced masonry

Review Article

- 491 **Ali İhsan Çelik**
Evaluation of energy retention capacity of composite CFRP and GFRP in RC beam strength

Research Article

- 519 **Megha Bhatt, Sandip A. Vasanwala**
Moment-curvature relationships for RC chimney sections

Review Article

- 535 **T. V. Sheeja, S. V. S. Jebadurai, D. Tensing**
Additive manufacturing techniques in construction

Research Article

- 553 **Afreen Nissar, M. Hanief, Fasil Qayoom Mir**
Experimental assessment of recycling methods of used engine oil for sustainable environment

Research Article

- 569 **Samson Olalekan Odeyemi, Michael Oluwasegun Adisa, Olumoyewa Dotun Atoyebi, Uwemedimo Nyong Wilson³, Omolola Titilayo Odeyemi**
Optimal water-cement ratio and volume of superplasticizers for blended cement-bamboo leaf ash high-performance concrete

Research Article

583 **P.N. Ojha, Pranay Singh, Brijesh Singh, Abhishek Singh, Piyush Mittal**

Fracture behavior of plain and fiber-reinforced high strength concrete containing high strength steel fiber

Research Article

603 **Moulshree Dubey, Shirish V Deo, Gangadhar Ramtekkar**

Effect of metakaolin and steel slag on performance of binary blended concrete

Research Article

615 **Badrinarayan Rath**

Effect of asphalt pavement construction on the environment of Ethiopia

Technical Note

633 **Deepan Rajendran, Chella Gifta Christopher, Malaiappan Sindhu Muthu**

Self - compacting concrete made with partial replacement of lime stone and quarry dust powder

Free access to tables of content, abstracts and full text of papers for web visitors.

Copyright © 2022

Research on Engineering Structures & Materials

MIM Reseach Group Publications

P-ISSN: 2148-9807

E-ISSN: 2149-4088

<http://www.jresm.org>



ABSTRACTING / INDEXING

The international journal of Research on Engineering Structures and Materials (RESM) is currently Abstracted/Indexed by Asos Indeks, CiteFactor, Cosmos, CrossRef, Directory of Research Journal Indexing, Engineering Journals (ProQuest), EZB Electronic Journal Library, Global Impact Factor, Google Scholar, International Institute of Organized Research (I2OR), International Scientific Indexing (ISI), Materials Science & Engineering Database (ProQuest), Open Academic Journals Index, Publication Forum, Research Bible/Scientific Indexing Service, Root Indexing, Scopus, Ulakbim TR Index (Tubitak), Universal Impact Factor and under evaluation by many other respected indexes.

Check web site for current indexing info, www.jresm.org

Scopus®





Research Article

Effect of blowing ratio on adiabatic effectiveness for effusion cooling in gas turbine combustor liners

KR Yellu Kumar^{1,a}, Adnan Qayoum^{*1,b}, Shahid Saleem^{1,c}, Fasil Qayoom Mir^{2,d}

¹Mechanical Engineering Department, National Institute of Technology Srinagar, J&K, India-190006.

²Chemical Engineering Department, National Institute of Technology Srinagar, J&K, India-190006

Article Info

Article history:

Received 28 Oct 2021

Revised 14 Feb 2022

Accepted 11 Mar 2022

Keywords:

Effusion cooling;

Adiabatic effectiveness;

Blowing ratio;

Injection angle;

Combustor liners;

Gas turbine

Abstract

The current study involves a computational investigation on the cooling of the combustion chamber liners in a gas turbine engine. Effusion cooling is a high-efficiency, lightweight and low-cost cooling system widely used in combustion chamber liners nowadays. The effect of blowing ratio and effusion hole injection angle on adiabatic effectiveness is investigated. The simulations are carried using COMSOL Multiphysics 5.4 with the standard $k-\epsilon$ turbulence model. A 3D computational model consisting of mainstream duct, effusion plate and effusion holes has been incorporated for the analysis. The blowing ratios used in the study are 0.25, 0.5, 1, 1.25 and 1.5 at constant density ratio of 1.0 for different injection angles of 30° and 60°. The simulation results show a strong dependence of adiabatic effectiveness on the blowing ratios. For low blowing ratios the adiabatic effectiveness in effusion hole region is high on account of coolant being attached to the surface. On the contrary, for high blowing ratios the adiabatic effectiveness is low near the effusion holes region. In the downstream region of effusion holes the adiabatic effectiveness raises for high blowing ratios. In addition, it has been observed that injection angle of 30° provides better adiabatic effectiveness compared to injection angle of 60°. The velocity and temperature profiles are investigated to demonstrate the behavior of coolant flow on the effusion surface and the influence on adiabatic effectiveness. This study concludes that the proper selection of blowing ratio and injection angle improves combustion chamber's efficiency and lifetime.

© 2022 MIM Research Group. All rights reserved.

1. Introduction

To achieve the high thermal efficiency of a gas turbine or aero engines the turbine inlet temperatures are maintained around 1200°C-1500°C [1-4] which is clearly above the metallurgical limit of the metals. As a consequence, cooling has to be initiated to avoid local thermal cracks and reduces the chances of failure. A proper cooling method should be introduced on the hot sections of gas turbines such as combustion chamber, turbine blades, and nozzle to enhance their operational life. However, to follow the strict emission legislation it is mandatory to maintain the NO_x and CO levels within the permissible limits. Coolant consumption plays a vital role in the design aspect of a cooling system which is a key point to increase the cycle efficiency and utilization of lean burn mixture combustion. This will automatically ensure NO_x reduction to fulfill the emission legislation.

Compared to other cooling techniques, effusion cooling is considered as most advanced cooling concept in which the coolant or secondary flow is injected through an array of closely spaced holes or slots which enters the thermal boundary layer of combustion liners

*Corresponding author: adnan@nitsri.ac.in

^a orcid.org/0000-0001-9793-7577; ^b orcid.org/0000-0002-4894-3425; ^c orcid.org/0000-0001-6998-0324; ^d orcid.org/0000-0002-3211-2395

DOI: <http://dx.doi.org/10.17515/resm2022.359me1028>

Res. Eng. Struct. Mat. Vol. 8 Iss. 3 (2022) 431-445

resulting in the formation of film. This film serves as the protection layer between the hot gases and wall surface. Effusion cooling involves injection of air through holes whose size and number may vary. The hole density on the surface increases as large number of holes is arranged at very close spacing in arrays. Due to this, coalescence of adjacent jet increases by increasing the overall cooling performance on the surface. Effusion cooling involves two heat exchange effects, the first one being the convective cooling inside the wall as the coolant passes through the holes and other is the formation of coolant film on the wall as coolant passes over the wall surface. Since last two decades researchers have focused on the improvement of effusion cooling performance due to its simplicity and reliability for providing continuous cooling over the hot sections of gas turbine. Due to high fabrication cost and challenging technical issues, it is difficult to carry out experimentation for the complete combustion chamber. Numerical studies provide an important complimentary design tool and refine overall results due to availability of advanced computational fluid dynamics. Still experimentation is carried out on a flat plate with drilled holes similar to real as combustion liners a set up similar to the conventional wind tunnel. Considering the past literature review, it is observed that both geometrical and flow parameters such as hole shape, hole diameter, hole injection angle, blowing ratio, density ratio and thermal conductivity etc., have a strong influence on the effusion cooling performance. Yuen and Matinez [1] studied the effect of hole injection angle (α) by measuring adiabatic effectiveness and heat transfer coefficient on a flat plate with various geometries for different blowing ratios ranging from 0.33 to 2.0. Roger and Buck [5] concluded that the use of the k- ϵ turbulence model generates better data that were close to the predicted results, Lamyaa and Deborah [6] compared the standard k- ϵ turbulence model with Yang-Shih turbulence model for cross-flow conditions through angled holes with the experimental results. Silieti et al. [7] computationally investigated film cooling over flat surface using five turbulence model; the standard k- ϵ model, the realizable k- ϵ model, the RNG k- ϵ model, the standard k- ω model and the SST k- ω model. He concluded that the standard k- ϵ turbulence model predicted close conformity to the experimental results for the center line adiabatic effectiveness in the downstream region. Baldauf et al. [8] investigated experimentally and measured the laterally averaged adiabatic effectiveness (η) over a flat plate at different blowing ratios and found that the value of η increases first and then decreases. This is on account of overshooting into the mainstream flow by detaching the coolant flow from the surface. Ligrani et al. [9] measured the heat transfer coefficient and adiabatic effectiveness for effusion cooling system by studying the impact of blowing ratio and spacing of coolant holes over the adiabatic effectiveness.

Bailey et al. [11] investigated the heat transfer characteristics of impingement cooling for a stationary combustor comprising of trip strip tabulators for enhancement of heat transfer and studied the distribution of heat transfer coefficient over the flat plate by using steady state liquid crystal method. Investigations on effusion cooling performance were examined by Liu and Zheng [12] on four deflection angles and it was observed that cooling performance decrease after the primary holes due to the local combustion. The authors used 3D fluid-solid coupling to measure the effusion cooling performance. Andrew et al. [13-15] performed number of experiments to study the geometrical parameter effects such as cooling hole shape, hole diameter and hole injection angle. The authors [16-17] investigated both experimentally and numerically to study the pitch-to-pitch hole spacing in streamwise and spanwise direction, different hole injection angles and deflection angles by measuring the adiabatic film effectiveness at different blowing ratios. Legar et al. [18] examined the effect of pressure difference between the hot and cold gas for effusion cooling system with different geometry and flow parameters. They conducted experimentation in temperature range of 860K-1400K similar to a real combustor condition. From their observations they suggested two zones system for effusion cooling which can improve the cooling performance by reducing the coolant mass flow rate.

Gaustafsson [19] explained the effect of blowing ratio and temperature ratio on effusion cooling performance over a flat plate surface. Sasaki et al. [20] conducted experiments on staggered manner arrangement with spacing of holes in streamwise direction $S_x/d=10$ and $S_y/d=3$ at injection angles $\alpha=45^\circ$. They observed that array arrangement increases the lateral averaged effectiveness by increasing the blowing ratio than single row of holes. Cerri et al. [21] studied the effect of hole diameter and spacing of holes in streamwise direction (S_x/d) and (S_y/d) and suggested that an efficient cooling system can be achieved only by reducing the mass coolant flow consumption. Yellu et al. [22] has compiled a comprehensive review of effusion cooling in Gas turbine combustion chamber. The study shows a significant dependence of various parameters on the adiabatic efficiency.

The objective of this paper is to evaluate the adiabatic effectiveness of the effusion cooling plate with the purpose to study the effect of blowing ratio in the effusion holes region and downstream the effusion holes region at different injection angles. To characterize the effect of blowing ratio, a range of blowing ratios 0.25 to 1.5 with low and high values are used for the purpose. In addition, velocity and temperature profiles have been evaluated at a specified location in the streamwise direction for comprehensive understanding of the flow field.

2. Computational Model

The computational model and details of the effusion plate with inclined holes are shown in Fig. 1 and Fig. 2 respectively. The three-dimensional computational domain consists of three sub-sections i.e., mainstream flow zone, coolant flow zone and effusion plate zone. The mainstream flow (hot gases) passes over the effusion plate surface while cold stream (cool air) flows through the inclined effusion holes towards the effusion surface. The holes are arranged in staggered manner with first row located at $23d$ for an injection angle of 30° and $18d$ for an angle of 60° . The height of the mainstream flow duct is $30d$ (in Z-direction) and the corresponding width (in Y-direction) is twice the spanwise distance between the adjacent holes (see Fig. 2). The symmetric boundary conditions are applied on either side of domain. In order to understand, the temperature distribution over the surface in streamwise direction the mainstream flow domain is divided in three zones i.e., upstream region (X_1), effusion holes region (X_2) and downstream region (X_3). The coolant flow holes are present in the effusion holes region (X_2) only. The geometrical parameters of the effusion plate are shown in Table 1.

Table 1. The geometry parameters of the effusion plate are

d	1 mm
t	3 mm
S_x/d	4.9
S_y/d	4.9
α	30° and 60°

3. Boundary Conditions

Air is modelled as incompressible for both mainstream and coolant. The primary inlet of hot gas is set to specified velocity while the outlet is set to static pressure conditions. Inlet velocity of mainstream flow is fixed at a specified velocity $U_\infty=50$ m/s and coolant velocities are varied to study the effect of BR for different cases i.e., 0.25, 0.5, 1, 1.25 and 1.5. The inlet temperatures for mainstream and coolant flow are fixed at $T_\infty=350$ K and $T_c=300$ K respectively resulting in the density ratio (DR) approximately equal to one. The turbulence intensity for both inlets is specified as 5%. The properties of air such as ratio of specific heats, dynamic viscosity, heat capacity at constant pressure and thermal conductivity are dependent on the temperature. The effusion plate is set to adiabatic no-

slip condition with the interface between the primary flow and perforated plate as fluid-solid coupled boundary. To evaluate the adiabatic effectiveness the plate is assumed to be adiabatic. In this study adiabatic effectiveness is measured along centerline of the effusion as shown in Fig. 2

Velocity ratio (VR) is defined as ratio of coolant flow blowing to mainstream flow blowing.

$$VR = \frac{U_c}{U_\infty} \tag{1}$$

The most important parameter that affects the effusion cooling performance is Blowing ratio (BR). It is defined as the ratio of coolant mass flux to mainstream mass flux.

$$BR = \frac{\rho_c U_c}{\rho_\infty U_\infty} \tag{2}$$

The adiabatic effectiveness of effusion cooling is measured in terms of

$$\eta = \frac{T_\infty - T_{wt}}{T_\infty - T_c} \tag{3}$$

where T_∞ , T_{wt} and T_c represents the temperatures of mainstream flow, wall temperature of effusion plate and the coolant flow respectively. In these study blowing ratios 0.25 and 0.5 are considered as low, 1.0 as intermediate, as well 1.25 and 1.5 are considered as high.

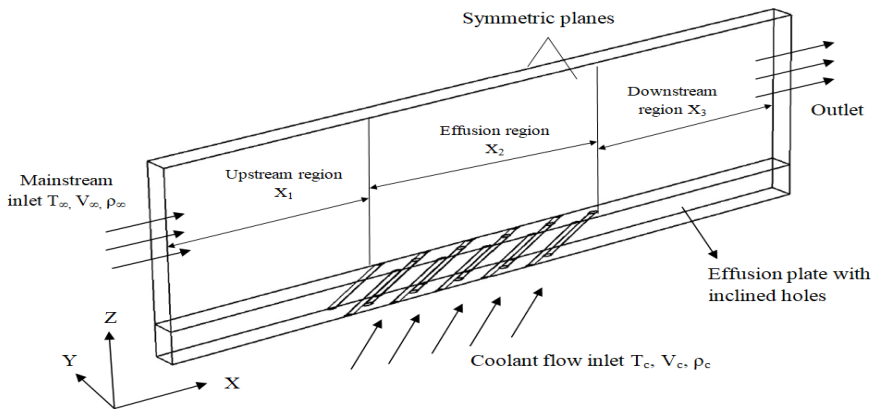


Fig. 1 Schematic of computational domain (XYZ)

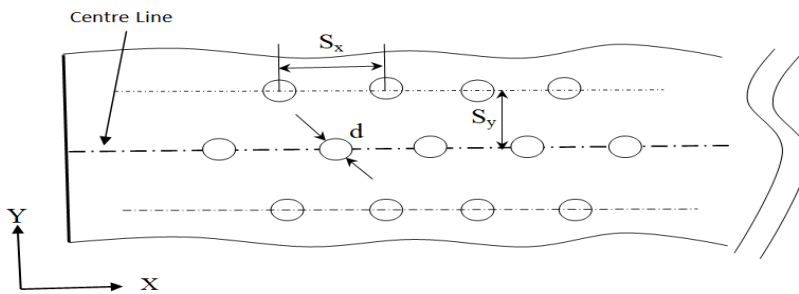


Fig. 2 Physical configuration of the problem (XY plane)

4. Computational Details

The simulations are carried using COMSOL Multiphysics 5.4 using standard k- ϵ turbulence model. Literature survey [5,6,7] has demonstrated that standard k- ϵ turbulence model can accurately predict the surface temperature distribution over the flat surface. The effectiveness of centerline film cooling can be correctly predicted by a typical k-turbulence model. User controlled mesh is used in this computational model. Free triangular mesh with extreme fine grid is chosen for the effusion plate surface and Swept mesh with fixed number of elements is distributed on the solid and fluid domain. A high resolution of grid is set near the effusion holes and effusion plate surface. At every location of the solid wall, the viscous clustering value y^+ is maintained at 7. To reduce the run time of computation the symmetry in transverse planes is applied and numbers of rows of effusion holes have been reduced to 5 compared to experimental data to reduce the computational run time. The Fig. 3 shows the overall view mesh of the computational model.

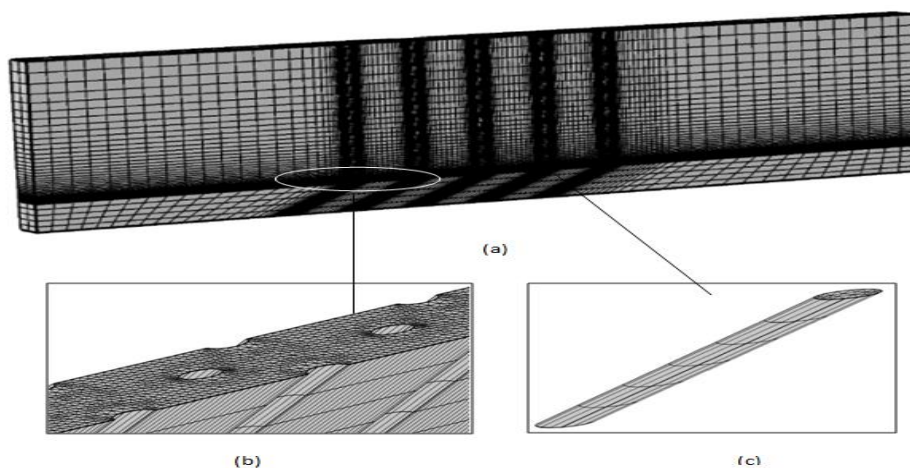


Fig. 3 Computational Mesh (a) Entire geometry (b) Effusion plate surface (c) Effusion hole

5. Grid Independence Test and Validation

The precision of numerical analysis results depends on the quality of grid used. To ensure the results obtained are independent of mesh size, the grid independence study was carried for three different grid sizes consisting of 363174 (extremely fine mesh), 151096 (fine mesh) and 52762 (coarse mesh) elements respectively. The averaged adiabatic efficiency on the centerline of effusion surface is plotted and compared with different grids as shown in Fig. 4 for blowing ratio 0.5 at injection angle $\alpha=30^\circ$. The grid size of 363174 (extremely fine) is found to be quite close to the experimental results [23], with improved viewing of temperature and blowing counters on the effusion surface in the near wall region. As a result, for the final simulation, a grid size of 363174 was used. The computational results were validated by comparing with the experimental results of Scrittore et al. [23]. To validate the simulations, the same geometrical and flow parameters were used as in ref [23]. The Fig. 5 shows the comparison of experimental results and present computational results of centerline adiabatic effectiveness along the stream wise direction for 20 rows of holes at BR=3.2 and 5.0. The present results show a good agreement with the experimental data.

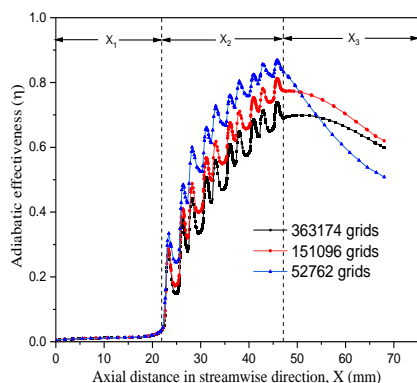


Fig. 4 Centerline adiabatic effectiveness on the effusion surface with different grid sizes for $\alpha=30^\circ$ and $BR=0.5$

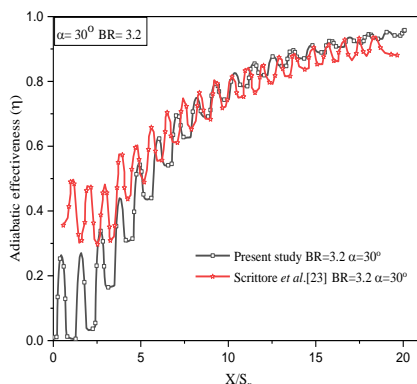


Fig. 5 Validation of experimental [23] and computational results. Note that the leading edge of first row $X/S_x=0$ and adiabatic effectiveness is measured from rows 1 to 20

6. Results and Discussion

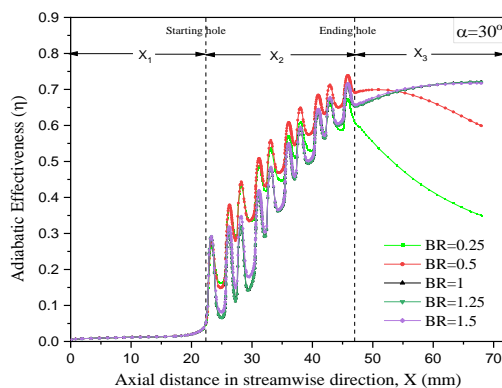
The adiabatic effectiveness and temperature distribution have been calculated for all blowing ratios (BR) at two injection angles of $\alpha=30^\circ$ and 60° . Since the first row of cooling holes start in the X_2 region, no heat transfer takes place before the region X_2 . This is because the plate wall is considered as adiabatic and area in region X_1 shows zero effectiveness. The results included in the study are temperature distribution over the effusion plate surface and temperature slice counters on the central plane of effusion plate for different blowing ratios.

6.1 Effect of Blowing Ratio on Adiabatic Effectiveness

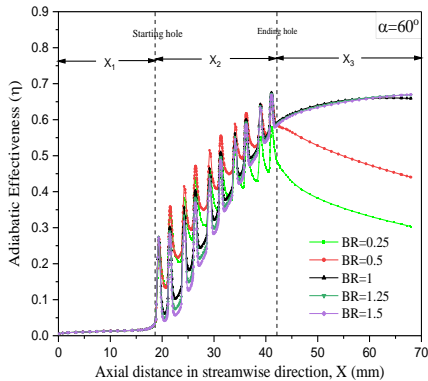
The Fig. 6 shows the behavior of adiabatic effectiveness (η) at different blowing ratios (BR) of 0.25, 0.5, 1, 1.25, 1.5 for injection angle (α) of 30° and 60° . The Figure clearly indicates the strong impact of blowing ratio on the adiabatic effectiveness for effusion cooling. The

adiabatic effectiveness is zero in the upstream region X_1 as there is no coolant flow. In the intermediate region X_2 , the adiabatic effectiveness (η) increases in the streamwise direction for all the values of the blowing ratios (BR). Further in the downstream region X_3 the adiabatic effectiveness (η) decreases at low BR (0.25 and 0.5) and increases at high BR (1, 1.25 and 1.5). On account of the low blowing ratio (BR) the coolant flow velocity is low as compared to the mainstream flow velocity so the coolant flow jet attaches to the surface without penetrating into the mainstream flow. This ensures that the hot gases do not reach the surface. At high blowing ratios (BR) the coolant jet separates from the surface by penetrating into mainstream flow and as such the hot gases reach the surface thereby increasing the surface temperature in the effusion region X_2 (see in Fig. 7 and Fig. 9). This causes the thickening of the thermal boundary layer leading to increased effectiveness. Also, it is observed from Fig. 6 that the adiabatic effectiveness (η) is high for low blowing ratio (BR) compared to that of high blowing ratios (BR) in the effusion hole region X_2 . Unlike this a different behaviour is observed in the downstream region X_3 . Extremely high values of adiabatic effectiveness (η) are exhibited for high blowing ratio (BR) as large amount of coolant mass flow rate is injected from effusion holes. For low blowing ratios the mass of cooling fluid injecting from effusion holes is very small and advection of mainstream gases bring hot air much closer to the wall so that the film formed over the surface become weaker as shown in Fig.7 and Fig.9. As a result, adiabatic effectiveness (η) decreases in downstream streamwise direction. But for higher blowing ratios the velocity of coolant is much higher than that of the mainstream velocity so a large amount of coolant mass flow rate is injected from the effusion holes and accumulated in the region X_3 by forming a thick film of cooling air on the surface (See in Fig. 7 and Fig 9 for high BR). This makes adiabatic effectiveness (η) high in this region at higher values of blowing ratios (see in Fig.6).

The temperature distribution on the effusion plate surface obtained for different blowing ratios (BR) at injection angles (α) of 30° and 60° are shown in Fig. 8 and Fig. 10. For lower values of blowing ratios (BR), the coolant flow remains on the surface as it does not have sufficient momentum to separate from the surface and penetrate into the mainstream flow. As such slight temperature variations can be seen as the coolant flow remains close to the surface. For higher values of blowing ratios (BR) opposite trend is observed.



(a)



(b)

Fig. 6 Centerline adiabatic effectiveness on the surface (a) $\alpha=30^\circ$ and (b) $\alpha=60^\circ$

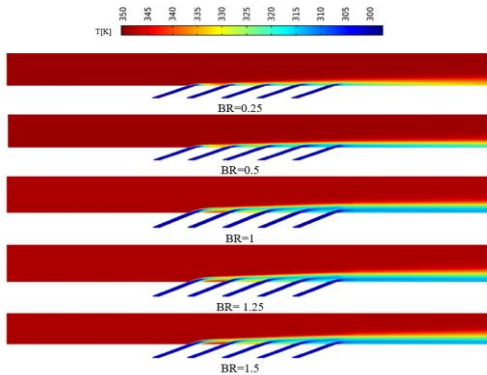


Fig. 7 Temperature slice counters on the center plane of effusion plate for different BR on XZ plane for $\alpha=30^\circ$

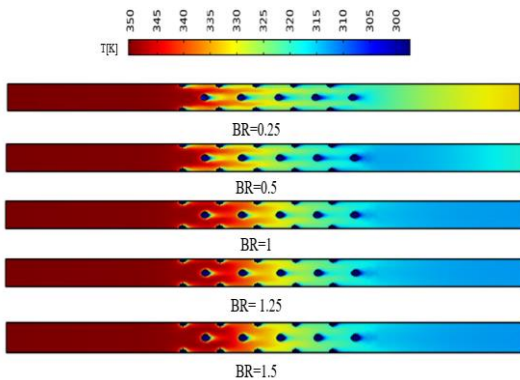


Fig.8 Temperature distribution on effusion plate surface for different BR on XY plane for $\alpha=30^\circ$

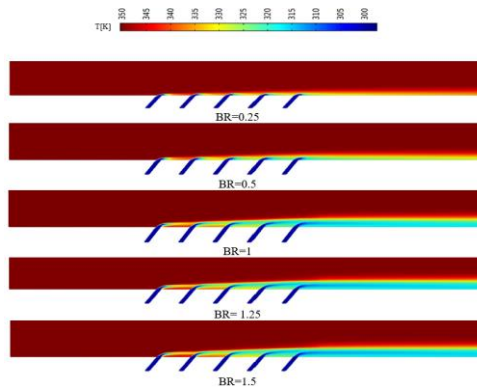


Fig.9 Temperature slice counters on the center plane of effusion plate for different BR on XZ plane for $\alpha=60^\circ$

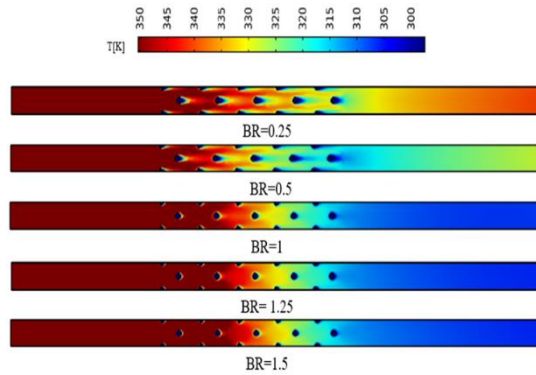


Fig.10 Temperature distribution on effusion plate surface for different BR on XY plane for $\alpha=60^\circ$

6.2 Velocity Boundary Profile

The discharged fluid from the coolant holes is mixed up with the mainstream flow in the streamwise direction and interacts with the coolant flow coming from the adjacent holes. The velocity components of the coolant jet from the effusion holes are divided into two parts, being the tangential velocity component in the streamwise direction and other being the normal velocity component in z-direction. The tangential velocity component makes the coolant to flow over the effusion wall while as the coolant flow in the normal direction penetrates into the mainstream flow. It is clear that the penetration height of the coolant flow through the effusion holes is different at various sections in streamwise direction i.e. from starting row to the ending row. Pietrzyk et al. [24] identified higher velocity fluid penetrating into wake region below the jet core causing a negative velocity gradient near the wall as such a double peaked velocity profiles can be seen in downstream of streamwise directions in the velocity profile [Fig. 11]. The double peaked velocity profiles are seen at high BR. These double peaked velocity profiles for higher value of BR are generated high due to cross flow of coolant into mainstream by the inclined jets. This is because inclined jets induce high velocity in the wake region than the normal jets on account of pressure drop and strong secondary motions. The Fig.12 shows the streamlines of mainstream flow (blue color) and coolant flow (red color) domain for blowing ratio 1.5 at injection angle 30° .

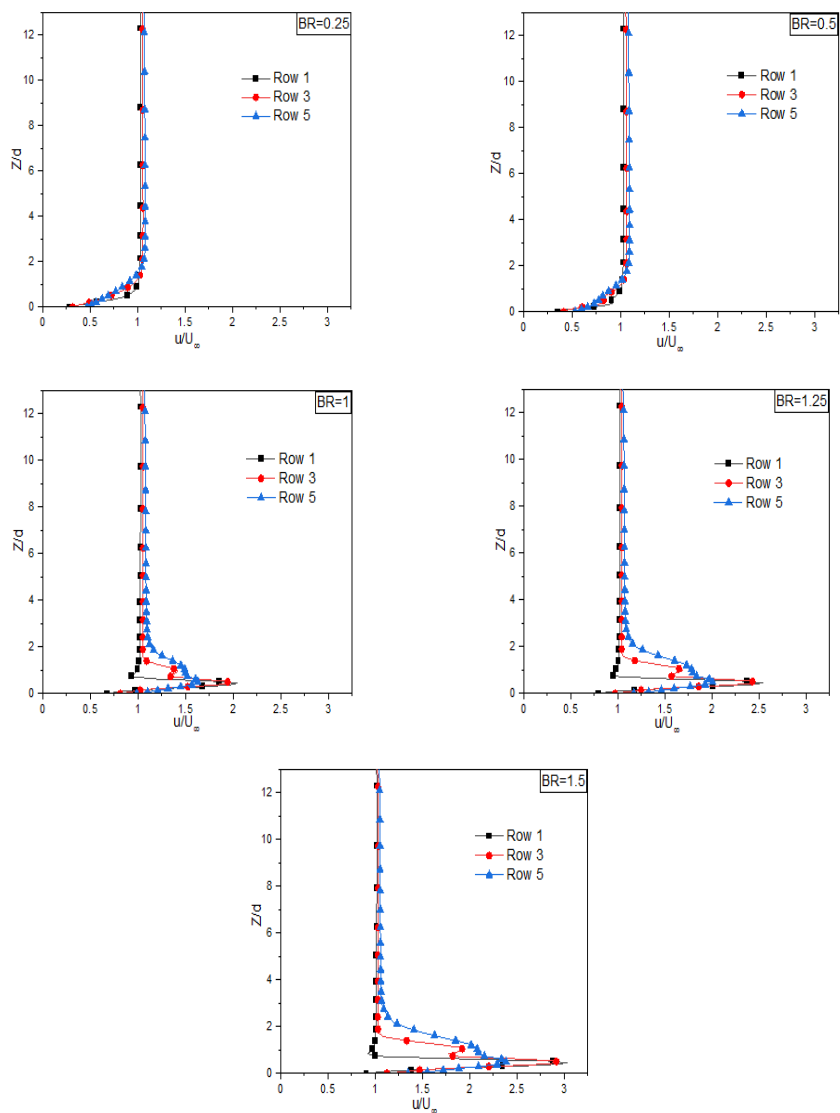


Fig.11 Velocity profiles downstream the effusion hole rows at different blowing ratios ($\alpha=30^\circ$)

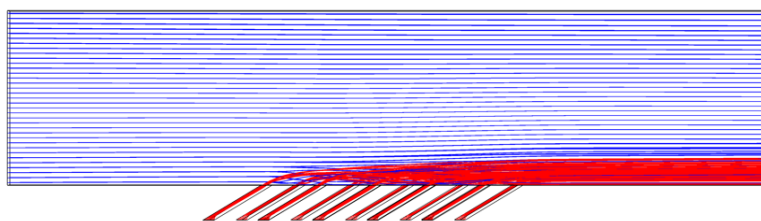


Fig.12 Velocity field streamlines along the solution domain for blowing ratio 1.5 at injection angle 30°

6.3 Temperature Boundary Profile

From the Fig. 13, it is observed for the row 1, the minimum penetration height is seen due to less interaction of coolant with the mainstream flow. Further in the downstream rows in streamwise direction at rows 3 and 5 the interaction between the fluid increases by interaction with the coolant flow from upstream rows together and this affects the flow field topology. From the Fig. 13 the kidney shaped counter rotating vortex pair is visible in each effusion holes and this flattens downstream in the streamwise direction due to addition of coolant flow coming from upstream holes. In the Fig.14 a coolant core formation is noticeable near the wall region $Z/d > 3$ as the coolant is injected from the effusion holes. The variations in temperature boundary layer are seen in the region $Z/d > 3$ and the outer portion $Z/d < 3$ remains unchanged as of mainstream flow. It is interesting to note that the thermal boundary layer thickness increases as BR increases from 0.25 to 1.5.

6.4 Effect of Injection Angle (α) on Adiabatic Effectiveness

Simulations have been carried for different blowing ratios (BR) at injection angles (α) of 30° and 60° . The values of adiabatic effectiveness obtained at blowing ratio (BR) equal to 0.25 have been plotted in Fig. 15. Adiabatic effectiveness (η) is high at $\alpha=30^\circ$ as compared to that at $\alpha=60^\circ$. It is an account of the fact that at low values of injection angle the coolant flow stays for more intervals and has more interaction with the main flow as compared to that at high values of injection angles. This leads to higher values of convection heat transfer at low injection angles. Unlike this at $\alpha=60^\circ$ (i.e., at high value of injection), the coolant attaches to the surface with less interactions with the main flow. In the region (X_2), there is maximum difference in the peak values of adiabatic efficiency (η) as compared to that in the region (X_3). The reason being that in the region (X_2) there is more interaction with the main flow at lower values of injection angles.

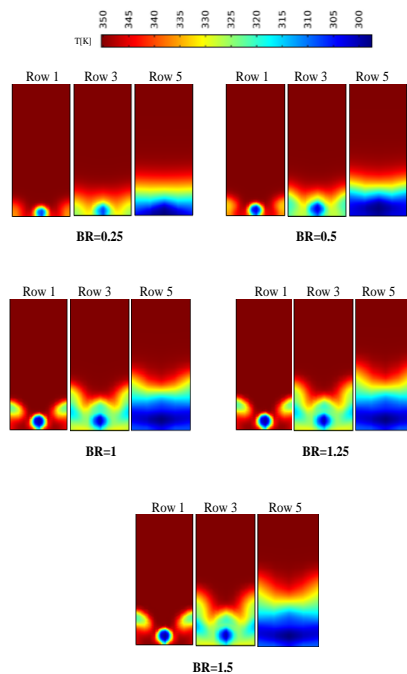


Fig. 13 Development of temperature fields on the YZ plane for different blowing ratios at $\alpha=30^\circ$

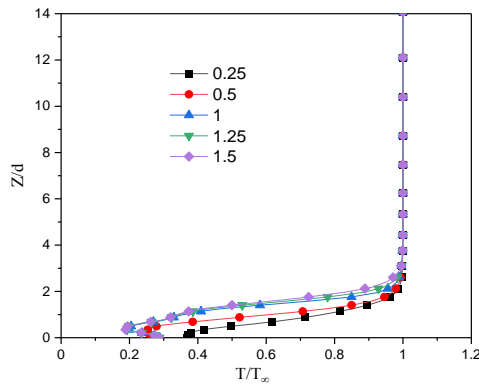


Fig. 14 Normalized Temperature boundary profiles at row 5 for $\alpha=30^\circ$

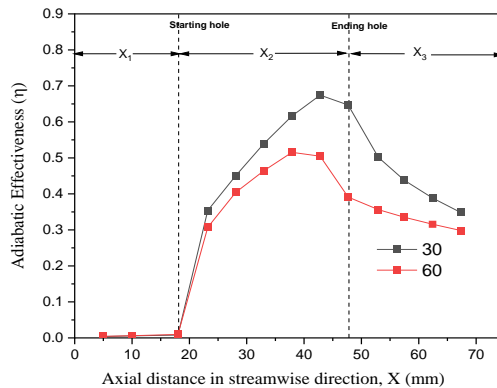


Fig. 15 Comparison of centerline adiabatic effectiveness at blowing ratio (BR) of 0.25 for different injection angles

6.5 Area-Averaged Adiabatic Effectiveness ($\bar{\eta}$)

The Fig. 16 shows the plot between the area-averaged adiabatic effectiveness ($\bar{\eta}$) at different BR in the regions X_2 and X_3 . It is observed that in the region X_2 , the $\bar{\eta}$ value is higher for low BR compared to high BR. The value of area-averaged adiabatic effectiveness ($\bar{\eta}$) is 0.49, 0.48, 0.47, 0.44 and 0.43 for blowing ratios 0.25, 0.5, 1.0, 1.25 and 1.5 respectively. But opposite behavior is observed in region X_3 . The value of area-averaged adiabatic effectiveness ($\bar{\eta}$) is 0.44, 0.58, 0.70, 0.71 and 0.71 for blowing ratios 0.25, 0.5, 1.0, 1.25 and 1.5 respectively. For both injection angles 30° and 60° it is observed that the $\bar{\eta}$ increases with increase in BR. However, value of $\bar{\eta}$ for 30° injection angle is more than of injection angle 60° . For higher value of BR, the large amount of coolant mass flow is injected through effusion holes which increases the thermal film layer this provide and ensures proper protection for combustion liners in the combustion chamber.

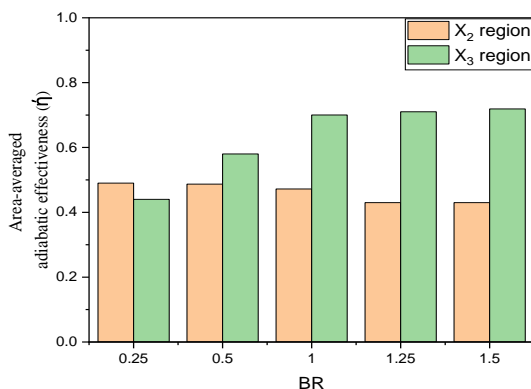


Fig. 16 Area-averaged adiabatic effectiveness ($\bar{\eta}$) with blowing ratio (BR) in the effusion region (X_2) and downstream region of effusion holes (X_3)

7. Conclusions

Computational investigations are carried to study the effect of blowing ratio (BR) and injection angle (α) on effusion cooling system of gas turbine combustor liners. The temperature and velocity profile shapes were obtained through simulation measured at different sections in streamwise direction for range of blowing ratios. The adiabatic effectiveness has been evaluated accordingly for all the cases.

The conclusions of the study are as follows:

- The adiabatic effectiveness is zero in the upstream region (X_1) as there is no coolant flow on the adiabatic surface.
- In the effusion region (X_2), the adiabatic effectiveness is high for low blowing ratios and the tendency decreases as the blowing ratio increases from 0.25 to 1.5. In the region (X_3) downstream of effusion region the value of adiabatic effectiveness is low for low blowing ratio and the value increases as the blowing ratio increases from 0.25 to 1.5.
- The adiabatic efficiency is more at injection angle of 30° as compared to that at injection angle of 60° .

Blowing ratio is a key parameter in the design aspect of effusion cooling system. The overall gas turbine efficiency will be impacted by the large need for coolant mass flow rate at high blowing ratios. For low blowing ratios, low coolant mass flow rate will not be enough to protect the liners. So, the selection of a blowing ratio for effusion system should be considered carefully to provide and ensure proper protection of combustion chamber.

Nomenclature

d	m	Diameter of effusion hole
t	m	Thickness of effusion plate
S_x/d	-	Streamwise distance between two adjacent holes in x-direction
S_y/d	-	Spanwise distance between two adjacent holes in y-direction
T	K	Temperature
U	m/s	Flow velocity
X	m	Streamwise coordinate
Y	m	Spanwise coordinate

Z	m	Normal coordinate
BR	-	Blowing ratio
DR	-	Density ratio
VR	-	Velocity Ratio
Greek letters		
α	$^{\circ}$	Injection angle
η	-	Adiabatic effectiveness
$\bar{\eta}$	-	Area-averaged adiabatic effectiveness
ρ	kg/m ³	Density
Subscripts		
wt		Wall temperature on adiabatic surface of effusion plate
c		Coolant flow
∞		Mainstream flow

References

- [1] Yuen CHN, Martinez-Botas RF. Film cooling characteristics of rows of round holes at various streamwise angles in a crossflow: Part I. Effectiveness. *International Journal of Heat and Mass Transfer*, 2005; 48(23-24), 4995-5016. <https://doi.org/10.1016/j.ijheatmasstransfer.2005.05.019>
- [2] Qayoum, A, Panigrahi P. Experimental investigation of heat transfer enhancement in a two-pass square duct by permeable ribs. *Heat Transfer Engineering*, 2019; 40:8 640-651. <https://doi.org/10.1080/01457632.2018.1436649>
- [3] Rasool A, Qayoum A. Numerical analysis of heat transfer and friction factor in two-pass channels with variable rib shapes. *Journal homepage: http://iieta.org/Journals/IJHT*, 2018; 36:1 40-48. <https://doi.org/10.18280/ijht.360106>
- [4] Rasool A, Qayoum A. Numerical Investigation of Fluid Flow and Heat Transfer in a Two-Pass Channel with Perforated Ribs. *Pertanika Journal of Science & Technology*, 2018; 26:4.
- [5] Röger M, Buck R, Müller-Steinhagen H. Numerical and experimental investigation of a multiple air jet cooling system for application in a solar thermal receiver, 2005; 863-876. <https://doi.org/10.1115/1.1928910>
- [6] El-Gabry LA, Kaminski DA. Numerical investigation of jet impingement with cross flow-comparison of yang-shih and standard k- ϵ turbulence models. *Numerical Heat Transfer, Part A*, 2005; 47:5 441-469. <https://doi.org/10.1080/10407780590891254>
- [7] Silieti M, Divo E, Kassab AJ. Numerical investigation of adiabatic and conjugate film cooling effectiveness on a single cylindrical film-cooling hole. In *ASME International Mechanical Engineering Congress and Exposition*, 2004; 4711: 333-343. <https://doi.org/10.1115/IMECE2004-62196>
- [8] Baldauf S, Scheurlen M, Schulz A, Wittig S. Heat flux reduction from film cooling and correlation of heat transfer coefficients from thermographic measurements at engine like conditions. In *Turbo Expo: Power for Land, Sea, and Air*, 2002; 36088: 163-174. <https://doi.org/10.1115/GT2002-30181>
- [9] Ligrani P, Goodro M, Fox M, Moon HK. Full-coverage film cooling: film effectiveness and heat transfer coefficients for dense and sparse hole arrays at different blowing ratios., *ASME J. Turbomach.*134, 2012; 061039. <https://doi.org/10.1115/1.4006304>
- [10] Bohn D, Kusterer K. Blowing ratio influence on jet mixing flow phenomena at the leading edge. In *37th Aerospace Sciences Meeting and Exhibit*, 1999; 670. <https://doi.org/10.2514/6.1999-670>
- [11] Bailey JC, Intile J, Fric TF, Tolpadi AK, Nirmalan NV, Bunker RS. Experimental and numerical study of heat transfer in a gas turbine combustor liner. *J. Eng. Gas Turbines Power*, 2003; 125:4 994-1002. <https://doi.org/10.1115/1.1615256>

- [12] Liu X, Zheng H. Influence of deflection hole angle on effusion cooling in a real combustion chamber condition. *Thermal Science*, 2015; 19:2 645-656. <https://doi.org/10.2298/TSCI140107043L>
- [13] Andrews GE, Alikhanizadeh M, Tehrani FB, Hussain CI, Azari MK. (1988). Small diameter film cooling holes: the influence of hole size and pitch. *International Journal of Turbo and Jet Engines*, 1998; 5:1-4 61-72. <https://doi.org/10.1515/TJJ.1988.5.1-4.61>
- [14] Andrews GE, Asere AA, Gupta ML, Mkpadi MC. Full coverage discrete hole film cooling: the influence of hole size. In *Turbo Expo: Power for Land, Sea, and Air American Society of Mechanical Engineers*, 1985; 79405: V003T09A003. <https://doi.org/10.1115/85-GT-47>
- [15] Andrews GE, Gupta ML, Mkpadi, MC. Full coverage discrete hole wall cooling: Cooling effectiveness. In *Turbo Expo: Power for Land, Sea, and Air American Society of Mechanical Engineers*, 1984; 79498; V004T09A018. <https://doi.org/10.1115/84-GT-212>
- [16] Lin Y, Song B, Li B, Liu G, Wu Z. (Investigation of film cooling effectiveness of full-coverage inclined multihole walls with different hole arrangements. In *Turbo Expo: Power for Land, Sea, and Air*, 2003; 36886: 651-660. <https://doi.org/10.1115/GT2003-38881>
- [17] Zhang C, Lin Y, Xu Q, Liu G, Song B. Cooling effectiveness of effusion walls with deflection hole angles measured by infrared imaging. *Applied thermal engineering*, 2009; 29:5-6 966-972. <https://doi.org/10.1016/j.applthermaleng.2008.05.011>
- [18] Leger B, Miron P, Emidio JM. Geometric and aero-thermal influences on multiholed plate temperature: application on combustor wall. *International Journal of Heat and Mass Transfer*, 2003; 46:7 1215-1222. [https://doi.org/10.1016/S0017-9310\(02\)00396-4](https://doi.org/10.1016/S0017-9310(02)00396-4)
- [19] Gustafsson KB. Experimental studies of effusion cooling. Chalmers University of Technology, 2001.
- [20] Sasaki M, Takahara K, Kumagai T, Hamano M. Film cooling effectiveness for injection from multirow holes, *J. Eng. Power* 101, 1979; 101-108. <https://doi.org/10.1115/1.3446430>
- [21] Cerri G, Giovannelli A, Battisti L, Fedrizzi R. Advances in effusive cooling techniques of gas turbines. *Applied Thermal Engineering*, 2007; 27:4 692-698. <https://doi.org/10.1016/j.applthermaleng.2006.10.012>
- [22] Kumar KY, Qayoum A, Saleem, S, Qayoum F. Effusion Cooling In Gas Turbine Combustion Chambers-A Comprehensive Review. In *IOP Conference Series: Materials Science and Engineering*, 2020; 804:1 012003. <https://doi.org/10.1088/1757-899X/804/1/012003>
- [23] Scrittore JJ, Thole KA, Burd SW. Investigation of velocity profiles for effusion cooling of a combustor liner, *Journal of Turbomachinery*.129, 2007; 518-526. <https://doi.org/10.1115/1.2720492>
- [24] Pietrzyk JR, Bogard DG, Crawford ME. Hydrodynamic measurements of jets in crossflow for gas turbine film cooling applications, *J. Turbomach* 111, 1989; 139-145. <https://doi.org/10.1115/1.3262248>

Blank Page



Synthesis and characterization of high-quality multi layered graphene by electrochemical exfoliation of graphite

Bisma Ali^{1, a}, Adnan Qayoum^{*1, b}, Shahid Saleem^{1, c}, Fasil Qayoom Mir^{2, d}

¹Mechanical Engineering Department, National Institute of Technology Srinagar, J&K, India-190006.

²Chemical Engineering Department, National Institute of Technology Srinagar, J&K, India-190006

Article Info

Article history:

Received 11 Jan 2022

Revised 16 Mar 2022

Accepted 07 April 2022

Keywords:

Graphite;
Electrochemical
exfoliation;
Graphene;
Intercalation;
Synthesis

Abstract

Graphene is an emerging carbon material, with wide range of practical applications on a large scale. The yield and quality control of the resultant graphene are significant trade-offs in graphene production. The research is focused on fabricating high quality multi layered graphene using an electrochemical exfoliation approach by adjusting the electrolysis parameters, such as type, composition, concentration of electrolyte and DC Voltage. An aqueous solution of 0.3M (H₂SO₄) and 30% KOH has been used as an electrolyte. A constant DC voltage supply of +10 V has been incorporated for the electrolysis for investigation of the relationship between characterization and synthesis parameters. The structure, chemical properties and morphology of the synthesized graphene material were investigated using XRD, FTIR, Raman, UV-vis spectroscopy, FESEM, AFM and TEM/HRTEM techniques. FTIR spectrum showed the appearance of C-O and C-OH functional groups, along with C=C stretching of hexagonal network of graphene. The electronic transition of $\pi-\pi^*$ and $n-\pi^*$ are visible in UV-vis spectra of graphene. XRD pattern of graphene sample exhibits a characteristic peak at $2\theta = 26.45$, corresponding to a 3.412 Å interlayer distance. The development of multi-layered graphene was demonstrated by the shape and location of the 2D band in the Raman spectra. These studies reveal a comprehensive and detailed morphology showing the wrinkled layered surface with crumpled edges of few layer graphene. Further, this study reinforces the tremendous potential of electrochemical exfoliation for fabricating huge amounts of relatively perfect graphene structures for applications of practical importance.

© 2022 MIM Research Group. All rights reserved.

1. Introduction

To achieve Graphene, a single layer form of sp² hybridized carbon atoms arranged in a two dimensional hexagonal honeycomb crystal lattice, has gained huge interest owing to its intriguing properties in various applications [1]. The exceptional electrical, mechanical, thermal and optical properties make graphene use in multiple technological applications [2-5]. Graphene has a number of distinct physical and chemical properties such as, high intrinsic carrier mobility (200,000 cm²V⁻¹s⁻¹), specific surface area of the order of 2630 m²g⁻¹, an excellent mechanical strength (1,100Gpa), superior thermal conductivity (5,000 Wm⁻¹K⁻¹), high electrical conductivity (10⁻⁶ Ω cm) and is nearly transparent to visible light (97.7%) [5-8]. Graphene show promising application in several fields such as solar cells [9-10], sensors [11-12], optical devices [13], super capacitors [14-15], bioscience/biotechnologies [16-17] and electronic devices [18] etc. A. K Geim and K. S. Novoselov discovered graphene in 2004 using a scotch tape method via mechanical exfoliation [7]. This method was reported to produce high-quality graphene

*Corresponding author: adnan@nitsri.ac.in

^a orcid.org/0000-0003-1124-0934; ^b orcid.org/0000-0002-4894-3425; ^c orcid.org/0000-0001-6998-0324;

^d orcid.org/0000-0002-3211-2395

DOI: <http://dx.doi.org/10.17515/resm2022.384na0121>

Res. Eng. Struct. Mat. Vol. 8 Iss. 3 (2022) 447-462

with excellent mobility. The major limitations of this approach are its time consuming and low manufacturing yield [19]. Producing graphene without collateral damage to its structure on large scale with desirable properties, and with few functional groups is still a significant challenge.

Various methods for producing graphene with a huge surface area and exceptional quality have been identified in recent years. Some prominent methods are chemical vapor deposition (CVD) [20], mechanical exfoliation [21], liquid phase exfoliation [22-23], epitaxial growth [24], chemical exfoliation [25-26] and electrochemical exfoliation [27-28]. Mechanical exfoliation and epitaxially grown graphene results in highly controllable and perfect structured graphene layers [21-29] but are not suitable for high-yield production. CVD is a scalable method using catalytic metal substrates for producing large area and relatively perfect structure graphene [30-31]. The requirement of elevated temperature, sacrificial metal, and multistep transfer operations onto the appropriate substrates is, however, a key disadvantage of this approach. The transition of graphene from the fabrication process to the end-use substrate frequently introduces defects that severely damage the properties of synthesized graphene.

Chemical exfoliation methods based on Hummer's approach, involves oxidizing graphite to thin hydrophilic graphite oxide accompanied by thermal or chemical reduction, has come as new area of research anticipated by the beneficial cost effective and solution treated synthesis [32-33]. The oxidation method may induce significant structural defects and inevitably introduces several functional groups severely damaging the honey comb pattern of graphene, resulting in poor electric conduction. Although the Liquid phase exfoliation process can manufacture multi layer graphene, yet the production of fabricated graphene remains moderate [34], and the utilization of elevated boiling point organic solvents posing a significant challenge.

However, majority of these methods go through a series of limitations, such as lower yield, attached functional groups, agglomerated sheets and higher defect densities etc. To control above-mentioned drawbacks, research has been carried to develop a novel, green, economic, scalable and highly productive route for graphene synthesis for large-scale graphene synthesis. Electrochemical exfoliation of graphite has recently developed as a viable method for producing graphene using mild chemical processes on an industrial scale with less defect and an economical hierarchical structure with minimal impact on environmental pollution [11, 19, 27]. The electrochemical method relies on the expansion of the interlayer gap among graphite layers through ion intercalations. Ion intercalations are mainly influenced by the type, composition, concentration and nature of electrolyte used in an electrochemical process [35-36].

Various electrolytes, including, ionic liquids [37-38], acidic liquids and elevated temperature molten salts [27-39] were utilized in the electrochemical process. In ionic liquids, electrochemical exfoliation produces graphene with a low yield and small lateral dimensions. Acidic electrolytes, on the other hand, can produce better-quality graphene. Acidic nature results not only severe exfoliation but also ungovernable exfoliation due to incomplete intercalation. Therefore, it is important to determine the experimental conditions with proper electrolyte system for obtaining the better quality for bulk fabrication of graphene material.

In the past, chemical intercalation of formic acid or sulfuric acid aided in the expansion of graphite, followed by subsection of high heat. Graphite was rapidly expanded due to the formation of gaseous species released from the intercalant [40-41]. However, higher concentration of sulfuric solution affects exfoliation of graphite into much thinner graphene sheets because of the presence of SO_4^{2-} [42], while the high acidity of sulfuric

acid results in structural disorder which is highly undesirable. As such, KOH is added to suppress oxidation of graphene layers, on account of its possible reducing effect [43].

Present study reports the H₂SO₄-KOH solution system to fabricate graphene via highly efficient electrochemical exfoliation route by reducing the utilization of corrosive and toxic chemicals. By controlling synthesis parameters such as applied electric potentials, composition of electrolyte, concentration and type of electrolyte, graphene material with few layers number with less defect and with large lateral size has been obtained. The study involves tuning of the parameters for synthesis leading to better quality of graphene. Furthermore, the quality of produced graphene has been assessed using a variety of techniques including XRD, FTIR, UV-vis, Raman, FE-SEM, TEM/HRTEM, and AFM.

2. Experimental Procedure

2.1. Materials

A high purity graphite foil (measuring 0.3×300×300 mm and of purity of 99.9%) was purchased from AST Works. The commercially available reagents Sulfuric acid (H₂SO₄) and Potassium Hydroxide (KOH) were procured from AVANTOR, India ltd. Platinum wire (measuring 0.5mm×100mm) was purchased from Polymet Galvanotech, Germany.

2.2. Synthesis of Graphene

For the fabrication of graphene, a two-electrode arrangement was employed, with graphite foil as the electrode material and supply of natural graphite, and platinum as the counter electrode. As illustrated in the Figure (1a, 1b and 1c), the anode and cathode are made of pure graphite foil and platinum wire, which are separated by 4 cm in the electrolyte. Both sulfuric acid (H₂SO₄) and potassium hydroxide (KOH) are combined as electrolytes. Using Sulphuric acid alone as electrolyte produce graphene with high structural defects due to intense oxidation [44]. As a result, Potassium hydroxide (KOH) is utilized to counteract reduce the acidic electrolyte's oxidative effects [45]. The experimental setup for electrochemical exfoliation process is depicted in Figure 1.

Wires were used to connect the electrodes to the DC power source, and immersed in the electrolyte solution. Table 1 shows the various parameters investigated for better graphene production via electrochemical exfoliation of graphite. These parameters include voltage and concentration of the electrolytes. It has been observed that the electrolyte solution with the concentration of 0.3M (H₂SO₄) and 30% KOH at a DC supply of +10 V provides best exfoliation efficiency. The electrochemical exfoliation was conducted at room temperature with a constant Voltage of +10 until the anode was exhausted.

The gradual exfoliation of the graphite electrode is initiated by applying a +10 V DC voltage across the cathode and anode electrodes. In the electrolyte solution, the graphitic flakes begin to expand, dissociate substantially, and spread (Figure 1c). The graphene powder is extracted from the beaker using vacuum filtration and rinsed with DI water multiple times to eliminate any remaining salts. The graphene powder is collected and dispersed in ethanol. Further sonication is carried for 30 minutes. The mixture has been found to be stable for several weeks without apparent agglomeration (Figure 1d). The suspension was also centrifuged for 20 minutes at a low speed of 1000 rpm to remove any remaining salt ions from the dispersion. After drying the sample at 60°C in an oven to remove any traces of water, dry graphene powder is obtained. Figure 2 depicts a schematic of the entire electrochemical process.

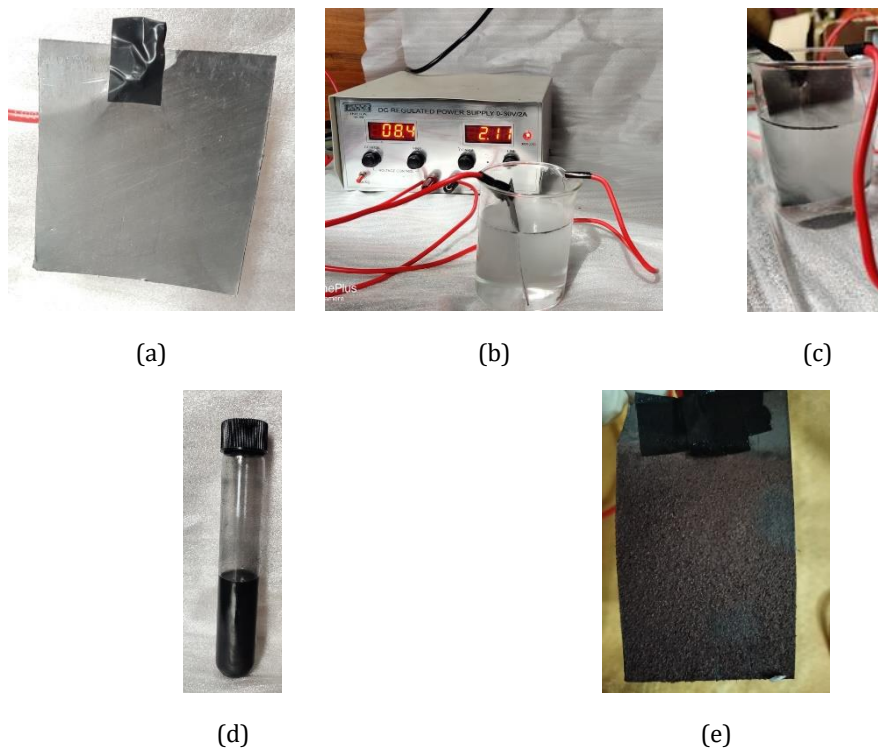


Fig. 1 (a) Optical image of graphite foil before electrochemical exfoliation, (b) Experimental set-up of the electrochemical exfoliation process, (c) Graphene flakes floating on top of electrolyte, (d) Synthesized graphene material dispersed in ethanol and (e) Image of graphite foil obtained after exfoliation process

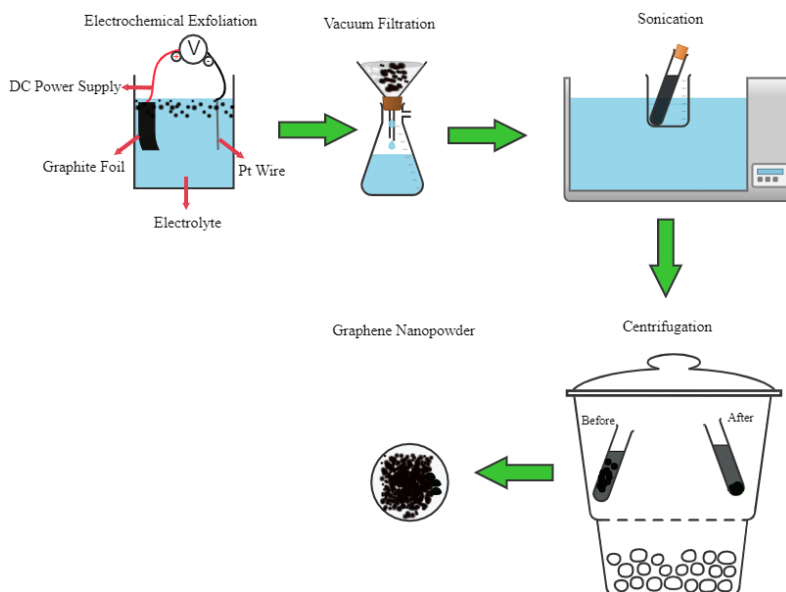


Fig. 2 Schematic illustration of the electrochemical exfoliation process of graphene

Table 1. Experimental parameters for the electrochemical exfoliation

Voltage	Concentration of H ₂ SO ₄	Concentration of KOH
10	0.3M H ₂ SO ₄	30 % KOH
10	0.3M H ₂ SO ₄	35 % KOH
12	0.3M H ₂ SO ₄	40% KOH

2.3. Material Characterization of Electrochemically Exfoliated Graphene

Fourier transform infrared (FTIR) spectra recorded on Perkin Elmer (UATR Two) spectrometer with a typical wavenumber of 500 cm⁻¹ to 4000 cm⁻¹ were used to investigate the presence of functional groups and bond stretch interactions of the synthesized graphene sample. The optical properties of exfoliated graphene were examined by Ultraviolet-visible (UV-vis) absorption spectrum obtained on a Shimadzu ISR-603 spectrometer. UV-vis spectra were recorded in the range of wavelength from 200 nm to 850. X-Ray diffraction (XRD) using Cu K-beta radiation ($\lambda = 1.541858$) was used to investigate structural parameters and phase analysis using a Rigaku diffractometer. With a step width of 0.200 degree and a scan speed of 21.6746 degrees per minute, XRD patterns were obtained at 40 kV, 30mA with angles 2θ ranging from 10 to 70. The degree of disorder in the crystal structure was examined using Raman spectroscopy. At a wavelength of ($\lambda = 532$ nm), the Raman spectra were obtained using a Renishaw inVia Raman spectrometer with an Argon-Krypton laser. The surface morphology and microstructures of graphite anode was investigated by field emission scanning electron microscope (FESEM, ZEISS GeminiSEM 500). The morphology was acquired on graphene material via atomic force microscope (AFM, MFP3D-BIO) and a (TEM, Jeol JEM-1400) was used for Transmission electron microscope analysis at an accelerating voltage of 120 kV.

3. Results and Discussion

3.1. Mechanism Adopted for Electrochemical Exfoliation of Graphite Foil Anode Into Multi Layered Graphene Sheets

In this study, an electrolyte solution of H₂SO₄ and KOH has been employed for the electrochemical exfoliation of graphite. When positive potential +10 V is applied, the oxidation occurs at the plane periphery or grain structure of the graphite foil anode. Under the electric effect, the solvated ions intercalate into graphite interlayer's in a sequence of well-defined steps. The internal stress induced by the intercalated ions aids the expansion of graphite anode by weakening the Vander wall forces between the successive graphite layers. OH⁻ ions generated during the electrolysis process, on the other hand, open the edges due to electrostatic contact. The co-intercalation of SO₄²⁻, OH⁻, and H₂O contribute to the more effective intercalation, thereby allowing more particle insertion into graphite layers and thereby expanding graphite layer more rapidly by destroying the long-range morphology related to the c-axis. Finally, on account of the voltage these gases overcome numerous Vander wall forces within graphite layers, and thus facilitate entire exfoliation of graphite anode to be separated as isolated graphene sheets.

3.2 Morphological Changes in Different Exfoliation Time

Figure 3 presents the structural morphology changes at different exfoliation times using SEM. These changes confirm with the procedure carried during the present study. The morphology changes of graphite foil anode for a time span of (1-5 min) at various scales have been captured. It is observed that as soon as a voltage of + 10 V is supplied to graphite foil the morphology at sides and edges changes abruptly within 1 min (see

Figure 3a and 3d). The structure exhibits irregular and non-uniform microstructures including network of ripples and corrugated nets mostly on the edges of graphite anode, on account of the deformation due to exfoliation and restacking processes. Due to the visible gas evolution leading to the rapid expansion and rippling of the graphite layers, cracks, bulges, and crumples appear on the surface and boundaries of the graphite anode within 1 minute (Figure 3b and 3e). A significant amount of graphene has left the anode and diffused in the electrolyte solution as the time passes from 3 to 5 minutes. Curled morphology with thin, wrinkled tissue-like features has been achieved. These observations strongly lend credibility to the logic corners and surface of graphite electrode oxidize throughout the electrochemical process, opening the sites of oxidation, promoting intercalation into graphite and subsequently towards the exfoliation of graphene sheets.

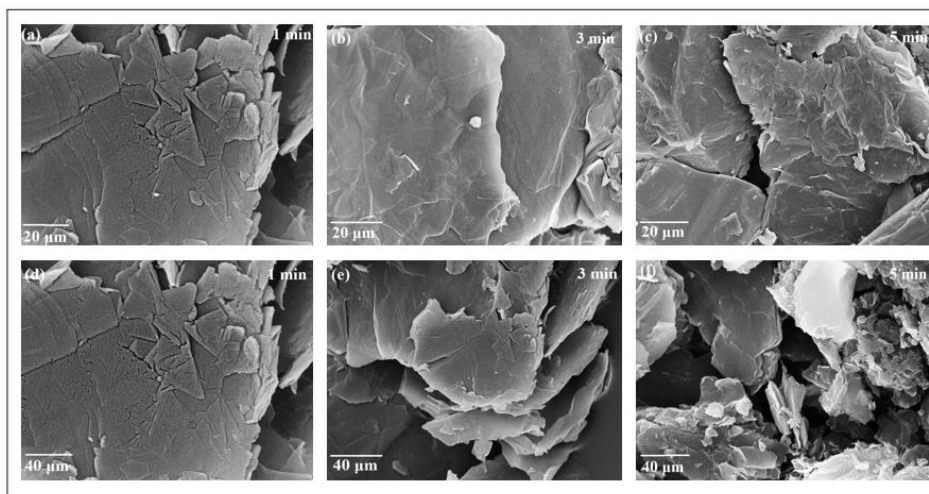


Fig. 3 SEM images of the graphite foil electrode after applying a DC voltage +10 V for 1 min (a, d), 3 min (b, e) and 5 min (c, f) in solution respectively. Scale bar: (a-c) 20 μ m, (d-f) 40 μ m

3.3. Structural Characterization of Electrochemically Exfoliated Graphene

3.3.1. X-ray Diffraction (XRD) Analysis

The XRD pattern obtained for both natural graphite and electrochemically treated graphite is illustrated in Figure 4. XRD provides the crystalline structure of the natural graphite foil and electrochemically exfoliation graphene powder. The pattern of the graphite exhibits a well-defined diffraction pattern at $2\theta = 26.7^\circ$ for the plane (002) with the interlayer d-spacing of 3.347 Å and a less significant and wide diffraction peak at $2\theta = 54.8^\circ$ with a d spacing of 1.6736 Å, as determined by Bragg's law.

$$n\lambda = 2d\sin\theta \quad (1)$$

where $n = 1$, λ is the wavelength, d is the interlayer distance of the lattices and θ is the Bragg's angle. This is in accordance with the interlayer distance of graphite according to JCPDS Card data base (00-041-1487). The synthesized graphene exhibits a significant peak centered at $2\theta = 26.45^\circ$ corresponding to the (002) plane and has an interlayer spacing of 3.412 Å. After the exfoliation of the graphene sheets, the diffraction peak reduces to a substantial order of magnitude, suggesting that the hexagonal lattice ring

may expand during exfoliation. This is a prerequisite to successful exfoliation of graphene [46, 47]. The XRD characterization indicates that the long-chain morphology of natural graphite around the *c*-axis has been successfully modified and results in the generation of few layer graphene. Using Scherrer's equation, the crystallite size of the sample is estimated from the full width half maximum (FWHM) of the diffraction peak corresponding to the 002 plane.

$$L = \frac{k\lambda}{B\cos\theta} \quad (2)$$

where, *L* is crystallite size (5.32 nm,) *k* is constant (*k*=0.89), *B* is FWHM.

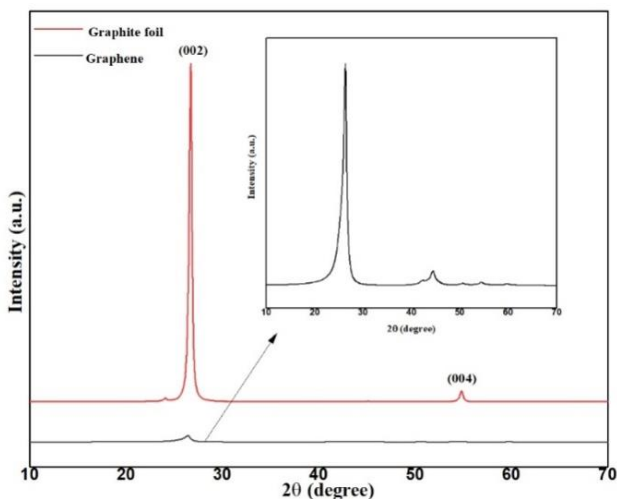


Fig. 4 XRD patterns of graphite foil and synthesized graphene powder

3.3.2. Ultra Violet-Visible Absorption (UV-vis) Analysis

Figure 5 depicts the UV-vis spectra of synthesized graphene. The absorption peaks in the spectra of exfoliated graphene are observed at two different wavelengths. The presence of characteristic peak at 250 nm is attributed to the electronic transition from π - π^* molecular orbital of aromatic C=C bond present in sp^2 domains of exfoliated graphene structure [13]. A broad peak shoulder around 320-350 nm is associated with n - π^* electronic transitions of C=O bonds present in the sp^3 network of hexagonal structure of exfoliated graphene [48]. Similar findings have been reported in the literature as well [49-50]. As shown in the inset of Figure 5, the optical band gap for the graphene sample is determined using a Tauc plot with a linear extrapolation. An approximate band gap observed ranges over 2.9-3.9 eV, showing an intrinsic semiconductor like characteristics [51] and making it suitable for electronic and optoelectronic applications.

3.3.3. Fourier Transform Infrared (FTIR) Analysis

FTIR spectroscopy were used to examine the functional groups and bond stretch interaction of the exfoliated graphene. Figure 6 displays a prominent and powerful peak at 1070 cm^{-1} in the FTIR spectra of produced graphene. This is due to the stretching vibration of C-O bond suggesting the presence of oxygen functional groups introduced through the electrochemical process of graphene [45-52]. The C=C bond stretching is

responsible for the peak at 1572 cm^{-1} [13]. The broad peak with a reduced intensity appears at 3178 cm^{-1} refers to the development of C-O-H stretching vibration and clearly shows the presence OH radicals in conjunction with exfoliated graphene [43]. The FTIR result indicates that the exfoliated graphene is of good quality with rare functional groups and the peaks obtained are characteristics of the graphene.

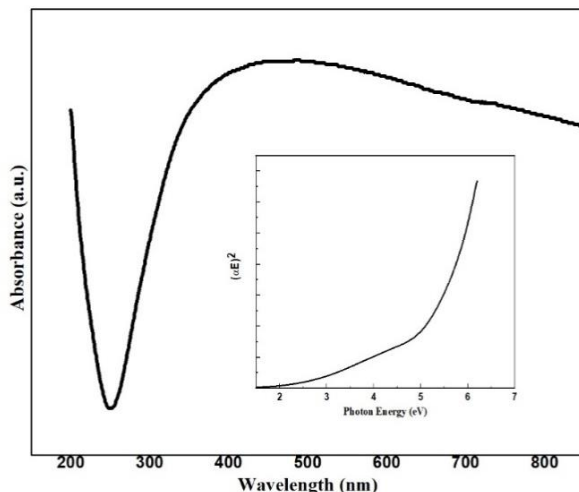


Fig. 5 UV-vis spectra of graphene with inset Tauc plot

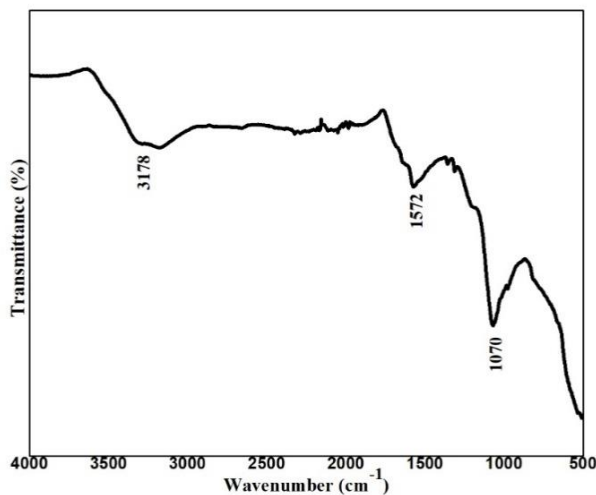


Fig. 6 FTIR spectrum of synthesized graphene

3.3.4. Raman Analysis

Figure 7 exhibits a Raman spectrum for the exfoliated graphene sample. The D, G, and 2D peaks in the Raman spectra of graphene material are three characteristic peaks [45-53]. The significant D band at 1350 cm^{-1} is due to structural disorders, edges, and graphitic surface oxidation, and is connected with the breathing mode of the sp^2 bound carbon atoms [38]. The G band at 1588 cm^{-1} arises from Stokes Raman scattering. The optical

phonon (E_{2g}) near the Brillouin zone centre is caused by the radial stretching of the C-C bond of sp^2 bonded Carbon [54]. The I_D/I_G ratio provides information about the degree of defects/disorder of Carbon structures [55]. The graphene material has an I_D/I_G ratio of 0.8, indicating the presence of structural defects. The G peak at 1588 cm^{-1} is more pronounced than the D peak at 1350 cm^{-1} , confirming that the synthesized material has a low defect content, lower than chemically or thermally reduced graphene [44-45]. The results obtained are in agreement with that obtained from the FTIR analysis which shows the presence of oxygen functionalities formed during the exfoliation process. These functional groups are related to the defects in the graphene material and cause partial disorder at the edges. The number of layers of graphene is determined by the shape and intensity of its 2D peak [39-56]. A double-resonant transition excites the 2D band, resulting in the formation of two phonons with opposite momentum. The presence of a 2D band at 2699 cm^{-1} and an intensity ratio of $I_{2D}/I_G = 0.147$ indicate that the synthesized material is made up of a few layers of graphene. This is also supported by the widening of the 2D band, as illustrated in Figure 7.

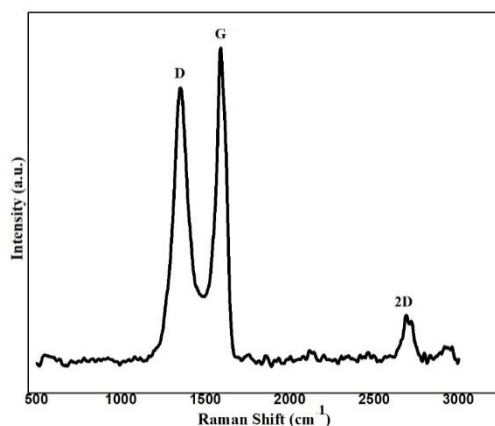


Fig.7 Raman spectrum of synthesized graphene

3.4. Morphological Characterization of Electrochemically Exfoliated Graphene

3.4.1. Scanning Electron Microscope (SEM) Analysis

The micromorphology of the surface of exfoliated graphene sample has been characterized by FESEM, AFM and TEM. Figure 8 displays FE-SEM micrograph of graphene deposited on a gold substrate. FE-SEM image reveals that the graphene comprises of haphazardly aggregated, thin crumpled/ruptured sheets and has wrinkled paper like morphology with well-arranged stacked sheets. Crumpling and scrolling are inherent characteristics of graphene sheets, as previously stated [45].

3.4.2. Transmission Electron Microscope (TEM) Analysis

Transmission electron microscope (TEM) images of graphene material is displayed in Figure 9a and 9b. Figure 9a depicts a typical low magnification TEM image of graphene material. The sample for TEM was prepared by suspending graphene in ethanol and sonicating it, after which a few drops of dispersion were dropped on a carbon coated copper TEM grid and dried at room temperature. A high magnification TEM image clearly shows a homogeneous wrinkled film-like structure (Figure 9b). Most of the sheets are

stacked multilayers. HR-TEM images were taken to determine the number of layers in a graphene sample. Figure 9c and 9d display the high-resolution TEM (HR-TEM) micrographs of the material, indicate that the electrochemically exfoliated material is preferably few layered graphene. The estimated d- spacing is 0.35 nm, which is consistent and similar with measurements given in the literature for graphene material and greater than regular graphite (0.335 nm). Exfoliated graphene was subjected to a selected area electron diffraction pattern, and the resulting SAED pattern is shown in Figure 9e. The hexagonal diffraction spots are seen in SAED pattern, originating from the sp^2 -bonded carbon frameworks, indicating that the synthesized material mainly contains few layer graphene and presence of few defects. These defects arise mainly due to the insertion of oxygen functionalities during the electrochemical process as observed in FTIR and Raman spectroscopy. The intensity of the spots with Bravais-Miller (hkl) indices (1-210) plane and then from the (0 101) plane show a typical 6-fold symmetric diffraction in the specified area electron diffraction, confirming the strong crystallinity of graphene [57]. Furthermore, the inner and outer spots' relative intensities were found to be < 1 , indicating multi-layered graphene [52, 58]

3.4.3. Atomic Force Microscope (AFM) Analysis

Drop casting graphene dissolved in ethanol on a mica substrate was used to create the graphene sample. Figures 10(a) and 10(b) show 2D and 3D AFM images of an exfoliated graphene sample. The graphene on the mica substrate is irregularly distributed, as shown by the height profile in Figure 10c. The topographic heights of the sheets, as determined by the cross-sectional contour, range from 1.8-5.67 nm, indicating few layer graphene. In this study, the electrochemically exfoliated graphene corresponds to a few layers of graphene. AFM indicated the appearance of irregularly formed graphene sheets with lateral dimensions reaching to a few nanometers and a non-uniform thickness.

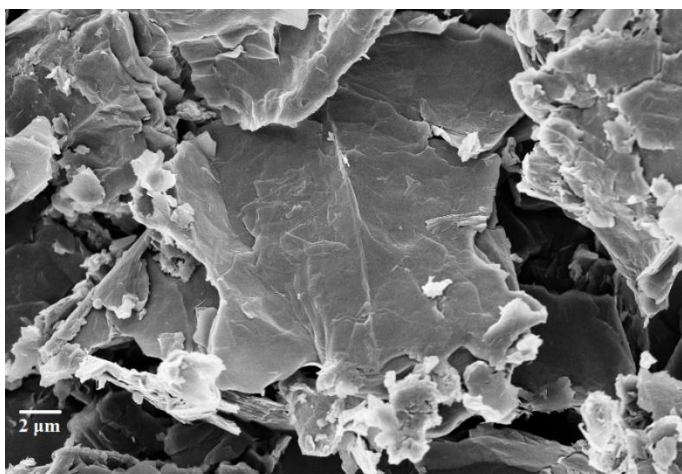


Fig. 8 SEM image of exfoliated graphene coated over a gold substrate

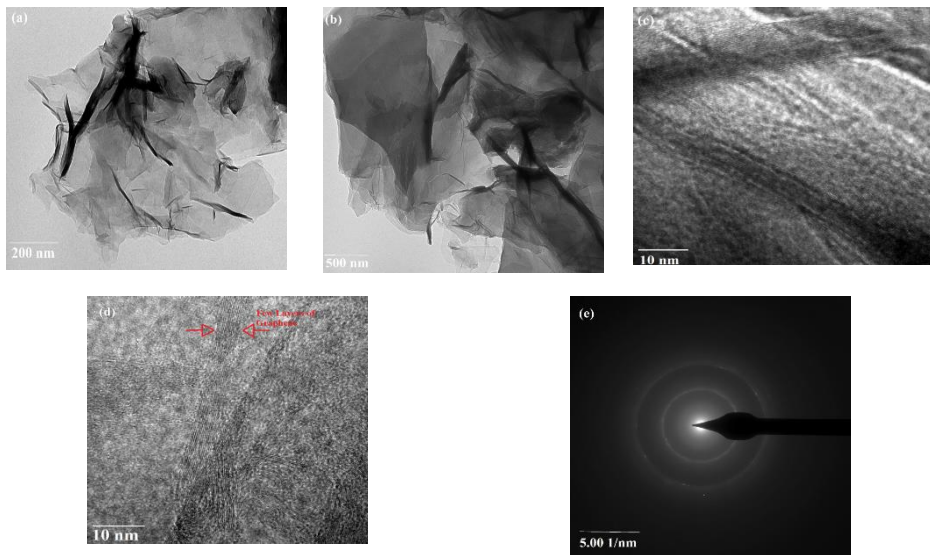
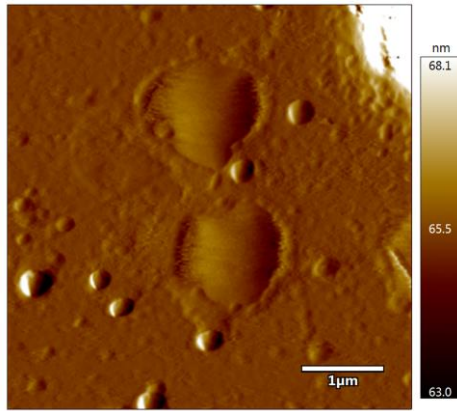


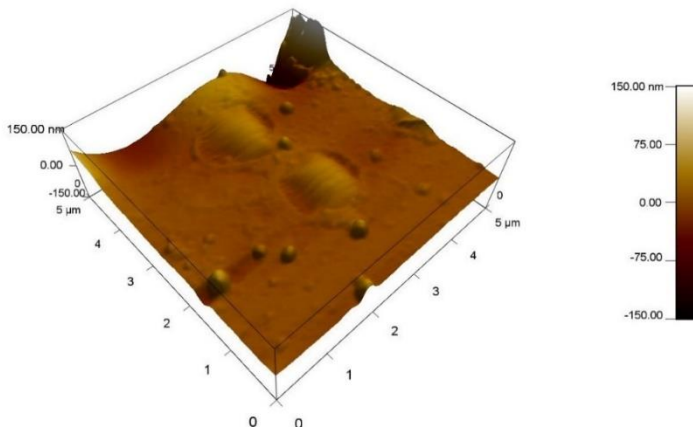
Fig. 9 (a, b) Typical TEM images of stacked graphene at low and high magnification (c, d) Typical HR-TEM images of exfoliated graphene (e) SAED pattern obtained for exfoliated graphene

4. Conclusions

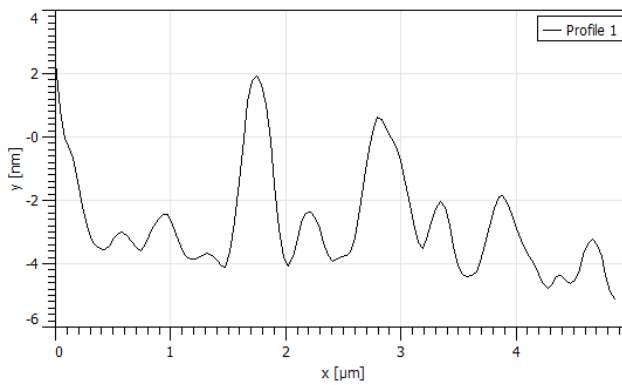
The current study uses a Sulfuric acid/ Potassium Hydroxide/ Water ($\text{H}_2\text{SO}_4/\text{KOH}/\text{H}_2\text{O}$) electrolyte system to demonstrate a simple, easy, green controlled, and environmental friendly technique for the industrial-scale production of graphene. This approach leads to low-cost large-scale production of multi layered graphene, with few defects and low degree of contamination at ambient reaction conditions. The study involves tuning of the parameters for synthesis leading to better quality of graphene. Exfoliation occurs due to the complicated interaction between anodic oxidation of SO_4^{2-} and OH^- ions. The exfoliated graphene has been characterized using XRD, UV-vis, Raman, FTIR, FE-SEM, AFM and TEM/HRTEM. The synthesized graphene exhibits a significant peak centered at $2\theta = 26.45$ corresponding to the (002) plane and has an interlayer spacing of 3.412 \AA . The $\pi-\pi^*$ and $n-\pi^*$ transitions are represented in the UV-vis absorption spectra by a strong peak at 250 nm and an adjacent band at $320-350 \text{ nm}$, respectively. Raman spectroscopy shows an electrochemically exfoliated graphene exhibits a lower $I_D/I_G = 0.8$ degree of defect, lower than chemically derived graphene. The G peak at 1588 cm^{-1} is more pronounced than the D peak at 1350 cm^{-1} , confirming that the synthesized material has low defect content, lower than chemically or thermally reduced graphene. From morphological studies, the layers with wrinkled surface and crumpled edges morphology of few layer graphene are seen. Further, the morphological change in different exfoliated time has been studied from FE-SEM. Raman and AFM analysis confirms that the graphene material is exfoliated successfully into multi layer graphene. The topographic heights of the sheets, as determined by the cross-sectional contour, range from $1.8-5.67 \text{ nm}$, indicating few layer graphene. The adopted method resulted in the synthesis of structurally controlled graphene material provides an important insight for scaling up the synthesis of graphene for industrial applications of practical importance.



(a)



(b)



(c)

Fig. 10 (a) 2D AFM image of exfoliated graphene deposited on mica substrate (b) Typical 3D AFM image of exfoliated graphene (c) Height profile of exfoliated graphene

Nomenclature

JCPDS	: Joint committee on powder diffraction standards
XRD	: X-ray diffraction
FE-SEM	: Field emission scanning electron microscope
TEM	: Transmission electron microscope
FTIR	: Fourier transform infra-red
AFM	: Atomic force microscope
HRTEM	: High resolution transmission electron microscope
CVD	: Chemical vapor deposition
SAED	: Selected area electron diffraction
KOH	: Potassium hydroxide
H ₂ SO ₄	: Sulfuric acid
FWHM	: Full width half maximum
d	: Interlayer distance
L	: Crystallite size

Greek Symbols

θ	: Diffraction angle
λ	: Wavelength (Angstrom)

References

- [1] Shao Y, Wang J, Engelhard M, Wang C, Lin Y. Facile and controllable electrochemical reduction of graphene oxide and its applications. *J Mater Chem*, 2010; 20: 743-748. <https://doi.org/10.1039/B917975E>
- [2] Bolotin KI, Sikes KJ, Jiang Z, Klima M, Fudenberg G, Hone J, Kim P, Stormer HL. Ultrahigh electron mobility in suspended graphene. *Solid State Commun*; 2008; 146: 351-355. <https://doi.org/10.1016/j.ssc.2008.02.024>
- [3] Chabot V, Kim B, Sloper B, Tzoganakis C, Yu A. High yield production and purification of few layer graphene by Gum Arabic assisted physical sonication. *Sci Rep*, 2013; 3:. <https://doi.org/10.1038/srep01378>
- [4] Balandin AA, Ghosh S, Bao W, Calizo I, Teweldebrhan D, Miao F, Lau CN. Superior thermal conductivity of single-layer graphene. *Nano Lett*, 2008; 8:902-907. <https://doi.org/10.1021/nl0731872>
- [5] Geim AK, Novoselov KS. The rise of graphene. *Nanosci Technol A Collect Rev from Nat Journals*, 2009; 11-19.
- [6] Allen JM, Vincent TC, Richard KB. (2010) Honeycomb carbon : A Review of Graphene What is graphene? *Chem Rev*, 2010; 110:132-145 <https://doi.org/10.1021/cr900070d>
- [7] Novoselov KS, Geim AK, Morozov SV, Jiang D, Zhang Y, Dubonos SV, Grigorieva IV, Firsov AA. Electric field effect in atomically thin carbon films. *Science*. 2004 Oct 22; 306 (5696): 666-9. <https://doi.org/10.1126/science.1102896>
- [8] Geim AK. Graphene: Status And Prospects A. K. Geim Manchester Centre for Mesoscience and Nanotechnology, University of Manchester, Oxford Road M13 9PL, Manchester, UK. *Prospects*, 2009; 324: 1-8.
- [9] Wang X, Zhi L, Tsao N, Tomovic Z, Li J, Mullen K. Transparent Carbon Films as Electrodes in Organic Solar Cells. *Angew Chemie*, 2008; 120: 3032-3034. <https://doi.org/10.1002/ange.200704909>
- [10] Wu J, Becerril HA, Bao Z, Zunfteng Wu, Yongsheng C, Peter P. Organic solar cells with solution-processed graphene transparent electrodes. *Appl Phys Lett*, 2008; 92:. <https://doi.org/10.1063/1.2924771>

- [11] Li SJ, Deng DH, Shi Q, Liu SR. Electrochemical synthesis of a graphene sheet and gold nanoparticle-based nanocomposite, and its application to amperometric sensing of dopamine. *Microchim Acta*, 2012; 177: 325-331. <https://doi.org/10.1007/s00604-012-0782-9>
- [12] Brownson DAC, Banks CE. Graphene electrochemistry: An overview of potential applications. *Analyst*, 2010; 135: 2768-2778. <https://doi.org/10.1039/c0an00590h>
- [13] Parveen N, Ansari MO, Cho MH. Simple route for gram synthesis of less defective few layered graphene and its electrochemical performance. *RSC Adv*, 2015; 5: 44920-44927. <https://doi.org/10.1039/C5RA06404J>
- [14] Liu J, Xue Y, Zhang M, Dai L. Graphene-based materials for energy applications. *MRS Bull*, 2012; 37: 1265-1272. <https://doi.org/10.1557/mrs.2012.179>
- [15] Zhang LL, Zhou R, Zhao XS. Graphene-based materials as supercapacitor electrodes. *J Mater Chem*, 2010; 20: 5983-5992. <https://doi.org/10.1039/c000417k>
- [16] Chen H, Müller MB, Gilmore KJ, Wallace GG, Li D. Mechanically strong, electrically conductive, and biocompatible graphene paper. *Adv Mater*, 2008; 20: 3557-3561. <https://doi.org/10.1002/adma.200800757>
- [17] Liu Z, Robinson JT, Sun X, Dai H. Pegylated nanographene oxide for delivery of water-insoluble cancer drugs. *J Am Chem Soc*, 2008; 130: 10876-10877. <https://doi.org/10.1021/ja803688x>
- [18] Hass J, De Heer WA, Conrad EH. The growth and morphology of epitaxial multilayer graphene. *J Phys Condens Matter*, 2008; 20: <https://doi.org/10.1088/0953-8984/20/32/323202>
- [19] Pingale AD, Owhal A, Katarkar AS, Belgamwar SU, Jitendra SR. Facile synthesis of graphene by ultrasonic-assisted electrochemical exfoliation of graphite. *Mater Today Proc*, 2021; 44: 467-472. <https://doi.org/10.1016/j.matpr.2020.10.045>
- [20] Ruan M, Hu Y, Guo Z, Dong R, Palmer J, Hankinson J, Berger C, De Heer WA. Epitaxial graphene on silicon carbide: Introduction to structured graphene. *MRS Bull*, 2012; 37: 1138-1147. <https://doi.org/10.1557/mrs.2012.231>
- [21] Chen J, Duan M, Chen G. Continuous mechanical exfoliation of graphene sheets via three-roll mill. *J Mater Chem*, 2012; 22: 19625-19628. <https://doi.org/10.1039/c2jm33740a>
- [22] Liang B, Liu K, Liu P, Qian L, Zhao G, Pan W, Chen C. Organic salt-assisted liquid-phase shear exfoliation of expanded graphite into graphene nanosheets. *J Mater*, 2021; 1-9. <https://doi.org/10.1016/j.jmat.2021.03.007>
- [23] Hernandez Y, Nicolosi V, Lotya M, Fiona MB, Zhenyu S, Sukanta D, I.T M, Brendan H, Michele B. High-yield production of graphene by liquid-phase exfoliation of graphite. *Nat Nanotechnol*, 2008; 3: 563-568. <https://doi.org/10.1038/nnano.2008.215>
- [24] Yang W, Chen G, Shi Z, Liu CC, Zhang L, Xie G, Cheng M, Wang D, Yang R, Shi D, Watanabe K, Taniguchi T, Yao Y, Zhang Y, Zhang G. Epitaxial growth of single-domain graphene on hexagonal boron nitride. *Nat Mater*, 2013; 12: 792-797. <https://doi.org/10.1038/nmat3695>
- [25] Stankovich S, Dikin DA, Piner RD, Kohlhaas KA, Kleinhammes A, Jia Y, Wu Y, Nguyen SBT, Ruoff RS. Synthesis of graphene-based nanosheets via chemical reduction of exfoliated graphite oxide. *Carbon* N Y, 2007; 45: 1558-1565. <https://doi.org/10.1016/j.carbon.2007.02.034>
- [26] Park S, Ruoff RS. Erratum: Chemical methods for the production of graphenes, *Nature Nanotechnology*. 2010; 5: 309.
- [27] Wu J, Wang H, Qiu J, Shao J, Zhang K, Yan L. Electrochemical exfoliation for few-layer graphene in molybdate aqueous solution and its application for fast electrothermal film. *Prog Nat Sci Mater Int*, 2020; 30: 312-320. <https://doi.org/10.1016/j.pnsc.2020.05.007>
- [28] Paredes JI, Munuera JM. Recent advances and energy-related applications of high quality/chemically doped graphenes obtained by electrochemical exfoliation

- methods. *J Mater Chem A*, 2017; 5: 7228-7242. <https://doi.org/10.1039/C7TA01711A>
- [29] Berger C, Song Z, Li X, Wu X, Brown N, Naud C, Mayou D, Li T, Hass J. Electronic confinement and coherence in patterned epitaxial graphene. *Science*, 2006; 312: 1191-1196. <https://doi.org/10.1126/science.1125925>
- [30] Hawaldar R, Merino P, Correia MR, Bdikin I, Gracio J, Mendex J, Martin-Gago JA, Singh MK. Large-area high-throughput synthesis of monolayer graphene sheet by Hot filament thermal chemical vapor deposition. *Sci Rep*, 2012; 2: 2-10. <https://doi.org/10.1038/srep00682>
- [31] Yoon JC, Lee JS, Kim SI, kwang H.K, Ji HJ. Three-dimensional graphene nano-networks with high quality and mass production capability via precursor-assisted chemical vapor deposition. *Sci Rep* 2013; 3:.
- [32] Gao W, Alemany LB, Ci L, Ajayan PM. New insights into the structure and reduction of graphite oxide. *Nat Chem*, 2009; 1: 403-408. <https://doi.org/10.1038/nchem.281>
- [33] Li D, Müller MB, Gilje S. Processable aqueous dispersions of graphene nanosheets. *Nat Nanotechnol*, 2008; 3: 101-105. <https://doi.org/10.1038/nnano.2007.451>
- [34] Biswas S, Drzal LT. A novel approach to create a highly ordered monolayer film of graphene nanosheets at the liquid-liquid interface. *Nano Lett*, 2009; 9: 167-172. <https://doi.org/10.1021/nl802724f>
- [35] Singh R, Charu Tripathi C. Electrochemical Exfoliation of Graphite into Graphene for Flexible Supercapacitor Application. *Mater Today Proc*, 2018; 5: 1125-1130. <https://doi.org/10.1016/j.matpr.2017.11.192>
- [36] Liu F, Wang C, Sui X. Synthesis of graphene materials by electrochemical exfoliation: Recent progress and future potential. *Carbon Energy*, 2019; 1: 173-199. <https://doi.org/10.1002/cey2.14>
- [37] Lu J, Yang J, Wang J, Lim A, Wang S, Loh KP. One-Pot Synthesis of Fluorescent Carbon Graphene by the Exfoliation of Graphite in Ionic Liquids. *ACS Nano*. 200. *ACS Nano*, 2009; 3: 2367-2375 <https://doi.org/10.1021/nn900546b>
- [38] Mao M, Wang M, Hu J. Simultaneous electrochemical synthesis of few-layer graphene flakes on both electrodes in protic ionic liquids. *Chem Commun*, 2013; 49: 5301-5303. <https://doi.org/10.1039/c3cc41909f>
- [39] Jibrael RI, Mohammed MKA. Production of graphene powder by electrochemical exfoliation of graphite electrodes immersed in aqueous solution. *Optik (Stuttg)*, 2016; 127: 6384-6389. <https://doi.org/10.1016/j.jileo.2016.04.101>
- [40] Variable I, Tal S, Garcia T. (2011) (12) United States Patent (10) Patent No. : 2:
- [41] Kang F, Leng Y, Zhang TY. Influences of H₂O₂ on synthesis of H₂SO₄-GICs. *J Phys Chem Solids*; 1996 57: 889-892
- [42] Jung SM, Mafra DL, Te LC, Young JH, Kong J. Controlled porous structures of graphene aerogels and their effect on supercapacitor performance. *Nanoscale*, 2015; 7: 4386-4393. <https://doi.org/10.1039/C4NR07564A>
- [43] Tripathi P, Patel CRP, Shaz MA, Srivastava ON. Synthesis of High-Quality Graphene through Electrochemical Exfoliation of Graphite in Alkaline Electrolyte
- [44] Parvez K, Li R, Puniredd SR, Hernandez Y, Hinkel F, Wang S, Feng X, Mullen K(2013) Electrochemically exfoliated graphene as solution-processable, highly conductive electrodes for organic electronics. *ACS Nano*, 2013; 7 :3598-3606. <https://doi.org/10.1021/nn400576v>
- [45] Wang G, Wang B, Park J, Wang Y, Sun B, Yao J. Highly efficient and large-scale synthesis of graphene by electrolytic exfoliation. *Carbon N Y*, 2009; 47: 3242-3246. <https://doi.org/10.1016/j.carbon.2009.07.040>
- [46] Kumar N, Srivastava VC. Simple Synthesis of Large Graphene Oxide Sheets via Electrochemical Method Coupled with Oxidation Process. *ACS Omega*, 2018; 3: 10233-10242. <https://doi.org/10.1021/acsomega.8b01283>

- [47] Chen K, Xue D, Komarneni S. Nanoclay assisted electrochemical exfoliation of pencil core to high conductive graphene thin-film electrode. *J Colloid Interface Sci*, 2017; 487: 156-161. <https://doi.org/10.1016/j.jcis.2016.10.028>
- [48] Thema FT, Moloto MJ, Dikio ED, Nyangiwe N.N, Kotsedi L, Maaza M, Khenfouch M. Synthesis and characterization of graphene thin films by chemical reduction of exfoliated and intercalated graphite oxide. *J Chem*, 2013; 3:.
- [49] Zhou M, Tang J, Cheng Q, Xu G, Cui P, Chang QL. Few-layer graphene obtained by electrochemical exfoliation of graphite cathode. *Chem Phys Lett*, 2013; 572: 61-65. <https://doi.org/10.1016/j.cplett.2013.04.013>
- [50] Kuila T, Khanra P, Kim NH, et al. Effects of sodium hydroxide on the yield and electrochemical performance of sulfonated poly(ether-ether-ketone) functionalized graphene. *J Mater Chem A*, 2013; 1: 9294-9302. <https://doi.org/10.1039/c3ta11014a>
- [51] Sahoo SK, Ratha S, Rout CS, Mallik A. Physicochemical properties and supercapacitor behavior of electrochemically synthesized few layered graphene nanosheets. *J Solid State Electrochem*, 2016; 20: 3415-3428. <https://doi.org/10.1007/s10008-016-3304-6>
- [52] Mir A, Shukla A. Bilayer-rich graphene suspension from electrochemical exfoliation of graphite. *Mater Des*, 2018; 156:62-70. <https://doi.org/10.1016/j.matdes.2018.06.035>
- [53] Sahoo SK, Behera AK, Chandran R, Mallik A. Industrial scale synthesis of few-layer graphene nanosheets (FLGNSs): an exploration of electrochemical exfoliation approach. *J Appl Electrochem*, 2020; 50: 673-688. <https://doi.org/10.1007/s10800-020-01422-3>
- [54] You A, Be MAY, In I. Synthesis of few layer graphene by direct exfoliation of graphite and a Raman spectroscopic study, 2017; 027116.
- [55] Yang S, Brüller S, Wu Z, Parvez K, Dong R, Richard F, Samori P, Liu Z. Organic radical-assisted electrochemical exfoliation for the scalable production of high-quality graphene Organic radical-assisted electrochemical exfoliation for the scalable production of high-quality graphene, 2015. <https://doi.org/10.1021/jacs.5b09000>
- [56] Gurzęda et al. - 2016 - Graphene material prepared by thermal reduction of the electrochemically synthesized graphite oxide-annotated.pdf <https://doi.org/10.1039/C6RA10903A>
- [57] Wang J, Manga KK, Bao Q, Loh KP. High-Yield Synthesis of Few-Layer Graphene Flakes through Electrolyte. *J Am Chem Soc*, 2011; 133: 8888-8891 <https://doi.org/10.1021/ja203725d>
- [58] Zhou H, Yu WJ, Liu L, Cheng R, Cheng C. Chemical vapour deposition growth of large single crystals of monolayer and bilayer graphene. *Nat Commun*, 2013; 4: 1-8. <https://doi.org/10.1038/ncomms3096>



Research Article

Capabilities and limitations of existing finite element simplified micro-modeling techniques for unreinforced masonry

Nitin Kumar^{*1,a}, Michele Barbato^{1,b}, Erika L. Rengifo-López^{2,c}, Fabio Matta^{2,d}

¹Department of Civil and Environmental Engineering, University of California, Davis, U.S.A.

²Department of Civil and Environmental Engineering, University of South Carolina, Columbia, U.S.A.

Article Info

Article history:

Received 26 Feb 2022

Revised 13 May 2022

Accepted 17 May 2022

Keywords:

Unreinforced masonry;
Finite element
modeling;
Simplified micro-
models;
Earthen masonry;
Nonlinear constitutive
models

Abstract

Finite element (FE) simplified micro-modeling techniques are commonly used to investigate and predict the mechanical behavior of masonry structures because they provide a good compromise between accuracy and computational cost. These FE techniques generally discretize masonry structural elements into expanded masonry units and zero-thickness interface joints of assumed known locations. These joints correspond to actual masonry joints and to preferential cracking surfaces, which are often placed vertically in the middle of the expanded masonry units to simulate the cracking mechanisms that are typically observed in masonry bricks and blocks. Three different versions of simplified micro-models (SMMs) are widely used in the literature to model the response of masonry walls and assemblies: SMMs with rigid, elastic, and elasto-plastic constitutive models for the expanded masonry units. All SMMs are based on the hypothesis that the masonry inelastic behavior and cracking are concentrated along the pre-defined zero-thickness interface joints. The hypothesis is often satisfied for ordinary masonry, in which masonry units are generally stronger than the masonry joints, i.e., mortar and unit-mortar interface. However, this hypothesis is not always satisfied for historical masonry with units of irregular shapes or for earth block masonry, in which masonry units and masonry joint can have similar mechanical properties. This paper highlights the capabilities and limitations of SMM techniques by comparing the experimentally-measured and numerically-simulated response of ordinary and earth block masonry walls, for which well-documented experimental results are available in the literature. It is found that SMMs can properly reproduce the mechanical behavior of masonry when the masonry units are significantly stronger than the masonry joints; however, SMMs produce poor estimates of the mechanical response when this hypothesis is not satisfied. This finding highlights the need to develop more general FE models to investigate the mechanical behavior of different masonry materials and construction techniques, as well as to identify the parameters controlling the cracking patterns and the conditions under which SMM techniques can be accurately use.

© 2022 MIM Research Group. All rights reserved.

1. Introduction

Over the last three decades, finite element (FE) simplified micro-modeling techniques have been commonly employed to investigate the local and global mechanical response of masonry structures [1-12]. Simplified micro-models (SMMs) have been used as a computationally efficient alternative to detailed micro-models, which require the FE discretization of all masonry constituents, i.e., masonry units (bricks or blocks), mortar layers, and unit-mortar interfaces, and have been used only for small masonry components due to their high computational cost [13-19]. In SMMs, the mortar joint and the two

*Corresponding author: ntnkumar@ucdavis.edu

^a orcid.org/0000-0002-4045-300X; ^b orcid.org/0000-0003-0484-8191; ^c orcid.org/0000-0002-2136-2639;

^d orcid.org/0000-0001-7018-6611

DOI: <https://dx.doi.org/10.17515/resm2022.408st0226>

Res. Eng. Struct. Mat. Vol. 8 Iss. 3 (2022) 463-490

adjacent unit-mortar interfaces (referred to as masonry joints hereinafter) are lumped into zero-thickness interfaces (referred to as masonry joint interfaces hereinafter), which connect expanded masonry units (with dimensions equal to those of the masonry unit and half of the mortar thickness) [20]. In addition, a zero-thickness interface (referred to as potential crack interface hereinafter), is vertically placed in the middle of the expanded masonry units to simulate the potential cracking mechanism that is often experimentally observed in masonry units [20]. Based on the different constitutive models adopted for the expanded masonry units, three SMMs are commonly found in the literature, i.e., SMMs with rigid (referred to SMM-I hereinafter), elastic (referred to SMM-II hereinafter), and inelastic (referred to SMM-III hereinafter) constitutive models for the expanded masonry units.

Early uses of SMMs did not include potential-crack elements [16,21], which were introduced only later to better describe the experimental behavior of unreinforced masonry [22,23]. Lourenço and Rots [6] proposed an SMM-II approach in which the response of the interface elements was described by a three-surface interface constitutive model based on softening plasticity. This constitutive model could simulate shear sliding, tensile cracking, and compressive crushing, and was later extended, based on plasticity theory, to simulate the cyclic response of masonry structures [10] in many different applications [24–31]. Macorini and Izzuddin [4] proposed a three-dimensional two-surface interface constitutive model that used a co-rotational approach to account for geometric nonlinearity. This model has also been widely used for numerical modeling of masonry structures [32–34], and has been extended based on a damage-plasticity framework to simulate the cyclic behavior of masonry [35]. More recently, Kumar and Barbato [5] proposed a new three-dimensional two-surface interface constitutive model with improved computational efficiency and robustness. Other SMM-II approaches available in literature are based on different interface constitutive models based on damage and friction [36–39], elasto-plasticity [2,3,12], damage-plasticity [35,40], softening fracture [41], and viscoplasticity [42]. More recently, SMM-I [31] and SMM-III approaches [43–46] have been developed to simulate the cyclic behavior of masonry systems. Bolhassani et al. [47] also used an SMM-III approach to investigate the nonlinear behavior of hollow and partially grouted concrete block masonry walls using a damage-plasticity traction–separation law for the masonry joint interfaces, and a damage-plasticity continuum constitutive model for expanded masonry units. The SMM-I was originally introduced to reduce the number of models’ degrees-of-freedom and the corresponding computational time; however, subsequent developments of the SMM-I lead to its most common use within a discrete element method framework [48–52].

The major assumption of existing SMMs is that most of the inelastic behavior of a masonry wall is concentrated at known locations that can be modeled using interface elements, i.e., at the masonry joint and potential crack interfaces [6]. This basic assumption is valid only when (1) the geometry of masonry units and mortar joints is regular (i.e., the masonry units have a uniform cuboid shape and the mortar layers have uniform thickness), and (2) the masonry units are significantly stronger in compression and shear than the masonry joints (i.e., for masonry built with fired clay bricks, concrete blocks, or regularly shaped stones [11]). However, specific instances exist in which the compressive and shear strengths of masonry units is similar to or smaller than those of the masonry joints, e.g., in earth block masonry, for which significant cracking through the earth blocks has been experimentally observed [53]. To the authors’ knowledge, the only study available in the literature that employed SMMs to reproduce the mechanical response of earth block masonry did not achieve an accurate match between experimental and numerical results when using the experimentally-measured modeling parameters [25]. The same study was able to numerically reproduce the experimental results only after modifying the modeling parameter values through a numerical parametric study.

This paper investigates the capabilities and limitations of different SMMs by comparing their relative performance for two different types of masonry, i.e., fired-clay brick (FCB) and compressed and stabilized earth block (CSEB) masonry. After describing the different SMMs, this paper provides recommendations on constitutive models, FE solvers, and discretization requirements for FE SMMs of unreinforced masonry. Appropriate error measures are suggested to facilitate this comparison. Two benchmark examples are investigated, which correspond to FCB walls and CSEB panels for which well-documented experimental results are available in the literature. The FE responses of the different SMMs considered in this study are compared with experimental results in terms of predicted load-displacement response, strength, initial stiffness, collapse mechanism, computational efficiency, and output information.

2. Research Novelty and Significance

This paper fills several gaps in knowledge with regard to the use of SMMs to model the inelastic response behavior of unreinforced masonry walls. In particular, this study investigates the FE modeling of unreinforced masonry walls that do not satisfy the basic hypothesis of inelastic behavior concentrated at known locations by providing useful information for: (1) selecting constitutive models, FE solvers, and mesh discretization; (2) identifying under which conditions different SMMs can be used; and (3) suggesting potential development directions for more accurate, robust, and computationally efficient FE models of unreinforced masonry walls. To the authors' knowledge, this paper also represents the first rigorous investigation of the performance (in terms of accuracy and computational cost) of different SMMs in modeling the inelastic response of earth block masonry, which also acknowledges and identifies the inherent limitations of SMM approaches applied to earth block construction.

The present study aims to advance the FE modeling of unreinforced masonry with masonry units and masonry joints of similar mechanical properties, e.g., earth block masonry. Although this type of masonry is currently uncommon among new constructions, it is representative of many constructions with important historical value [54] and has the potential to expand into a significant portion of new low-rise buildings because of its sustainability, affordability, and safety advantages over other ordinary industrial construction materials [55–57].

3. Existing Simplified Micro-Modeling Techniques

The typical FE discretization of an unreinforced masonry wall using SMMs is shown in Fig. 1. In general, the masonry joint and potential crack interfaces are represented by zero-thickness interface elements, the response of which is described by a relation between the traction vector, $\boldsymbol{\sigma} = \{\sigma, \tau_s, \tau_t\}^T$, and the relative displacement vector, $\boldsymbol{u} = \{u_n, u_s, u_t\}^T$, in which σ is the normal stress, τ_s is the in-plane shear stress, τ_t is the out-of-plane shear stresses, u_n is the normal displacement, u_s is the in-plane relative shear displacement, and u_t is the out-of-plane relative shear displacement [5]. By contrast, the expanded masonry units are modeled using continuum FE elements, the mechanical behavior of which can be described by different material constitutive models, i.e., rigid, elastic, and inelastic constitutive models, corresponding to SMM-I, SMM-II, and SMM-III, respectively.

In order to accurately model the masonry's local and global mechanical behavior, SMMs need to account for all major failure mechanisms of masonry under multi-axial stress conditions [58–66], i.e.: (a) masonry crushing, (b) diagonal tension cracking of masonry units, (c) cracking of masonry joints, (d) failure of masonry joints due to sliding under combined normal and shear stress, and (e) cracking of masonry units in direct tension. In

SMM-I and SMM-II, all failure mechanisms are modeled through the constitutive model of the interface elements used to describe the masonry joint and potential crack interfaces. In particular, failure mechanisms (a) through (d), i.e., crushing, unit diagonal cracking, joint cracking, and joint sliding, are modeled via the masonry joint interface elements, and failure mechanism (e), i.e., unit tensile cracking, is modeled via the potential crack interface elements. In SMM-III, failure mechanism (a), i.e., crushing, is modeled via the expanded masonry unit elements, failure mechanisms (b) through (d), i.e., unit diagonal cracking, joint cracking, and joint sliding, are modeled via the masonry joint interface elements, and failure mechanism (e), i.e., unit tensile cracking, is modeled via the potential crack interface elements. SMM-I also requires the addition of an auxiliary interface element between the rigid expanded masonry units and the interface elements to ensure compatibility under large relative displacements among the rigid components [31].

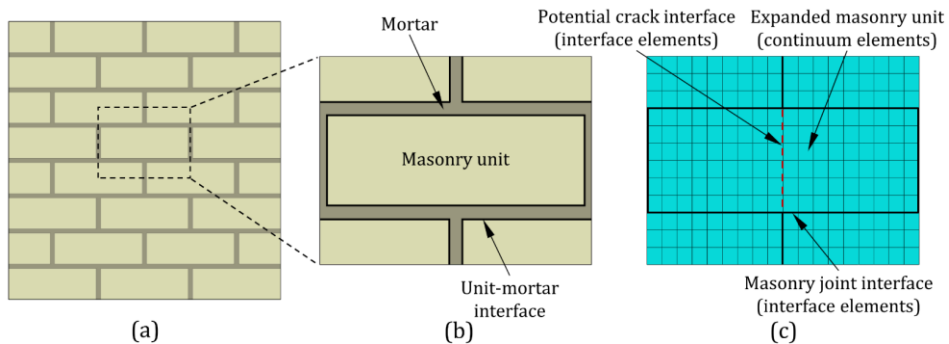


Fig. 1 Simplified micro-modeling techniques for unreinforced masonry: (a) masonry wall, (b) representative volume element of masonry, and (c) SMM representation.

In this paper, the capabilities and limitations of different SMMs were investigated using two benchmark examples representative of FCB and CSEB masonry, for which the SMMs were built using ABAQUS 6.14 [67], which is a general-purpose multi-physics commercial FE software widely used for unreinforced masonry modeling and simulation [3,5,12,31,46]. The accuracy, robustness, and computational efficiency of the different SMMs in simulating the structural response of masonry rely upon: (1) the material constitutive models used for the interface and expanded masonry unit element; (2) the FE solver; and (3) the FE mesh discretization. The selection of material constitutive models, FE solvers, and FE mesh discretization is discussed in the following sections.

3.1. Nonlinear Material Constitutive Models

SMMs employ nonlinear constitutive models for the interface elements corresponding to the masonry joint and potential crack interfaces in all SMMs and for the expanded masonry units in SMM-III. For SMM-I and SMM-II, rigid and elastic constitutive model, respectively, are used for the expanded masonry units. In this study, the recently developed coupled tension-shear interface model (CTSIM) [5] is employed for the interface elements, whereas the concrete damaged plasticity model (CDPM) [68,69] is used for the expanded masonry units in SMM-III.

The CTSIM is based on a convex composite failure surface comprising a tension-shear and a compression cap failure criterion [5], and requires the following input parameters: tensile strength (f_t); initial cohesion (C_0); apparent initial cohesion (C_{00}); initial friction angle (ϕ_0); residual friction angle (ϕ_r); initial dilatancy angle (ψ_0); residual dilatancy angle (ψ_r); mode-I fracture energy (G_r^I); mode-II fracture energy (G_r^{II}); compressive

stress at proportional limit ($\bar{\sigma}_0$); peak compressive stress ($\bar{\sigma}_p$); intermediate compressive stress corresponding to the inflection point in the softening branch ($\bar{\sigma}_m$); residual compressive yield stresses ($\bar{\sigma}_r$); plastic strain at peak compressive stress (κ_p); total plastic strain at intermediate compressive stress (κ_m); and parameter that controls the width of the compression cap failure surface in the shear stress axis (C_{ss}). These input parameters are derived from the experimental testing of: (1) masonry couplet specimens under uniaxial tensile loading, which provide f_t and G_f^I [53,70]; (2) masonry triplet specimens subjected to direct shear test with different pre-compression loads, which provide C_0 , C_{Q0} , ϕ_0 , ϕ_r , ψ_0 , ψ_r and G_f^{II} [53,58–60]; (3) masonry prism or wallette specimens subjected to compression load, which provide $\bar{\sigma}_0$, $\bar{\sigma}_p$, $\bar{\sigma}_m$, $\bar{\sigma}_r$, κ_p , and κ_m [53,71,73]; and (4) masonry wallettes subjected to biaxial compression loads, which provide C_{ss} [62,63]. The compression cap failure criterion in the CTSIM can be easily disabled to better simulate the behavior of the potential crack interfaces, which cannot fail in compression in SMMs. Thus, when used in potential crack interfaces, the CSTIM requires only the following input parameters: f_t , C_0 , C_{Q0} , ϕ_0 , ϕ_r , ψ_0 , ψ_r , G_f^I , and G_f^{II} . Of these parameters, f_t and G_f^I are obtained from a tensile test of masonry units [72]; $\tan \phi_0$, $\tan \phi_r$, $\tan \psi_0$ and $\tan \psi_r$ are assumed equal to 1; and other parameters (C_0 , C_{Q0} , and G_f^{II}) are defined as function of f_t and/or G_f^I [4,5].

The CDPM is a continuum, plasticity-based, damage model for concrete and other quasi-brittle materials such as rocks, mortar, bricks, and ceramics [68,69]. This model requires the following input parameters: compressive stress-plastic strain curve, tensile stress-plastic strain curve, dilation angle (ψ_c), eccentricity (e_c), ratio of bi-axial compressive strength and uniaxial compressive strength (β_{bc}), ratio of the second stress invariant on the tensile meridian and on the compressive meridian (K_c), and viscosity parameter (η). These input parameters are derived from the experimental testing of: (1) masonry unit specimens under uniaxial tensile loading [72], which provide the tensile stress-plastic strain curve; (2) masonry prism or wallette subjected to compression load [53,71,73], which provide the compressive stress-plastic strain curve; and (3) masonry wallettes subjected to biaxial loads, which provide ψ_c , e_c , β_{bc} , and K_c [62,63,74]. Typically, the parameter η is obtained from calibration of the constitutive model to the experimental results used to obtain the other parameters [75].

3.2. FE Solver

The FE solver represents the set of algorithms used to solve the system on nonlinear equilibrium equations corresponding to a given FE model [67,76,77]. Three different families of FE solvers have been commonly used to simulate the nonlinear structural response of masonry structures: (1) implicit static FE solvers [6,28], (2) implicit dynamic FE solvers [78,79], and (3) explicit dynamic FE solvers [4,31,43]. The implicit static FE solvers are based on an iterative method (e.g., the Newton-Raphson method [76,80]) to solve the system of nonlinear equilibrium equations corresponding to a quasi-static loading (i.e., without inertial effects) applied incrementally. The implicit dynamic FE solvers use the same type of iterative algorithms for the system of nonlinear equilibrium equations as the implicit static FE solvers in conjunction with a time-stepping scheme that accounts for inertial forces, e.g., the Newmark-beta family of algorithms [76,81]. The

explicit dynamic FE solvers are based on an explicit integration algorithm (e.g., a central difference time integration or a predictor-corrector algorithm [82]) to extrapolate the nonlinear response of the structural model under consideration by using sufficiently small time increments to avoid instability (i.e., without using the equation of motion of the current time step to determine the current time step displacement) [67,77]. Implicit methods can be conditionally or unconditionally stable [67,76], whereas explicit methods are always conditionally stable with a maximum critical time step $\Delta t_{crit} = \min(L_e/C_d)$ [67,77], in which L_e denotes the characteristic length of any FE within the model, and C_d denotes the dilatational wave speed of the material in the given FE. In addition, static solvers can be used only for problems in which inertial effects can be neglected, whereas dynamic solvers can be used for problems in which inertial effects are significant or negligible. In fact, implicit static FE solvers used to simulate the mechanical behavior of masonry with SMMs could be affected by convergence issues due to the sudden release of elastic energy when cracks spread along the masonry joint interfaces and potential crack interface [4]. For these problems, dynamic FE solvers have been adopted to balance this sudden release of elastic energy through changes in the kinetic and viscous energy [4]. All three types of FE solvers are available in the FE software ABAQUS [67].

3.3. FE Discretization

A general SMM requires the full three-dimensional discretization of expanded masonry units and interface elements, which in general is very computationally demanding. The computational cost of three-dimensional SMMs can be reduced when the loads are applied in the plane of a wall by assuming a two-dimensional plane stress condition [20,28]. This assumption can provide accurate results for structures with single-wythe masonry walls and moderate levels of compressions [28,83]. When this assumption is not satisfied, a generalized or kinematic-enriched plane state can be used with good approximation for nonlinear analysis of masonry subjected to high levels of compressions [83,84].

A mesh sensitivity analysis must also be performed to ensure a good compromise between accuracy (i.e., convergence of FE response to a unique solution) and computational cost for a given SMM. For unconditionally stable implicit (static and dynamic) FE solvers, the mesh sensitivity analysis alone is sufficient to determine an acceptable FE mesh size [67]. However, for explicit dynamic FE solvers that are only conditionally stable, the maximum stable time step depends on both the mesh size and the material properties of the FE model. Therefore, the mesh sensitivity and the determination of the stable time step must be performed simultaneously for SMMs developed using explicit dynamic FE solvers. The identification of the coarser converged mesh and the corresponding maximum stable time step is needed to ensure the best compromise between accuracy, computational costs, and stability of the FE model.

In the investigation presented in this paper, plane stress conditions were assumed for all the SMMs because the two benchmark examples considered in this study (i.e., FCB and CSEB masonry walls) were single-wythe walls and these walls were not subjected to extreme compression stress. Therefore, the two-dimensional plane stress assumption can provide reasonably accurate results while considerably reducing the computational cost [28].

4. Performance Comparison of FE Response Analyses Using SMMs

The performance of different SMMs can be expressed in terms of the comparison between the experimentally-measured and numerically-estimated force-displacement responses, deformed shapes, stress distributions, and strain distributions. Often, a few global response parameters such as peak strength and initial stiffness are sufficient for design

purposes; however, these parameters need to be integrated at least with the information regarding the failure mode identified by the FE model. In this study, the FE response are compared with the experimental results by estimating the following point-wise relative error in the peak load (P_{max}), initial stiffness (k), and displacement at failure (Δ_f):

$$\epsilon_x = \frac{X_{FE} - X_{exp}}{X_{exp}} \tag{1}$$

where $X_{FE} = P_{max}, k, \text{ or } \Delta_f$ obtained from a FE analysis. When multiple nominally-identical replicas are experimentally tested, X_{exp} is taken as the average of the corresponding experimentally-measured values. In this study, the initial stiffness is defined as the secant stiffness evaluated at 1/10 of the average experimentally-measured peak load. Furthermore, the accuracy of the different FE models in estimating the force-displacement response curve is evaluated using three different global relative errors, i.e., the mean error (ϵ_{mean}), root mean squared error (ϵ_{RMS}), and mean absolute error (ϵ_{abs}), which are defined as follows:

$$\epsilon_{mean} = \frac{1}{n_s} \sum_{j=1}^{n_s} \left[\frac{1}{n_j} \sum_{i=1}^{n_j} \frac{(P_{FE}^{(i)} - P_{exp,j}^{(i)})}{P_{exp,j}^{(i)}} \right] \tag{2}$$

$$\epsilon_{RMS} = \frac{1}{n_s} \sum_{j=1}^{n_s} \left[\sqrt{\frac{1}{n_j} \sum_{i=1}^{n_j} \left[\frac{P_{FE}^{(i)} - P_{exp,j}^{(i)}}{P_{exp,j}^{(i)}} \right]^2} \right] \tag{3}$$

$$\epsilon_{abs} = \frac{1}{n_s} \sum_{j=1}^{n_s} \left[\frac{1}{n_j} \sum_{i=1}^{n_j} \left| \frac{P_{FE}^{(i)} - P_{exp,j}^{(i)}}{P_{exp,j}^{(i)}} \right| \right] \tag{4}$$

in which $P_{exp,j}^{(i)}$ and $P_{FE}^{(i)}$ denote the experimentally-measured and numerically-simulated values, respectively, of the reaction force for a given masonry wall measured at a given level of displacement, $\Delta^{(i)}$; n_j denotes the number of recorded displacement levels for the j -th experimental sample, in which the maximum displacement level corresponding to the experimental displacement at failure; and n_s denotes the number of experimental specimens.

Another comparison criterion is provided by the computational efficiency of FE models with similar accuracy in reproducing the experimental behavior of masonry. The computational efficiency of different SMMs is expressed hereinafter in terms of computational time ratio (CTR), which is defined as the ratio of the computational CPU time corresponding to two different models and obtained using the same computer for a given FE response simulation.

5. Benchmark Example #1: Fired-Clay Brick (FCB) Masonry

The first benchmark example considered in this study consists of a series of FCB masonry shear walls, tested by Vermeltoort and Raijmakers [85,86], in which the masonry units are considerably stronger than the mortar and the unit-mortar interfaces. For this type of

masonry, most of the inelastic behavior is expected to be concentrated at the masonry joints.

5.1. Description of Experimental Tests

The masonry shear walls considered in this example had a width-to-height ratio approximately equal to one, with dimensions 990 mm (length) \times 1000 mm (height) \times 100 mm (thickness). The walls were single-wythe walls consisting of 18 courses, with the bottom and top courses clamped to steel beams, as shown in Fig. 2(a). The masonry shear walls comprised wire-cut solid clay bricks with dimensions of 210 mm \times 52 mm \times 100 mm, and mortar layers of thickness equal to 10 mm. The experimental test involved a uniformly distributed normal pressure (p) applied vertically at the top of the walls, followed by a monotonically increasing horizontal displacement (Δ_H) applied to the top steel beam, while the bottom boundary was fixed.

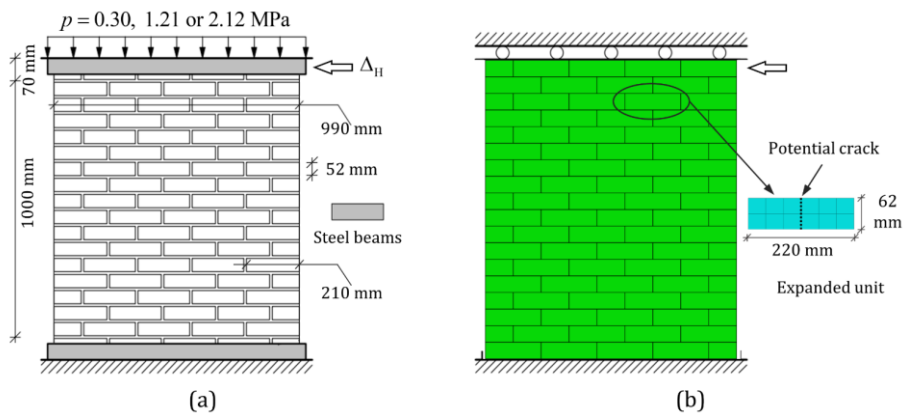


Fig. 2 FCB masonry: (a) shear walls and (b) SMM discretization of the shear wall.

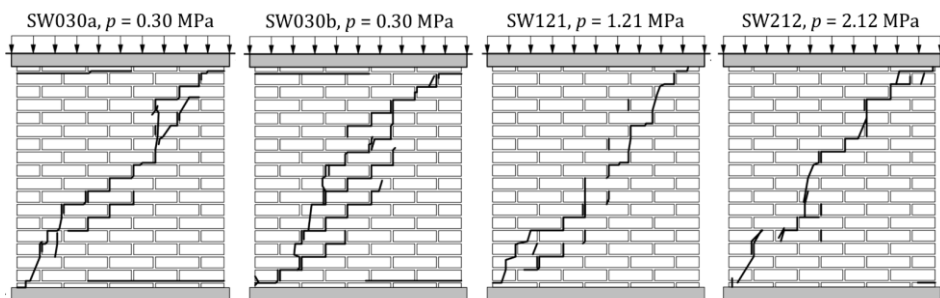


Fig. 3 Experimental crack patterns of the different FCB unreinforced masonry shear walls.

The FCB unreinforced masonry shear walls were experimentally tested for three different vertical pressures, i.e., wall SW030 (with two specimens SW030a and SW030b) was subjected to a constant pressure equal to 0.30 MPa, wall SW121 to a constant pressure equal to 1.21 MPa, and wall SW212 to a constant pressure equal to 2.12 MPa. The experimental failure patterns for the different walls are shown in Fig. 3. All the walls exhibited very similar experimental failure mechanisms and as expected, most of the cracking and inelastic behavior was concentrated at the masonry joints. During the

application of the monotonically increasing horizontal displacement, horizontal tensile cracks developed first at the bottom and top of the wall in the bed joints at earlier loading stages and were followed by diagonal stepped cracks. Finally, the crushing of the toes of the masonry and the tensile cracking in the middle of some masonry units led to the overall failure of each shear wall.

5.2. Description of SMMs Developed for the FCB Unreinforced Masonry

Fig. 2 (b) shows the SMM discretization of the FCB unreinforced masonry shear walls. The FE models were constructed using two-dimensional elements under the assumption of plane stress. The masonry joints and potential cracks interface were modeled by using a 4-node two-dimensional cohesive element, i.e., the COH2D4 element in ABAQUS 6.14 [67], and the expanded masonry units (having dimensions 220 mm × 62 mm) were modeled using a 4-node bilinear plane stress quadrilateral element with reduced integration and hourglass control, i.e., the CPS4R element in ABAQUS 6.14 [67]. Auxiliary interface elements were not needed in the SMM-I because the shear deformations in the masonry joints and potential crack interfaces were sufficiently small [31].

The material properties used for developing different SMMs were obtained from existing experimental results on tension, shear, and compression tests available in the literature [85,86]. An elastic modulus $E_b = 16,700$ MPa and a Poisson ratio $\nu_b = 0.15$ were used for the expanded masonry units in SMM-II and SMM-III. The elastic and inelastic properties of the masonry joint interface for the different SMMs are given in Table 1, where k_n^b and k_s^b denote the normal and shear stiffness, respectively, of the masonry joint interfaces corresponding to the bed masonry joints; and k_n^h and k_s^h denote the normal and shear stiffness, respectively, of the masonry joint interfaces corresponding to the head masonry joints. The compressive input parameters given in the Table 1, i.e., $\bar{\sigma}_0$, $\bar{\sigma}_p$, $\bar{\sigma}_m$, $\bar{\sigma}_r$, κ_p and κ_m , were used to describe the stress-strain curve for the expanded masonry units in SMM-III based on a hardening/softening constitutive law used for the compression cap failure criterion of the CTSIM [5]. The values of the other parameters needed to fully define the CDPM for the expanded masonry units in the SMM-III were taken from the literature [74,75,87] and are: $\psi_c = 38^\circ$, $e_c = 0.1$, $\beta_{bc} = 1.16$, $K_c = 0.67$, $\eta = 8.5 \times 10^{-5}$. The properties of potential crack interfaces used in the different SMMs are given in Table 2, where k_n and k_s are the normal and shear stiffness, respectively, of the potential crack interfaces.

5.3. Selection of FE Solver and Mesh Size

The implicit static, implicit dynamic, and explicit dynamic FE solvers, which are available in the FE software ABAQUS [67], were compared in terms of accuracy and computational effort for the SMM-IIs of the FCB masonry shear wall SW030. In the FE model based on the implicit static solver, all the degrees of freedoms were restrained at all the nodes at the top edge of the model, and a monotonically increasing horizontal displacement was applied on the side of the top course of the FE model while keeping the top edge of the FE model vertically fixed. A general procedure for static loading based on an incremental-iterative globally convergent Newton-Raphson method with the line search technique was used in ABAQUS [67]. In addition, an automatic load step increment technique was adopted for efficient and robust simulation of the response of the different FE models with initial, minimum, and maximum normalized increment sizes equal to 1×10^{-4} , 1×10^{-9} , 5×10^{-4} , respectively. In the FE model based on the implicit dynamic and explicit dynamic FE solvers, all the degrees of freedoms were restrained at the bottom edge of the model, and a fixed value of velocity $V = 0.1$ mm/s was applied at all nodes of the top edge of the wall. In addition, zero acceleration was assigned to the top edge of the model during the analysis

to ensure a linear variation with time of the top wall displacements. A density $\rho_b = 1.9 \times 10^3$ kg/m³ and mass-proportional damping, corresponding to a damping ratio $\zeta = 5\%$, were used for the solid elements to represent inertia and damping effects. For the implicit dynamic FE solver, a general implicit dynamic procedure was used, which was based on an incremental-iterative version of the globally convergent Newton-Raphson method [67] and an automatic load step increment having minimum normalized increment sizes equal to 5×10^{-4} . For the explicit dynamic FE solver, an explicit dynamic procedure based on the central-difference time integration was employed, with the critical time step equal to 3.3×10^{-6} s. The FE simulations were performed by increasing the applied displacement until the FE models became numerically unstable (i.e., due to collapse of the shear wall) or reached a 5.0 mm displacement at the top of the wall.

Table 1. Properties of masonry joint interfaces (SMM-I, SMM-II, and SMM-III) and inelastic compressive properties for the expanded masonry units (SMM-III) of the FCB unreinforced masonry shear walls.

Properties	SMM-I			SMM-II			SMM-III		
	SW030	SW121	SW212	SW030	SW121	SW212	SW030	SW121	SW212
k_n^b (N/mm ³)	62.9	78.1	62.9	82	110	82	82	110	82
k_s^b (N/mm ³)	27.6	35.5	27.6	36	50	110	36	50	110
k_n^h (N/mm ³)	39.4	63.8	39.4	82	110	82	82	110	82
k_s^h (N/mm ³)	17.3	29.0	17.3	36	50	110	36	50	110
f_t (MPa)	0.250	0.160	0.160	0.250	0.160	0.160	0.250	0.160	0.160
C_0 (MPa)	0.362	0.232	0.232	0.362	0.232	0.232	0.362	0.232	0.232
C_{Q0} (MPa)	18.125	11.6	11.6	18.125	11.6	11.6	18.125	11.6	11.6
$\tan \phi_0$ (-)	0.75	0.75	0.75	0.75	0.75	0.75	0.75	0.75	0.75
$\tan \phi_r$ (-)	0.75	0.75	0.75	0.75	0.75	0.75	0.75	0.75	0.75
$\tan \psi_0$ (-)	0.001	0.001	0.001	0.001	0.001	0.001	0.001	0.001	0.001
$\tan \psi_r$ (-)	0.0001	0.0001	0.0001	0.0001	0.0001	0.0001	0.0001	0.0001	0.0001
G_f^I (N/mm)	0.018	0.012	0.012	0.018	0.012	0.012	0.018	0.012	0.012
G_f^{II} (N/mm)	0.125	0.050	0.050	0.125	0.050	0.050	0.125	0.050	0.050
$\bar{\sigma}_0$ (MPa)	3.50	3.83	3.83	3.50	3.83	3.83	<u>3.50</u>	<u>3.83</u>	<u>3.83</u>
$\bar{\sigma}_p$ (MPa)	10.50	11.50	11.50	10.50	11.50	11.50	<u>10.50</u>	<u>11.50</u>	<u>11.50</u>
$\bar{\sigma}_m$ (MPa)	5.25	5.75	5.75	5.25	5.75	5.75	<u>5.25</u>	<u>5.75</u>	<u>5.75</u>
$\bar{\sigma}_r$ (MPa)	1.50	1.64	1.64	1.50	1.64	1.64	<u>1.50</u>	<u>1.64</u>	<u>1.64</u>
κ_p (-)	0.090	0.090	0.090	0.090	0.090	0.090	<u>0.007</u>	<u>0.007</u>	<u>0.007</u>
κ_m (-)	0.490	0.490	0.490	0.490	0.490	0.490	<u>0.033</u>	<u>0.033</u>	<u>0.033</u>
C_{ss} (-)	9.0	9.0	9.0	9.0	9.0	9.0	-	-	-

Note: underlined values are for expanded masonry units of SMM-III.

Fig. 4 shows the experimental and numerical load-displacement responses and the CTR of the SMM-II corresponding to the different FE solvers and same mesh discretization. The CPU time for the explicit dynamic solver is used as reference (i.e., CTR = 1.0). Table 3 reports the different error estimates. All the FE solvers were able to simulate the behavior of the FCB masonry shear wall SW030 up to failure, and the FE load-displacement responses corresponding to the different solvers are similar. The value of ϵ_{RMS} and ϵ_{abs} for the different FE solvers are almost identical, varying between 8.22% and 8.61%

(approximately a 5.0% variation) and between 6.19% and 6.79% (approximately a 9.0% variation), respectively. The ϵ_{mean} values indicate that all solvers have a similar level of accuracy and slightly underestimate the FE response of the masonry wall, i.e., by 1.42%, 3.17% and 3.67% corresponding to implicit static, implicit dynamic, and explicit dynamic FE solvers, respectively. Also, the $\epsilon_{P_{\text{max}}}$ and ϵ_k corresponding to the different FE solvers are small, i.e., less than 4.0% and 6.0%, respectively, showing that the different FE solvers can very accurately predict the peak load, P_{max} , and initial stiffness, k , of FBC masonry walls. By contrast, the ϵ_{Δ_r} is equal to 26.66%, 10.34%, and 15.43% for implicit static, implicit dynamic, and explicit dynamic FE solvers, respectively, which indicates that all FE solvers tend to overestimate the ultimate displacement of the masonry walls. This observation is not surprising, as it is known that the prediction of the structural response of unreinforced masonry walls after the peak strength has been reached is a very complex problem affected by significant uncertainties [88,89]. However, this discrepancy between experimental and numerical estimates of the displacement at failure could also be due to the fact that the criterion used to terminate the physical experiments is unknown (e.g., the experiments may have been interrupted before the complete collapse of the walls in order to protect the laboratory equipment); thus, the numerical results relative to the displacements at failure may or may not be representative of the experimental results. In Fig. 4(b), the comparison of the different CTRs shows that the explicit dynamic solver is the most computationally efficient solver among those considered in this study, as it produces FE analysis results 5.62 and 34.76 times faster than the implicit static and implicit dynamic FE solver, respectively. Based on these results, the explicit dynamic solver seems to provide the best compromise between accuracy and computational cost in simulating the behavior of masonry among the three FE solvers considered in this study.

Table 2. Properties of potential crack interfaces used in the SMMs of the FCB unreinforced masonry shear walls.

FE Model (-)	k_n (N/mm ³)	k_s (N/mm ³)	f_t (MPa)	C_0 / C_{00} (MPa)	$\tan \phi_0 / \tan \phi_r$ (-)	$\tan \psi_0 / \tan \psi_r$ (-)	G_f^I / G_f^{II} (N/mm)
SMM-I	159	69	2.0	2.9/2.9	1.0/1.0	1.0/1.0	0.008/0.5
SMM-II	16700	7260	2.0	2.9/2.9	1.0/1.0	1.0/1.0	0.008/0.5
SMM-III	16700	7260	2.0	2.9/2.9	1.0/1.0	1.0/1.0	0.008/0.5

Table 3. FE results of the FCB unreinforced masonry shear walls in term of errors between the experimental and FE load-displacement curve corresponding to different FE solvers.

FE Solver (-)	$\epsilon_{P_{\text{max}}}$ (%)	ϵ_k (%)	ϵ_{Δ_r} (%)	ϵ_{mean} (%)	ϵ_{RMS} (%)	ϵ_{abs} (%)
Implicit Static	1.89	3.05	26.66	-1.42	8.48	6.45
Implicit Dynamic	3.82	5.99	10.34	-3.17	8.22	6.19
Explicit Dynamic	0.31	4.01	15.43	-3.67	8.61	6.79

A mesh sensitivity analysis of the FE SMM-II model of masonry shear wall SW030 was performed. The FE models were analyzed by using the explicit dynamic FE solver and a maximum time increment equal to the critical time step. It was found that the critical time step of the SMMs depends only on the thickness of the interface elements, and the mesh size of the expanded masonry units does not affect the critical time step for any practical FE discretization. Thus, the thickness of the interface elements was set equal to 0.05 mm, giving a critical time step equal to 3.3×10^{-6} s, and the mesh sensitivity analysis was performed by developing SMM-IIs with four different mesh sizes for the expanded

masonry units of the FCB masonry shear wall SW030. These meshes are identified by two numbers representing the number of elements used along the length and height of the expanded masonry units, respectively. The mesh sensitivity analysis was performed starting from a coarse 6×2 mesh, and progressively increasing the number of elements in each direction in a proportional manner until convergence was achieved. Convergence was verified by calculating the point-wise changes in peak load ($\delta_{P_{max}}$), initial stiffness (δ_k), and displacement at failure (δ_{Δ_f}), defined as:

$$\delta_x = \frac{X_{m2} - X_{m1}}{X_{m1}} \tag{5}$$

in which X_{m_1} and $X_{m_2} = P_{max}, k, \text{ or } \Delta_f$ obtained from the FE analysis corresponding to the two mesh discretization being compared; as well as the global relative difference (δ_{abs}), which is defined as:

$$\delta_{abs} = \frac{1}{n_m} \sum_{i=1}^{n_m} \left| \frac{P_{m_2}^{(i)} - P_{m_1}^{(i)}}{P_{m_1}^{(i)}} \right| \tag{6}$$

in which $P_{m_1}^{(i)}$ and $P_{m_2}^{(i)}$ denote the reaction forces at displacement $\Delta^{(i)}$ obtained from the FE analysis corresponding to the two mesh discretization being compared; and n_m denotes the minimum of the number of displacement levels before failure for the two meshes being compared. In particular, it was assumed the convergence was achieved when the four convergence measures reached an absolute value smaller than 1%. The following meshes were developed: 6×2, 12×4, 18×6, and 24×8. The horizontal load-displacement responses of the considered SMM-IIIs are shown in Fig. 5(a), and the corresponding CTRs are compared in Fig. 5(b), in which mesh 18×6 is used as reference. It is observed that the FE load-displacement curves corresponding to meshes 18×6 and 24×8 are almost overlapped, whereas the other meshes provide significantly different response results. In addition, it is observed that the computational cost increases by a factor approximately equal to 3 going from one mesh size to the next finer mesh.

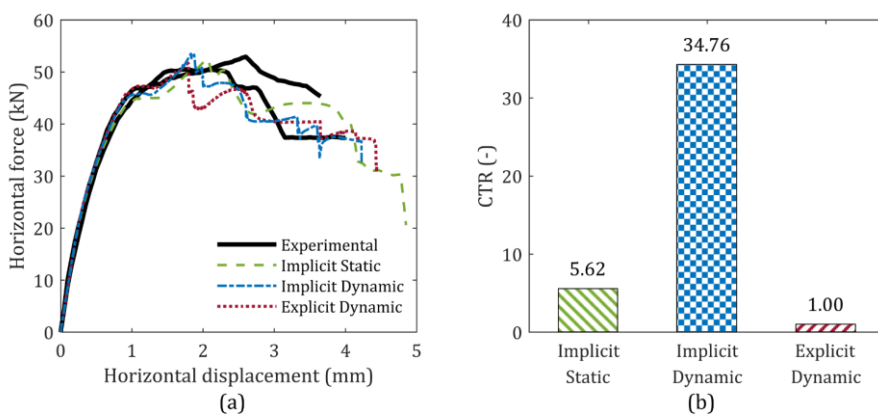


Fig. 4 FE results corresponding to different FE solvers: (a) comparison of experimental and FE load-displacement curves, and (b) comparison of CTR for different FE solvers.

The values of the convergence measures are reported in Table 4. As expected, the convergence measures rapidly decrease in absolute value when refining the mesh, and they are all smaller than 1% in absolute value going from mesh 18×6 to mesh 24×8, which indicates that convergence has been achieved. Based on the results obtained in this mesh convergence analysis, mesh 18×6 was used for SMM-II and SMM-III hereinafter in conjunction with the FE explicit dynamic solver and a maximum time increment equal to 3.3×10^{-6} s.

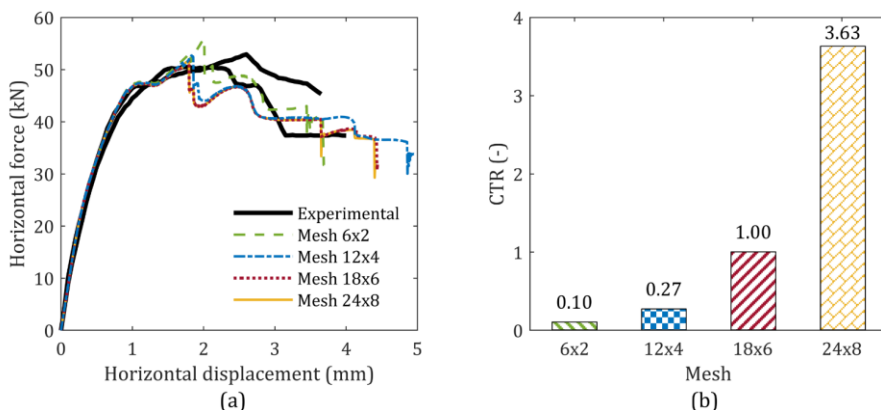


Fig. 5 Comparison of different mesh discretization for the SMM-IIs: (a) load-displacement curves, and (b) CTRs with mesh 18x6 as reference mesh.

Table 4 FE response of the SMM-IIs corresponding to the four different meshes in term of relative difference among the FE load-displacement curve.

Mesh		$\delta_{p_{max}}$	δ_k	δ_{Δ_f}	δ_{abs}
m1	m2	(%)	(%)	(%)	(%)
6×2	12×4	-4.60	-0.39	34.15	3.27
12×4	18×6	-1.95	-0.22	-10.30	1.54
18×6	24×8	-0.01	-0.01	-0.68	0.21

5.4. Comparison of the FE Results Obtained Using Different SMMs

The FE results corresponding to the different SMMs of the FCB unreinforced masonry shear wall having different initial pressure, i.e., SW030, SW121, and SW212 are presented in Fig. 6(a-c) compares the experimentally-measured horizontal force-horizontal displacement response of the shear walls with the corresponding numerically-estimated FE responses of the different SMMs considered in this investigation. The sudden load drops in the FE force-displacement responses are due to cracking of expanded masonry units at the potential crack locations. The FE results show that all SMMs can reproduce the complete load path of the FCB unreinforced masonry shear wall up to and beyond the peak strength. Fig. 6(d) presents the CTRs corresponding to different FE models. All the FE simulations for the SMMs of the FCB unreinforced masonry shear wall were run on a Microsoft Windows-based personal computer having an Intel(R) Core (TM) i7-8700 CPU @ 3.19 GHz with 16.0 GB RAM, with only one CPU core used in each simulation. The CPU time for the SMM-II is used as reference (i.e., CTR = 1.0) for each FCB unreinforced masonry shear wall. As expected, the results show that the computation demand is lowest for SMM-I and highest for SMM-III for all modeled shear walls.

The different error measures for all models are reported in Table 5. For the SW030 shear wall, SMM-II provides the most accurate predictions for the peak load and the initial stiffness, SMM-I provides the best prediction of the displacement at failure, and SMM-III presents the lowest global relative errors (i.e., $\varepsilon_{\text{mean}} = 2.58\%$, $\varepsilon_{\text{RMS}} = 8.33\%$, and $\varepsilon_{\text{abs}} = 6.42\%$), although these errors are very similar to those for SMM-II ($\varepsilon_{\text{mean}} = -3.67\%$, $\varepsilon_{\text{RMS}} = 8.61\%$, and $\varepsilon_{\text{abs}} = 6.79\%$), whereas they are significantly (approximately two to four times) higher for SMM-I. For the SW121 shear wall, SMM-I provides the most accurate estimate of P_{max} , SMM-II provides the most accurate estimate of k and Δ_f , and SMM-III has the lowest value for $\varepsilon_{\text{mean}}$, ε_{RMS} , and ε_{abs} , i.e., 1.32%, 4.15%, and 3.36%, respectively. For the SM212 shear wall, The SMM-II always provides the lowest errors between the experimental and numerical estimates, with the exception of $\varepsilon_{P_{\text{max}}}$, for which SMM-I gives the lowest value, i.e., $\varepsilon_{P_{\text{max}}} = 8.18\%$. SMM-I generally underestimate all response quantities for all walls considered in this study, with the exception of the peak strength of the SW212 wall, for which $\varepsilon_{P_{\text{max}}} = 8.18\%$. The SMM-I also presents the largest ε_k , $\varepsilon_{\text{mean}}$, ε_{RMS} , and ε_{abs} among all the SMMs, these errors increase in magnitude for increasing values of the initial vertical pressure applied to the shear wall. SMM-II always slightly overestimates the peak load (with $0.31\% \leq \varepsilon_{P_{\text{max}}} \leq 15.20\%$) and initial stiffness (with $1.59\% \leq \varepsilon_k \leq 5.34\%$), with errors $\varepsilon_{P_{\text{max}}}$, $\varepsilon_{\text{mean}}$, ε_{RMS} , and ε_{abs} increasing in magnitude for increasing values of the initial vertical pressure applied to the shear wall. SMM-III presents largest error in Δ_f for all the shear walls (with $24.43\% \leq \varepsilon_{\Delta_f} \leq 26.71\%$), always overestimating the displacement at failure. However, SMM-III has also the lowest global relative errors for the SW030 and SW121 walls.

It is noted that the numerical value of $\varepsilon_{P_{\text{max}}}$ for all SMMs increases for increasing levels of initial vertical pressure, whereas this phenomenon is not observed for ε_k or ε_{Δ_f} , for which no simple pattern can be identified. The magnitude of $\varepsilon_{P_{\text{max}}}$ also increasing for increasing initial vertical pressure for SMM-II and SMM-III, whereas it achieves a minimum value in correspondence to SW121 for SMM-I. This phenomenon is likely due to the use of a single vertical potential crack interface at a prescribed location, which provides a proper representation of the cracking pattern observed for walls with lower initial vertical pressure. However, for higher values of initial vertical pressure, the experimental cracking pattern show diagonal cracks in the masonry units, which cannot be properly represented by the vertical potential crack interfaces in the expanded masonry units of the SMMs.

The FE crack patterns and the distribution of the in-plane minimum principal stress for the SMMs of the FCB unreinforced masonry shear walls are presented in Fig. 7(a-c) for SMM-I, Fig. 7(d-f) for SMM-II, and Fig. 7(g-i) are for SMM-III. In order to make the cracks visible, the deformed shape in Fig. 7 is magnified by a factor 10. The numerically-simulated inelastic behavior of the shear wall is similar to the actual behavior observed in the experimental tests: horizontal tensile cracks start developing first at the bottom and top of the shear walls at approximately 1.0 mm of horizontal displacement, followed by a diagonal stepped crack in the shear wall. After approximately 2.5 mm of horizontal displacement, a combined shear and crushing mechanism develops at the toe of the shear wall, which leads to the failure of the model. All the different SMMs reproduce almost the same crack patterns for each of the walls, and these patterns are very similar to those observed experimentally. The distribution of the in-plane minimum principal stress in the SMM-II and SMM-III shows that small diagonal compressive struts, which pass through the center of the bricks, form in all SMMs when horizontal cracks develop at the bottom and top of the shear wall. With further increase in the displacement, the formation of additional

compressive struts is averted by the initiation of the diagonal crack in the SMMs. Finally, when the diagonal crack is fully open, two distinct struts are formed on each side of the diagonal crack, as shown in the Fig. 7. The compressive stress in the struts increases with increasing levels of initial vertical pressure, i.e., the compressive stress is lowest in the SW030 walls and highest in the SW212 walls. The maximum compressive stress values in the SMM-II for the SW030 and SW121 shear walls remain below 8.0 and 9.9 MPa, respectively, which indicates that the assumption of linear elastic behavior in the expanded masonry units is reasonable. In fact, the compressive strength of the masonry units is not available [6,46]; however, it can be estimated as approximately equal to 20 MPa. This estimate is based on the tensile strength, which is equal to 2.0 MPa, and the reasonable assumption of a ratio of compressive to tensile strength equal to 10 [46,90]. In SMM-III, the compressive stress values for the SW030 and SW121 shear walls are found to be slightly lower, i.e., approximately 7.5 and 9.4 MPa, respectively, than the corresponding compressive stress values in the SMM-II (i.e., 8.0 and 9.9 MPa, respectively), with a negligible plastic strain in the expanded masonry units, i.e., less than 1.0×10^{-4} . The maximum compressive stress in the SMM-II for the SW212 wall reaches approximately 13.9 MPa, which is closer to the compressive strength of the masonry units when compared to the maximum compressive stress values in the SMM-II for the SW030 and SW121 shear walls. In the SMM-III of the SW212 wall, the compressive stress is approximately equal to 12.5 MPa (which is achieved at a horizontal displacement of approximately 2.9 mm, when a drop in horizontal force is observed), and the plastic strain is approximately equal to 9.8×10^{-3} , indicating a significant plasticization of the expanded masonry units.

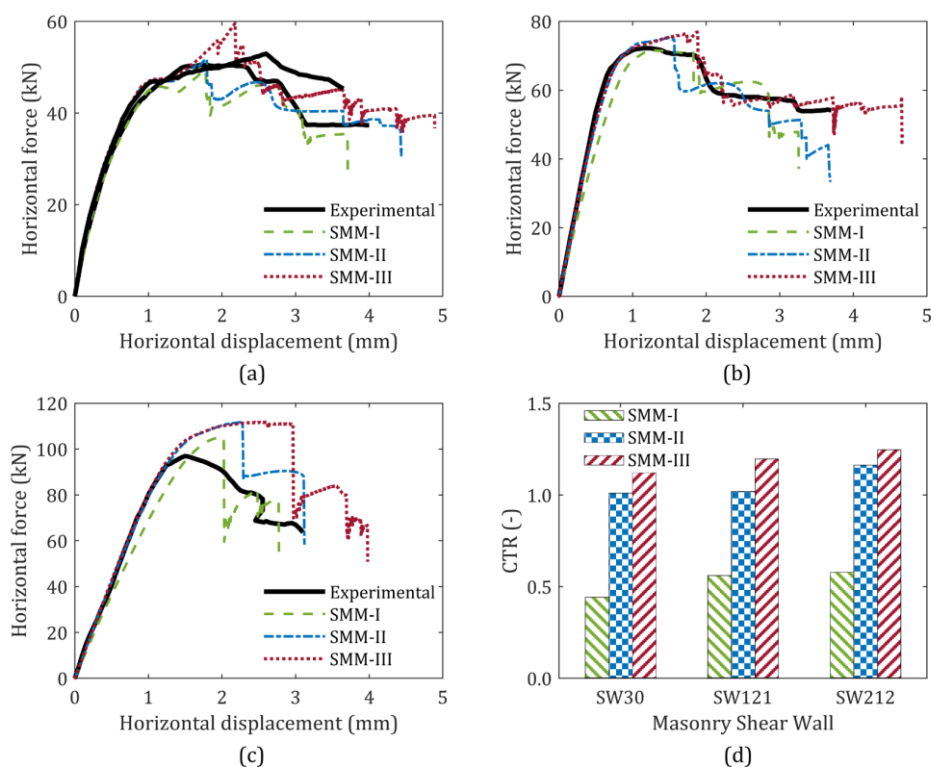


Fig. 6 Comparison of the experimentally-measured and numerically-simulated force-displacement response for the SMMs of the FCB unreinforced masonry shear walls: (a) SW030, (b) SW121, (c) SW212, and (d) CTR corresponding to different FE models.

Table 5. FE Simulation results for the SMMs of the FCB unreinforced masonry shear walls in term of errors between the experimental and FE load-displacement curve.

Shear Wall (-)	FE Modal (-)	$\epsilon_{F_{max}}$ (%)	ϵ_k (%)	ϵ_{Δ_f} (%)	ϵ_{mean} (%)	ϵ_{RMS} (%)	ϵ_{abs} (%)
SW030	SMM-I	-4.08	-10.01	-3.24	-12.78	21.53	12.82
	SMM-II	0.31	4.01	15.43	-3.67	8.61	6.79
	SMM-III	14.95	5.13	27.71	2.58	8.33	6.42
SW121	SMM-I	-0.59	-10.56	-13.22	-17.02	35.31	19.48
	SMM-II	4.40	5.34	-2.27	-6.02	14.71	8.28
	SMM-III	6.70	6.29	24.43	1.32	4.15	3.36
SW212	SMM-I	8.18	-11.40	-11.49	-17.37	36.11	20.85
	SMM-II	15.20	1.59	-0.61	11.48	18.33	13.09
	SMM-III	15.26	1.80	26.86	16.70	28.23	18.96

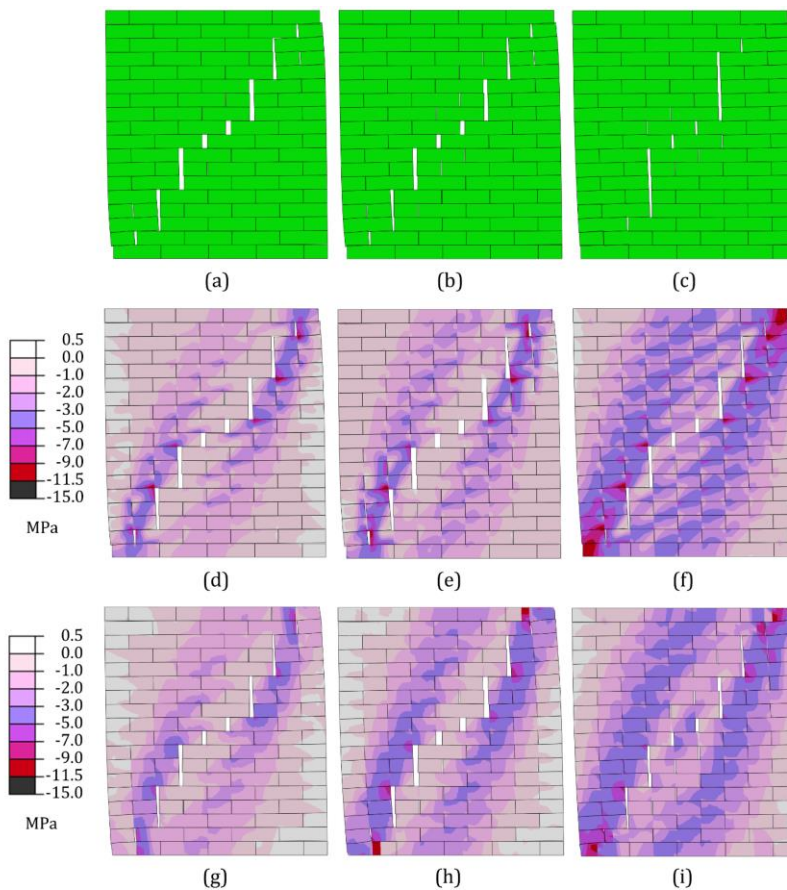


Fig. 7 FE crack patterns and distribution of in-plane minimum principal stress for the SMMs of the FCB unreinforced masonry shear walls: (a-c) SW030, SW121 and SW212 for SMM-I; (d-f) SW030, SW121 and SW212 for SMM-II; and (g-i) SW030, SW121 and SW212 for SMM-III.

The level of information provided by the different models increases with the computational cost: SMM-I are associated with the lowest computational cost but also with the lowest level of information, which is limited to the global load and deformation level and the cracking pattern; SMM-III is the most computationally expensive models but provide information on stresses and strains in both elastic and plastic ranges within the expanded masonry units.

It is concluded that all three SMMs considered in this study can properly simulate the global horizontal load-displacement behavior of the FCB unreinforced masonry shear walls and can capture the experimentally observed failure mechanism of these walls, for which the inelastic behavior is concentrated along the mortar-unit interfaces and in potential cracks of known locations. However, the SMMs may not be able to properly predict the experimental displacement at failure, although this result may also depend on the lack of knowledge for the termination criterion used in the experimental tests. SMM-II and SMM-III present similar levels of accuracy and perform better than SMM-I in capturing the experimental behavior of the shear walls. However, their accuracy slightly degrades for increasing levels of initial vertical pressure applied to the walls.

6. Benchmark Example #2: Compressed and Stabilized Earth Block (CSEB) Masonry

The second application example considered in this study is a CSEB unreinforced masonry wallette, in which cracking and inelastic behavior is spread across the different components (i.e., masonry units, mortar, and unit-mortar interfaces) of the masonry walls.

6.1. Description of Experimental Tests

A diagonal compression test performed on three replicate CSEB masonry wallettes (Wall-1, Wall-2 and Wall-3), reported in [53], was selected for this investigation. Each specimen consisted of a single-leaf, eight-course CSEB masonry wallette having dimensions of 864 mm (length) \times 787 mm (height) \times 178 mm (thickness), as shown in Fig. 8(a). The specimens were built using: (1) CSEBs with dimensions equal to 254 mm \times 178 mm \times 89 mm and fabricated using silty loam soil and 6% cement; and (2) earthen mortar layers of thickness equal to 13 mm and fabricated using a cement:soil:sand proportion by weight equal to 1:1:6 and water-to-cement ratio equal to 2.4. The CSEB masonry wallettes were tested under diagonal compression force that was imparted through steel shoes that were placed at the top and bottom corner of each specimen, as illustrated in Fig. 8(a). The experimental test involved a monotonically increasing vertical displacement on the steel shoe at the top of the masonry wallettes, while keeping the boundaries of the steel shoe at bottom of the masonry wallette fixed. The horizontal extension and vertical contraction were recorded using two displacement transducers, which are labeled as "A" and "B", respectively, in Fig. 8(a).

Fig. 9 shows the experimental crack patterns of the three wallettes at the end of the diagonal compression test. The specimens exhibited consistent failure modes with diagonal cracks parallel to the direction of the load and inclined by approximately 45° with respect to the bed joints. As shown in Fig. 9, the cracks at failure were observed mainly through the CSEBs and to a lesser extent along the head and bed joints and affected in a minor manner the mortar joints. This behavior is common for CSEB masonry and is fundamentally different from that of ordinary masonry, in which specimens typically fail mostly along the bed and head joints.

6.2. Description of the SMMs for the CSEB Masonry Wallette

Fig. 8(b) presents a schematic of the FE models that were developed to simulate the response of the CSEB masonry wallettes. The models were constructed using the two-dimensional elements under the assumption of plane stress as those used for the FCB

masonry walls, i.e., the CPS4R and COH2D4 elements in ABAQUS 6.14 [67]. Also in this case, auxiliary interface elements were not used in SMM-I. All FE models were analyzed using the explicit dynamic FE solver with time step equal to the critical time step of 2.5×10^{-6} s. All degrees of freedoms at the bottom edge of the bottom steel shoe were fixed in the FE models, and a constant vertical velocity of $V = 0.1$ mm/s (i.e., with zero acceleration) was applied downward to the top edge of the top steel shoe. A density $\rho_b = 1.8 \times 10^3$ kg/m³ and mass-proportional damping corresponding to a damping ratio $\zeta = 5\%$ were used for the solid elements of the wall to model inertia and damping effects. Based on a mesh sensitivity analysis performed as described for the previous benchmark example, the mesh used for the SMMs of the CSEB masonry wallettes consisted of 12 interface elements employed for each bed joints (i.e., six interface elements for the bed joint of each half masonry unit), five interface elements for each head joint and for the potential vertical cracks, and 30 elements for each half of the expanded masonry units (having dimensions 267 mm \times 102 mm). Each half of the expanded masonry units was represented by a rigid element for the SMM-I.

The steel shoes were modeled as linear elastic for all the SMMs, with a surface-based tie constraint [67] imposed between the masonry and the steel shoes. The steel shoes were modeled also using CPS4R elements [67], with elastic modulus $E_{\text{steel}} = 21,000$ MPa, Poisson ratio $\nu_{\text{steel}} = 0.30$, density $\rho_{\text{steel}} = 7.85 \times 10^3$ kg/m³, and damping ratio $\zeta_{\text{steel}} = 5\%$. The mesh of the steel shoes was extruded from the masonry wallettes in order to obtain a continuous mesh. The steel shoes were discretized using two elements in the direction orthogonal to that of the extrusion.

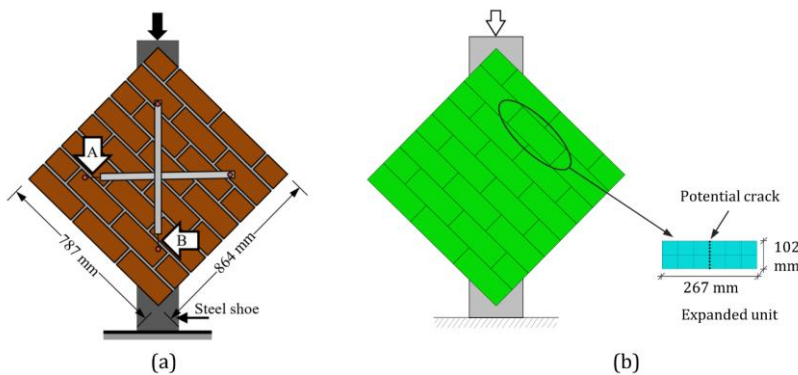


Fig. 8 CSEB masonry wallette: (a) test setup and (b) SMM discretization.

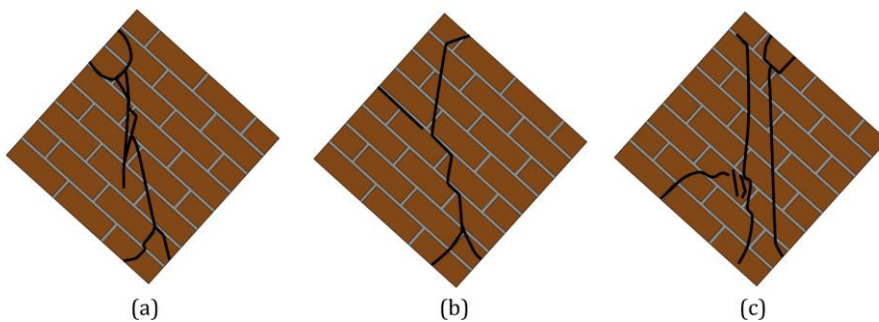


Fig. 9 Experimental crack patterns of the CSEB masonry wallettes: (a) Wall-1, (b) Wall-2, and (c) Wall-3.

The material properties of the different components used in the SMMs were obtained from existing experimental results on tension, shear, and compression tests available in [53,91,92]. These experimental tests were performed on the same batch of CSEBs, and mortar used to build the CSEB masonry wallettes analyzed in this study. An elastic modulus $E_b = 2550$ MPa and a Poisson ratio $\nu_b = 0.17$ were used for the expanded masonry units in SMMs-II and SMM-III. The properties of the masonry joint and potential crack interface used in the different SMMs are given in Table 6, where k_n^b and k_s^b denote the normal and shear stiffness, respectively, of the masonry joint interfaces corresponding to the bed masonry joints; and k_n^h and k_s^h denote the normal and shear stiffness, respectively, of the masonry joint interfaces corresponding to the head masonry joints. For the potential crack interfaces, $k_n^b = k_n$ denote the normal stiffness, and $k_s^b = k_s$ denote the shear stiffness of the interface. Similar to the FCB unreinforced masonry shear wall, the input parameters given in the Table 6 were used to describe the stress-strain curve for the expanded masonry units in SMM-III based on a hardening/softening constitutive law used for the compression cap failure criterion of the CTSIM [5]. The other CDPM parameters used in the SMM-III are: $\psi_c = 38^\circ$, $e_c = 0.1$, $\beta_{bc} = 1.16$, $K_c = 0.67$, $\eta = 8.5 \times 10^{-5}$ [91,92].

Table 6. Properties of masonry joint/potential crack interfaces (SMM-I, SMM-II, and SMM-III) and inelastic compressive properties for the expanded masonry units (SMM-III) of the CSEB masonry wallettes.

Properties		Masonry joint interface			Potential crack interface		
		SMM-I	SMM-II	SMM-III	SMM-I	SMM-II	SMM-III
k_n^b	(N/mm ³)	24.38	907.10	907.10	159.00	2555.00	2555.00
k_s^b	(N/mm ³)	10.44	429.67	429.67	69	1091.45	1091.45
k_n^h	(N/mm ³)	17.89	907.10	907.10	-	-	-
k_s^h	(N/mm ³)	7.66	429.67	429.67	-	-	-
f_t	(MPa)	0.146	0.146	0.146	0.510	0.510	0.510
C_0	(MPa)	0.290	0.290	0.290	0.714	0.714	0.714
C_{Q0}	(MPa)	29.000	29.000	29.000	0.714	0.714	0.714
$\tan \phi_0$	(-)	1.51	1.51	1.51	1.00	1.00	1.00
$\tan \phi_r$	(-)	1.51	1.51	1.51	1.00	1.00	1.00
$\tan \psi_0$	(-)	0.440	0.440	0.440	1.00	1.00	1.00
$\tan \psi_r$	(-)	0.044	0.044	0.044	1.00	1.00	1.00
G_f^I	(N/mm)	0.00212	0.00212	0.00212	0.0090	0.0090	0.0090
G_f^{II}	(N/mm)	0.02120	0.02120	0.02120	0.0495	0.0495	0.0495
$\bar{\sigma}_0$	(MPa)	1.29	1.29	<u>1.29</u>	-	-	-
$\bar{\sigma}_p$	(MPa)	3.88	3.88	<u>3.88</u>	-	-	-
$\bar{\sigma}_m$	(MPa)	1.94	1.94	<u>1.94</u>	-	-	-
$\bar{\sigma}_r$	(MPa)	0.55	0.55	<u>0.55</u>	-	-	-
κ_p	(-)	0.011	0.011	<u>0.011</u>	-	-	-
κ_m	(-)	0.044	0.044	<u>0.044</u>	-	-	-
C_{ss}	(-)	9.0	9.0	-	-	-	-

Note: underlined values are for expanded masonry units of SMM-III

6.3. FE Results

Fig. 10(a) compares the FE force-displacement responses obtained using the different SMMs considered in this investigation with the corresponding experimentally-measured response obtained from the diagonal compression test. Positive and negative displacements correspond to horizontal extension and vertical contraction, respectively, which were experimentally recorded using the displacement transducers A and B, as shown in the Fig. 10(a). Fig. 10(b) presents the CTRs corresponding to the different FE models, which shows that SMM-I is the least computationally demanding model, whereas SMM-III is the most computationally expensive one. The six error measures considered in this study and corresponding to the different SMMs are reported in Table 7. All SMMs significantly overestimate the peak axial force, P_{max} , of the CSEB masonry wallettes, with errors $\epsilon_{P_{max}} = 129.85\%$, 68.44% , and 53.96% for SMM-I, SMM-II, and SMM-III, respectively. In addition, all FE models underestimate the initial stiffness, k , both in the horizontal direction, with ϵ_k varying between -44.20% (SMM-I) and -31.04% (SMM-II and SMM-III), and in the vertical direction, with ϵ_k varying between -25.71% (SMM-II and SMM-III) and -10.63% (SMM-I). SMM-I and SMM-III highly overestimate the displacements at failure in both horizontal ($\epsilon_{\Delta_r} = 507.53\%$ and 49.95% , respectively) and vertical ($\epsilon_{\Delta_r} = 44.50\%$ and 39.55% , respectively) directions. The errors are significantly smaller for the SMM-II, with $\epsilon_{\Delta_r} = 1.80\%$ and -6.96% in the horizontal and vertical directions, respectively. The discrepancies between the force-displacement responses are also larger than for the FCB masonry walls, as reported in Table 5. It is noteworthy that, given the definition of n_j in Eqs. (2) through (4), the global relative errors ϵ_{mean} , ϵ_{RMS} , and ϵ_{abs} are less meaningful when large discrepancies are observed between the experimental and numerical estimates of the displacement at failure, as it is the case here.

Table 7. Comparison of the FE simulation results for the CSEB masonry wallettes in term of errors between experimental and FE load-displacement curves.

Displacements (-)	FE Model (-)	$\epsilon_{P_{max}}$ (%)	ϵ_k (%)	ϵ_{Δ_r} (%)	ϵ_{mean} (%)	ϵ_{RMS} (%)	ϵ_{abs} (%)
Horizontal extension	SMM-I	129.85	-44.20	507.53	-11.59	22.95	18.35
	SMM-II	68.44	-31.04	1.80	10.01	27.62	22.39
	SMM-III	53.96	-31.04	49.95	4.51	20.54	17.45
Vertical contraction	SMM-I	-	-10.63	44.50	53.09	59.24	54.45
	SMM-II	-	-25.71	-6.96	16.49	47.32	39.87
	SMM-III	-	-25.71	39.55	20.97	26.84	24.77

The crack patterns and distribution of in-plane minimum principal stress observed at 0.25mm displacement and the displacement at failure for the SMMs of the CSEB masonry wallettes are presented in Fig. 11(a) and (d) for SMM-I, Fig. 11(b) and (e) for SMM-II, and Fig. 11(c) and (f) for SMM-III. In order to make the cracks visible, the deformed shape in Fig. 11 is magnified by a factor 10. The FE crack patterns of the SMMs do not match the experimental crack patterns of the CSEB masonry wallettes shown in Fig. 11. In fact, the cracks simulated in all SMMs are mostly concentrated at the bottom two masonry bed joints and at the head joints and potential crack interfaces of the bottom two courses of the masonry wallette. As expected, the SMMs are unable to simulate the diagonal cracks observed experimentally in the earthen blocks and, thus, cannot capture the experimental failure mode of the CSEB masonry wallettes.

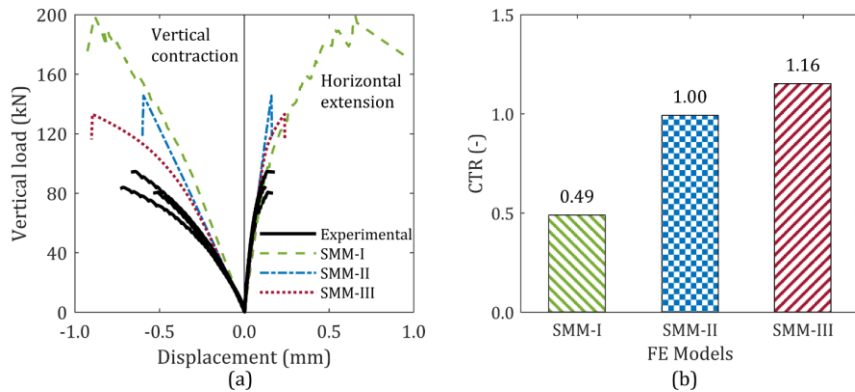


Fig. 10 FE results for the CSEB masonry wallettes: (a) comparison of the experimental and FE load-displacement responses, and (b) CTRs corresponding to different FE models.

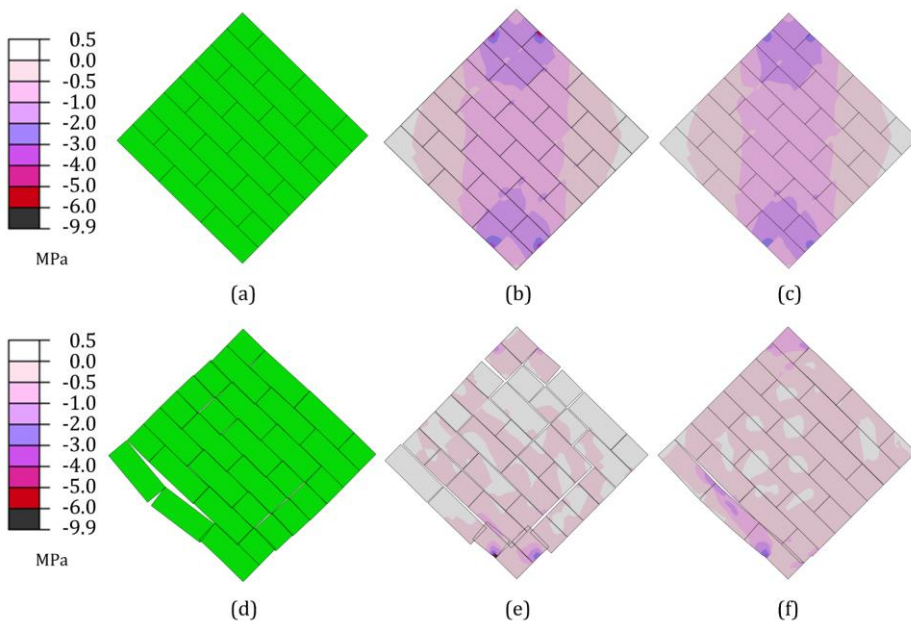


Fig. 11 FE crack patterns and distribution of in-plane minimum principal stress for the SMMs of the CSEB masonry wallettes: (a-c) SMM-I, SMM-II and SMM-III, respectively, at 0.25 mm displacement; and (d-f) SMM-I, SMM-II and SMM-III, respectively, at failure displacement.

It is concluded that the SMMs are unable to simulate the behavior of the CSEB masonry wallettes subjected to a diagonal compression test. This result is due to the fact that CSEB masonry does not satisfy the hypothesis that mortar and unit-mortar interfaces are significantly weaker than the masonry units, which is at the basis of the SMMs. In fact, the assumption that the inelastic behavior is concentrated along the masonry joints and the middle plane of the masonry units is not valid for CSEB masonry, where the experimental evidence shows cracking patterns that are similarly distributed across joints and masonry units. It is also concluded that a modeling approach different than SMM is needed to

properly describe the mechanical behavior of CSEB masonry walls with masonry units of similar strength and stiffness as the mortar and the unit-mortar interfaces. Such new modeling approach needs to be able to model the propagation of cracks with any inclination within the masonry units and the mortar.

5. Conclusions

In this study, the capabilities and limitations of FE simplified micro-modeling techniques were investigated through a comparative analysis of their simulation capabilities with respect to two different types of masonry, i.e., fired-clay brick (FCB) and compressed and stabilized earth block (CSEB) masonry. In the simplified micro-modeling technique, mortar and adjacent unit-mortar interfaces in the masonry are represented by zero-thickness interface elements between expanded masonry units, with a vertical potential crack interface placed in the middle of the expanded masonry units. Different simplified micro-models (SMMs) can be developed based on the different material constitutive models used for the masonry units. This study considered rigid (SMM-I), elastic (SMM-II), and elasto-plastic (SMM-III) constitutive models. The comparative analysis was made between experimentally-measured and numerically-simulated responses of benchmark unreinforced masonry walls that are representative of the two masonry types and for which well-documented experimental data are available in the literature.

This paper also provides recommendations on the use of different FE solvers and on the mesh and time step discretization for developing accurate and robust SMMs within the FE framework. In particular, it is shown that implicit static, implicit dynamic, and explicit dynamic solvers produce similar mechanical responses when used to simulate the nonlinear inelastic behavior of unreinforced masonry walls; however, the explicit dynamic solver is significantly more efficient than the other solvers from a computational point of view.

The FCB unreinforced masonry shear walls showed experimental inelastic behavior and cracks concentrated in the masonry joints (i.e., mortar and unit-mortar interfaces) and in potential crack zones corresponding to the vertical middle plane of the masonry units, whereas CSEB masonry had an experimental inelastic behavior and cracks spread across all masonry constituents. This different behavior is likely because, in the FCB masonry walls, the masonry units are significantly stronger and have higher stiffness than the mortar and the unit-mortar interfaces, whereas the different masonry components have similar strength and stiffness in the CSEB masonry walls.

The FE simulation results indicate that simplified micro-modeling techniques can properly simulate the FE behavior for the FCB masonry shear walls. In fact, all three SMM approaches (i.e., SMM-I, SMM-II, and SMM-III) appear to provide similarly accurate results in terms of global load-displacement responses, peak loads (with errors contained between -4.08 and 15.26%), and initial stiffnesses (with errors contained between -11.40 and 6.29%). The models are less accurate in estimating the displacements at failure (with errors contained between -13.22% and 27.71%); however, this result may also be due to the lack of knowledge on the specific criterion used to terminate the experimental tests. It is observed that: (1) the computational costs increase from SMM-I to SMM-II and from SMM-II to SMM-III, (2) the accuracy in predicting the mechanical response of FCB masonry walls is similar for SMM-II and SMM-III and slightly better than SMM-I, and (3) the accuracy slightly degrades for increasing axial compression applied on the walls.

By contrast, these simplified micro-modeling techniques are in general not suitable for modeling the mechanical response of CSEB masonry walls, because they are unable to reproduce the failure mechanisms produced by cracks propagating across all masonry components. Therefore, a different modeling approach is needed to describe the

mechanical behavior of masonry walls and systems in which the different masonry components have similar strength and stiffness, as for CSEB masonry systems. A possible alternative that should be investigated in future studies is the use of a FE detailed micro-modeling approach, in which each component of a masonry system is modeled separately from the others through an appropriate nonlinear constitutive model.

Conflict of interest

The authors declare that they have no known competing financial interests or personal relationships that could have influenced or appeared to influence the work reported in this paper.

Acknowledgments

Partial support for this research by the Louisiana Board of Regents through the Economic Development Assistantship Program, by the National Science Foundation through awards CMMI #1537078, #1537776 and #1850777, and by the University of California Office of the President (UCOP) Lab Fees program through award LFR-20-651032, is gratefully acknowledged. Any opinions, findings, conclusions, or recommendations expressed in this publication are those of the writers and do not necessarily reflect the views of the sponsors.

The authors thank the anonymous reviewers for their insightful comments, which helped us further improve the clarity of this paper.

References

- [1] Giambanco G, Di Gati L. A cohesive interface model for the structural mechanics of block masonry, *Mechanics Research Communications*, 1997; 24: 503–512. [https://doi.org/10.1016/S0093-6413\(97\)00055-4](https://doi.org/10.1016/S0093-6413(97)00055-4).
- [2] Giambanco G, Rizzo S, Spallino R. Numerical analysis of masonry structures via interface models, *Computer Methods in Applied Mechanics and Engineering*, 2001; 190: 6493–6511. [https://doi.org/10.1016/S0045-7825\(01\)00225-0](https://doi.org/10.1016/S0045-7825(01)00225-0).
- [3] Citto C. (2008). Two-dimensional interface model applied to masonry structures, MS thesis, University of Colorado, Denver, Colorado.
- [4] Macorini L, Izzuddin BA. A non-linear interface element for 3d mesoscale analysis of brick-masonry structures, *International Journal for Numerical Methods in Engineering*, 2011; 85: 1584–1608. <https://doi.org/10.1002/nme.3046>.
- [5] Kumar N, Barbato M. New constitutive model for interface elements in finite-element modeling of masonry, *Journal of Engineering Mechanics*, 2019; 145: 04019022. [https://doi.org/10.1061/\(ASCE\)EM.1943-7889.0001592](https://doi.org/10.1061/(ASCE)EM.1943-7889.0001592).
- [6] Lourenço PB, Rots JG. Multisurface interface model for analysis of masonry structures, *Journal of Engineering Mechanics*, 1997; 123: 660–668. [https://doi.org/10.1061/\(ASCE\)0733-9399\(1997\)123:7\(660\)](https://doi.org/10.1061/(ASCE)0733-9399(1997)123:7(660)).
- [7] Abdulla KF, Cunningham LS, Gillie M. Simulating masonry wall behaviour using a simplified micro-model approach, *Engineering Structures*, 2017; 151: 349–365. <https://doi.org/10.1016/j.engstruct.2017.08.021>.
- [8] Pulatsu B, Erdogmus E, Lourenço PB, Lemos J V, Hazzard J. Discontinuum analysis of the fracture mechanism in masonry prisms and wallettes via discrete element method, *Meccanica*, 2020; 55: 505–523. <https://doi.org/10.1007/s11012-020-01133-1>.
- [9] Baraldi D, Cecchi A. A full 3d rigid block model for the collapse behaviour of masonry walls, *European Journal of Mechanics - A/Solids*, 2017; 64: 11–28. <https://doi.org/10.1016/j.euromechsol.2017.01.012>.

- [10] Oliveira DV, Lourenço PB. Implementation and validation of a constitutive model for the cyclic behaviour of interface elements, *Computers & Structures*, 2004; 82: 1451–1461. <https://doi.org/10.1016/j.compstruc.2004.03.041>.
- [11] D'Altri AM, Sarhosis V, Milani G, Rots J, Cattari S, Lagomarsino S, Sacco E, Tralli A, Castellazzi G, de Miranda S. Modeling strategies for the computational analysis of unreinforced masonry structures: review and classification, *Archives of Computational Methods in Engineering*, 2019; 1: 1–33. <https://doi.org/10.1007/s11831-019-09351-x>.
- [12] Kumar N, Amirtham R, Pandey M. Plasticity based approach for failure modelling of unreinforced masonry, *Engineering Structures*, 2014; 80. <https://doi.org/10.1016/j.engstruct.2014.08.021>.
- [13] Drougkas A, Roca P, Molins C. Experimental analysis and detailed micro-modeling of masonry walls subjected to in-plane shear, *Engineering Failure Analysis*, 2019; 95: 82–95. <https://doi.org/10.1016/j.engfailanal.2018.08.030>.
- [14] Calderón S, Sandoval C, Arnau O. Shear response of partially-grouted reinforced masonry walls with a central opening: testing and detailed micro-modelling, *Materials & Design*, 2017; 118: 122–137. <https://doi.org/10.1016/j.matdes.2017.01.019>.
- [15] Pourfalah S, Cotsovos DM, Suryanto B. Modelling the out-of-plane behaviour of masonry walls retrofitted with engineered cementitious composites, *Computers & Structures*, 2018; 201: 58–79. <https://doi.org/10.1016/j.compstruc.2018.02.004>.
- [16] Page AW. Finite element model for masonry, *Journal of the Structural Division*, 1978; 104: 1267–1285. <https://doi.org/10.1061/JSDEAG.0004969>.
- [17] Andreotti G, Graziotti F, Magenes G. Detailed micro-modelling of the direct shear tests of brick masonry specimens: the role of dilatancy, *Engineering Structures*, 2018; 168: 929–949. <https://doi.org/10.1016/j.engstruct.2018.05.019>.
- [18] Sacco E, Toti J. Interface elements for the analysis of masonry structures, *International Journal for Computational Methods in Engineering Science and Mechanics*, 2010; 11: 354–373. <https://doi.org/10.1080/15502287.2010.516793>.
- [19] Arnau O, Sandoval C, Murià-Vila D. Determination and validation of input parameters for detailed micro-modelling of partially grouted reinforced masonry walls, 10th Pacific Conference on Earthquake Engineering, vol. 68, 2015.
- [20] Lourenço PB. (1996). Computational strategies for masonry structures, PhD Dissertation, Technische Universiteit Delft, Delft, Netherlands.
- [21] Arya SK, Hegemier GA. On nonlinear response prediction of concrete masonry assemblies, *Proceedings of the North American Masonry Conference*, The Masonry Society, Boulder, Colorado, 1978, 11–19.
- [22] Rots JG. *Structural masonry*, CRC Press, London, UK, 2021. <https://doi.org/10.1201/9781003077961>.
- [23] Rots JG. Numerical simulation of cracking in structural masonry, *Heron*, 1991; 36: 49–63.
- [24] Senthivel R, Lourenço PB. Finite element modelling of deformation characteristics of historical stone masonry shear walls, *Engineering Structures*, 2009; 31: 1930–1943. <https://doi.org/10.1016/j.engstruct.2009.02.046>.
- [25] Miccoli L, Garofano A, Fontana P, Müller U. Experimental testing and finite element modelling of earth block masonry, *Engineering Structures*, 2015; 104: 80–94. <https://doi.org/10.1016/j.engstruct.2015.09.020>.
- [26] Furukawa A, Spence R, Ohta Y, So E. Analytical study on vulnerability functions for casualty estimation in the collapse of adobe buildings induced by earthquake, *Bulletin of Earthquake Engineering*, 2010; 8: 451–479. <https://doi.org/10.1007/s10518-009-9156-z>.
- [27] Tarque N. (2011). Numerical modelling of the seismic behaviour of adobe buildings, PhD Dissertation, Università Degli Studi Di Pavia, and Istituto Universitario Di Studi Superiori.

- [28] Petracca M, Pelà L, Rossi R, Zaghi S, Camata G, Spacone E. Micro-scale continuous and discrete numerical models for nonlinear analysis of masonry shear walls, *Construction and Building Materials*, 2017; 149: 296–314. <https://doi.org/10.1016/j.conbuildmat.2017.05.130>.
- [29] Vemuri J, Ehteshamuddin S, Kolluru S. Numerical simulation of soft brick unreinforced masonry walls subjected to lateral loads, *Cogent Engineering*, 2018; 5: 1–21. <https://doi.org/10.1080/23311916.2018.1551503>.
- [30] van Zijl GPAG. Modeling masonry shear-compression: role of dilatancy highlighted, *Journal of Engineering Mechanics*, 2004; 130: 1289–1296. [https://doi.org/10.1061/\(ASCE\)0733-9399\(2004\)130:11\(1289\)](https://doi.org/10.1061/(ASCE)0733-9399(2004)130:11(1289)).
- [31] Dolatshahi KM, Aref AJ. Two-dimensional computational framework of meso-scale rigid and line interface elements for masonry structures, *Engineering Structures*, 2011; 33: 3657–3667. <https://doi.org/10.1016/j.engstruct.2011.07.030>.
- [32] Chisari C, Macorini L, Amadio C, Izzuddin BA. An inverse analysis procedure for material parameter identification of mortar joints in unreinforced masonry, *Computers & Structures*, 2015; 155: 97–105. <https://doi.org/10.1016/j.compstruc.2015.02.008>.
- [33] Zhang Y, Macorini L, Izzuddin BA. Mesoscale partitioned analysis of brick-masonry arches, *Engineering Structures*, 2016; 124: 142–166. <https://doi.org/10.1016/j.engstruct.2016.05.046>.
- [34] Chisari C, Macorini L, Amadio C, Izzuddin BA. Identification of mesoscale model parameters for brick-masonry, *International Journal of Solids and Structures*, 2018; 146: 224–240. <https://doi.org/10.1016/j.ijsolstr.2018.04.003>.
- [35] Minga E, Macorini L, Izzuddin BA. A 3d mesoscale damage-plasticity approach for masonry structures under cyclic loading, *Meccanica*, 2018; 53: 1591–1611. <https://doi.org/10.1007/s11012-017-0793-z>.
- [36] Alfano G, Sacco E. Combining interface damage and friction in a cohesive-zone model, *International Journal for Numerical Methods in Engineering*, 2006; 68: 542–582. <https://doi.org/10.1002/nme.1728>.
- [37] Parrinello F, Failla B, Borino G. Cohesive–frictional interface constitutive model, *International Journal of Solids and Structures*, 2009; 46: 2680–2692. <https://doi.org/10.1016/j.ijsolstr.2009.02.016>.
- [38] Formica G, Sansalone V, Casciaro R. A mixed solution strategy for the nonlinear analysis of brick masonry walls, *Computer Methods in Applied Mechanics and Engineering*, 2002; 191: 5847–5876. [https://doi.org/10.1016/S0045-7825\(02\)00501-7](https://doi.org/10.1016/S0045-7825(02)00501-7).
- [39] Gambarotta L, Lagomarsino S. Damage models for the seismic response of brick masonry shear walls. part i: the mortar joint model and its applications, *Earthquake Engineering & Structural Dynamics*, 1997; 26: 423–439. [https://doi.org/10.1002/\(SICI\)1096-9845\(199704\)26:4%3C423::AID-EQE650%3E3.0.CO;2-%23](https://doi.org/10.1002/(SICI)1096-9845(199704)26:4%3C423::AID-EQE650%3E3.0.CO;2-%23).
- [40] Greco F, Leonetti L, Luciano R, Trovalusci P. Multiscale failure analysis of periodic masonry structures with traditional and fiber-reinforced mortar joints, *Composites Part B: Engineering*, 2017; 118: 75–95. <https://doi.org/10.1016/j.compositesb.2017.03.004>.
- [41] Chaimoon K, Attard MM. Modeling of unreinforced masonry walls under shear and compression, *Engineering Structures*, 2007; 29: 2056–2068. <https://doi.org/10.1016/j.engstruct.2006.10.019>.
- [42] Shing PB, Manzouri T. Analysis of unreinforced masonry structures using elastic/viscoplastic models, *Sísmica 2004–6° Congresso Nacional de Sismologia e Engenharia Sísmica Livro de Actas, Universidade Do Minho, Guimaraes, Portugal*, 2004, 137–150.

- [43] Dolatshahi KM, Nikoukalam MT, Beyer K. Numerical study on factors that influence the in-plane drift capacity of unreinforced masonry walls, *Earthquake Engineering & Structural Dynamics*, 2018; 47: 1440–1459. <https://doi.org/10.1002/eqe.3024>.
- [44] Dolatshahi KM, Yekrangnia M. Out-of-plane strength reduction of unreinforced masonry walls because of in-plane damages, *Earthquake Engineering & Structural Dynamics*, 2015; 44: 2157–2176. <https://doi.org/10.1002/eqe.2574>.
- [45] Dolatshahi KM, Aref AJ. Multi-directional response of unreinforced masonry walls: experimental and computational investigations, *Earthquake Engineering & Structural Dynamics*, 2016; 45: 1427–1449. <https://doi.org/10.1002/eqe.2714>.
- [46] Aref AJ, Dolatshahi KM. A three-dimensional cyclic meso-scale numerical procedure for simulation of unreinforced masonry structures, *Computers & Structures*, 2013; 120: 9–23. <https://doi.org/10.1016/j.compstruc.2013.01.012>.
- [47] Bolhassani M, Hamid AA, Lau ACW, Moon F. Simplified micro modeling of partially grouted masonry assemblages, *Construction and Building Materials*, 2015; 83: 159–173. <https://doi.org/10.1016/j.conbuildmat.2015.03.021>.
- [48] Tang C, Shi B, Gao W, Chen F, Cai Y. Strength and mechanical behavior of short polypropylene fiber reinforced and cement stabilized clayey soil, *Geotextiles and Geomembranes*, 2007; 25: 194–202. <https://doi.org/10.1016/j.geotexmem.2006.11.002>.
- [49] Aghababaei Mobarake A, Khanmohammadi M, Mirghaderi SR. A new discrete macro-element in an analytical platform for seismic assessment of unreinforced masonry buildings, *Engineering Structures*, 2017; 152: 381–396. <https://doi.org/10.1016/j.engstruct.2017.09.013>.
- [50] Caliò I, Marletta M, Pantò B. A new discrete element model for the evaluation of the seismic behaviour of unreinforced masonry buildings, *Engineering Structures*, 2012; 40: 327–338. <https://doi.org/10.1016/j.engstruct.2012.02.039>.
- [51] Baraldi D, Cecchi A. Discrete approaches for the nonlinear analysis of in plane loaded masonry walls: molecular dynamic and static algorithm solutions, *European Journal of Mechanics - A/Solids*, 2016; 57: 165–177. <https://doi.org/10.1016/j.euromechsol.2015.12.008>.
- [52] Bui T-T, Limam A, Sarhosis V. Failure analysis of masonry wall panels subjected to in-plane and out-of-plane loading using the discrete element method, *European Journal of Environmental and Civil Engineering*, 2019; 1: 1–17. <https://doi.org/10.1080/19648189.2018.1552897>.
- [53] Cuellar-Azcarate MC. (2016). Engineered earthen masonry structures for extreme wind loads, PhD Dissertation, University of South Carolina, Columbia, South Carolina.
- [54] Jaquin P. History of earth building techniques, *Modern Earth Buildings: Materials, Engineering, Constructions and Applications*, 2012, 307–323. <https://doi.org/10.1533/9780857096166.3.307>.
- [55] Kumar N, Barbato M, Holton R. Feasibility study of affordable earth masonry housing in the U.S. Gulf Coast region, *Journal of Architectural Engineering*, 2018; 24. [https://doi.org/10.1061/\(ASCE\)AE.1943-5568.0000311](https://doi.org/10.1061/(ASCE)AE.1943-5568.0000311).
- [56] Ben-Alon L, Loftness V, Harries KA, Hameen EC, Bridges M. Integrating earthen building materials and methods into mainstream construction, *Journal of Green Building*, 2020; 15: 87–106. <https://doi.org/10.3992/1943-4618.15.1.87>.
- [57] Matta F, Cuellar-Azcarate MC, Garbin E, Cuéllar-Azcárate MC, Garbin E. Earthen masonry dwelling structures for extreme wind loads, *Engineering Structures*, 2015; 83: 163–175. <https://doi.org/10.1016/j.engstruct.2014.10.043>.
- [58] Atkinson RH, Amadei BP, Saeb S, Sture S. Response of masonry bed joints in direct shear, *Journal of Structural Engineering*, 1989; 115: 2276–2296. [https://doi.org/10.1061/\(ASCE\)0733-9445\(1989\)115:9\(2276\)](https://doi.org/10.1061/(ASCE)0733-9445(1989)115:9(2276)).
- [59] Hofmann P, Stockl S. Tests on the shear-bond behaviour in the bed-joints of masonry, *Masonry Int*, 1986; 9: 1–15.

- [60] Van der Pluijm R. Shear behaviour of bed joints, Proceedings of 6th North American Masonry Conference, The Masonry Society, Boulder, Colorado, 1993, 125–136.
- [61] Van der Pluijm R. Overview of deformation controlled combined tensile and shear tests, Eindhoven University of Technology, Eindhoven, The Netherlands, 1998, vol. Technical.
- [62] Page AW. The biaxial compressive strength of brick masonry, Proceedings of the Institution of Civil Engineers, 1981; 71: 893–906. <https://doi.org/10.1680/iicep.1981.1825>.
- [63] Page AW. The strength of brick masonry under biaxial tension-compression, International Journal of Masonry Construction, 1983; 3: 26–31.
- [64] Andreaus U. Failure criteria for masonry panels under in-plane loading, Journal of Structural Engineering, 1996; 122: 37–46. [https://doi.org/10.1061/\(ASCE\)0733-9445\(1996\)122:1\(37\)](https://doi.org/10.1061/(ASCE)0733-9445(1996)122:1(37)).
- [65] Roberts JJ, Edgel GJ, Rathbone AJ. BS 5628:1985: British standard code of practice for use of masonry part 2: structural use of reinforced and prestressed masonry, Palladian Publications Limited, London, UK, 2018. <https://doi.org/10.1201/9781482275636>.
- [66] Pelà L. (2009). Continuum damage model for nonlinear analysis of masonry structures, PhD Dissertation, Universitat Politècnica de Catalunya, Catalonia, Spain, & Università Degli Studi Di Ferrara, Italy.
- [67] Dassault Systèmes. Abaqus 6.13 documentation, Dassault Systèmes, Providence, RI, 2013.
- [68] Lubliner J, Oliver J, Oller S, Oñate E. A plastic-damage model for concrete, International Journal of Solids and Structures, 1989; 25: 299–326. [https://doi.org/10.1016/0020-7683\(89\)90050-4](https://doi.org/10.1016/0020-7683(89)90050-4).
- [69] Lee J, Fenves GL. Plastic-damage model for cyclic loading of concrete structures, Journal of Engineering Mechanics, 1998; 124: 892–900. [https://doi.org/10.1061/\(ASCE\)0733-9399\(1998\)124:8\(892\)](https://doi.org/10.1061/(ASCE)0733-9399(1998)124:8(892)).
- [70] ASTM International. ASTM C952-12 (withdrawn 2018) standard test method for bond strength of mortar to masonry units, ASTM Standards, ASTM International, West Conshohocken, PA, 2012. <https://doi.org/10.1520/C0952-12>.
- [71] ASTM International. ASTM C1314-21 standard test method for compressive strength of masonry prisms, ASTM Standards, ASTM International, West Conshohocken, PA, 2021. <https://doi.org/10.1520/C1314-21>.
- [72] Lourenço PB, Almeida JC, Barros JAO. Experimental investigation of bricks under uniaxial tensile testing, Journal of British Masonry Society Masonry International, 2005; 18: 11–20.
- [73] Masonry Standards Joint Committee. TMS 402/602-16 Building code requirements and specification for masonry structures, The Masonry Society, Boulder, Colorado, 2016. ISBN: 978-1-929081-52-3.
- [74] Jankowiak T, Lodygowski T. Identification of parameters of concrete damage plasticity constitutive model, Foundations of Civil and Environmental Engineering, 2005; 6: 53–69.
- [75] Michał S, Andrzej W. Calibration of the CDP model parameters in ABAQUS, The 2015 World Congress on Advances in Structural Engineering and Mechanics (ASEM15), 2015.
- [76] Hughes TJR. The finite element method: linear static and dynamic finite element analysis, Courier Corporation, 2012. ISBN:0486135020.
- [77] Wu SR, Gu L. Introduction to the explicit finite element method for nonlinear transient dynamics, Wiley, 2012. <https://doi.org/10.1002/9781118382011>.
- [78] Ferrante A, Clementi F, Milani G. Dynamic behavior of an inclined existing masonry tower in Italy, Frontiers in Built Environment, 2019; 5: 33. <https://doi.org/10.3389/fbuil.2019.00033>.

- [79] Silva LC, Lourenço PB, Milani G. Numerical homogenization-based seismic assessment of an english-bond masonry prototype: structural level application, *Earthquake Engineering & Structural Dynamics*, 2020; 49: 841–862. <https://doi.org/10.1002/eqe.3267>.
- [80] Simo JC, Hughes TJR. *Computational inelasticity*, Springer-Verlag, New York, USA, 1998, vol. 7. <https://doi.org/10.1007/b98904>.
- [81] Newmark NM. A method of computation for structural dynamics, *Journal of the Engineering Mechanics Division*, 1959; 85: 67–94. <https://doi.org/10.1061/JMCEA3.0000098>.
- [82] Chopra AKCA. *Dynamics of structures: theory and applications to earthquake engineering*, Pearson, Boston, Massachusetts, USA, 2014, 4th ed. ISBN:0273774247.
- [83] Anthoine A. Homogenization of periodic masonry: plane stress, generalized plane strain or 3d modelling?, *Communications in Numerical Methods in Engineering*, 1997; 13: 319–326. [https://doi.org/10.1002/\(SICI\)1099-0887\(199705\)13:5<319::AID-CNM55>3.0.CO;2-S](https://doi.org/10.1002/(SICI)1099-0887(199705)13:5<319::AID-CNM55>3.0.CO;2-S).
- [84] Addressi D, Sacco E. Nonlinear analysis of masonry panels using a kinematic enriched plane state formulation, *International Journal of Solids and Structures*, 2016; 90: 194–214. <https://doi.org/10.1016/j.ijsolstr.2016.03.002>.
- [85] Vermeltfoort AT, Raijmakers TMJ. Deformation controlled tests in masonry shear walls, part 2 (in Dutch), Technische Universiteit Delft, Eindhoven, The Netherlands, 1993.
- [86] Raijmakers TMJ, Vermeltfoort AT. Deformation controlled tests in masonry shear walls (in dutch), Technische Universiteit Delft, Eindhoven, The Netherlands, 1992.
- [87] Kupfer HB, Gerstle KH. Behavior of concrete under biaxial stresses, *Journal of the Engineering Mechanics Division*, 1973; 99: 853–866. <https://doi.org/10.1061/JMCEA3.0001789>.
- [88] Hendry AW. *Structural masonry*, Scholium International, London, UK, 1998, 2nd ed. ISBN:134914827X.
- [89] D'Altri AM, Sarhosis V, Milani G, Rots J, Cattari S, Lagomarsino S, Sacco E, Tralli A, Castellazzi G, de Miranda S. A review of numerical models for masonry structures, *Numerical Modeling of Masonry and Historical Structures*, Elsevier, 2019, 3–53. <https://doi.org/10.1016/B978-0-08-102439-3.00001-4>.
- [90] Danso H, Akwaboah M. Assessment of the quality of burnt bricks produce in Ghana: the case of Ashanti region, *Case Studies in Construction Materials*, 2021; 15: e00708.
- [91] Rengifo-López EL, Kumar N, Matta F, Barbato M. Experimental and numerical study of uniaxial compression behavior of compressed and stabilized earth blocks, *Proceedings of the 13th North American Masonry Conference*, The Masonry Society, Longmont, Colorado, 2019, 925–936. ISBN:1053-2366.
- [92] Rengifo-López EL, Kumar N, Matta F, Barbato M. Experimental characterization and numerical simulation of compressive behavior of compressed and stabilized earth block specimens, *Proceedings for the Tenth International Earthbuilding Conference (Earth USA 2019)*, Adobe in Action, La Madera, New Mexico, 2019, 314–320.



Reivew Article

Evaluation of energy retention capacity of composite CFRP and GFRP in RC beam strength

Ali İhsan Çelik

Tomarza Mustafa Akıncioğlu Vocational School, Kayseri University, Tomarza, 38280 Kayseri, Turkey

Article Info

Article history:

Received 02 Jan 2022

Revised 13 Feb 2022

Accepted 04 Mar 2022

Keywords:

*EBR technique;
Fiber-reinforced
polymer (FRP);
Composite materials;
Carbon fiber sheet;
Strengthening*

Abstract

Energy dissipation capacity and ductility are two significant parameters to improve structural performance in construction. Although there are many traditional methods of strengthening studies of beams are strengthened with fiber polymers draw attention, especially in recent years. In this study, the strengthening of the beams by the externally bonded reinforcing (EBR) method are investigated. The current studies in the literature are comprehensively reviewed and significant results have been presented. The energy dissipation capacities and ductility values of the important forty CFRP-GFRP beam strengthening studies of the last 10 years have been determined as nearly value based on the load-deflection graphs. The results are given in the table, and the accuracy hypothesis of the mean values of the two groups are statistically made with usage of the T-test. The values were chosen from within the acceptable range to increase the accuracy of the T-test. The average of the selected ultimate load values is very close to each other, CFRPs have also slightly higher load carrying capacity than GFRPs. When it comes to ductility analysis with T-test, it is seen that GFRPs have higher ductility values.

© 2022 MIM Research Group. All rights reserved.

1. Introduction

Beams are significant part of the reinforced concrete structure. Fiber-reinforced polymers Fiber reinforcement polymers (FRP) are significant composite materials for strengthening of RC beams [1]. FRPs are widely used to strengthen reinforced concrete (RC) beams in the last twenty years to provide additional improvement in the mechanical behavior of reinforced structures in terms of strength and rigidity. Since the reinforcement studies using Externally Bonded Reinforcement (EBR) fabrics/laminates in the late 1990s, the method has received considerable attention and development. Composite materials having high strength and elasticity modulus have been developed to strengthen the RC beams externally. According to Razaqpur et al., FRPs are highly efficient in the rehabilitation of RC beams due to their high strength, high elastic modulus, and low density [2]. The use of FRP composite materials in strengthening and repairing RC structures is a received engineering practice. Despite the current code provisions, the design of strengthened of RC beams with FRP composites include several challenges [3]. T.F.El-Shafiey mentioned that the use of delaminates in the strengthening of RC beams have received a significant share in research on the external strengthening of beams [4]. FRP systems for strengthening RC structures have emerged as an alternative to traditional strengthening techniques such as steel plate bonding, section enlargement, and external stretching[2,4]. Fiber selection often controls the properties of composite materials. Carbon, Glass, Aramid, and Basalt materials are the four main types of fibers used in construction. The composite is often referred to as reinforcing fibers, such as, Carbon Fiber Reinforced Polymer (CFRP) and Glass Fiber Reinforced Polymer (GFRP).

*Corresponding author: acelik@kayseri.edu.tr

^a orcid.org/ 0000-0001-7233-7647

DOI: <http://dx.doi.org/10.17515/resm2022.379st0102>

Res. Eng. Struct. Mat. Vol. 8 Iss. 3 (2022) 491-518

There are two main techniques to strengthen of RC beams, which are externally bonded reinforcing (EBR) and near-surface mounted (NSM) techniques. In this study, it has been focused on the EBR techniques that find out their advantages, disadvantages, and application are detailed in the subtitles. Many curves in the literature have been redrawn to better understand the use of the EBR technique in the RC beams. In addition to the application technique used in beam strengthen, the type of fabrics attached is also important. CFRP and GFRP fabrics are widely used in strengthening of RC BEAMS. Hence, mainly focused on the beams that are strengthened with CFRP and GFRP laminates using the EBR technique. Moreover, important findings compiled from studies conducted in the last ten years, which have been added to the tables. The table includes a total of 40 experimental studies reinforced with 20 CFRP and 20 GFRP laminates according to the EBR technique. It is understood from the studies performed that while high strength is generally obtained in the studies with FRP, the energy holding capacity and ductility remain at low levels. This is mostly due to the linear elastic behavior of FRP type materials. In some studies, with additional methods, namely changes in the volumetric ratios of FRPs, the ductility has been increased a little more by increasing the thickness or by methods such as anchoring. The significant consequence of this is the need for external strengthening composites to strength the elastic behavior of the reinforcement.

The maximum strength of CFRPs is higher than GFRPs on average, but GFRPs have higher elongation at break, they also can consume more energy and ductility is slightly higher. As a comparison study, 20 CFRP and 20 GFRP results of articles were analyzed by statistical T-test and the accuracy hypothesis of the mean values was presented mutually. The results show that the standard deviation of the energy and ductility values of GFRPs are normal compared to the means. In addition, when the proximity of the standard deviations between CFRP and GFRP with the mean value is tested with 95% accuracy, it is seen that the value 0 from the results obtained remains in the mean of both groups. These results require the accuracy of the hypothesis.

Hence, many parameters and results of the studies are presented together, and the researchers will have the opportunity to see the results of the studies made with the EBR technique using CFRP and GFRPs. In addition, compiling important studies of the last 10 years and revealing the energy dissipation capacities and ductility according to the load-deflection graphs makes the study unique.

2. Strengthening of RC Beams Using FRP

The composite materials were first used in aerospace applications such as aircraft and spacecraft. Since the 1970s, its usage in other areas has continued to increase. FRP materials are used as reinforcement material for concrete structures as well as reinforcing various structures made of plates, strips, concrete, walls, timber and even steel. The use of FRPs to improve the seismic performance of structures is increasing day by day.

Spadea et al., strengthened the RC beams with EBR- CFRP sheets to observe structural behavior of beams. They tested four beams under displacement controlling. The results show that the adherence between a CFRP plate and the surface of a RC beam that may cause an important deterioration in response of coating beam regardless of an anchor stress and the bond shear between the slab and the concrete substrate [6]. Kotynia et al., conducted an experimental study and numerical analysis of RC beams strengthened in flexure with various externally bonded CFRP configurations. They tested ten rectangular RC specimens with clear span of 4.2 m, as two series to appreciate the influence of using the additional U shaped CFRP system on the intermediate crack stripping of the bottom laminate [7]. In order to take in consideration of the orthotropic behaviour of the CFRP laminates, a numerical analysis was performed in the parametric study, which it was showed that

increasing the FRP thickness increases the load carrying capacity when the failure mode is FRP rupture, and increasing the limiting effect increases load carrying capacity when the failure mode occurs as a FRP breakage. A design method was proposed to obtain sufficient load carrying capacity and ductility performance [8].

RC beams should be resistant to various impact and burst loads. Thanks to FRP strengthening techniques can be provided improvements in the strength and flexibility of RC beams [9]. Siddika et al., conducted a review paper for characteristic performance of RC beams reinforced with the FRP that under different loading. Their review study showed that the RC beams can be strengthened with FRP type materials to eliminate damages, provide better strength, flexibility and insulation [9,10].

There are two strengthening techniques of RC beams with FRP materials: externally bonded reinforcing (EBR) laminates near-surface mounted (NSM) bars/strips strengthening techniques [11]. The EBR system is the most strengthening technique in terms of ease of application. It is widely used in strengthen structural elements for shear, flexure, torsion and axial. NSM strengthening technique is used in the feasibility to effectively increase shear load carrying capacity and deformation properties of reinforced structural members. In general, the NSM system consists of placing additional reinforcements inside the concrete cover of the deficient structural element. This technique has outperformed most of the other methods due to the ease of providing a significant increase in the capacity of the structural member [12–15]. Mechanical anchoring systems, grooving methods or without adhesive have been used FRP techniques. In addition, throughout the thickness of the RC element to be reinforced FRP fabrics can be joined by threading or sewing [16–18]. It may be a good idea to round the beam edges before wrapping with FRP to reduce excessive stress on the beam edges and increase compressive strength and also enhance the interaction between FRP and concrete [19–21]. External CFRP sheets are the most common method used to strengthening, rehabilitating or repairing RC members. CFRP increases the bending, shear capacity of the deteriorated members, and extends their useful life [22]. These techniques are schematically illustrated in Fig. 1.

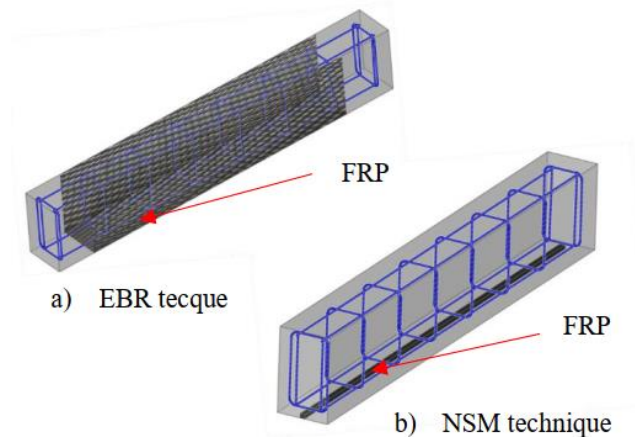


Fig. 1 Illustrated EBR and NSM techniques

There are some techniques such as preparation of the concrete surface for EBR and NSM methods during the strengthening of RC beams, cleaning, epoxy resin adhesive injection and placement of laminates. These preparation steps can be listed as surface preparation,

adhesive operation and anchorage provision [16,17,23,24]. Concrete surface preparation can increase the ultimate load by 3-10% [25].

Grooves of special width and thickness are drilled from the concrete surface in NSM technique. Then FRP strips and epoxy resin can be used to fill the concrete. Epoxy resin is applied to fasten FRP boards directly through the specified cavity [26]. Since the NSM technique is applied from the inside, which by opening a channel along the beam, the delamination and environmental adverse effects caused by the EBR technique do not occur. For this reason, the NSM is considered by researchers as a superior technique [9]. In order to remove impurities hidden on the concrete surface, the weak layer is removed in traditional surface preparation and a surface with visible aggregates is obtained. This ensures proper and sufficient adhesion between the concrete surface and the FRP composite [27]. Surface bonding by external bonding is a common method for attaching FRP boards to the surface of concrete beams. Researches have shown that removing a thin concrete surface with water pressure will increase the effect of surface preparation [25]. It was proved that beams softened by water pressure carry more load than those softened by grinding [28].

Epoxy adhesives are an important equipment of the class of structural adhesives, which includes polyurethane, acrylic, cyanoacrylate and other chemistries. These high-performance adhesives are widely used in the construction [29]. Resins are solid and viscous polymers. Applications of epoxy-based materials are wide-ranging, which include coatings, adhesives or clay mineral reinforcements [30]. These polymeric materials, which are properties polyester, epoxy or phenolic forms, provide excellent adhesion strength [26]. There are many types of epoxy resins. Epoxies are known as materials with excellent adhesion and chemical heat resistance properties as well as good and excellent mechanical properties [30]. Manufacturers obtain epoxy resin by mixing certain proportions of epoxy and hardener components in their specifications. This ratio usually ranges from 1:1 to 5:1, unless the epoxy and hardener components are especially specified. Epoxy resins weight approximately 0.5 kg/m² per unit surface area [26,31]. Epoxy adhesives are better than other common adhesives in terms of heat and chemical resistance. In general, thermosetting epoxy adhesives are more heat and chemical resistant than those hardened at room temperature. Maximum elongation in case of failure occurs in the tensile stress range of 30 MPa to 90 MPa 0.9-4.5% and 1.1 GPa - 6 GPa elastic modulus. The epoxy curing period is generally between 3 days and 14 days and 16 °C - 23 °C temperature [33]. As disadvantages, the strength of epoxy adhesives decreases at temperatures above 177 °C. [31,33-35].

Generally, there are four wrapping methods of FRP sheets to enhancing load carrying capacity of beams. These methods are full wrap on four faces (Fig. 2a), U shape wrap on bottom and two side faces (Fig. 2b), under bound as band (Fig. 2c) and two-side bound on lateral sides method (Fig. 2d). The configurations of FRP shown in Fig. 6 can be continuous sheets, spaced or diagonally bounded. Flexible and U-shaped FRP strips can be used to resist delamination in beams under intense loads. The sheets can be placed in the center line of the point load, covering the beam tensile face [36]. The method of FRP strips on two lateral faces has the disadvantage like decomposition on the faces. The method of FRP strips on two lateral faces has the disadvantage like debonding. In order to prevent or delay separation of FRP sheets used in shear and flexural strengthening, anchoring methods to conventional EBR are used to anchor FRP sheets to the structural member (GM) [13,37,38].

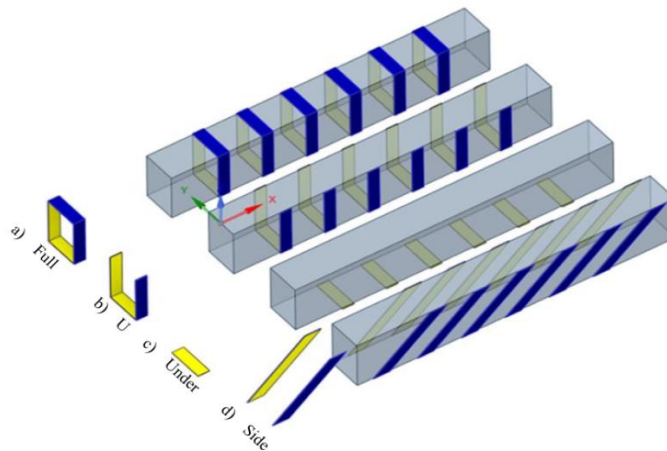


Fig. 2 Wrapping types of FRP on the beams

2.1. Strengthening Beams using EBR Technique

EBR strengthening of damaged beams helps the beams to recover as well as increase shear capacity. Moreover, a CFRP split strip layer increased the total capacity of shear-deficient beams by more than 60%, and an additional layer increased the cutting capacity by another 30% [39]. The quality of the strengthening materials and the technique used play an important role in increasing the load carrying capacity of RC beams. RC beams have many different wrapping techniques. For instance, application of EBR to the external bonding of the beam member along the tension face can effectively increase the flexural strength [9,20,40,41]. In another experimental study, the increase in shear strength of the beam strengthened with U-Wrapped CFRP plates was observed. As a result of the observation, the increase in shear capacity of the fully wrapped WBR1 and WBR2 beams compared to the control samples was observed to be 69.28% and 201.63%, respectively [42]. When the beams with shear deficiency reinforced with GFRP externally and internally, were subjected to the bending test at three points, it was observed that the load bearing capacity increased significantly compared to the control sample. Concrete beams built from individual segments connected to each other by special mechanism referred as segmental beams have a higher ratio of CFRP area and less deflection, in which can maintain the ultimate loading value of 38.4% [43].

There can also be a significant increase in flexural flexibility, energy dissipation and non-elastic performance of the RC beams. The performance of the external GFRP wrapped RC beam makes up for better than the internal wrapped beam [44]. ACI 440.2R for predicting the shear strength of RC beams strengthened with EBR gives conservative estimates of shear capacity due to its inability to capture the variation of β and θ [45]. Recently, EBROG, which is a new method called Externally Bonded Reinforcement on Grooves has been introduced as an alternative to the EBR method to retrofit RC beams. The EBROG method has also been studied by many researchers [37,46,47,56]. Axial and flexural strengthening of RC columns and seismic strengthening of RC beam-column joints are discussed as detail [16,47–49]. The use of the EBROG method in specimens resulted in a significant increase up to the maximum load-carrying capacity compared to the EBR technique in terms of area under the ultimate load capacity, mid-span deviation, and load deviation curve [50]. In most cases, by increasing the number of CFRP layers, seismic parameters such as failure stress, energy absorption and ductility increase. However, in beams with higher strength concrete, the effect of CFRP on mechanical properties and seismic parameters is more

pronounced [51]. In another experimental study that reinforced and non-reinforced beams are mutually adjusted, which has been shown that it is possible to obtain economical and higher performance beams by reducing the amount of reinforcement in reinforced beams [52]. The beam that failed by delamination of the CFRP sheets experienced debonding strain of 3341 micro strain which represented 19% of the rupture strain of CFRP sheets. The analytical procedure provided accurate and consistent estimates for the shear capacity of beams tested with CFRP strengthening [53]. An experimental study was conducted on one unreinforced RC box-girder and four RC box-girders strengthened by different CFRP wrapping schemes. In addition, the characteristics of each strengthening scheme are also revealed through comparing the strain distribution pattern of box-girders strengthened with CFRP and that of contrast box-girder.

3. The Strengthening Applications

Reinforcement in RC beams is generally done to increase shear strength, flexural strength, fatigue life, earthquake performance, impact and burst strength [9]. Shear crack and flexural failures widely occur in beams so that shear and flexural strengthening of beams should be considered. Strengthening methods are described in detail below. In the EBR technique, the correct application of the laminates on the desired surface depends on the correct knowledge of the stress surface. It is possible to adhere more than one laminate to the stress side [54,55].

3.1. Shear Strength Performance of RC Beams

sliding and tearing of the molecules of concrete materials of beams. Many studies have been carried out in recent years due to the development of high performance FRP materials to increase the shear performance of the structures [38,56–59]. The FRP composites are effective in the rehabilitation of structures as they stop the propagation of cracks. They increase the hardness and resistance and prolong their lifecycle [60]. The beams are reinforced with steel stirrups to resist shear stresses, also strengthened with longitudinal steel reinforcing bars to withstand flexure stresses. The shear reinforcement of the RC beams adds an external shear reinforcement to support the internal shear reinforcement (stirrups). Test results of beams reinforced using the EBR FRP technique have shown that the high corrosion level of stirrups significantly reduces the shear capacity of both the strengthened and unstrengthen beams [61]. The beam wrapped with three layers of GFRP sheet in the shear spans and anchored with A3 type anchorage system, increases the shear strength by 55.5% with ductile behavior than the non-strengthened beam [62]. As a winding technique, higher strength can be obtained in beams wrapped in a U shape compared to other winding techniques. However, FRP fabrics can be mounted on the surface with techniques such as anchors to increase energy retention capacity and density after bounded with epoxy resin [63]. The failure mode in the strengthened beam can be transformed from shear failure to flexural failure thanks to the CFRP winding. Strengthening of beam with CFRP increased the shear capacity of beams [64]. Shear cracks usually take place at an angle of 45° as shown in Fig. 3 in the compression zone between the applied load and the supports. Shear cracks are closer to the load application area.

It was stated that with the CFRP bars applied using the NSM technique, the shear strength of RC slender beams can be increased between 17% and 25% [65]. In an experimental study conducted by Ibrahim, which was showed that the effectiveness of using both NSM and EB strengthening systems to enhance the shear capacity of RC rectangular deep beams. In the experimental research conducted by comparing the winding system of the CFRP strips with both sides U-shaped and fully wrapped on both sides, the presence of horizontal CFRP strips in the vertical strips increases the shear capacity of the beams ranged between 3-27% for beams with the same properties, while the increase in the ultimate loads ranged

between 20-26% and 39.5-46% [66]. In another experimental study strength, stiffness, ductility and crack were compared of specimen before and after retrofit. The experiment showed the ultimate load of beam was enhanced after strengthening, but the ductility and stiffness of the beam were decreased. Shape of cracks also changes between original and wrapped beam [67]. In addition, as the CFRP strip spacing decreases, shear capacity, final deflection and bending stiffness increase. In order to increase the effectiveness of the EBR technique, an increase in the performance of the EBR technique with the help of external reinforcement with a new method called EBROG was observed [68]. The bond strength of the EBROG sample was 42-67% higher than that of the EBR sample [69]. Beams strengthened in shear with externally bonded reinforcement in grooves (EBROG) method the beams shear capacity was increased with and without stirrups by an average value of 40% and 69%, respectively, compared to the corresponding controls. Based on the results of analytical models to estimate shear contribution in traditional methods, the proposed formulations can be used to estimate shear gain due to EBROG laminates [70]



Fig. 3 Shear failures of RC beam

3.2. Flexural Strength Performance of RC Beams

The RC beams commonly undergo flexural fracture in the middle span [71]. Flexural fracture of beam is shown in Fig. 3.4. CFRP laminates with the EBR are an effective technology to increase service life and maximum RC beam loads even when made with low quality concrete [72]. According to some researchers, conventional method for flexural strengthening of RC beams is made by means of EBR, which is adhered to the tension base [73-76]. Thanks to EBROG method longitudinal grooves with a depth of 10 mm resulted in complete elimination of separation and significantly increased load-bearing capacity and also retained 100% capacity of FRP sheets [16]. Moreover, in an experimental study used on the EBR and EBROG methods, in three vertical and inclined configurations demonstrated the effectualness of inclined orientation load carrying capacity of strengthening sheets [77]. According to Daugevicius's estimate deflection method, the deflection of the strengthened RC beam can be calculated, and the deflection can be estimated when the steel yield is reached. In the strengthened the RC beam, maximum bending moment occurs at higher rates due to increasing reinforcement stress, while it occurs at lower values in the non-strengthened beam [78].

Bonding FRP laminates to increase the flexural strength along the tensile face of the RC beams (usually the lower part) is an effective method that has gained interest in recent years [35,79]. Strengthening the RC beams against bending is also an effective method preferred in terms of repair. These preferences increase the confidence in the material and the method used. Singh and Munjal [80] strengthened of tension zone with one layer of the

CFRP lamina for flexural failure. First, they cleaned bottom surface of the beam for dust before applying epoxy adhesive. Then, they strengthened the RC beam by gluing CFRP along the beam by applying epoxy resin uniform to the beam base by means of a roller brush. Similarly, some researchers used steel plates for the flexural strengthening of RC structures with the EBR [81–85]. On the other hand, there are also researchers who argue that the using of steel plates for externally bonded reinforcement is associated with potential corrosion, poor strength, increased dead loads and premature failure of reinforced structural members [86–88]. The application of the adhesive and FRP under the RC beam is shown schematically in Fig. 5.

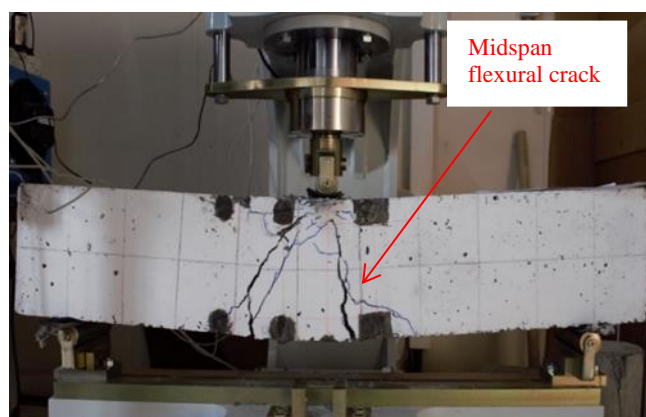


Fig. 4 Flexural failures of RC beam

Bonding FRP laminates to increase the flexural strength along the tensile face of the RC beams (usually the lower part) is an effective method that has gained interest in recent years [35,79]. Strengthening the RC beams against bending is also an effective method preferred in terms of repair. These preferences increase the confidence in the material and the method used. Singh and Munjal [80] strengthened of tension zone with one layer of the CFRP lamina for flexural failure. First, they cleaned bottom surface of the beam for dust before applying epoxy adhesive. Then, they strengthened the RC beam by gluing CFRP along the beam by applying epoxy resin uniform to the beam base by means of a roller brush. Similarly, some researchers used steel plates for the flexural strengthening of RC structures with the EBR [81–85]. On the other hand, there are also researchers who argue that the using of steel plates for externally bonded reinforcement is associated with potential corrosion, poor strength, increased dead loads and premature failure of reinforced structural members [86–88]. The application of the adhesive and FRP under the RC beam is shown schematically in Fig. 5.

It is known that the U-shaped or completely wrapped beams with FRP fibers show very good strength performance, but it is quite complicated to apply in practice completely beams with FRP strips [89]. Flexural strength, stiffness and deflection resistance can be increased in beams by wrapping the FRPs in the form of a U-wrap [35,45]. The thickness of the U-shaped wrapped FRPs can be decisive in determining the strengthening performance of RC beams. For instance, in the flexural tests, which has been observed in several studies that the deflection resistance of RC beams reinforced with two-layer U-wound FRP sheet is reduced by about 39% compared the U-wound FRP strengthened RC beams with a single layer FRP. It can be understood from this that the high ratio of flexural strength weakens the reinforcement [90,91]. The side-externally bonded (S-EBR) strengthening technique with CFRP fabric significantly could enhance the flexural capacity of non-pre-cracked and pre-cracked lightweight RC beams [92]. Anchoring systems are

more effective and useful to increase the flexural behavior of beams when use CFRP laminates for flexural strengthening [93,94]. CFRP and GFRP composite fabrics are widely preferred in beam strengthening. Although BFRP fabric is not economical, the RC beam can significantly increase its bending capacity [95].

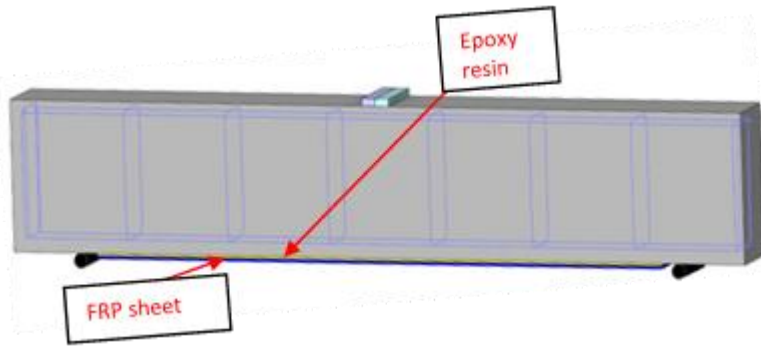
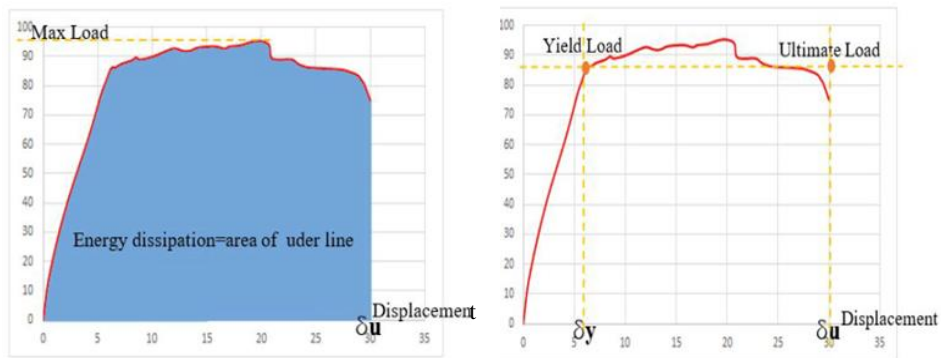


Fig. 5 Activated blind shear ram and shear sequence

3.3. Energy Dissipation and Ductility Performances

The most common composites used in strengthening RC beams using the EBR technique are CFRP and GFRP. Based on this, the studies conducted with both methods in the last 10 years has been examined in detail and the results have been written in Table 4. A total of 40 valuable study data have studied, including 20 from CFRP and 20 from GFRP. As a result of the examined studies, comparisons have been made by giving load-bending graphics of the beams.

With the high strength expected from structural beams, the increase in energy dissipation capacity and the increase of ductility, respectively. As a result of 40 studies examined in Table 1, very little energy retention capacity and ductility values were determined. The energy dissipation capacity is given by the area shown in blue in the load displacement graph in Fig. 6a. Ductility is calculated by dividing the displacement at the ultimate load case by the displacement at the yield point as shown in the graph in Fig. 6b.



(a) Energy dissipation = $\int_0^F F \cdot d\delta$

(b) Ductility = δ_u / δ_y

Fig. 6 Representation of energy dissipation and ductility

These values, which are not given in the majority, were calculated one by one and added to the Table 1. Thus, a significant compilation and contribution has been achieved in the literature. In addition to these, the energy holding capacities of the reinforced beams and their ductility values are discussed and various assumptions are presented below the Table 1.

Table 1. Mechanical properties of composite

Beam Label	FRP type	Wrapping	Lamina Strength	Lamina Elasticities	Thickness	Lay up	F _c (MPa)	Beam Length(mm)	Depth of beam(mm)	Width of Beam (mm)	Failure	Strength (kN)	Energy Dissipation (kN)	Ductility (mm/mm)
[89](Gemi et al. 2019)														
P2	CFRP	F	-	0	-	±45	30	3200	315	80	B	123	2722	2,17
P3	CFRP	U	-	0	-	±45	30	3200	315	80	B	116.4	5252	3.17
P4	CFRP	U	-	0	-	±45	30	3200	315	80	S	118.9	3124	1.67
P5	CFRP	F	-	0	-	±45	30	3200	315	80	S	132.5	5697	2.08
[96](Arslan et al. 2019)														
CFRP-1-RB	CFRP	F	-	0	-	0/90	0	2500	250	125	B	117.2	6482	4.07
CFRP-1-D75	CFRP	F	-	0	-	0/90	0	2500	250	125	B	117	6073	3.57
CFRP-1-D110	CFRP	F	-	0	-	0/90	0	2500	250	125	S	117.1	1557	1.49
CFRP-1-D160	CFRP	F	-	0	-	0/90	0	2500	250	125	S	68.4	861.6	1.37
CFRP-2-D75	CFRP	F	-	0	-	0/90	0	2500	250	125	B	113	6404	4.39
CFRP-2-D110	CFRP	F	-	0	-	0/90	0	2500	250	125	B	128.5	8785	4.46
CFRP-2-D160	CFRP	F	-	0	-	0/90	0	2500	250	125	S	85.6	1304	1.43
[32] (Hawileh et al. 2014)														
BC	CFRP	B	1548	119.25	0.34	±45	50	1840	240	125	SY	92.44	1216	2.37
[31](Attari et al. 2012)														
PA1	CFRP	U	0	19.2	1.5	±45	39	1500	160	100	S	77.86	8.84	4.05
[40](Shannag et al. 2014)														
B1-J100	CFRP	U	-	-	0.17	0	35	1600	200	100	C	144	678.5	1.06
B1-S100	CFRP	B	-	-	0.17	0	35	1600	200	100	C	132	733.4	1.1
B1-Sh100	CFRP	B	-	-	0.17	0	35	1600	200	100	C	130	987.9	1.35
B2-J100	CFRP	U	-	-	0.17	0	35	1600	200	100	C	112	745.9	1.13
B2-S100	CFRP	B	-	-	0.17	0	35	1600	200	100	C	91	530.3	1.24
B2-Sh100	CFRP	B	-	-	0.17	0	35	1600	200	100	C	83	836.8	1.23
[97](Altin et al. 2010)														
1	CFRP	U	4100	231	0.12	90	25	4000	360	120	S	49.51	677.1	2.23
2	CFRP	U	4100	231	0.12	90	25	4000	360	120	S	82.55	1192	1
3	CFRP	U	4100	231	0.12	90	25	4000	360	120	S	81.99	1042	1
4	CFRP	U	4100	231	0.12	90	25	4000	360	120	S	69.04	823.8	-
5	CFRP	U	4100	231	0.12	90	25	4000	360	120	F	87.68	4508	3.03
6	CFRP	U	4100	231	0.12	90	25	4000	360	120	F	86.31	4081	2.77
7	CFRP	U	4100	231	0.12	90	25	4000	360	120	F	86.63	4032	2.19
8	CFRP	U	4100	231	0.12	90	25	4000	360	120	F	86.36	3318	2.02
9	CFRP	U	4100	231	0.12	90	25	4000	360	120	F	85.21	3805	1.99
10	CFRP	U	4100	231	0.12	90	25	4000	360	120	F	85	4169	1.97
[98]Gamino et al., 2010)														
VTC1	CFRP	U	3500	230	0.13	90	60	1500	360	120	S	220	626.6	2.9
VTC2	CFRP	U	2728	221	0.11	90	59	1500	360	120	BF	305	818.4	3.5
VTC3	CFRP	U	2730	218	0.17	90	60	1500	360	120	D	243	610	2.7
VTC4	CFRP	U	3550	235	0.11	90	57	1500	360	120	BF	275	629.8	1.95
VTC5	CFRP	U	1250	310	1.4	90	55	1500	360	120	S	207	501.2	1.75

Table 1. (Con.) Mechanical properties of composite

Beam Label	FRP type	Wrapping	Lamina Strength	Lamina Elasticities	Thickness	Lay up	Fc. (MPa)	Beam Length(mm)	Depth of beam(mm)	Width of Beam (mm)	Failure	Strength (kN)	Energy Dissipation (kJ)	Ductility (mm/mm)
[99](Önal, M. M. 2014)														
KC301	CFRP	F	-	146	0.13	45	20	2200	360	120	S	116	1416	4.8
KC302	CFRP	F	-	146	0.13	45	20	2200	360	120	S	119	1358	5.7
KC303	CFRP	F	-	146	0.13	45	20	2200	360	120	S	117	1376	5.7
[100](Gao. et al. 2016)														
NS	CFRP	B	4286	256	0.11	-	33	2600	300	150	D	118	2022	3.16
PS1	CFRP	B	4286	256	0.11	-	19.8	2600	300	150	R	137	8772	3.77
PS2	CFRP	B	4286	256	0.11	-	15.9	2600	300	150	R	111	4389	3.29
PS3	CFRP	B	4286	256	0.11	-	19.8	2600	300	150	R	119	6791	2.96
PS4	CFRP	B	4286	256	0.11	-	19.8	2600	300	150	R	133	6565	3.53
WPS1	CFRP	B	4286	256	0.11	-	21.9	2600	300	150	R	103	7055	3.02
WPS2	CFRP	B	4286	256	0.11	-	33	2600	300	150	R	110	6971	2.25
SPS1	CFRP	B	4286	256	0.11	-	33	2600	300	150	R	116	5691	2.76
SPS2	CFRP	B	4286	256	0.11	-	33	2600	300	150	R	121	7658	2.77
SPS3	CFRP	B	4286	256	0.11	-	33	2600	300	150	R	115	4973	3
SPS4	CFRP	B	4286	256	0.11	-	24	2600	300	150	R	116	4964	2.36
[101](Moshiri et al. 2020)														
EBR-U	CFRP	U	2800	160	1.4	-	35	3400	500	150	F	30.7	1424	2.46
EBR-U-theoretical	CFRP	U	2800	160	1.4	-	35	3400	500	150	F	30.7	1424	2.46
[39](Karzad et al. 2019)														
RS-0-1L-28	CFRP	U	220	-	0.17	90	36	2700	330	230	SD	58	1798	1
RS-S-1L-30	CFRP	U	220	-	0.17	90	30	2700	330	230	SD	74	2210	1
RS-0-2L-38	CFRP	U	220	-	0.33	90	38	2700	330	230	SD	117.5	3885	2.2
RS-S-2L-38	CFRP	U	220	-	0.33	90	38	2700	330	230	FD	113	5682	1.6
[102](Kim and Shin 2011)														
CC	CFRP	F	2300	270	0.59	90	17.4	2400	250	150	D	78.2	1633.52	3
[103](Antony et al. 2019)														
UCB1L700BL	CFRP	B	4000	230	0.75	-	25	1000	140	120	F+D	42	494.1	2.8
UCB2L700BL	CFRP	B	4000	230	0.75	-	25	1000	140	120	F+D	45.6	436.9	2.5
UCB3L700BL	CFRP	B	4000	230	0.75	-	25	1000	140	120	D	46	363	3.33
UCB2L650BL	CFRP	B	4000	230	0.75	-	25	1000	140	120	D	44	484	3.25
UCB2L600BL	CFRP	B	4000	230	0.75	-	25	1000	140	120	D	42.8	430.9	3.45
[104](Bilotta et al. 2015)														
EBR_c_1.440_	CFRP	B	2052	171	1.44	-	21	2400	160	120	D	36.5	872.5	1.66
EBR_c_1.440_2	CFRP	B	2052	171	1.44	-	21	2400	160	120	D+CS	35.2	842.3	1.66
EBR_d_1.440_1	CFRP	B	2052	171	1.44	-	21	2400	160	120	D+CS	75.1	1810	2.22
EBR_d_1.440_2	CFRP	B	2052	171	1.44	-	21	2400	160	120	D	64.8	1625	2
[105](Triantafyllou et al. 2018)														
RC-COR1S1	CFRP	F	3800	242	1.2	-	50	2300	300	150	F	191.7	5959.52	2
RC-COR2S1	CFRP	F	3800	242	1.2	-	50	2300	300	150	F	226.6	7192.32	3.04
RC-COR3S1	CFRP	F	3800	242	1.2	-	50	2300	300	150	F	245.6	4755.37	4.6
[106](Skuturna and Valivonis. 2016)														
BW1-1	CFRP	U	3800	231	-	35	1500	150	100	R	105	133.5	2.73	
BW1-2	CFRP	U	3800	231	-	35	1500	150	100	R	97.8	130	2.6	
[68](Mofrad et al. 2019)														
A-EBR-V	CFRP	B	3900	230	0.17	90	42	1400	160	120	S	127.6	503	1
A-EBR-D	CFRP	B	3900	230	0.17	45	42	1400	160	120	S+D	169.3	903	1.4
B-EBRE-V	CFRP	U	3900	230	0.17	90	40.5	1400	160	120	S+D	164.3	592	1.58
B-EBRE-V	CFRP	U	3900	230	0.17	45	40.5	1400	160	120	S+D	153.6	774	1.78
C-EBR-V	CFRP	F	3900	230	0.17	90	42.5	1400	160	120	S+D	192.4	1103	1.4
C-EBR-D	CFRP	F	3900	230	0.17	45	42.5	1400	160	120	S+D	187.9	1280	1.28

Table 1. (Con.) Mechanical properties of composite

Beam Label	FRP type	Wrapping	Lamina Strength	Lamina Elasticities	Thickness	Lay up	F.c. (MPa)	Beam Length(mm)	Depth of beam(mm)	Width of Beam (mm)	Failure	Strength (kN)	Energy Dissipation (kN)	Ductility (mm/mm)
[106](Skuturna and Valivonis. 2016)														
BW1-1	CFRP	U	3800	231		-	35	1500	150	100	R	105	133.5	2.73
BW1-2	CFRP	U	3800	231		-	35	1500	150	100	R	97.8	130	2.6
[68](Mofrad et al. 2019)														
A-EBR-V	CFRP	B	3900	230	0.17	90	42	1400	160	120	S	127.6	503	1
A-EBR-D	CFRP	B	3900	230	0.17	45	42	1400	160	120	S+D	169.3	903	1.4
B-EBRE-V	CFRP	U	3900	230	0.17	90	40.5	1400	160	120	S+D	164.3	592	1.58
B-EBRE-V	CFRP	U	3900	230	0.17	45	40.5	1400	160	120	S+D	153.6	774	1.78
C-EBR-V	CFRP	F	3900	230	0.17	90	42.5	1400	160	120	S+D	192.4	1103	1.4
C-EBR-D	CFRP	F	3900	230	0.17	45	42.5	1400	160	120	S+D	187.9	1280	1.28
[8](Chen et al. 2019)														
EB-1-0	CFRP	B	4131	270.5	0.33	-	30	2400	250	150	D	51.58	1155	2.29
EB-4-0	CFRP	B	4131	270.5	0.33	-	31.7	2400	250	150	D	51.76	759.4	2.11
[107](Firmo et al. 2018)														
BG	CFRP	B	2076	189	1.4	-	37	1500	120	100	F	74	1397.24	1.2
[108](Choobbor et al. 2019)														
B	CFRP	B	3900	230	0.17	-	38.78	840	240	120	R	73.37	1330	3.17
BB	CFRP	B	3900	230	0.17	-	38.78	1840	240	120	R+C	93.07	1098	3.64
[109](Miruthun et al. 2020)														
RCb	GFRP	F	3450	72.4	3	-	25	2000	250	150	D	85.78	486	3.35
RCint	GFRP	F	3450	72.4	5	-	25	2000	250	150	D	64.8	327.1	5.79
RCcro	GFRP	F	3450	72.4	3	-	25	2000	250	150	D	54.2	291.3	2.34
RCinc	GFRP	F	3450	72.4	5	-	25	2000	250	150	D	86.6	810	2.28
[99](Önal M. M. 2014)														
KG301	GFRP	F	4500	146	0.13	45	20	2200	250	150	S	122	1466	3.88
KG302	GFRP	F	4500	146	0.13	45	20	2200	250	150	S	124	1147	2.8
KG303	GFRP	F	4500	146	0.13	45	20	2200	250	150	S	121	1255	4
[110](Ravichandran et al. 2012)														
RCC3	GFRP	B	126.2	7467	3	-	64	3000	250	150	F	66.19	1521	4.17
RCC5	GFRP	B	156	11387	5	-	64	3000	250	150	F	98.1	2417	3.96
RCU3	GFRP	B	446.9	13966	3	-	64	3000	250	150	F	102.8	3786	4.08
RCU5	GFRP	B	451.5	17365	5	-	64	3000	250	150	F	112.6	5087	4.09
[111](Josy and Johny. 2019)														
U1	GFRP	U	-	-	-	-	53	1800	200	120	F	45	177.5	1.71
U2	GFRP	U	-	-	-	-	53	1800	200	120	F	49	209.7	1.35
U3	GFRP	U	-	-	-	-	53	1800	200	120	F	57	271.8	1.75
B1	GFRP	B	-	-	-	-	53	1800	200	120	F	42	123.7	1.29
B2	GFRP	B	-	-	-	-	53	1800	200	120	F	45	276.2	1.19
B3	GFRP	B	-	-	-	-	53	1800	200	120	F	50	237.1	1.83
[112](Meikandaany adn Murthy,. 2017)														
F21	GFRP	B	-	-	1.2	-	-	1500	200	100	F+C	70	909.9	3.67
F22	GFRP	B	-	-	1.2	-	-	1500	200	100	F+C	65	1048	3.14
F23	GFRP	B	-	-	1.2	-	-	1500	200	100	F+C	70	769.6	1.8
[113](Ahmed, H. et al. 2019)														
B8-SG-sh-A	GFRP	B	2500	72000	0.17	-	25	1500	350	160	D	11.44	2764	5.4
B8-RG-sh-A	GFRP	B	2500	72000	0.17	-	35	1500	350	160	D	10.74	2685	4.5
[114](Mariappan et al. 2016)														
1.5SF-3UDC	GFRP	-	451.5	17365	3	-	24	3000	250	150	F	100	7585	5.63
1.5SF-5UDC	GFRP	-	147.4	6856	5	-	24	3000	250	150	F	120	9164	6
1.5SF-3WR	GFRP	-	178.1	8994	3	-	24	3000	250	150	F	83	5280	6.67
1.5SF-5WR	GFRP	-	451.5	17365	5	-	24	3000	250	150	F	90	5277	5.2
1.5SF-3CSM	GFRP	-	147.4	6856	3	-	24	3000	250	150	F	70	4190	5.44
1.5SF-5CSM	GFRP	-	178.1	8994	5	-	24	3000	250	150	F	75	5206	4.67

Table 1. (Con.) Mechanical properties of composite

Beam Label	FRP type	Wrapping	Lamina Strength		Lamina Elasticities	Thickness	Lay up	Fc. (MPa)	Beam Length(mm)	Depth of beam(mm)	Width of Beam (mm)	Failure	Strength (kN)	Energy Dissipation (kJ)	Ductility (mm/mm)
[115](Shrivastava and Tiwari. 2018)															
SFB1	GFRP	U	-	-	-	1.2	-	30	1000	150	150	S	53.33	219.2	1.15
SFB2	GFRP	U	-	-	-	1.2	-	30	1000	150	150	F	53.33	216.2	1.14
FB1	GFRP	B	-	-	-	1.2	-	30	1000	150	150	S	48.8	226.4	1.09
FB2	GFRP	B	-	-	-	1.2	-	30	1000	150	150	F	48.8	228.3	1
UB1	GFRP	U	-	-	-	1.2	-	30	1000	150	150	S	53.33	213.2	1.48
UB2	GFRP	U	-	-	-	1.2	-	30	1000	150	150	F	53.33	233.7	1.93
[116](Banjara and Ramanjaneyulu. 2017)															
SD2	GFRP	U	200	71000	0.17	45-90	30	1800	200	150	S	77.63	217	0.97	
SD3	GFRP	U	200	71000	0.17	45-90	30	1800	200	150	S	66.26	176.1	0.97	
SSD3	GFRP	U	200	71000	0.17	45-90	30	1800	200	150	S	95.4	20427	4.83	
[117](Nanda et al. 2018)															
CC150GFRP	GFRP	F	2400	70000	-	-	36	1050	150	150	S	69	244.3	1.15	
CC300GFRP	GFRP	F	2400	70000	-	-	29	1050	150	150	F	57.3	1167	2.06	
[118](Sundarraja and Rajamohan 2009)															
RF2	GFRP	S	3400	7300	1	-	29.11	1000	150	100	F	53	121.8	1	
RF2U	GFRP	U	3400	7300	1	-	29.11	1000	150	100	F	55	97.24	1	
RF3	GFRP	S	3400	7300	1	-	29.11	1000	150	100	F	50	95.96	1	
RF3U	GFRP	U	3400	7300	1	-	29.11	1000	150	100	F	52	76.18	1	
RF4	GFRP	S	3400	7300	1	-	29.11	1000	150	100	F	48	115	1	
RF4U	GFRP	U	3400	7300	1	-	29.11	1000	150	100	F	55	109.6	1	
RF5	GFRP	S	3400	7300	1	-	29.11	1000	150	100	C	49	175.9	1	
RF5U	GFRP	U	3400	7300	1	-	29.11	1000	150	100	F+C	50	114.7	1	
[119](Panigrahi. et al. 2014)															
SB1	GFRP	S	127.2	209.9	1	45	24.88	1300	150	125	D	172	399.3	1	
SB2	GFRP	S	172.8	209.9	1	45	24	1300	150	125	D	220	561.1	1	
SB3	GFRP	S	218.4	209.9	1	45	23.32	1300	150	125	D	228	429.3	1	
SB4	GFRP	U	264	209.9	1	45	23.13	1300	150	125	D	215	732.3	3.4	
SB5	GFRP	U	309.6	209.9	1	45	24.12	1300	150	125	D	200	470.5	1	
SB6	GFRP	U	355.2	209.9	1	45	23.68	1300	150	125	D	230	676.9	1.45	
SB7	GFRP	U	400.8	209.9	1	45	24.1	1300	150	125	D	232	685.9	2.5	
SB8	GFRP	U	446.4	209.9	1	45	24.06	1300	150	125	R	252	1439	1	
SB9	GFRP	U	492	209.9	2.5	45	23.08	1300	150	125	R	268	833.7	1.55	
[120](Ibrahim Syed et al. 2015)															
S0 L5	GFRP	B	1720	72	5	-	-	3000	250	150	D	88.29	1250	2.25	
S1 L5	GFRP	B	1720	72	5	-	-	3000	250	150	D	112.8	2529	2.12	
[121](Mohite et al. 2014)															
TB	GFRP	B	1800	70	-	-	20	1500	150	100	F	110	491.5	2.85	
SB	GFRP	B	1800	70	-	-	20	1500	150	100	F	110	794.2	4.21	
[122](Sivasankar et al. 2018)															
UW-1	GFRP	U	1500	45	-	-	60	1700	250	150	F	114.4	3033	1.18	
UW-2	GFRP	U	1500	45	-	-	60	1700	250	150	F	123.1	3598	1.31	
BW-1	GFRP	U	1500	45	-	-	60	1700	250	150	F	109.7	3804	1.29	
BW-2	GFRP	U	1500	45	-	-	60	1700	250	150	F	114.7	4138	1.71	
[123](Kumari and Nayak 2020)															
C-100-FS	GFRP	U	2040	16.07	2	-	27.65	1000	470	100	S	385.7	2022	1.18	
C-150-FS	GFRP	U	2040	16.07	2	-	28.2	1000	470	150	S	271.8	2251	1.38	
C-200-FS	GFRP	U	2040	16.07	2	-	27.8	1000	470	200	S	187.5	1974	1.37	
S-100-FS	GFRP	U	2040	16.07	2	-	27.55	1000	470	100	S	309.2	2960	1.35	
S-150-FS	GFRP	U	2040	16.07	2	-	27.65	1000	470	150	S	206.9	1944	1.43	
S-200-FS	GFRP	U	2040	16.07	2	-	27.2	1000	470	200	S	134.9	1463	1.41	

Table 1. (Con.) Mechanical properties of composite

Beam Label	FRP type	Wrapping	Lamina Strength	Lamina Elasticities	Thickness	Lay up	Fc. (MPa)	Beam Length(mm)	Depth of beam(mm)	Width of Beam (mm)	Failure	Strength (kN)	Energy Dissipation (kN)	Ductility (mm/mm)
[124](Saribiyik and Caglar 2016)														
G11	GFRP	U	2300	76	0.17	90	17	2000	250	150	F	119	3033	3.25
G21	GFRP	U	2300	76	0.17	90	17	2000	250	150	F	148.1	3598	2.84
G22	GFRP	U	2300	76	0.17	90	17	2000	250	150	F	153.7	3804	3.07
G21-1	GFRP	U	2300	76	0.17	45	17	2000	250	150	F	156.6	4138	3.03
[125](Mini et al. 2014)														
B2	GFRP	B	3450	-	-	-	35.26	700	150	150	F+S R+D	98.4	104.2	1.1
U2	GFRP	B	3450	-	-	-	35.26	700	150	150	F+S R+D	108	223	1
22U2	GFRP	U	3450	-	-	-	35.26	700	150	150	F+S R+D	86.4	127.5	1.1
15U2	GFRP	U	3450	-	-	-	35.26	700	150	150	F+S R+D	75.2	91.12	1
S2	GFRP	D	3450	-	-	-	35.26	700	150	150	F+S R+D	98.4	178.7	1
[31](Attari et al. 2012)														
PA2	GFRP	U	0	19.2	2	45/-45	39	1500	160	100	C	78.95	1601	4.5
[32] (Hawileh et al. 2014)														
BG	GFRP	B	3400	72	0.352	45/-45	50	1840	240	125	C	76,84	1397	2.8

Failure types = **B**: Bending, **S**: Shear, **C**: Cracking, **F**: Flexural, **D**: Debonding, **R**: Rupture, **CS**: Concrete cover Separation, **BF**: break of FRP, **SY**: Steel Yielding Wrapping types = **U**: U shapes, **F**: Full, **B**: Bottom bounded, **S**: Sides bonded.

According to the values in Table 1, the maximum load, energy dissipation capacity and ductility averages have been calculated for each study and listed for CFRP and GFRP respectively in Table 2. Thus, it will be easier to do some statistical analysis. Independent two samples t-test: It is applied to test whether two independent samples are different in terms of a certain variable in different averages. The critical point here is that the condition of being included in groups is completely independent from the variable under study. In other words, the two groups (or two samples) being compared should not be related to each other. Externally reinforcing beams using CFRP and GFRP composites include studies conducted independently in the literature. Therefore, an independent two samples T-test can be applied the for average values obtained such as ultimate load, energy dissipation capacities and ductility values between these two independent groups.

3.4. Outlier Data Control Tests

Before starting the analysis, it is necessary to check whether there is any discrepancy between the values used. The first outlier test has been made among the load values Fig. 7 shows that there is no outlier between the load values used. For example, while performing this check, since the ultimate load values obtained from an original study conducted by Alhamdan and Dirikgil, were greater than 350 kN, the upper levels of the graph gave a warning with red color [126], in which replaced to with study of Kim and Shin [102]. Thus, with the outlier test, all load values were selected within the testable range.

If the P value is greater than 0.05, there is no outlier. According to the data of Grubbs' test all data values come from same normal population as shown in Table 3. Smallest or largest data value is an outlier as shown in Fig. 7.

Although an outlier test has been performed for load values, it is also useful to perform an outlier test in the amount of energy dissipation. Here, in the original strengthening study with CFRP performed by Chellapandian et al. (2019) the average load value of 156.1 kN a

very high energy dissipation capacity of 9941.5 kN has been achieved. A high energy dissipation capacity was achieved, but it was omitted from this table as it did not conform to the normal distribution [127]. According to CFRP and GFRP Grubbs' Test values and P values are greater than 0.05, all energy dissipation values are data values come from same normal population as shown in Fig 8. It is useful to mention one more point. When Fig. 9 and Fig. 10. are compared, it can be understood from Fig. 8. that CFRP has higher load values, while GFRP has higher energy dissipation.

Finally, in the outlier test for ductility values, the results were within the normal range. In addition, it can be seen in Fig. 9 that higher ductility results were obtained in strengthening with GFRP compared to CFRP. CFRP and GFRP Grubbs' Test.

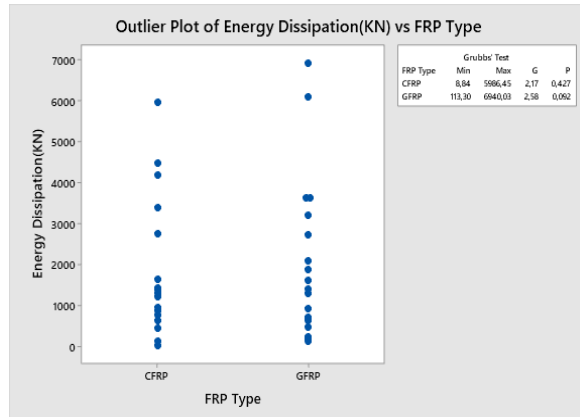


Fig. 8 Outlier test of energy dissipation capacity

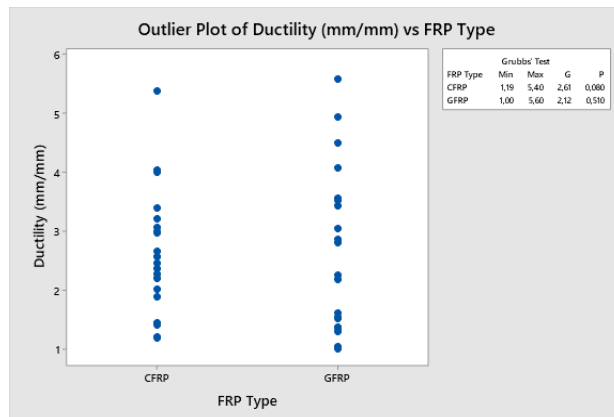


Fig. 9 Outlier test of ductility

3.4. Ultimate Load Carry Capacity

In this section is the comparison of the maximum ultimate strength values between CFRP and CFRP. When the averages of the groups are obtained, it cannot be determined at first sight whether they are different or not. A slight difference between the averages is found statistically significant in some cases, but not found in some cases. Testing differences between two group averages is possible via T-test. Here, it is determined with the help of Minitab statistics program whether the means differ significantly between two groups.

Analysis is carried out with the T- test, which is used to compare the mean values of two different groups with unknown variance.

Table 2. Average result values

No	References		Average		
			Maximum Strength (kN)	Energy (kN)	Ductility (mm/mm)
1	[89] (Gemi et al. 2019)	CFRP	122.7	4198.80	2.27
2	[96] (Arslan et al. 2019)	CFRP	106.69	4495.23	2.97
3	[32] (Hawileh et al. 2014)	CFRP	92.44	1216	2.37
4	[31] (Attari et al. 2012)	CFRP	77.86	8.84	4.05
5	[40] (Shannag et al. 2014)	CFRP	115.33	752.13	1.19
6	[97] (Altin et al. 2010)	CFRP	89.17	2764.79	2.02
7	[98] (Gamino et al. 2010)	CFRP	250	637.2	2.56
8	[99] (Önal, M. M. 2014)	CFRP	117.33	1383.33	5.4
9	[100] (Gao, et al. 2016)	CFRP	118.09	5986.45	2.99
10	[101] (Moshiri et al. 2020)	CFRP	30.7	1424	2.46
11	[39] (Karzad et al. 2019)	CFRP	90.625	3393.75	1.45
12	[102](Kim and Shin 2011)	CFRP	78,2	1633.52	4
13	[103] (Antony et al. 2019)	CFRP	44.08	441.78	3.07
14	[104] (Bilotta et al. 2015)	CFRP	52.9	1287.45	1.89
15	[105] (Triantafyllou et al. 2018)	CFRP	221.3	5969.07	3.21
16	[106] (Skuturna and Valivonis 2016)	CFRP	101.4	131.75	2.67
17	[68] (Mofrad et al. 2019)	CFRP	165.85	859.17	1.41
18	[8] (Chen et al. 2019)	CFRP	51.67	957.2	2.2
19	[107] (Firmo et al. 2018)	CFRP	33	1397.24	1.2
20	[108](Choobbor et al. 2019)	CFRP	83.22	1214	3.41
21	[109](Miruthun et al. 2020)	GFRP	72.85	478.6	3.44
22	[99](Önal M. M. 2014)	GFRP	122.33	1289.33	3.56
23	[110](Ravichandran et al. 2012)	GFRP	94.92	3202.75	4.08
24	[111](Josy and Johny. 2019)	GFRP	48	216	1.52
25	[112](Meikandaan,y adn Murthy,. 2017)	GFRP	68.33	909.17	2.87
26	[113](Ahmed, H. et al. 2019)	GFRP	11.09	2724.5	4.95
27	[114](Mariappan et al. 2016)	GFRP	89.67	6117	5.60
28	[115](Shrivastava and Tiwari. 2018)	GFRP	51.82	222.83	1.30
29	[116](Banjara and Ramanjaneyulu. 2017)	GFRP	79.76	6940.03	2.26
30	[117](Nanda et al. 2018)	GFRP	63.15	705.65	1.61
31	[118](Sundarraja and Rajamohan 2009)	GFRP	51.5	113.30	1
32	[119](Panigrahi. et al. 2014)	GFRP	224.11	692	1.54
33	[120](Ibrahim Syed et al. 2015)	GFRP	100.55	1889.5	2.19
34	[121](Mohite et al. 2014)	GFRP	110	642.85	3.53
35	[122](Sivasankar et al. 2018)	GFRP	115.48	3643.25	1.37
36	[123](Kumari and Nayak 2020)	GFRP	249.33	2102.33	1.35
37	[124](Saribiyik and Caglar 2016)	GFRP	144.35	3643.25	3.05
38	[125](Mini et al. 2014)	GFRP	93.28	144.90	1.04
39	[31](Attari et al. 2012)	GFRP	78.95	1601	4.5
40	[32] (Hawileh et al. 2014)	GFRP	76.84	1397	2.8

With the following T-test, it is tested whether the difference is 0 or not for the average maximum load values.

Two- sample T-test CI:CFRP;GFRP

According to the T-test method, μ_1 : mean of CFRP, μ_2 : mean of GFRP their means and Difference: $\mu_1 - \mu$ indicates the difference between the two groups

μ_1 : mean of CFRP

μ_2 : mean of GFRP

Difference: $\mu_1 - \mu_2$

Considering the following Descriptive Statistics results, although there are differences between the two groups, the mean significance is found to be 13.

Sample Mean	N	Mean	StDev	SE
CFRP	20	102.1	56.8	13
GFRP	20	97.3	56.3	13

According to the T-test with confidence level 95% accuracy, the hypothesis can be accepted because the value 0 is in the range below. Estimation for difference is shown in below, according to the T-test with 95% confidence level, the difference between CFRP and GFRP is 4.8. In fact, it can be stated that there are differences between (-31.4; 41.1) values. Therefore, since 0 value is between these two values the efficiency of the average ultimate load values of these two composites is equal to each other.

Difference 95% CI for Difference

4.8 (-31.4; 41.1)

In addition to what is written above, since the P value below is greater than 0.05, the average efficiency between the two groups is acceptable. If the P value was less than 0.05, the difference of two group would be too large and hypothesis would be unacceptable.

Null hypothesis $H_0: \mu_1 - \mu_2 = 0$

Alternative hypothesis $H_1: \mu_1 - \mu_2 \neq 0$

T-Value: 0.27 DF: 37 P-Value: 0.789

CFRP is the undisputed leader in terms of ultimate load strength capacity in beam strengthen with FRP. In the previous outlier test, a data above the normal distribution was changed. Thus, it is understood that from Fig. 10a and b the mean values are in the normal range and close to one another.

3.5. Energy Dissipation Capacity

The most important result obtained in this study is the energy dissipation capacity of the strengthened RC beams. Since the study is conducted over CFRP-GFRP comparison, it is checked whether the mean results are within the confidence interval with the statistical T-test. According to the Descriptive Statistics in below, the mean of CFRP and GFRP is so close. However, the SE Mean of GFRP is bigger than Se mean GFRP. Hence, it can be mentioned that GFRPs have more energy dissipation capacity than CFRP.

Sample Mean	N	Mean	StDev	SE
CFRP	20	2008	1834	410
GFRP	20	1934	1943	435

According to the T-test with confidence level 95% accuracy, the hypothesis can be accepted because the value 0 is in the range below.

Estimation for Difference

Difference 95% CI for Difference
 74 (-1137; 1284)

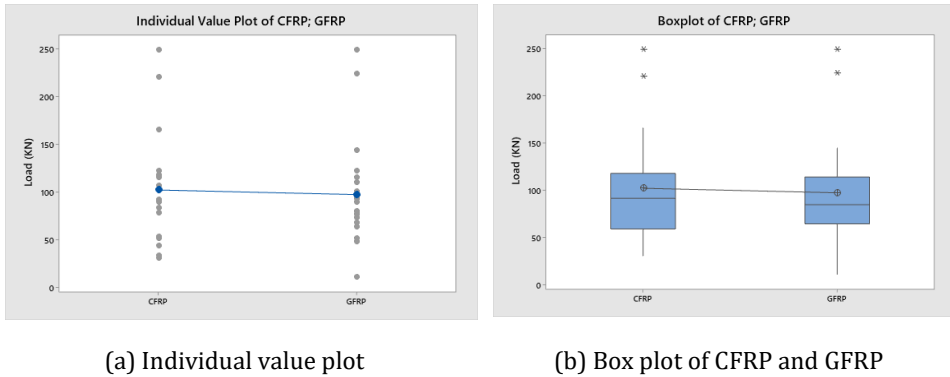


Fig. 10 Result of individual and box plot

According to the results, the P value is bigger than 0.05, so it can be, the accuracy hypothesis of the energy holding capacities between CFRP and GFRP can be accepted.

Test

Null hypothesis $H_0: \mu_1 - \mu_2 = 0$

Alternative hypothesis $H_1: \mu_1 - \mu_2 \neq 0$

T-Value : 0.12 DF: 37 P-Value: 0.902

In Fig. 11 a) and b), it is seen that CFRP-GFRP average energy dissipation capacities are in the confidence interval. In the graph, it is understood that the mean values between CFRP-GFRP are in the confidence level from line them. Moreover, the GFRP energy dissipation capacity is more than CFRP according to average of the mean values. Because individual energy dissipation value plot GFRP has more value above mean of its performed with the values selected in the acceptable range by the T-test showed that the ductility of GFRPs is higher than CFRPs.

3.6. Ductility Capacity

Ductility refers to the flexible behavior of a structure. Ductility also refers to the structure's resistance to collapse from the pour point of the structure to the moment of collapse. If this value is high, it also indicates the energy absorption capacity of the building.

This section reveals the originality of this work. According to statistical results the ductility of the beam strength with GFRP is higher than that of CFRP and it is in the considered range.

Descriptive Statistics

Sample Mean	N	Mean	StDev	SE
CFRP	20	2.64	1.06	0.24
GFRP	20	2.68	1.31	0.31

Estimation for Difference

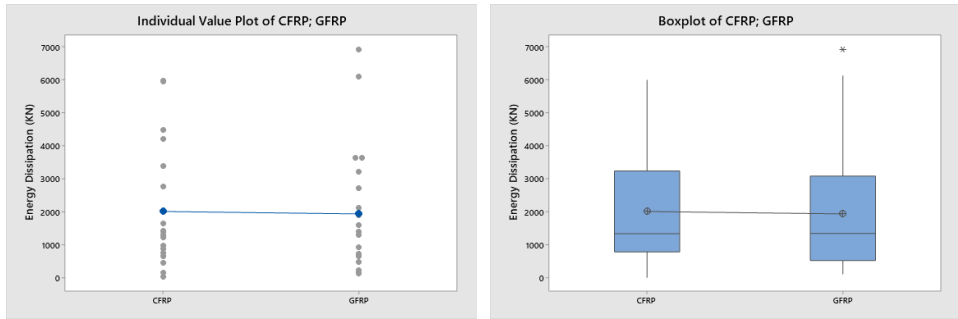
Difference 95% CI for Difference
 -0,039 (-0.830; 0.751)

Test

Null hypothesis $H_0: \mu_1 - \mu_2 = 0$

Alternative hypothesis $H_1: \mu_1 - \mu_2 \neq 0$

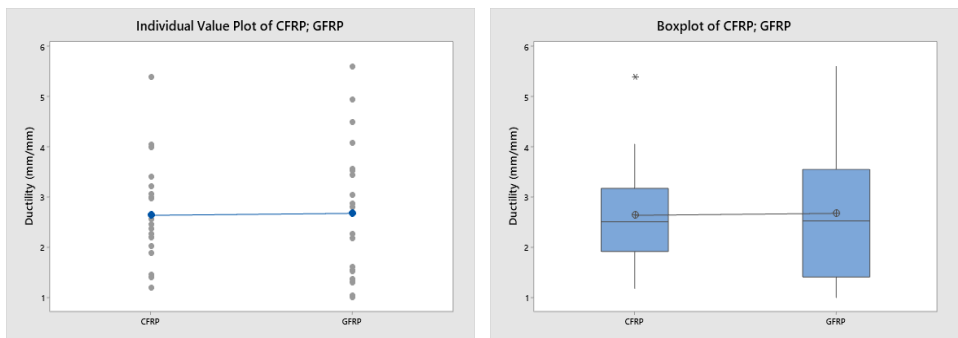
T-Value : -0.10 DF:35 P-Value:0.920



(a) Individual energy dissipation value plot (b) Sum of CFRP-GFRP energy dissipation

Fig. 11 Individual and sum of energy dissipation

It is clear from Fig. 12. that the average ductility value of GFRPs is higher than CFRP. It has been stated before that CFRPs have higher strength. However, the results of the T-test.



(a) Individual ductility value plot (b) Sum of ductility plot of CFRP-GRP

Fig. 12 Individual and sum of ductility

4. Conclusion

As an important structural element, beams are exposed to very different loads. Under these different loads, different damages occur in the beams. All research is an effort to minimize these damages. Composite materials of FRP type are the most preferred reinforcement materials. The aim is to minimize the degree of damage of the concrete to give the structure an elastic behavior and to change from permanent deformation to a recoverable deformation. This study presents the overall design of beams and their strengthening methods with FRP composite materials.

The ultimate strength of RC beams can be doubled thanks to FRP composite materials. EB and NSM methods come to the fore as the basic winding technique. The layers and angles of the fabrics used in the EBR technique significantly affect the shear and flexural beam

performance in practice. In addition, it is seen that the strength capacity increases even more when additional anchors are used after the construction.

When the beams are strengthened with the EBR technique, the energy dissipation capacity and ductility of FRP fabrics remain at very low levels. Ductility generally remains around 1. Moreover, in some studies, ductility can be increased a little by methods such as volume increase, layer thickness or anchorage. It can even be increased even more with some hybrid methods.

Comparing the mechanical properties and behavior of CFRP, GFRP, BFRP and AFRP, carbon-reinforced polymers (CFRP) appear to be more advantageous with the 120-580 GPa elastic modulus. Elastic modulus of GFRP is seen at the lowest levels with 35-51 GPa. But in good a EBR strengthening application, it shows more energy dissipation capacity and ductility than CFRP.

Thanks to this study, failure states have been given separately for each study in the table. The combination of failure states obtained from recent studies is an important resource for researchers. Analyzes on the failures can be done in detail in another study. However, here, it is worth noting that delamination and separation failures states are caused by low ductility.

By using the EBR technique, it can be provided great advantages in beam strengthen with CFRP and GFRP composites. However, CFRP, which has very high strength, breaks in overloads and the steel remains alone in the plastic behavior. GFRP has lower strength than CFRP, but it can be preferred for more energy dissipation capacity and ductility in areas that do not require much strength.

In statistics, the T test is used to test the meaningfulness of the difference between two arithmetic means. Based on this, from the T-test analysis performed between CFRP and GFRP, it was proved by graphs that the mean of ultimate load, energy dissipation capacity and ductility were 95% accurate. The mean values obtained in the test were less than 0 and more, so the accuracy hypothesis was accepted. This analysis is also the most original value of this study.

Acknowledgement

I would like to thank dear Ahmet Şener for his contribution to the editing of the Reference text.

References

- [1] Yumnam M, Gupta H, Ghosh D, Jaganathan J. Inspection of concrete structures externally reinforced with FRP composites using active infrared thermography: A review. *Construction and Building Materials*. 2021; 310, 125265. <https://doi.org/10.1016/j.conbuildmat.2021.125265>
- [2] Dias S, Silva J, Structures JB-C, undefined. Flexural and shear strengthening of reinforced concrete beams with a hybrid CFRP solution. *Composite Structures*. 2021; 256, 113004. <https://doi.org/10.1016/j.compstruct.2020.113004>
- [3] Naser MZ, Hawileh RA, Abdalla J. Modeling Strategies of Finite Element Simulation of Reinforced Concrete Beams Strengthened with FRP: A Review. *Journal of Composites Science*. 2021. 5(1), 19. <https://doi.org/10.3390/jcs5010019>
- [4] T.F.El-Shafiey M.Hussein And M.M.El-Bosiely EEE. Behavior of strengthened RC beams using different techniques under static loading. *International Conference on Advances in Structural and Geotechnical Engineering* 2017.
- [5] Esmaili J, Aghdam OR, Andalibi K, Kasaei J, Gencel O. Experimental and numerical investigations on a novel plate anchorage system to solve FRP debonding problem in

- the strengthened RC beams. *Journal of Building Engineering*. 2022; 45:103413. <https://doi.org/10.1016/j.jobe.2021.103413>
- [6] Spadea G, Bencardino F, Swamy RN. Structural behavior of composite RC beams with externally bonded CFRP. *Journal of Composites for Construction* 1998; 2:132-7. [https://doi.org/10.1061/\(ASCE\)1090-0268\(1998\)2:3\(132\)](https://doi.org/10.1061/(ASCE)1090-0268(1998)2:3(132))
- [7] Kotynia R, Abdel Baky H, Neale KW, Ebead UA. Flexural strengthening of RC beams with externally bonded CFRP systems: Test results and 3D nonlinear FE analysis. *Journal of Composites for Construction*. 2008;12:190-201. [https://doi.org/10.1061/\(ASCE\)1090-0268\(2008\)12:2\(190\)](https://doi.org/10.1061/(ASCE)1090-0268(2008)12:2(190))
- [8] Chen C, Wang X, Sui L, Xing F, Chen X, Zhou Y. Influence of FRP thickness and confining effect on flexural performance of HB-strengthened RC beams. *Composites Part B: Engineering*. 2019;161:55-67. <https://doi.org/10.1016/j.jobe.2019.100798>
- [9] Siddika A, al Mamun MA, Alyousef R, Amran YHM. Strengthening of reinforced concrete beams by using fiber-reinforced polymer composites: A review. *Journal of Building Engineering*. 2019;100798. <https://doi.org/10.1016/j.jobe.2019.100798>
- [10] Siddika A, Saha K, Mahmud MS, Roy SC, al Mamun MA, Alyousef R J SNAS. Performance and failure analysis of carbon fiber-reinforced polymer (CFRP) strengthened reinforced concrete (RC) beams. *SN Applied Sciences*. 2019;1:1617. <https://doi.org/10.1007/s42452-019-1675-x>
- [11] Rezazadeh M. Innovative methodologies for the enhancement of the flexural strengthening performance of NSM CFRP technique for RC beams. 2015; PhD Thesis. Universidade do Minho (Portugal).
- [12] Barros JAO, Dias SJE. Near surface mounted CFRP laminates for shear strengthening of concrete beams. *Cement and Concrete Composites*. 2006; 28:276-92. <https://doi.org/10.1016/j.cemconcomp.2005.11.003>
- [13] Gemi, L., Madenci, E., & Özkılıç, Y. O. Experimental, analytical and numerical investigation of pultruded GFRP composite beams infilled with hybrid FRP reinforced concrete. *Engineering Structures*. 2021; 244, 112790. <https://doi.org/10.1016/j.jobe.2020.102119>
- [14] Costa IG, Barros JAO. Flexural and shear strengthening of RC beams with composite materials-The influence of cutting steel stirrups to install CFRP strips. *Cement and Concrete Composites*. 2010; 32:544-53. <https://doi.org/10.1016/j.cemconcomp.2010.03.003>
- [15] Bilotta A, Ceroni F, di Ludovico M, Nigro E, Pecce M, Manfredi G. Bond efficiency of EBR and NSM FRP systems for strengthening concrete members. *Journal of Composites for Construction*. 2011; 15:757-72. [https://doi.org/10.1061/\(ASCE\)CC.1943-5614.0000204](https://doi.org/10.1061/(ASCE)CC.1943-5614.0000204)
- [16] Mostofinejad D, Kashani AT. Experimental study on effect of EBR and EBROG methods on debonding of FRP sheets used for shear strengthening of RC beams. *Composites Part B: Engineering*. 2013; 45:1704-13. <https://doi.org/10.1016/j.compositesb.2012.09.081>
- [17] Charalambidi BG, Rousakis TC, Karabinis AI. Fatigue behavior of large-scale reinforced concrete beams strengthened in flexure with fiber-reinforced polymer laminates. *Journal of Composites for Construction*. 2016; 20:4016035. [https://doi.org/10.1061/\(ASCE\)CC.1943-5614.0000689](https://doi.org/10.1061/(ASCE)CC.1943-5614.0000689)
- [18] Hawileh RA, Abdalla JA, Hasan SS, Ziyada MB, Abu-Obeidah A. Models for predicting elastic modulus and tensile strength of carbon, basalt and hybrid carbon-basalt FRP laminates at elevated temperatures. *Construction and Building Materials*. 2016;114:364-73. <https://doi.org/10.1016/j.conbuildmat.2016.03.175>
- [19] Deifalla A, Ghobarah A. Strengthening RC T-beams subjected to combined torsion and shear using FRP fabrics: Experimental study. *Journal of Composites for Construction*. 2010;14:301-11. [https://doi.org/10.1061/\(ASCE\)CC.1943-5614.0000091](https://doi.org/10.1061/(ASCE)CC.1943-5614.0000091)

- [20] Pham TM, Hao H. Behavior of fiber-reinforced polymer-strengthened reinforced concrete beams under static and impact loads. *International Journal of Protective Structures*. 2017;8:3-24. <https://doi.org/10.1177/2041419616658730>
- [21] Gemi L. Investigation of the effect of stacking sequence on low velocity impact response and damage formation in hybrid composite pipes under internal pressure. A comparative study. *Composites Part B: Engineering*. 2018; 153:217-32. <https://doi.org/10.1016/j.compositesb.2018.07.056>
- [22] Mashrei M, Makki J, Sultan AA. Flexural Strengthening of Reinforced Concrete Beams Using Carbon Fiber Reinforced Polymer (CFRP) Sheets with Grooves. *Latin American Journal of Solids and Structures*. 2019;16. <https://doi.org/10.1590/1679-78255514>
- [23] Emerging technology series ACIC 440. ACI 440.2R-08. Guide for the design and construction of externally bonded FRP systems for strengthening concrete structures. 2008; 76.
- [24] Elgabbas F, El-Ghandour AA, Abdelrahman AA, El-Dieb AS. Different CFRP strengthening techniques for prestressed hollow core concrete slabs: experimental study and analytical investigation. *Composite Structures*. 2010; 92:401-11. <https://doi.org/10.1016/j.compstruct.2009.08.015>
- [25] Chajes MJ, Finch WW, Thomson TA. Bond and force transfer of composite-material plates bonded to concrete. *Structural Journal*. 1996; 93:209-17. <https://doi.org/10.14359/1491>
- [26] Supian ABM, Sapuan SM, Zuhri MYM, Zainudin ES, Ya HH. Hybrid reinforced thermoset polymer composite in energy absorption tube application: A review. *Defence Technology*. 2018;14:291-305. <https://doi.org/10.1016/j.dt.2018.04.004>
- [27] Hollaway LC, Leeming M. Strengthening of reinforced concrete structures: Using externally-bonded FRP composites in structural and civil engineering. Elsevier. 1999; <https://doi.org/10.1533/9781855737617>
- [28] Toutanji H, Ortiz G. The effect of surface preparation on the bond interface between FRP sheets and concrete members. *Composite Structures*. 2001; 53:457-62. [https://doi.org/10.1016/S0263-8223\(01\)00057-5](https://doi.org/10.1016/S0263-8223(01)00057-5)
- [29] Madenci, E., Özkılıç, Y. O., & Gemi, L. Buckling and free vibration analyses of pultruded GFRP laminated composites: Experimental, numerical and analytical investigations. *Composite Structures*. 2020; 254, 112806. <https://doi.org/10.1016/j.compstruct.2020.112806>
- [30] Gemi, L., Köroğlu, M. A., & Ashour, A. Experimental study on compressive behavior and failure analysis of composite concrete confined by glass/epoxy±55 filament wound pipes. *Composite Structures*. 2018; 187, 157-168. <https://doi.org/10.1016/j.compstruct.2017.12.049>
- [31] Attari N, Amziane S, Chemrouk M. Flexural strengthening of concrete beams using CFRP, GFRP and hybrid FRP sheets. *Construction and Building Materials*. 2012; 37:746-57. <https://doi.org/10.1016/j.conbuildmat.2012.07.052>
- [32] Hawileh RA, Rasheed HA, Abdalla JA, Al-Tamimi AK. Behavior of reinforced concrete beams strengthened with externally bonded hybrid fiber reinforced polymer systems. *Materials & Design*. 2014; 53:972-82. <https://doi.org/10.1016/j.matdes.2013.07.087>
- [33] Pham TM, Hao H. Impact behavior of FRP-strengthened RC beams without stirrups. *Journal of Composites for Construction*. 2016; 20:4016011. [https://doi.org/10.1061/\(ASCE\)CC.1943-5614.0000671](https://doi.org/10.1061/(ASCE)CC.1943-5614.0000671)
- [34] Huang H, Wang W-W, Dai J-G, Brigham JC. Fatigue behavior of reinforced concrete beams strengthened with externally bonded prestressed CFRP sheets. *Journal of Composites for Construction*. 2017; 21:4016108. [https://doi.org/10.1061/\(ASCE\)CC.1943-5614.0000766](https://doi.org/10.1061/(ASCE)CC.1943-5614.0000766)
- [35] Chen W, Pham TM, Sichembe H, Chen L, Hao H. Experimental study of flexural behaviour of RC beams strengthened by longitudinal and U-shaped basalt FRP sheet.

- Composites Part B: Engineering. 2018; 134:114-26.
<https://doi.org/10.1016/j.compositesb.2017.09.053>
- [36] Al-Saidy AH, Al-Harthy AS, Al-Jabri KS, Abdul-Halim M, Al-Shidi NM. Structural performance of corroded RC beams repaired with CFRP sheets. *Composite Structures*. 2010;92:1931-8. <https://doi.org/10.1016/j.compstruct.2010.01.001>
- [37] Mostofinejad D, Mahmoudabadi E. Grooving as alternative method of surface preparation to postpone debonding of FRP laminates in concrete beams. *Journal of Composites for Construction*. 2010; 14:804-11. [https://doi.org/10.1061/\(ASCE\)CC.1943-5614.0000117](https://doi.org/10.1061/(ASCE)CC.1943-5614.0000117)
- [38] Galal, K., & Mofidi, A. Shear strengthening of RC T-beams using mechanically anchored unbonded dry carbon fiber sheets. 2010; 24:31-9. [https://doi.org/10.1061/\(ASCE\)CF.1943-5509.0000067](https://doi.org/10.1061/(ASCE)CF.1943-5509.0000067)
- [39] Karzad AS, Leblouba M, al Toubat S, Maalej M. Repair and strengthening of shear-deficient reinforced concrete beams using Carbon Fiber Reinforced Polymer. *Composite Structures*. 2019; 223:110963. <https://doi.org/10.1016/j.compstruct.2019.110963>
- [40] Shannag MJ, Al-Akhras NM, Mahdawi SF. Flexure strengthening of lightweight reinforced concrete beams using carbon fibre-reinforced polymers. *Structure and Infrastructure Engineering*. 2014; 10:604-13. <https://doi.org/10.1080/15732479.2012.757790>
- [41] Gemi, L., Morkavuk, S., Köklü, U., & Gemi, D. S. An experimental study on the effects of various drill types on drilling performance of GFRP composite pipes and damage formation. *Composites Part B: Engineering*. 2019; 172, 186-194. <https://doi.org/10.1016/j.compositesb.2019.05.023>
- [42] Mhanna HH, Hawileh RA, Abdalla JA. Shear Strengthening of Reinforced Concrete Beams Using CFRP Wraps. *Procedia Structural Integrity*. 2019; 17:214-21. <https://doi.org/10.20944/preprints201906.0097.v1>
- [43] Abdulhameed A, Said A. Evaluation of Wedge-Block Concrete Beams Reinforced with EBR-CFRP Laminates by Modified ACI 440.2 R-2017 Guide. 2019; <https://doi.org/10.20944/preprints201906.0097.v1>
- [44] Nanda RP, Behera B. Experimental Study of Shear-Deficient RC Beam Wrapped with GFRP. *International Journal of Civil Engineering*. 2020;1-10. <https://doi.org/10.1007/s40999-020-00498-4>
- [45] Baghi H, Menkulasi F. Alternative Approaches to Predict Shear Strength of Slender RC Beams Strengthened with Externally Bonded Fiber-Reinforced Polymer Laminates. *Journal of Composites for Construction*. 2020; 24:4020002. [https://doi.org/10.1061/\(ASCE\)CC.1943-5614.0001003](https://doi.org/10.1061/(ASCE)CC.1943-5614.0001003)
- [46] Ghorbani M, Mostofinejad D, Hosseini A. Bond behavior of CFRP sheets attached to concrete through EBR and EBROG joints subject to mixed-mode I/II loading. *Journal of Composites for Construction*. 2017; 21:4017034. [https://doi.org/10.1061/\(ASCE\)CC.1943-5614.0000816](https://doi.org/10.1061/(ASCE)CC.1943-5614.0000816)
- [47] Mostofinejad D, Moshiri N. Compressive strength of CFRP composites used for strengthening of RC columns: Comparative evaluation of EBR and grooving methods. *Journal of Composites for Construction*. 2015; 19:4014079. [https://doi.org/10.1061/\(ASCE\)CC.1943-5614.0000545](https://doi.org/10.1061/(ASCE)CC.1943-5614.0000545)
- [48] Mostofinejad D, Torabian A. Experimental study of circular RC columns strengthened with longitudinal CFRP composites under eccentric loading: comparative evaluation of EBR and EBROG methods. *Journal of Composites for Construction*. 2016; 20:4015055. [https://doi.org/10.1061/\(ASCE\)CC.1943-5614.0000618](https://doi.org/10.1061/(ASCE)CC.1943-5614.0000618)
- [49] Mostofinejad D, Akhlaghi A. Experimental investigation of the efficacy of EBROG method in seismic rehabilitation of deficient reinforced concrete beam-column joints using CFRP sheets. *Journal of Composites for Construction*. 2017; 21:4016116. [https://doi.org/10.1061/\(ASCE\)CC.1943-5614.0000781](https://doi.org/10.1061/(ASCE)CC.1943-5614.0000781)

- [50] Sabzi J, Esfahani MR, Ozbakkaloglu T, Farahi B. Effect of concrete strength and longitudinal reinforcement arrangement on the performance of reinforced concrete beams strengthened using EBR and EBROG methods. *Engineering Structures*. 2020; 205:110072. <https://doi.org/10.1016/j.engstruct.2019.110072>
- [51] Haj Seiyed Taghia SA, Darvishvand HR, Ebrahimi M. Economic Analyses for Low-Strength Concrete Wrapped with CFRP to Improve the Mechanical Properties and Seismic Parameters. *Journal of Construction Engineering and Management*. 2020; 146:4019117. [https://doi.org/10.1061/\(ASCE\)CO.1943-7862.0001760](https://doi.org/10.1061/(ASCE)CO.1943-7862.0001760)
- [52] El Battawy OM, el Kashif KF, Abdalla HA. Experimentally Comparative Study on Different Strengthening Methods of Reinforced Concrete Deep Beams. 2019;5:1997-2006. <https://doi.org/10.28991/cej-2019-03091388>
- [53] Hadhood A, Agamy MH, Abdelsalam MM, Mohamed HM, El-Sayed TA J ES. Shear strengthening of hybrid externally-bonded mechanically-fastened concrete beams using short CFRP strips: Experiments and theoretical evaluation. *Civil Engineering Journal*, 2019;201:109795. <https://doi.org/10.1016/j.engstruct.2019.109795>
- [54] Chen JF, Teng JG. Anchorage strength models for FRP and steel plates bonded to concrete. *Journal of Structural Engineering*. 2001;127:784-91. [https://doi.org/10.1061/\(ASCE\)0733-9445\(2001\)127:7\(784\)](https://doi.org/10.1061/(ASCE)0733-9445(2001)127:7(784))
- [55] Chen JF, Teng JG. Anchorage strength models for FRP and steel plates bonded to concrete. *Journal of structural engineering*. 2001; 127:784-91. [https://doi.org/10.1061/\(ASCE\)0733-9445\(2001\)127:7\(784\)](https://doi.org/10.1061/(ASCE)0733-9445(2001)127:7(784))
- [56] Aksoylu, C., Yazman, Ş., Özkılıç, Y. O., Gemi, L., & Arslan, M. H. Experimental analysis of reinforced concrete shear deficient beams with circular web openings strengthened by CFRP composite. *Composite Structures*. 2020, 249, 112561. <https://doi.org/10.1016/j.compstruct.2020.112561>
- [57] Aksoylu, C., Özkılıç, Y. O., Yazman, Ş., Gemi, L., & Arslan, M. H. Experimental and Numerical Investigation of Load Bearing Capacity of Thinned End Precast Purlin Beams and Solution Proposals. *Teknik Dergi*. 2021; 10823-10858, Yazı 614. <https://doi.org/10.18400/tekderg.667066>
- [58] Al-Rousan RZ, Issa MA. The effect of beam depth on the shear behavior of reinforced concrete beams externally strengthened with carbon fiber-reinforced polymer composites. *Advances in Structural Engineering*. 2016; 19:1769-79. <https://doi.org/10.1177/1369433216649386>
- [59] Foster RM, Brindley M, Lees JM, Ibell TJ, Morley CT, Darby AP, et al. Experimental investigation of reinforced concrete T-beams strengthened in shear with externally bonded CFRP sheets. *Journal of Composites for Construction*. 2017; 21:4016086. [https://doi.org/10.1061/\(ASCE\)CC.1943-5614.0000743](https://doi.org/10.1061/(ASCE)CC.1943-5614.0000743)
- [60] Tahar HD, Abderezak R, Rabia B, Tounsi A. Impact of thermal effects in FRP-RC hybrid cantilever beams. *Structural Engineering and Mechanics*. 2021; 78:573-8. <https://doi.org/https://doi.org/10.12989/sem.2021.78.5.573>
- [61] Li W, Huang Z, Huang Z, Yang X, Shi T, Xing F. Shear Behavior of RC Beams with Corroded Stirrups Strengthened Using FRP Laminates: Effect of the Shear Span-to-Depth Ratio. *Journal of Composites for Construction*, 2020; 24:4020033. [https://doi.org/10.1061/\(ASCE\)CC.1943-5614.0001042](https://doi.org/10.1061/(ASCE)CC.1943-5614.0001042)
- [62] Kumari, A., & Nayak, A. N. Strengthening of shear deficient RC deep beams using GFRP sheets and mechanical anchors. *Canadian Journal of Civil Engineering*. 2021; 48(1), 1-15. <https://doi.org/10.1139/cjce-2019-0333>
- [63] Oller E, Pujol M, Marí A J CPBE. Contribution of externally bonded FRP shear reinforcement to the shear strength of RC beams 2019; 164:235-48. [https://doi.org/10.1061/\(ASCE\)0733-9445\(1990\)116:4\(978\)](https://doi.org/10.1061/(ASCE)0733-9445(1990)116:4(978))
- [64] Remennikov A, Goldston M, Sheikh MN. Impact performance of concrete beams externally bonded with carbon FRP sheets. *Mechanics of Structures and Materials: Advancements and Challenges-Hao & Zhang (Eds). Conference: Proceedings of the 24th*

- Australian Conference on the Mechanics of Structures and Materials (ACMSM24), At Perth, Australia, 2016, p. 1695-9.
- [65] Islam AKMA. Effective methods of using CFRP bars in shear strengthening of concrete girders. *Engineering Structures* 2009; 31:709-14. <https://doi.org/10.1016/j.engstruct.2008.11.016>
- [66] Abdulqader SS, Makki RF, Mousa M. Behavior Of Scc Beams Strengthened With Cfrp Under Shear. *Kufa Journal of Engineering*. 2019; 10:111-26. <https://doi.org/10.30572/2018/kje/100109>
- [67] Dewi SM, Susanti L, Triyuliani NI, Saputra A. Repair of reinforced concrete beam by adding external reinforcement. IOP Conference Series: Materials Science and Engineering, vol. 669, IOP Publishing. 2019; p. 12010. <https://doi.org/10.1088/1757-899X/669/1/012010>
- [68] Mofrad MH, Mostofinejad D, Hosseini A. A generic non-linear bond-slip model for CFRP composites bonded to concrete substrate using EBR and EBROG techniques. *Composite Structures*. 2019; 220:31-44. <https://doi.org/10.1016/j.compstruct.2019.03.063>
- [69] Tajmir-Riahi A, Moshiri N, Mostofinejad D. Bond mechanism of EBROG method using a single groove to attach CFRP sheets on concrete. *Construction and Building Materials*. 2019;197:693-704. <https://doi.org/10.1016/j.conbuildmat.2018.11.204>
- [70] Shomali A, Mostofinejad D, Esfahani MR. Engineering C. Shear strengthening of RC beams using EBRIG CFRP strips: a comparative study. *European Journal of Environmental and Civil Engineering*. 2019:1-17. <https://doi.org/10.1080/19648189.2019.1633413>
- [71] Gemi L, Madenci E, Özkılıç YO. (2020). Çelik, Cam FRP ve hibrit donatılı betonarme kirişlerin eğilme performansının incelenmesi. *Düzce Üniversitesi Bilim ve Teknoloji Dergisi*, 8(2), 1470-1483. <https://doi.org/10.29130/dubited.629354>
- [72] Bodzak P. Flexural behaviour of concrete beams reinforced with different grade steel and strengthened by CFRP strips. *Composites Part B: Engineering*. 2019; 167: 411-21. <https://doi.org/10.1016/j.compositesb.2019.02.056>
- [73] Ross CK, Stelmack JA, Stelmack TR, Guihan M, Fraim M. Development and sensitivity to visual impairment of the Low Vision Functional Status Evaluation (LVFSE). *Optometry and Vision Science: Official Publication of the American Academy of Optometry*. 1999; 76: 212-20. <https://doi.org/10.1097/00006324-199904000-00024>
- [74] Rasheed HA, Abdalla J, Hawileh R, Al-Tamimi AK. Flexural behavior of reinforced concrete beams strengthened with externally bonded Aluminum Alloy plates. *Engineering Structures*. 2017; 147: 473-85. <https://doi.org/10.1016/j.engstruct.2017.05.067>
- [75] Mohammed A. Flexural Behavior of Reinforced Concrete Beams Strengthened with Externally Bonded Hybrid Systems. Master Thesis. 2017.12.07
- [76] Qeshta IMI, Shafigh P, Jumaat MZ, Abdulla AI, Ibrahim Z, Alengaram UJ. The use of wire mesh-epoxy composite for enhancing the flexural performance of concrete beams. *Materials & Design*. 2014; 60: 250-9. <https://doi.org/10.1016/j.matdes.2014.03.075>
- [77] Arabzadeh A, Karimizadeh H. Materials B. Experimental study of RC deep beams with opening and FRP composites installed by means of EBR and EBROG methods. *Construction and Building Materials*. 2019; 208: 780-91. <https://doi.org/10.1016/j.conbuildmat.2019.03.055>
- [78] Daugevičius M, Valivonis J, Skuturna T. Prediction of deflection of reinforced concrete beams strengthened with fiber reinforced polymer. *Materials* 2019; 12: 1367. <https://doi.org/10.3390/ma12091367>
- [79] Daghash SM, Ozbulut OE. Flexural performance evaluation of NSM basalt FRP-strengthened concrete beams using digital image correlation system. *Composite Structures*. 2017; 176: 748-56. <https://doi.org/10.1016/j.compstruct.2017.06.021>

- [80] Singh SB, Munjal P. Flexural response of strengthened masonry beam with CFRP. National conference of recent advancements in civil and environmental engineering. 2015. <https://doi.org/10.13140/RG.2.1.1790.3449>
- [81] Özkılıç, Y. O., Yazman, Ş., Aksoyulu, C., Arslan, M. H., & Gemi, L. . Numerical investigation of the parameters influencing the behavior of dapped end prefabricated concrete purlins with and without CFRP strengthening. *Construction and Building Materials*. 2021; 275, 122173. <https://doi.org/10.1016/j.conbuildmat.2020.122173>
- [82] Hussain M, Sharif A, Baluch IABMH, Al-Sulaimani GJ. Flexural behavior of precracked reinforced concrete beams strengthened externally by steel plates. *Structural Journal* 1995; 92: 14-23. <https://doi.org/10.14359/1466>
- [83] Charif A. Structural behaviour of reinforced concrete beams strengthened by epoxy bonded steel plates. University of Sheffield, 1983.
- [84] Roberts TM, Hajikazemi H. Theoretical Study Of The Behaviour Of Reinforced Concrete Beams Streng-Thened By Externally Bonded Steel Plates. *Proceedings of the Institution of Civil Engineers* 1989; 87: 39-55. <https://doi.org/10.1680/iicep.1989.1452>
- [85] Oehlers DJ, Ali MSM, Luo W. Upgrading continuous reinforced concrete beams by gluing steel plates to their tension faces. *Journal of Structural Engineering* 1998; 124: 224-32. [https://doi.org/10.1061/\(ASCE\)0733-9445\(1998\)124:3\(224\)](https://doi.org/10.1061/(ASCE)0733-9445(1998)124:3(224))
- [86] Rahimi H, Hutchinson A. Concrete beams strengthened with externally bonded FRP plates. *Journal of Composites for Construction*. 2001; 5:1 44-56. [https://doi.org/10.1061/\(ASCE\)1090-0268\(2001\)5:1\(44\)](https://doi.org/10.1061/(ASCE)1090-0268(2001)5:1(44))
- [87] Hamoush SA, Ahmad SH. Debonding of steel plate-strengthened concrete beams. *Journal of Structural Engineering*. 1990; 116: 356-371. [https://doi.org/10.1061/\(ASCE\)0733-9445\(1990\)116:2\(356\)](https://doi.org/10.1061/(ASCE)0733-9445(1990)116:2(356))
- [88] Jones R, Swamy RN, Charif A. Plate separation and anchorage of reinforced concrete beams strengthened by epoxy-bonded steel plates. *Structural Engineer* 1988; 66. <http://worldcat.org/issn/14665123>
- [89] Gemi L, Aksoyulu C, Yazman Ş, Özkılıç YO, Arslan MH. Experimental investigation of shear capacity and damage analysis of thinned end prefabricated concrete purlins strengthened by CFRP composite. *Composite Structures*. 2019; 229: 111399. <https://doi.org/10.1016/j.compstruct.2019.111399>
- [90] Dong J, Wang Q, Guan Z. Structural behaviour of RC beams with external flexural and flexural-shear strengthening by FRP sheets. *Composites Part B: Engineering* 2013; 44: 604-12. <https://doi.org/10.1016/j.compositesb.2012.02.018>
- [91] El-Ghandour AA. Experimental and analytical investigation of CFRP flexural and shear strengthening efficiencies of RC beams. *Construction and Building Materials*. 2011; 25: 1419-29. <https://doi.org/10.1016/j.conbuildmat.2010.09.001>
- [92] Hosen MA, Jumaat MZ, Alengaram UJ, Sulong NHR, Islam AS. Structural performance of lightweight concrete beams strengthened with side-externally bonded reinforcement (S-EBR) technique using CFRP fabrics. *Composites Part B: Engineering*. 2019; 176: 107323. <https://doi.org/10.1016/j.compositesb.2019.107323>
- [93] Kadhim AMH, Numan HA, Özakça M. Flexural strengthening and rehabilitation of Reinforced concrete beam using BFRP composites: finite element approach. *Advances in Civil Engineering*. 2019. <https://doi.org/10.1155/2019/4981750>
- [94] Zhuang N, Chen J, Zheng M, Chen D. Flexural experimental study on reinforced concrete beams strengthened with carbon fiber-reinforced polymer laminates using anchorage systems. *Materials Express*. 2019; 9: 923-30. <https://doi.org/10.1166/mex.2019.1575>
- [95] Surwase H, Narule GN, Walke SB. Behavior of RC T-Beam Strengthen Using Basalt Fiber Reinforced Polymer (FRP) Sheet 2019.

- [96] Musa Hakan Arslan Lokman Gemi Yasin Onuralp Özkılıç CA. Effect of Circular Holes in Shear Region on the Behavior of CFRP Strengthened RC Beams. Conference: 4th Eurasian Conference on Civil and Environmental Engineering (ECOCEE) 2019.
- [97] Altin S, Anil Ö, Koprman Y, Mertoğlu Ç, Kara ME. Improving shear capacity and ductility of shear-deficient RC beams using CFRP strips. Journal of reinforced plastics and composites. 2010; 29:19 2975-2991. <https://doi.org/10.1177/0731684410363182>
- [98] Gamino AL, de Oliveira JLA, Manzoli OL, Bittencourt TN. R/C structures strengthened with CFRP part II: analysis of shear models. Revista IBRACON de Estruturas e Materiais. 2010; 3, 24-49.
- [99] Önal MM, Engineering. Strengthening reinforced concrete beams with CFRP and GFRP. Advances in Materials Science and Engineering. 2014. <https://doi.org/10.1155/2014/967964>
- [100] Gao P, Gu X, Mosallam AS. Flexural behavior of preloaded reinforced concrete beams strengthened by prestressed CFRP laminates. Composite Structure 2016; 157: 33-50. <https://doi.org/10.1016/j.compstruct.2016.08.013>
- [101] Moshiri N, Czaderski C, Mostofinejad D, Hosseini A, Sanginabadi K, Breveglieri M, et al. Flexural strengthening of RC slabs with nonprestressed and prestressed CFRP strips using EBROG method. Composites Part B: Engineering, 2020; 201: 108359. <https://doi.org/10.1016/j.compositesb.2020.108359>
- [102] Kim HS, Shin YS. Flexural behavior of reinforced concrete (RC) beams retrofitted with hybrid fiber reinforced polymers (FRPs) under sustaining loads. Composite structures. 2011; 93: 802-11. <https://doi.org/10.1016/j.compstruct.2010.07.013>
- [103] Antony A, Reshmi PR, Prabhakaran P. EBR and GM Methods for External Flexural Strengthening of RC Beams. International Research Journal of Engineering and Technology (IRJET). 2019.
- [104] Bilotta A, Ceroni F, Nigro E, Pecce M. Efficiency of CFRP NSM strips and EBR plates for flexural strengthening of RC beams and loading pattern influence. Composite Structures 2015; 124: 163-75. <https://doi.org/10.1016/j.compstruct.2014.12.046>
- [105] Triantafyllou GG, Rousakis TC, Karabinis AI. Effect of patch repair and strengthening with EBR and NSM CFRP laminates for RC beams with low, medium and heavy corrosion. Composites Part B: Engineering. 2018; 133: 101-11. <https://doi.org/10.1016/j.compositesb.2017.09.029>
- [106] Skuturna T, Valivonis J. Experimental study on the effect of anchorage systems on RC beams strengthened using FRP. Composites Part B: Engineering. 2016; 91: 283-90. <https://doi.org/10.1016/j.compositesb.2016.02.001>
- [107] Firmo JP, Arruda MRT, Correia JR, Rosa IC. Three-dimensional finite element modelling of the fire behaviour of insulated RC beams strengthened with EBR and NSM CFRP strips. Composite Structures 2018; 183: 124-36. <https://doi.org/10.1016/j.compstruct.2017.01.082>
- [108] Choobbor SS, Hawileh RA, Abu-Obeidah A, Abdalla JA. Performance of hybrid carbon and basalt FRP sheets in strengthening concrete beams in flexure. Composite Structures. 2019; 227: 111337. <https://doi.org/10.1016/j.compstruct.2019.111337>
- [109] Miruthun G, Vivek D, Remya PR, Elango KS, Saravanakumar R, Venkatraman S. Experimental investigation on strengthening of reinforced concrete beams using GFRP laminates. Materials Today: Proceedings. 2020. <https://doi.org/10.1016/j.matpr.2020.08.544>
- [110] Ravichandran RS, Suguna K, Raghunath PN. An Experimental and Analytical Study On Composite High Strength Concrete-Fibre Reinforced Polymer Beams. International Journal of Engineering Inventions 2012; 1: 58-67.
- [111] Josy J, Johny MA. Effect Of Gfrp Wrapping On Flexural Behaviour Of Reinforced Concrete Beams. Int. Res. J. Eng. Technol., 2019; 6(5), 4348-4353.

- [112] Meikandaan TP, Murthy D A R, Technology. Flexural Behaviour of RC Beam Wrapped with GFRP Sheets. *International Journal of Civil Engineering and Technology*. 2017; 8.
- [113] Ahmed H. Abdel-kareem M. H. Makhoulouf and M. Badw ASD. Repairing and strengthening of RC beams using thin lower concrete layer reinforced by FRP bars. *International Journal of Civil Engineering and Technology (IJCIET)* 2019; 10: 1949-1966.
- [114] Mariappan M, Raghunath PN, Sivaraja M. Technology. Structural Behavior of SFRC Beams strengthened with GFRP Laminates: An Experimental and Analytical Investigation. *Brazilian Archives of Biology and Technology*. 2016; 59. <https://doi.org/10.1590/1678-4324-2016161071>
- [115] Sameer Shrivastava A. Tiwari., Strengthening of Beams Using Glass Fiber Reinforced Polymer (GFRP) Laminate. *International Journal of Engineering Development and Research* 2018; 6: 231-9.
- [116] Banjara NK, Ramanjaneyulu K., J C, Materials B. Experimental and numerical investigations on the performance evaluation of shear deficient and GFRP strengthened reinforced concrete beams. *Construction and Building Materials*. 2017; 137: 520-34. <https://doi.org/10.1016/j.conbuildmat.2017.01.089>
- [117] Nanda RP, Behera B, Majumder S, Khan H. A. Research. RC Beam Strengthening by Glass Fibre Reinforced Polymer. *International Journal of Engineering Technology Science and Research*. 2018; 5: 21-6.
- [118] Sundarraja MC, Rajamohan S. Strengthening of RC beams in shear using GFRP inclined strips-An experimental study. *Construction and building materials*. 2009; 23: 856-64. <https://doi.org/10.1016/j.conbuildmat.2008.04.008>
- [119] Panigrahi AK, Biswal KC, Barik MR. Strengthening of shear deficient RC T-beams with externally bonded GFRP sheets. *Construction and Building Materials* 2014; 57: 81-91. <https://doi.org/10.1016/j.conbuildmat.2014.01.076>
- [120] Ibrahim SS, Eswari S, Sundararajan T. Experimental investigation on FRC beams strengthened with GFRP laminates. *Journal of Structural Engineering*. 2015; 15:1.
- [121] Mohite SS, Awati DMM, Patil RA. Engineering A. Flexural Behaviour of RC Beams with Side Bonded GFRP Laminates. *International Journal of Emerging Technology and Advanced Engineering*, 2014; 230: 124-30.
- [122] Sivasankar S, Bharathy T, Vinodh Kumar R, Student PG. Flexural Behaviour of RC beams using GFRP Composites. 2018. vol. 7. <https://doi.org/10.14419/ijet.v7i3.12.16493>
- [123] Kumari A, Nayak AN. An experimental approach for strengthening of RC deep beams with web openings using GFRP fabrics and gas actuated fasteners. *Journal of Building Engineering*, 2020: 102027. <https://doi.org/10.1016/j.jobbe.2020.102027>
- [124] Saribiyik A, Caglar N. Flexural strengthening of RC beams with low-strength concrete using GFRP and CFRP. *Structural Engineering and Mechanics*. 2016; 58: 825-45. <https://doi.org/10.12989/sem.2016.58.5.825>
- [125] Mini KM, Alapatt RJ, David AE, Radhakrishnan A, Cyriac MM, Ramakrishnan R. Experimental study on strengthening of RC beam using glass fibre reinforced composite. *Structural Engineering and Mechanics*. 2014; 50: 275-86. <https://doi.org/10.12989/sem.2014.50.3.275>
- [126] Alhamdan Y, Dirikgil T. Experimental Investigation of the Flexural Strengthening of Fixed-Supported RC Beams. *International Journal of Civil Engineering* 2020: 1-18. <https://doi.org/10.1007/s40999-020-00531-6>
- [127] Chellapandian M, Prakash SS, Sharma A. Experimental and finite element studies on the flexural behavior of reinforced concrete elements strengthened with hybrid FRP technique. *Composite Structures*. 2019; 208:466-78. <https://doi.org/10.1016/j.compstruct.2018.10.028>



Research Article

Moment-curvature relationships for RC chimney sections

Megha Bhatt^a, Sandip A. Vasanwala^b

Department of Civil Engineering, SV National Institute of Technology, Surat, India

Article Info

Article history:

Received 25 Nov 2021

Revised 25 Jan 2022

Accepted 23 Feb 2022

Keywords:

ACI: 307 – 08;

CICIND 2011;

IS: 4998 – 2015;

Moment-Curvature Curve;

RC Chimney

Abstract

The 3rd revision of IS: 4998 i.e. 2015 edition adopted a limit state method of design for RC chimney and gave a new model of stress-strain relationship for concrete and steel. RC chimneys are tall cantilever columns having thin-walled hollow circular sections and subjected to axial compression resulting from self-weight and bending moment resulting from lateral forces. It has been seen that there are many disparities between the stress-strain relationship of these materials adopted by IS: 4998 – 2015 and other well-established design standards. This paper compares and discusses these disparities in terms of strength, ductility factor and energy absorption with the help of plotted moment-curvature charts. For the comparison, design recommendations of IS: 4998 – 2015, CICIND 2011, ACI: 307 – 08 are used. Moment-curvature curves are plotted using the major two conditions of the section i.e. yielding of tension reinforcement and crushing of concrete in compression. It is obtained from the study that CICIND 2011 gives higher results for all parameters, namely strength, ductility factor and energy absorption.

© 2022 MIM Research Group. All rights reserved.

1. Introduction

In the 3rd revision of IS: 4998 proposed in 2015 [1], limit state design approach has been adopted to design a section of reinforced concrete (RC) chimney. Many researchers have contributed to this field before this revision took place. The load-moment (P_u-M_u) interaction curves for the tubular sections like chimney were plotted and compared by Durgesh C. Rai and others in 2006 [2] using limit state theory according to IS: 456 – 2000 [3] provisions and also using working stress theory according to the provisions of IS: 11628 – 1985 [4] and IS: 4998 – 1975 [5]. The comparison showed that it would be preferable to use limit state design approach rather than using the working stress method for the tubular section like RC chimneys, TV towers, etc.

To plot load-moment (P_u-M_u) diagrams, a computer program has been developed by K. S. Babu Narayan and Subhash C. Yaragal in 2007 [6]. It is to be noted here that the computer program uses simplified rectangular stress-strain curve to plot the load-moment interaction curve of hollow circular section. But behaviour of thin-walled hollow circular sections under the action of axial compressive stress and flexure is different than the regular solid beam or column section and hence, for such tubular thin-walled sections the direct use of stress-strain curve for concrete specified in IS: 456 – 2000 as well as rectangular stress block should be avoided.

A new model that represents the stress-strain relationship of concrete for thin-walled hollow circular sections has been proposed by P. Srinivasa Rao and Devdas Menon in 1995 [7]. Using this proposed new model of stress-strain relationship for concrete, the P_u-M_u interaction curves were plotted for the tubular sections and the same were

^aCorresponding author: megha211984@gmail.com

^aorcid.org/0000-0001-6588-9531; ^borcid.org/0000-0003-0083-6257

DOI: <http://dx.doi.org/10.17515/resm2022.369st1125>

Res. Eng. Struct. Mat. Vol. 8 Iss. 3 (2022) 519-533

compared with interaction curves plotted using the criteria of various other well-established codes namely ACI: 307 – 88 [8], CICIND 1984 [9], DIN 1056 – 1984 [10] as well as using the criteria given in the book of Pinfold 1984 [11]. This new model of stress-strain curve for concrete has been adopted for the limit state design approach in IS: 4998 – 2015. A comparison of various prevalent design provisions with regards to strength reduction factors, maximum strain limits for concrete and steel, and modulus of elasticity of steel for RC chimney sections are shown in Table 1 that reveal significant disparities. Thus, the comparison of these codes becomes necessary to enhance the knowledge base on this topic.

Table 1. Design criteria in different design codes

Design Standard	Load Factor		Strength Reduction Factor			Strain Limit		Elastic Modulus (MPa)
	Dead Load	Wind Load*	Concrete (γ_c)	Steel (γ_s)	Overall	Concrete ($\epsilon_{c, max}$)	Steel ($\epsilon_{s, max}$)	Steel (E_s)
IS: 4998 – 2015	0.9	1.6	1.5	1.15	-	0.002	0.05	2×10^5
	or 1.2							
CICIND 2011	1.0	1.6	1.5	1.15	-	0.003	0.01	2.1×10^5
ACI: 307 – 08	0.9	1.6	-	-	0.8	0.003	0.07	2×10^5
	or 1.2							

* Factor 1.6 shall be used for Along Wind Load

To carry out non-linear analysis of reinforced concrete elements, moment-curvature relationship is widely used [12]. The bilinear law having first division going from the zero-load condition up to the point representing the yielding of tension reinforcement, and the second division going from this yield point to the point representing the crushing of concrete in compression is the modest yet satisfactorily correct description of moment-curvature ($M-\phi$) relationship for RC sections. In this paper, moment-curvature curves are plotted to compare the values of ultimate strength, ductility and energy absorption obtained from the design approaches stated in IS: 4998 – 2015 [1], CICIND 2011 [13] and ACI: 307 – 08 [14].

2. Comparison of Stress-Strain Relationship for Materials

In this section the relationship between stress and strain for concrete and steel recommended by IS: 4998 – 2015 [1], CICIND 2011 [13] and ACI: 307 – 08 [14] for yield and ultimate conditions are compared in detail.

2.1 Relationship between Stress and Strain for Concrete

In the 3rd revision of IS: 4998 i.e. in IS: 4998 – 2015, it is assumed that the concrete compressive stress is increasing parabolically from zero at neutral axis location to the peak value at the strain of 0.002 as indicated in (Fig. 1(a)). When compared to the other two codes, it is found that IS: 4998 – 2015 introduces the short-term loading factor and specifies the stringent value of strain in concrete at the center of the thickness of shell at failure as 0.002. This effect of short-term loading was specifically presented in the CICIND 1984 [9] edition, in which parabolic stress-strain relation is assumed for concrete when the section is analyzed under long-term loading, and linear stress-strain relation for the same under short-term loading. The compressive strain in concrete at failure was assumed to be 0.001, which is based on the research work of Schueller, G.I. and Bucher

C.G. in 1983 [15] which concludes that the fracture is not caused by repeated oscillation loading due to wind but by a single wind gust in reinforced concrete chimneys.

The above-mentioned material law for concrete was adopted from the results of the experimental research work carried out by Naokowski in 1981 [16]. The reinforced concrete test specimens were tested under reversed cyclic loading by him for the study. However, the results of this experimental research work based on reverse cyclic loading do not apply to the typical along wind conditions considered in the CICIND 1984 code, as the behaviour of along-wind loading is better approximated by monotonic loading rather than reverse cyclic loading as the along-wind loading and its response is somewhat quasi-static. However, in the newest edition of the CICIND Code i.e. CICIND 2011 this short-term loading effect is ignored and the parabolic stress-strain relationship for concrete in flexural compression under permanent loading is considered and the concrete strain at the center of the thickness at failure is limited to 0.003 as shown in (Fig. 1(b)).

On the other hand, IS: 4998 – 2015 brings in the short-term wind loading effect. To consider this effect the short-term loading factor (C_{sf}) is presented which was first introduced by P. Srinivasa Rao and Devdas Menon in 1995. This C_{sf} factor is influenced by the amount of axial compression (P_u) on the RC chimney section. The C_{sf} factor varies from 1.12 to 1 for $P_u = 0$ to $P_u = P_{u, max}$ i.e. under pure compression respectively. In his research paper P. Srinivasa Rao and Devdas Menon in 1995 [7], established the foundation of a new model of stress-strain curve of concrete for RC chimney sections which is currently adopted in the newly revised edition of IS: 4998 – 2015. Further expanding the research works of Rusch in 1960 [17] and Ellingwood in 1980 [18], a logical formwork for the concrete stress-strain relationship has been proposed by P. Srinivasa Rao and Devdas Menon [7], which accounts for the effects of tubular geometry and short-term loading effect in the form of short-term loading factor.

Based on a large number of experiments carried out on eccentrically loaded concrete tubular sections under varying load durations, a family of stress-strain curves was presented by Rusch in 1960 [17]. The observations of these tests led towards the conclusion that if the maximum concrete strain is limited to 0.002 then it is reasonable to assume an increase of approximately 10% in stress for relatively short-term loading. In their reliability study of reinforced concrete columns in 1980, Ellingwood and others [18] had also recommended a similar strength improvement factor; under wind loading conditions. The short-term loading factor, C_{sf} can be calculated using the equation given in the IS: 4998 – 2015 as follows:

$$C_{sf} = [0.95 - 0.1 (P_u/P_{u, max})] / 0.85 \tag{1}$$

where; P_u = Factored axial load and

$$P_{u, max} = 2\pi r t \left[\left(\frac{0.67 f_{ck}}{\gamma_c} \right) \left(1 - \frac{P_t}{100} \right) + f_s (\epsilon_{cu}) \left(\frac{P_t}{100} \right) \right] \tag{2}$$

As the diameter of the RC chimney is very large compared to its thickness, the strain gradient across the thickness at the extreme compression location is minimal and hence, the stringent value of 0.002 for maximum strain in concrete in axial compression seems to be valid even in the presence of bending.

However, ACI: 307 – 08 follows Whitney’s rectangular stress block as prescribed in ACI: 318 – 2002 [19]. This stress block is proved to be valid for rectangular and flanged sections but it cannot be directly used without modification for the RC chimney section

(thin-walled hollow circular section) in which the maximum compressive strain in concrete is less than 0.003 when the fracture limit of steel is reached i.e. the compressive stress block is not fully developed and hence, some modification as shown in (Fig. 1(c)) are adopted in ACI: 307 – 08. The $\varepsilon_{c, max}$ in compression is assumed as 0.003 and to include the above consequences, the modification factor (Q) is introduced in the stress block of concrete which is based on the experimental work of Morkin and Rumman in 1985 [20] and the numerical study carried out by the committee.

Where, Q can be derived by the following equations:

For $\alpha \leq 5$ degrees

$$Q = (-0.523 + 0.181\alpha - 0.0154\alpha^2) + (41.3 - 13.2\alpha + 1.32\alpha^2)(t/r) \quad (3)$$

For 5 degrees $< \alpha \leq 10$ degrees

$$Q = (-0.523 + 0.181\alpha - 0.0154\alpha^2) + (41.3 - 13.2\alpha + 1.32\alpha^2)(t/r) \quad (4)$$

For 10 degrees $< \alpha \leq 17$ degrees

$$Q = (-0.488 + 0.076\alpha) + (9.758 - 0.640\alpha)(t/r) \quad (5)$$

For 17 degrees $< \alpha \leq 25$ degrees

$$Q = (-1.345 + 0.2018\alpha + 0.004434\alpha^2) + (15.83 - 1.676\alpha + 0.03994\alpha^2)(t/r) \quad (6)$$

For 25 degrees $< \alpha \leq 35$ degrees

$$Q = (0.993 - 0.00258\alpha) + (-3.27 + 0.0862\alpha)(t/r) \quad (7)$$

For $\alpha > 35$ degrees

$$Q = 0.89 \quad (8)$$

Where α is the one-half of the central angle subtended by neutral axis on the chimney section

2.2 Relationship Between Stress and Strain for Steel

The idealized elastoplastic stress-strain relationship for steel in tension and compression is adopted by ACI: 307 – 08 and CICIND 2011, which assumes that steel shows sharp yielding behaviour. IS: 4998 – 2015 on the other hand, has incorporated the offset approach to determine the yield strength. In this approach, the characteristic strength of steel is taken as that stress at which it shows definite limiting deviation from stress-strain proportionality, the value of which is taken as 0.2% of proof stress. Conrad Paulson and others in 2016 [21] have compared the ultimate strength of reinforced concrete column and beam sections using different stress-strain relationships of steel i.e. for sharp yield plateau and for gradually yielding curves wherein the offset values are taken as 0.1% and 0.2%, and concluded that the approach of using 0.2% offset is safe and practical.

Stress-strain relationship for concrete and steel for yield conditions are shown in (Fig. 2)

3. Methodology

Curves for moment-curvature ($M-\phi$) relationship for the above-mentioned design standards are plotted using four important points as follows:

Point 1: This point is start of loading. At zero loading there is zero moment and hence zero curvature i.e. the coordinates for this point are (0, 0).

Point 2: Since the concrete is not crushed and the steel is not yielded, the elastic moment capacity of the full section is used. This point is calculated from the linear stress-strain relationship of steel and concrete.

Point 3: The yield characteristics of the section are calculated by using the yield strain of steel in tension. For the most accurate solution, this point is obtained using the actual stress-strain relationship of steel and concrete given in the three design standards.

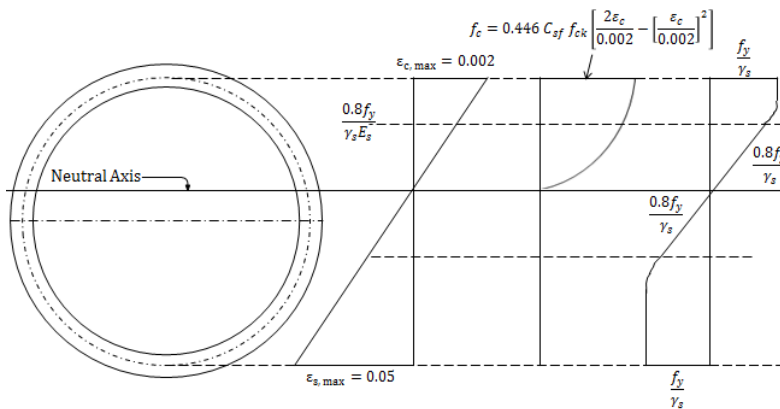
Point 4: The ultimate characteristics of the section are calculated by limiting the strain of concrete in compression at which it crushes. This point is obtained using the actual stress and strain relationship of steel and concrete as presented in (Fig. 1).

The above four points of the moment-curvature relationship curve generate three important regions of the curve.

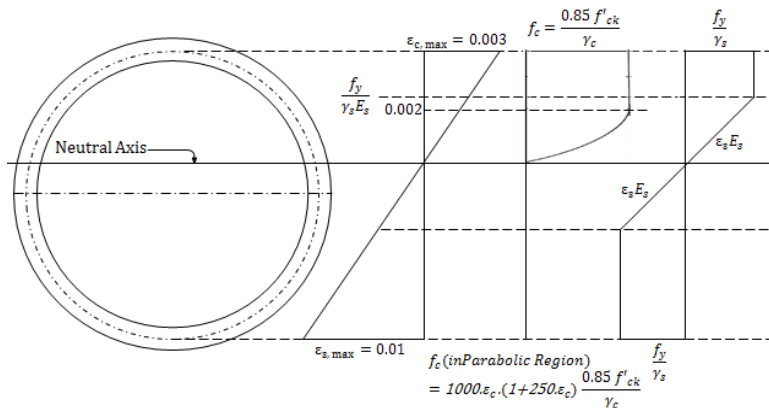
Region 1: between points 1 and 2. This region is called the uncracked response region.

Region 2: between points 2 and 3. This region is called the cracked linear response region.

Region 3: between points 3 and 4. This region is called the inelastic response region.



(a)



(b)

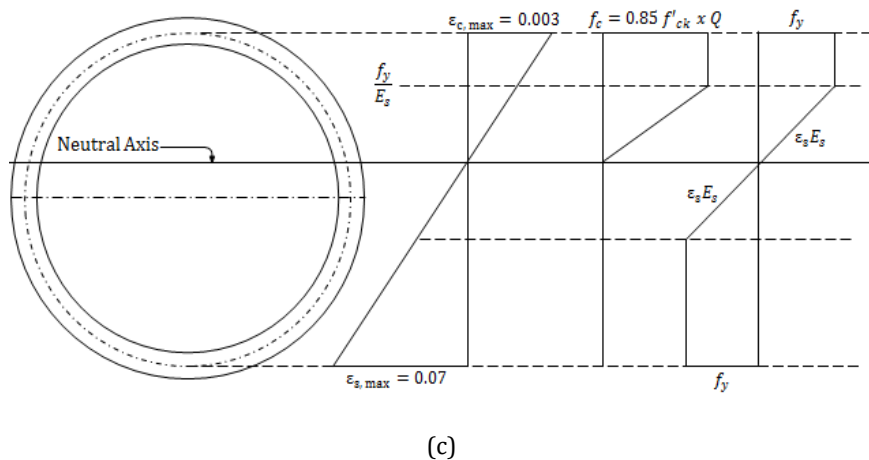
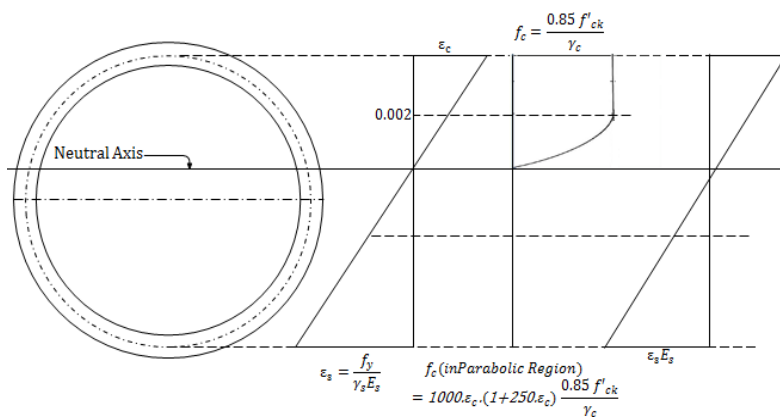
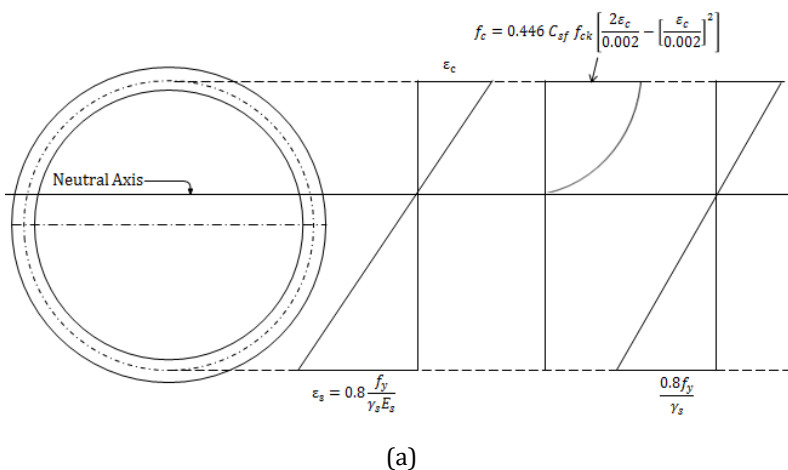


Fig. 1 Stress-strain relationship for concrete and steel for ultimate conditions as per (a) IS: 4998 - 2015 (b) CICIND 2011 (c) ACI: 307 - 08 (a) IS: 4998 - 2015 (b) CICIND 2011 (c) ACI: 307 - 08



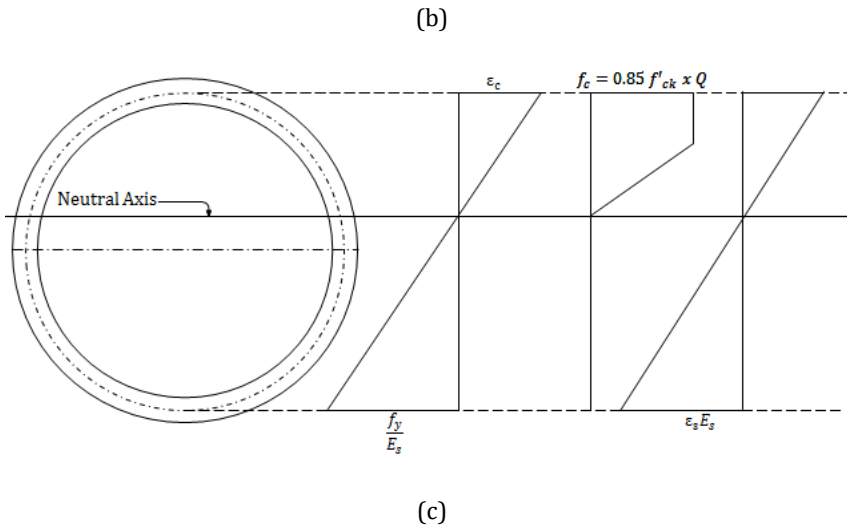


Fig. 2 Stress-strain relationship for concrete and steel for yield conditions as per (a) IS: 4998 - 2015 (b) CICIND 2011 (c) ACI: 307 - 08

4. Development of Spreadsheet Program

To calculate the x and y coordinates of each point of this moment-curvature relationship curve of RC chimney section, a generalized spreadsheet program is developed using MS Excel. The inputs of this program are material properties like concrete characteristic compressive cube strength (f_{ck}) as per IS: 456 - 2000, characteristic cylindrical compressive strength ($f'_{ck} = 0.8 f_{ck}$) as per CICIND 2011 and ACI: 307 - 08, steel yield strength (f_y), elastic modulus of concrete (E_c) and elastic modulus of steel (E_s) and geometrical properties of the section like outer diameter (D), thickness (t), location of steel bars and percentage of steel (p_t). The axial force is also an indirect input, which is obtained by adjusting the depth of the neutral axis (X_u).

For the comparative study, a typical RC chimney cross-section comprising of $D = 10$ m, and $t = 0.45$ m, $f_{ck} = 40$ MPa and $f_y = 500$ MPa is selected with variation in $p_t = 0.5\%$, 0.75% , 1.5% and 2.0% and variation in $(n = f_{ca}/f_{ck}) = 0.025$, 0.05 , 0.1 , 0.15 and 0.2 for the comparative study. (f_{ca}) is the axial stress generated due to the axial compression force on the section.

The moment capacity of the uncracked section, M_c and curvature for the uncracked section, ϕ_c (point 2 on $M-\phi$ curve) is calculated using the stress-strain relationship shown in (Fig. 3).

The moment capacities M_u and M_y are determined by solving the following equilibrium equations:

$$P_u = P_{uc} + P_{us} \quad (9)$$

$$P_y = P_{yc} + P_{ys} \quad (10)$$

$$M_u = M_{uc} + M_{us} \quad (11)$$

$$M_y = M_{yc} + M_{ys} \tag{12}$$

Where P_{uc} and P_{us} are the resultant ultimate forces obtained from concrete and steel stress blocks, and M_{uc} and M_{us} denote the moments about the centerline of that tubular section. Similarly P_{yc} and P_{ys} are the resultant yield forces and M_{yc} and M_{ys} are yield moment capacity of the tubular section.

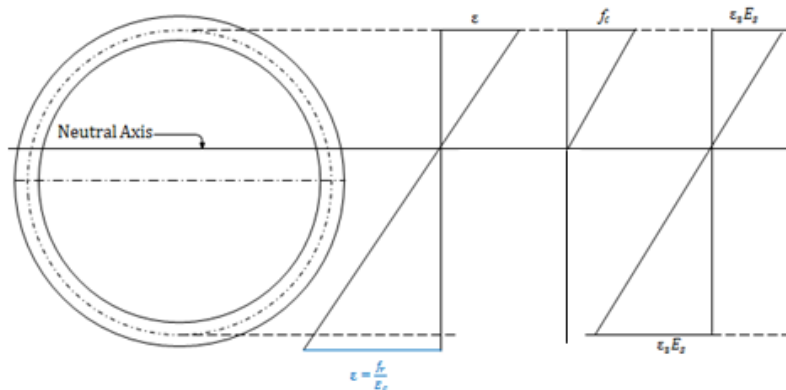


Fig. 3 Stress-strain relationship for concrete and steel for uncracked section

f_r = Modulus of rupture of concrete

(As per IS [3], $f_r = 0.7\sqrt{f_{ck}}$ MPa, as per CICIND [13] and ACI [19], $f_r = 7.5\sqrt{f'_{ck}}$ psi)

E_c = Modulus of elasticity of concrete

(As per IS [3], $E_c = 5000\sqrt{f_{ck}}$ MPa, as per CICIND [13] and ACI [19], $E_c = 57000\sqrt{f'_{ck}}$ psi)

General procedure followed to obtain the points 3 and 4 on the moment-curvature curves are as follows:

Step 1: The cross-section is entirely divided into several small strips parallel to the neutral axis. To maintain the accuracy of the results, the width of each strip is maintained as 1 mm.

Step 2: Then considering the assumption that plane section remains plane before and after bending, the value of strain at the geometrical center of each strip ϵ_c and the location of reinforcement ϵ_s is calculated separately. It is to be noted here that to obtain the yield properties of the section, the strain limit at which steel yields is fixed at the level of reinforcement located at extreme tension face and to obtain the ultimate properties of the section, the strain limit at which concrete crushes is fixed at the center of the shell thickness in compression zone. The different design standards gives different strain limits for both conditions.

Step 3: After this, concrete stress at the geometrical center of each strip and the steel stress at the location of reinforcement is calculated individually. It is to be noted here that the stresses for yield and ultimate conditions for these design standards are calculated as per their design recommendations shown in the form of stress block in (Fig. 1 and 2). The concrete stresses f_c are calculated as per equations 13, 14 and 15 for IS: 4998 – 2015, CICIND 2011 and ACI: 307 – 08 respectively for yield and ultimate conditions.

$$f_c = \frac{0.67 C_{sf} f_{ck}}{1.5} \left\{ 2 \left(\frac{\varepsilon_c}{0.002} \right) - \left(\frac{\varepsilon_c}{0.002} \right)^2 \right\} \quad (13)$$

Where the short term loading factor can be calculated using (Eq. 1)

$$\begin{aligned} \text{For } \varepsilon_c \leq 0, & \quad f_c = 0 \\ -0.002 \leq \varepsilon_c < 0, & \quad f_c = 1000 \cdot \varepsilon_c \cdot (1 + 250 \varepsilon_c) \cdot (0.85 f'_{ck} / 1.5) \\ -0.003 \leq \varepsilon_c < -0.002, & \quad f_c = - (0.85 f'_{ck} / 1.5) \end{aligned} \quad (14)$$

$$f_c = 0.85 f'_{ck} \times Q \quad (15)$$

Where Q can be calculated using (Eqs. 3 – 8)

Step 4: The concrete stresses at different levels are then multiplied with the area of the respective strip to get concrete compressive force and the steel stresses at different locations are multiplied with the associated area of reinforcement to calculate the net force offered by reinforcement i.e. the compressive force minus the tensile force obtained at either side of the neutral axis. Then to get the resultant force (P_u and P_y) the concrete compressive force and net force of steel are algebraically added.

Step 5: The depth of the neutral axis is then adjusted using the 'Goal Seek' function of the MS Excel so that the obtained P_u from the above steps could be matched with the P_u which is an input in the form of axial stress ratio (f_{ca}/f_{ck}) as mentioned above.

Step 6: Then these concrete and steel forces are multiplied with their centroidal distances separately to get the moment from concrete and steel respectively. These moments are then algebraically added to get the resultant moment (M_u and M_y).

5. Results and Discussion

The outcomes of the comparative study are discussed here in terms of ultimate strength, ductility and energy absorption in the forms of Tables 2, 3 and 4 and (Fig. 4).

The plotted moment-curvature curves shows that CICIND gives higher values of curvature in all the cases and IS gives the highest values of ultimate moments for almost all cases excepts at higher stress ratios and higher percentage of steel i.e. for stress ratios 0.15 and 0.2 and for percentage of steel 1.5% and 2%. The differences in the following moment-curvature curves are mainly due to the different stress-strain relationships adopted by the three design codes. These differences are further elaborated through the comparison of ultimate moment, ductility ratio and energy absorption obtained from the plotted ($M-\phi$) curves (Fig. 4 (a-e)).

5.1 Comparison of Ultimate Strength

The ultimate moment carrying capacity defines the ultimate strength of RC chimney section when the section is subjected to an axial compressive load associated with a specific neutral axis depth within the section.

It can be seen from (Table 2) that for CICIND and ACI, ultimate capacity of section is increased with an increase in axial stress ratio and percentage of steel but for IS when stress ratio is more than 0.15 and percentage of steel is more than 1.5% the ultimate moment capacity decreases. Although, the differences are not significant between the values obtained from the three design standards. When the stress ratio is small and the percentage of steel is low, the differences between the three design standards are small.

The difference increases with increase in axial stress ratio and percentage of steel. When the RC chimney section is comprised of low axial stress ratio and lightly reinforced with steel bars, the governing condition is the extreme tension condition in which there is hardly any influence from the stress-strain conditions of concrete. The section is subjected to more compression when the axial stress ratio increases and hence, the difference between the three design approaches gets emphasized.

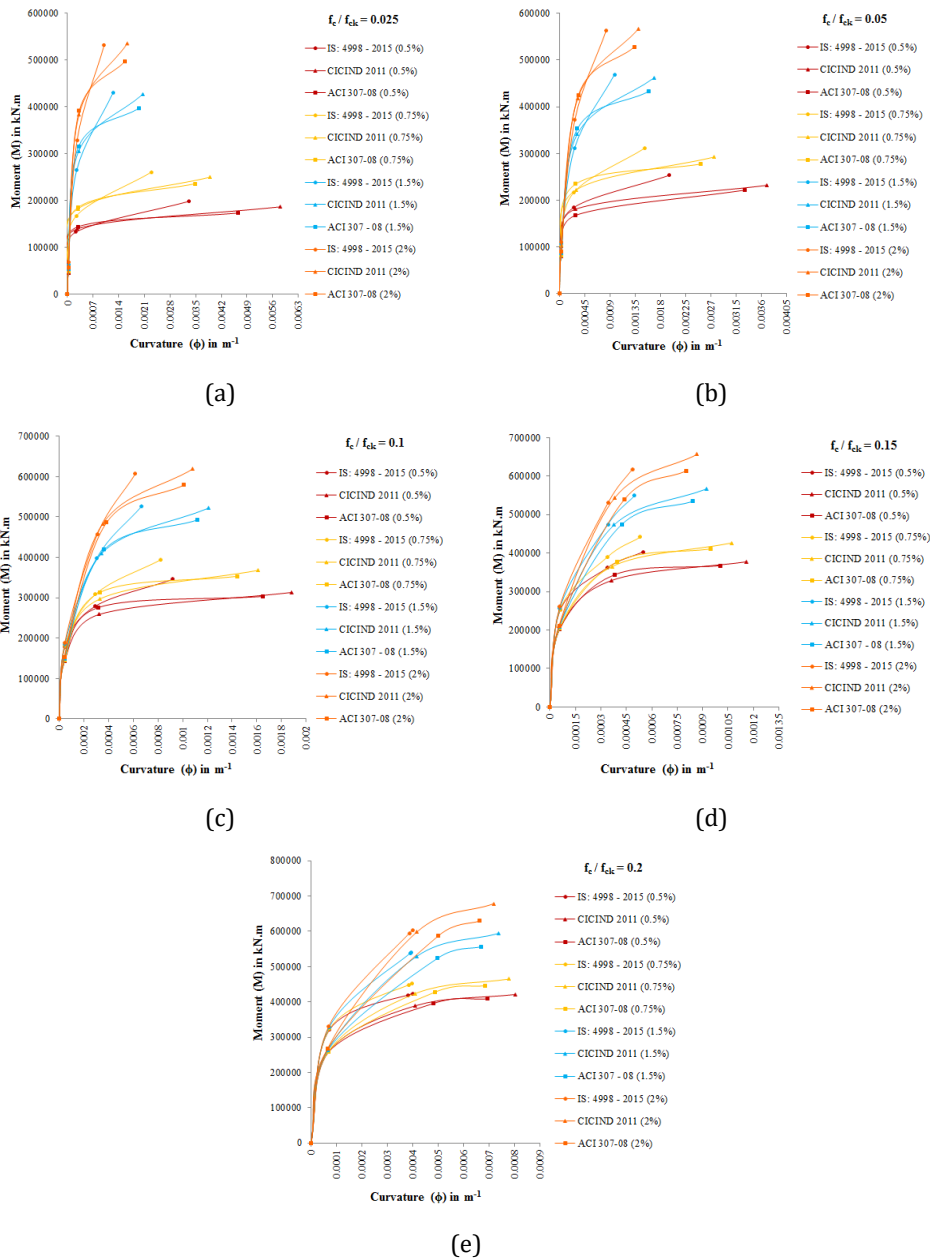


Fig. 4 Moment-curvature ($M-\phi$) interaction curves for stress ratios
 (a) 0.025 (b) 0.05 (c) 0.1 (d) 0.15 (e) 0.2

Table 2. Ultimate strength in kN.m (x 10⁴)

f_{ca}/f_{ck}	p_t %											
	IS: 4998-2015				CICIND 2011				ACI: 307 - 08			
	0.5	0.75	1.5	2.0	0.5	0.75	1.5	2.0	0.5	0.75	1.5	2.0
0.025	19.8	26.0	43.0	53.2	18.6	25.0	42.7	53.6	17.3	23.6	39.7	49.7
0.05	25.3	31.1	46.9	56.4	23.2	29.3	46.2	56.7	22.2	27.7	43.3	52.8
0.1	34.6	39.4	52.7	60.7	31.3	36.8	52.2	61.9	30.3	35.3	49.2	57.9
0.15	40.3	44.1	55.0	61.9	37.7	42.6	56.7	65.7	36.7	41.1	53.5	61.4
0.2	41.9	44.9	54.1	60.3	42.1	46.5	59.4	67.9	40.9	44.6	55.7	62.9

Compared to the other two design standards, the tables also suggest that IS: 4998 - 2015 which gives the highest values of ultimate moments up to lower axial stress ratios is reducing (non-linearly) substantially and drops below the values calculated from ACI: 307 - 08 and CICIND 2011; and at a higher percentage of steel i.e. at 1.5% and 2.0% this decline is substantial.

Contribution of ultimate moment capacity (M_u) of both the materials i.e. steel (M_{us}) and concrete (M_{uc}) in ultimate moment capacity (M_u) of the RC chimney section is also studied separately to understand the above mentioned differences.

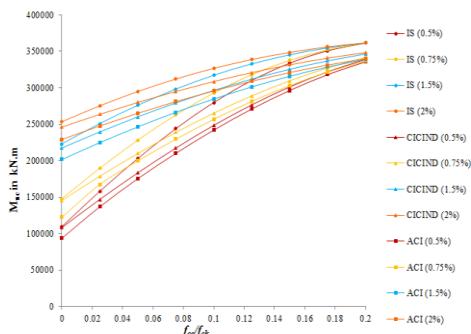


Fig. 5 Comparisons of the contribution of concrete in ultimate moments

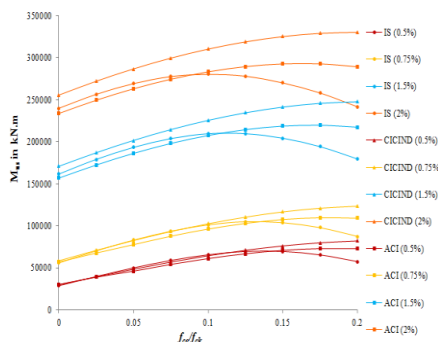


Fig. 6 Comparisons of the contribution of steel in ultimate moments

It is seen from this separate study (Fig. 5) that the contribution of ultimate moment capacity of concrete (M_{uc}) increases with an increase in axial stress ratio (n) for all three methods. It can also be witnessed here that the contribution of concrete obtained using recommendations IS: 4998 - 2015 is higher than the concrete contribution calculated using the recommendations of ACI: 307 - 08 and recommendations of CICIND 2011. This increase in the contribution of concrete calculated using the stress-strain relationship given in IS: 4998 - 2015 is more significant at a lower percentage of steel and higher axial stress ratio.

It can also be noticed here from (Fig. 6) that the contribution of steel in ultimate moment capacity (M_{us}) is reduced at a higher axial stress ratio, when calculated using the recommendations given in IS: 4998 - 2015 as compared to the same calculated using methodologies given in ACI: 307 - 08 and CICIND 2011 and hence, it can be concluded from this separate study that the decrement in the total ultimate moment capacity (M_u) of RC chimney section obtained using the recommendations of IS: 4998 - 2015 in comparison with the other two design recommendations is due to the reduction in the contribution of steel (M_{us}).

It can be concluded that at a lower percentage of steel and up to axial stress ratio of 0.15, the values of M_u is higher for IS: 4998 - 2015 compared to ACI: 307 - 08 and CICIND 2011 as the contribution of concrete (M_{uc}) is higher in this range.

Beyond the axial stress ratio of 0.15, the decrease in ultimate moment capacity calculated from IS: 4998 - 2015 is predominantly because of the decrease in the M_{us} which is significant at a high percentage of steel, as the share of concrete is still increasing but this share is having only a negligible increase in comparison with ACI: 307 - 08 and CICIND 2011 at a higher percentage of steel.

5.2 Comparison of Ductility

The ratio of the deformation at ultimate load to the deformation at yielding is known as the "Ductility Factor". It is an assessment of the RC member's ability to undergo large deformation before failure of the RC member takes place. It can be seen from Table 3 that the RC chimney sections designed using codal provision given in the CICIND 2011 gives higher ductility in all the cases. The values of ductility ratio for the particular percentage of steel decrease with an increase in the axial stress ratios.

Table 3. Ductility ratio

f_{ca}/f_{ck}	p_t %											
	IS: 4998-2015				CICIND 2011				ACI: 307 - 08			
	0.5	0.75	1.5	2.0	0.5	0.75	1.5	2.0	0.5	0.75	1.5	2.0
0.025	14.4	9.67	4.95	3.86	21.5	14.0	6.83	5.24	16.7	12.1	6.48	4.92
0.05	7.81	5.96	3.67	3.04	12.8	9.33	5.36	4.33	11.5	8.66	4.97	3.96
0.1	3.17	2.81	2.21	2.01	5.80	4.88	3.51	3.07	5.17	4.35	3.07	2.64
0.15	1.64	1.57	1.46	1.42	3.20	2.92	2.44	2.27	2.63	2.40	1.99	1.83
0.2	0.95	0.97	1.02	1.03	1.96	1.90	1.78	1.73	1.44	1.41	1.35	1.32

It can be seen from Table 3 that as per Indian Standard design methodologies, the ductility ratio decreases with an increase in the percentage of steel up to stress ratio, $f_{ca}/f_{ck} = 0.15$ but at a higher stress ratio i.e. $f_{ca}/f_{ck} = 0.2$ a little increase in the ductility ratio is observed with increase in the percentage of steel. However, it can be observed from Table 3 that as per design methodologies of CICIND 2011 and ACI: 307 - 08 the ductility ratio decreases with an increase in the percentage of steel for all stress ratios. A remarkable decrease is found in the ductility ratio at stress ratio $f_{ca}/f_{ck} = 0.025$ for all percentages of steel when compared the value of the same with a lower percentage of steel, this decrement is around 32% for all the three design standards.

In comparison with IS: 4998 - 2015, CICIND 2011 gives the higher ductility about 33.0% to 51.5% for $p_t = 0.5\%$, 30.7% to 48.7% for $p_t = 0.75\%$, 27.5% to 42.8% for $p_t = 1.5\%$ and 26.4% to 40.0% for $p_t = 2.0\%$.

In comparison with ACI: 307 - 08, CICIND 2011 gives the higher ductility about 10.4% to 26.5% for percentage of steel $p_t = 0.5\%$, 7.17% to 25.8% for $p_t = 0.75\%$, 5.02% to 24.1% for $p_t = 1.5\%$ and 6.19% to 23.3% for $p_t = 2.0\%$.

5.3 Comparison of Energy Absorption

The energy absorption is the area under the moment-curvature curve up to the chosen curvature level. Here for the comparison, the ultimate level is chosen for all three design standards. It can be seen from the tables below that the RC chimney sections designed using codal provision of CICIND 2011 in comparison with the other two codal provisions i.e. IS: 4998 - 2015 and ACI: 307 - 08 gives higher energy absorption values for all stress ratios and all percentage of steel. It can be seen that the values of energy absorption for the particular percentage of steel decrease with an increase in the axial stress ratios.

If the RC chimney section is designed as per the recommendations of IS 4998 – 2015, the energy absorption values decrease with an increase in the percentage of steel up to stress ratio 0.1 but at a higher stress ratio = 0.15 and 0.2 increase in the values of energy absorption is observed with increase in the percentage of steel as shown in Table 4.

However, it can also be observed from Table 4 that as per design methodologies of CICIND 2011 and ACI: 307 – 08 the values of energy absorption decrease with an increase in the percentage of steel for the stress ratios 0.15 and 0.2. For stress ratio of 0.1, it can be seen that with an increase in the percentage of steel, the value of energy absorption decreases according to CICIND 2011 and increases according to ACI: 307 – 08.

Table 4. Energy absorption in kN

f_{ca}/f_{ck}	p_t %											
	IS: 4998-2015				CICIND 2011				ACI: 307 – 08			
	0.5	0.75	1.5	2.0	0.5	0.75	1.5	2.0	0.5	0.75	1.5	2.0
0.025	542	476	397	378	952	842	725	704	739	730	671	650
0.05	407	382	340	332	760	703	640	635	647	639	586	579
0.1	263	257	255	250	519	508	509	522	450	452	452	462
0.15	180	183	198	208	378	384	412	435	326	331	354	371
0.2	132	140	160	173	287	299	338	365	240	249	282	304

In comparison with IS: 4998 – 2015, CICIND 2011 gives the higher energy absorption value about 43.0% to 53.9% for percentage of steel (p_t) = 0.5%, 43.4% to 53.2% for p_t = 0.75%, 45.2% to 52.5% for p_t = 1.5% and 46.2% to 52.6% for p_t = 2.0%.

In comparison with ACI: 307 – 08, CICIND 2011 gives the higher energy absorption value about 11.4% to 22.3% for percentage of steel (p_t) = 0.5%, 9.06% to 16.8% for p_t = 0.75%, 7.43% to 16.7% for p_t = 1.5% and 7.62% to 16.9% for p_t = 2.0%.

6. Conclusion

Moment-curvature ($M-\phi$) curves are plotted for hollow thin-walled tubular reinforced concrete sections like RC chimney and TV towers and from these curves, the comparison is carried out between the design recommendations for stress-strain relationship of concrete and steel plotted for IS: 4998 – 2015, ACI: 307 – 08 and CICIND 2011 in terms of strength, ductility and energy absorption.

Considerable disparities exist between the above three design codes which are used to calculate the ultimate and yield moment capacities of the tubular reinforced concrete section, subjected to lateral force and axial compression. These disparities are predominant at higher stress ratio and high steel ratio due to disparities between stress-strain models of concrete and steel adopted by the three codes.

It was concluded that up to the stress ratio of 0.15, M_u calculated from Indian standard is higher compared to the other standards, but the reduction of M_u occurs beyond this stress ratio. Even though the share of concrete is still increasing, the reduction in contribution of steel in M_u induces only a marginal increase in comparison with ACI and CICIND.

The strain limit for concrete in compression specified in the ACI: 307 – 08 and CICIND 2011 (0.003) methods are larger than those specified in the IS: 4998 - 2015 method (0.002); hence the corresponding steel stresses are also larger, both in compression and tension. But this is offset by the descending branch of the concrete stress-strain curve of the ACI: 307 – 08 method, which results in a smaller concrete stress block area.

At lower values of steel percentage, this influence of concrete is overriding; also, at higher values of steel percentage, the increased influence of steel results in ACI: 307 – 08 and CICIND 2011 predicting larger strengths than IS: 4998 – 2015, as in this code none of the steel in the tension zone reaches the yield strength whereas, in the ACI: 307 – 08 and CICIND 2011, most of the steel in the tension zone acquires the full yield strength.

It is very evident from the study that CICIND 2011 gives a comparatively higher value of area under the load-deflection of stress strain curve (i.e. moment-curvature curve) as compared to the values obtained as per codal provisions of IS: 4998 – 2015 and ACI: 307-08. As a result, the chimney sections designed using CICIND 2011 exhibit a much higher absorption capacity comparatively. Further, the value of deviation between the deformations (i.e. strain values) at ultimate strength and that at yield strength, when determined by CICIND 2011 is found to be relatively higher than the other two codes and as an outcome of this only, chimney sections designed using CICIND 2011 exhibit higher ductility as well.

Further, the plotted curves in this study ignore the tensile strength of concrete even in calculation of section properties for uncracked section. This results in the curves indicating lower initial slope (initial stiffness) as well as energy absorption. Hereby, the future scope of this study involves the comparison and differences in the stiffness and energy absorption when the tensile strength of concrete is considered and disregarded for the uncracked section. Also, the variations in the three design code further signify the need to compare the results of these theories with the results of experimental study in order to find the methodology which uses most precision in depicting the stress-strain relationship of these materials and hence, to understand the actual scenario that may occur in practice.

Acknowledgement

I would like thank Mr. Rakesh Shah, Director at S3M consultants, Ahmedabad for his guidance support by constantly informing and updating about the recent requirements in industrial discipline related to Chimneys.

References

- [1] IS: 4998 - 2015. Indian standard code of practice for design of reinforced concrete chimneys: design criteria (third revision), IS: 4998 - 2015, Bureau of Indian Standards, New Delhi.
- [2] Rai DC, Kumar K, Kaushik HB. Ultimate flexural strength of reinforced concrete circular hollow sections. *The Indian Concrete Journal*, December 2006; 80(12): 39-45.
- [3] IS: 456 - 2000. Indian standard code of practice for plain and reinforced concrete for general building construction IS: 456 - 2000, Bureau of Indian Standards, New Delhi.
- [4] IS: 11628 - 1985. Criteria for design of RCC staging for overhead water tanks, IS: 11628 - 1985, Bureau of Indian Standards, New Delhi.
- [5] IS: 4998 - 1975. Indian standard code of practice for design of reinforced concrete chimneys: part 1: design criteria (first revision), IS: 4998 - 1975, Bureau of Indian Standards, New Delhi.
- [6] Narayan KSB, Yaragal SC. Load-moment interaction envelopes for design of tall stacks - A limit state approach. *The Indian Concrete Journal*, September 2007; 81(1): 21-25.
- [7] Rao PS, Menon D. Ultimate strength of tubular RC tower sections under wind loading. *The Indian Concrete Journal*, February 1995; 69(2): 117-123.
- [8] ACI: 307 - 88. Code requirements for reinforced concrete chimneys (ACI: 307-88) and commentary, ACI: 307 - 88, American Concrete Institute, Michigan.
- [9] CICIND 1984. Model code for concrete chimneys - part A: the shell, CICIND 1984, Comite International Des Chimness Industrielle, Zurich.

- [10] DIN - 1056. Solid Construction, Free Standing Stacks; Calculation, and Design, DIN - 1056, Deutsches Institut fur Normung, Germany.
- [11] PINFOLD. G. M. 1984. Design practice. Reinforced Concrete Chimneys and Towers, 2nd edition, Viewpoint Publication, 1984: 112 - 223, ISBN 0 - 7210 - 0993 - X.
- [12] Giorgio Monti and Floriana Petrone. Yield and ultimate moment and curvature closed-form equations for reinforced concrete sections. ACI Structural Journal, July-August 2015; 112(4): 463-473. <https://doi.org/10.14359/51687747>
- [13] CICIND 2011. Model code for concrete chimneys - part A: the shell, (third edition), CICIND 2011, International Committee for Industrial Construction, Germany.
- [14] ACI: 307 - 08. Code requirements for reinforced concrete chimneys (ACI: 307-08) and commentary, ACI: 307 - 08, American Concrete Institute, Michigan.
- [15] Schueller GJ, Bucher CG. On the failure mechanisms of reinforced concrete chimneys. CICIND Report, April 1983; 13(2): 6-10.
- [16] Naokowski P. The behaviour of the compressed zone of concrete industrial chimney. 4th international symposium on industrial chimneys, The Hauge, 85-96, May 1981.
- [17] Rusch H. Researches toward a general flexural theory for structural concrete. Journal of American Concrete Institute, July 1960; 57(1): 1-28. <https://doi.org/10.14359/8009>
- [18] Ellingwood B, Galambos TV, MacGregor JC, Cornell CA. Development of a Probability Based Load Criterion for American National Standard A58, Special Publication No. 577, National Bureau of Standards, Washington D. C., 1980. <https://doi.org/10.6028/NBS.SP.577>
- [19] ACI: 318 - 2002. Building code requirements for reinforced concrete, ACI: 318 - 2002, American Concrete Institute, Michigan.
- [20] Morkin ZAR, Rumman WS. Ultimate capacity of reinforced concrete members of hollow circular sections subjected on monotonic and cyclic bending. Journal of American Concrete Institute, September-October 1985; 82(5): 653-656. <https://doi.org/10.14359/10375>
- [21] Paulson C, Rautenberg JM, Graham SK, Darwin D. Defining yield strength for non-prestressed reinforcing steel. ACI Structural Journal, January-February 2016; 113(1): 169-178. <https://doi.org/10.14359/51688199>

Blank Page



Review Article

Additive manufacturing techniques in construction

T. V. Sheeja^a, S. V. S. Jebadurai^{*b}, D. Tensing^c

Department of Civil Engineering, Karunya Institute of Technology and Sciences, Coimbatore, Tamilnadu, India

Article Info

Abstract

Article history:

Received 14 Jan 2022

Revised 01 Mar 2022

Accepted 08 Mar 2022

Keywords:

Additive

Manufacturing;

3D printing;

Rheological properties;

Extrudability;

Buildability;

Geopolymer

In recent years, additive manufacturing (AM) technology has been one of the emerging innovations in the construction industry and has significant advantages over traditional casting methods. Current scenario mainly faces some challenges upon the material composition of printable materials. Earlier studies reveal a significant lack of experimental data and validated models on additive manufacturing materials. Researches should focus on developing materials with good rheological characteristics to guarantee acceptable fresh and hardened properties. This review paper provides insight into the properties of various printable mixtures and gives proper direction to developing a systematic procedure for mixture design by assessing their extrudability, buildability, robustness and workability retention along with their hardened properties.

© 2022 MIM Research Group. All rights reserved.

1. Introduction

3D printing is a computerized method of making layer-by-layer formation of products. This is opposed to making a product by gradually extracting materials, reducing an enormous mass to a smaller one of required dimension and form, thereby giving the technology the term “additive manufacturing.” Unlike other sectors, construction of buildings, highways and almost every other construction has been an additive development technology. [1]. According to [2], future construction will be a hybrid of conventional methods and additive manufacturing technologies. This will produce large scale printed structures without the use of temporary supports. Geometrical complexity, multifunctionality and structural effects can be enabled within the printed objects through additive manufacturing technology.

As progress to conventional subtractive manufacturing, 3D objects are constructed by successively depositing materials in layers. Additive manufacturing techniques' benefits compared to traditional building processes: 1) Reduction in labor requirements and construction cost. It provides a safer environment in the construction site. 2) Providing versatility in geometry and design that would allow a more advanced method for structural and aesthetic purposes. 3) Minimize the overall project cost and time through a formwork free construction technique provided through extrusion-based additive manufacturing.

Geopolymer is a green construction material since its main ingredients collected from various industrial wastes and its usage in additive manufacturing may contribute to a more sustainable environment [3]. Alkaline activation of alumino silicate minerals produces geopolymers that are eco-friendly. Due to their mechanical performance and strong

*Corresponding author: vincent@karunya.edu

^a orcid.org/0000-0002-9820-8103; ^b orcid.org/0000-0002-9820-8103; ^c orcid.org/0000-0001-7806-001X
DOI: <http://dx.doi.org/10.17515/resm2022.386ma1401>

durability features, these materials can assist alleviate the CO₂ emission and be an efficient alternative for the construction industry, [4]. At the time of mixture proportioning of geopolymers, for a particular type of binder composition important design parameters to be considered are activator to binder ratio, molar ratio of activators and molarity of alkaline solution [5]. There is significant effect upon the nature of binders with the molar ratio of corresponding alkaline solution [6]. [7] Study reveals that there is significant effect upon the fresh and hardened properties of geopolymer mix due to the design parameters like liquid to binder ratio, mass ratio of alkaline solution and curing temperature. Geopolymerization process involves the activities like mixing up of precursors, generation of primary gel and the end production of silicate network structure [8]. Another research work concludes that [9] the addition of micro fibres like poly propylene fibres impart compressive strength to the geopolymer concrete. Durability aspects of geopolymer concrete exhibit better performance than portland cement-based materials [10].

The development of additive manufacturing technology is very fast with its wide application in various industries. As far as the construction industry is concerned, suitable printable material is critical to successful printing. This review work covers the review of chemical and physical properties of various alkaline activated cementitious materials and its corresponding fresh as well as hardened properties for usage as an extrudable 3d printable mixture through various sections that are important in technology for additive manufacturing.

2. Additive Manufacturing Techniques

The 3D printing methods commonly adopted in the construction industry can be divided into two basic categories: Extrusion Based 3D Printing (Fused Deposition Modelling) where the printable material paste is extruded through a nozzle pushed by a robot-like device to realize the layer-by-layer final product. The system includes an extruder and a printing surface, S [11]. There are two different types of systems that are used within this technology. Frame-based system and ii) Robotic arm-based system, four – axis gantry and six-axis robot printers, [12] and [13]. Another method used in AM technology is binder jetting, which uses nozzles to spray binder in the form of liquid on top of a powder bed gluing together. Until a thin layer of powder is applied, the nozzle moves according to the planned course. Finally, the stacking of layers creates a 3D object.

3. Materials for Additive Manufacturing Technology

In Additive Manufacturing technology the development of printable material is a major concern. Main challenges in the selection of proper material by considering the rheological properties for the successful extrusion, buildability, material shear strength and open time ultimately the final product being able to provide the specified safety as well as serviceability aspects through additive manufacturing technology [14]. Cost and availability of the material and properties of the printing system may also considerable while choosing the material. Preparing a compatible material for large scale 3D printer is a tedious task [15]. Major properties of novel printing mortar are flowability and buildability, achieving these two parameters simultaneously, is a difficult task for researchers, more over it is important to identify the time for which each layer has to be attain its own yield stress [16]. 3D printed structures possess both isotropic and anisotropic properties. When oriented in different directions the printed specimen exhibits variation in bond strength between layers related with the corresponding time interval required for the construction of consecutive layers, whereas in case of casted specimen which have even distribution of material properties in all directions. Characteristics like viscosity of material, printing time gap between layers and contact area between consecutive layers have strong impact on mechanical properties of the printed

materials [17]. [18] Pointed out about the necessity of large-scale additive manufacturing technology in construction industry through an automated extrusion- based process. International developments in standards for non-Portland cement, specifically on alkali activated binders, are being monitored by RILEM Technical Committee 224-AAM. This committee considered the performance-based standards rather than chemistry for the acceptance of a particular binder. It is difficult to find out performance- based standards since there is not any specific procedure for conducting experiments and validating the results for a wide range of binder system [19].

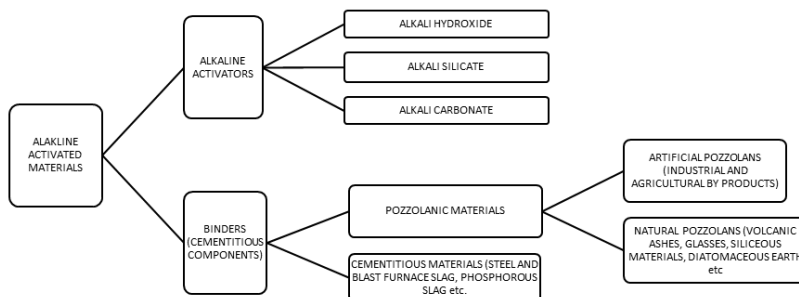


Figure 1. Process of Alkaline activated materials

The total Portland cement demand in the world is expected to rise 4.5% yearly, The production of around one ton of Ordinary Portland Cement in the atmosphere release almost one ton of CO₂. [20] and [21] used geopolymer material to minimize greenhouse gas emissions. [20] pointed out that the fundamental explanation for reducing CO₂ in geopolymer systems is the minimal amount of refined natural minerals and industrial waste to make the binding materials. Compared with Ordinary Portland Cement, the greenhouse gas emission reduced to approximately 44 to 64 % with the usage of geopolymer materials, [22]. Based on the growth and use trend, the existing limestone reserves available are projected to last only another 35-40 years. Replacement with geopolymer material in concrete construction will reduce cement consumption in concrete and provide durable and sustainable construction. Various studies have been carried out on traditional concrete mixes and propose modifications to obtain better quality concrete having both mechanical and durability requirements with advancements in technology and research. Using by-products such as fly ash (FA) and blast furnace slag (BFS) as alternative binders does not harm the climate based on the researchers' results,[23] Construction industry is in search of an alternative binding material, fly ash like geopolymer increases the performance of concrete mixes by providing better microstructure [24]. As per researchers it is important to provide fillers in concrete that enhances pozzolanic properties as well as hydration reaction[25]. Creation of geopolymers by using fly ash with alkaline activation as a construction material thus leads to sustainable and durable production by preventing the issues of fly ash disposal [26]. In recent years, alkali-activated cements have been of considerable significance for their possible use as building materials that could replace ordinary Portland cement. Performance of alkali activated materials as an alternative binder for Portland cement can reduce CO₂ emission by more than 80% [27]. Several studies reveal that alkali activated cements have exceptional mechanical properties with low density. Geopolymer foamed concrete had better thermal insulation qualities than standard Portland cement foam concrete at the

same density and strength,[28]and [29]. Figure 1 represents the Alkaline activated materials and its components.

3.1. Binders

Alkaline Activator Materials provides faster and large-scale production for a sustainable environment by reducing the amount of waste material deposited during construction [30]. For the preparation of alkali activated cementitious mortar, mainly used raw materials, exclusively aluminosilicate materials, are kaolinite, feldspar, industrial by products like fly ash, slag, mining waste etc. Reactivity towards alkaline solution depends on their chemical composition, shape, size, fineness and glassy as well as amorphous phases of solids. Raw materials used should possess highly reactive glassy contents and capable of releasing aluminium using less amount of water/binder ratio [31].

Ground granulated blast furnace slag composition includes lime and calcium magnesium aluminosilicate [32]. Addition of slag enhances the polymerization process and impart compressive strength to the product [33].

Metakaolin is an anhydrous aluminosilicate material, during the dihydroxylation process, it loses structural water and the product is in amorphous nature, which is highly reactive in presence of alkaline solution [34]. Inclusion of metakaolin demands higher binder/liquid ratio with increased surface area reduces the workability of the mix. Metakaolin is more reactive than fly ash at the time of polymerization [35].

3.2 Activators

The researcher [36] used the term ‘geopolymer’ in 1970’s to describe a class of materials which were produced by the activation of aluminosilicate powder through an alkaline solution. Some of the common binders used for making geopolymer concrete are flyash, metakaoline and blast furnace slag. Among these flyash and metakaoline are rich in aluminium and silica whereas calcium and silica are high in blast furnace slag [37]. In order to activate these type of aluminosilicate binders an alkaline medium is required, commonly used alkaline activators are alkaline hydroxide, alkaline silicates or blends of the two. The anions and cations have important role in the process of alkaline activation consequently in the characteristics of the final products Normally used anions are hydroxides, silicates, carbonates and to a lesser extent the sulfates [38]. Chemical reaction involved during activation process:



Under the polymerization of aluminosilicate in presence of highly reactive alkaline medium produces water as its one of the by products, hence it is used for improving the workability of the mixture [39]. Molarity of sodium hydroxide related with the reaction rate and strength of the final product.



Soluble silicate influences the workability, strength development and reduces the setting time for the mixture [40]. Addition of alkaline activators instead of water with binders will reduce the yield stress and increase the bond strength of mortar. [41] in their study reveals the printability of extrudable mortar using fly-ash, concurrent with the time dependent

yield stress. Metakaolin or fly-ash based alkaline activated cements produces sodium aluminosilicate hydrate gel with different Si/Al ratio whereas slag-based cements create calcium silicate hydrate gel with a low Ca/Si ratio [42].

3.3 Admixtures

Addition of admixtures impart high strength and produces high strength, durable concrete by reducing water cement ratio, [43]. Nano sized admixtures enhance the yield stress speed up the process of thixotropic shape retention property, [44]. In order to enhance the properties of alkaline activated materials ambient temperature conditions admixtures are proposed to be used, [45]. [46] in their study used nano silica as an admixture which increases the strength and durability of concrete due to its pore filling capacity. Due to its high fineness with specific surface area demands more water shows poor workability, [47]. Alccofine, an ultra-fine, amorphous material is added as an admixture in the study, [48] which is rich in calcium oxide hence produce more cementitious gel thus reduces the permeability and increase the durability of concrete. Alccofine increases the flowability and workability of mortar due to its water reducing capacity, [49]. Lignosulphate admixtures enhances workability of all type of activators while it retards the strength development, [50]. Research studies about viscosity modifying agents upon extrudable additive manufacturing technology [51], reveals that the extrusion pressure as well as buildability of printed filament increases with time moreover addition of VMA enhances yield stress and flow consistency.

4. Mix Design and Materials Composition of Alkaline Activated Geopolymer Materials

The mixture design adopted for additive manufacturing technology should have some specifications. These specifications depend on the printer equipment, the type of construction, and the conditions of the construction site. The attributes to be considered are pumpability, extrudability and buildability when designing the mixture design of concrete for a printer. [52]. They also emphasized the effect of admixtures and their interaction on rheological and mechanical properties [53]. In order to formulate an alkaline activated binder, it is necessary to determine the amount of reactive phase of precursors. Mainly used precursors in alkali activated cements are metakaolin, fly ash (class-f, class-c), silica fume and ground granulated blast furnace slag. Binders like metakaolin and class-F fly ash are rarely pure and having non-active crystalline phase in a basic environment with low solubility whereas slags are having fairly similar chemical composition and equivalent fineness, [54].

Activators are necessary for the polymeric reaction of aluminosilicate binders. Mainly used activators are alkali hydroxides, alkali silicates, alkali carbonates and alkali sulphates. Formulation of alkali activated materials depends upon the variety of precursors and suitable activators moreover the role of water depending on this precursor/activator couple

Buildability of the extrudable cement mortar with varying printer parameters are in direct relationship towards the force of attraction between the inter particle, particle size and its arrangement within the material, [55]. [56] in their studies found out that the increase in molarity of NaOH will make a viscous alkaline solution and produce better cohesive mixture with increased inter particle repulsion, hence it possible for the production of an extrudable mixture. [57], discovered in their study that yield stress values of a mortar related with the square of d_{50} . [58], have conducted a study by replacing certain % of fly ash with fine lime stone as filler material to increase the inter particle contact and hence support the overburden pressure for the suitable printability of mortar [59] analyzed the rheological properties of mortar containing fly ash and ground granulated blast furnace

slag, concludes that up to 50% addition of slag not at all improving any rheological properties of fresh mortar in the time range of 0 to 25 minutes. Further addition of slag shows increments in yield stress accompanied by a decrease in consistency.

[60] concludes in their study about the effect of ground granulated blast furnace slag mixed with fly ash, that addition of slag maintains inverse relation with workability due to the angular shape of the slag and accelerated reaction rate of calcium when compared to fly ash and it enhances the setting of mortar. Different researchers developed different geopolymer mixes for 3D printing. A few of the designed combinations and the properties considered for designing are summarized in Table 1.

Table 1. Design strategies in research for printable Geopolymer concrete mix

SI No	Title with Author	Materials used			Activators	Primary Findings	Conclusion
		Binders	Aggregates	Admixtures			
1	The study of the structure rebuilding and yield stress of 3D printing geopolymer pastes [61]	Blast Furnace Slag, Steel Slag	Sand	defoamer, super-plasticizer, and re dispersible latex	NaOH & Na ₂ SiO ₃	Addition of NaOH speed up the process of geo polymerization and rebuilding capacity.	Increment in Si/Na ratio causes a decrement in yield stress development hence in the structural rebuilding also.
2	Additive manufacturing of geopolymer for sustainable built environment [30]	Class-F-Fly ash, GGBFS and Silica Fume	River Sand	Thixotropic Filler	KOH & K ₂ SiO ₃	Plotted torque- speed graph using rheometer, and hence measured the thixotropy of mix.	Decrease of thixotropy over time indicates the open time for the material. Below this minimum value of thixotropy, material is not suitable for large scale printing
3	Experimental study on mix proportion and fresh properties of fly ash based geopolymer for 3D concrete printing[62]	Class-F-Fly ash, GGBFS and Silica Fume	River Sand	Micro glass fiber & Attapulgite clay	K ₂ SiO ₃ & NaOH	Find out the favorable yield stress value for smooth extrusion.	Novel 3D printable geo polymer mortar was developed for printing non- structural polymer mortar was developed for printing non-structural building components.
4	Optimization of mixture properties for 3D printing of geopolymer concrete [63]	Class-F-Fly ash, GGBFS and Silica Fume	River Sand	-	Sodium meta silicate powder	Increase in activator dosage speed up the reaction rate, yield stress and lower the setting time. Samples with lower % of activator shows higher strength.	Material properties like rheology, open time, compressive strength and printing parameters like pumping pressure, printing speed were studied to achieve a successful geopolymer mixture for 3D printing.
5	3D Printing of geopolymer Concrete [64]	Class-F-Fly ash, GGBFS and Silica Fume	River Sand	Actigel	NaOH & Na ₂ SiO ₃	-	Addition of higher % of GGBFS shows a linear increment in compressive strength and exponential decrement in setting time. Introduction of actigel enhances the rheological properties of the mixture.
6	Fresh and hardened	Class-F-Fly ash,	River Sand	Actigel,	KOH & K ₂ SiO ₃	-	To ensure better pumpability,

	properties of 3D printable cementitious materials for building and construction [65]	GGBFS and Silica Fume		Bentonite Sodium lingo sulfonate			thixotropic value should be more than 10000Nmm rpm.
7	Effect of 3D printing on mechanical properties of fly ash-based inorganic geopolymer [66]	Class-F-Fly ash, GGBFS and Silica Fume	River Sand	Thixotropic additives	K ₂ SiO ₃ & H ₂ O	-	In order to provide colloidal interaction in geopolymer (like OPC), thixotropic c additives are helpful to improve printing performances without disturbing the geopolymer mechanism
8	Method of optimization for ambient temperature cured sustainable geopolymers for 3D printing construction applications [67]	FA and Slag	Sand	Anhydrous borax (retarder), sodium carboxy methyl cellulose (VMA)	Combination on of sodium silicate and potassium silicate & Sodium hydroxide & potassium hydroxide	Initial and final setting time significantly reduced, from 295 minutes to 45 minutes (25%)	Formation of additional geopolymeric gel along with C-S-H may be the reason for Accelerated setting.
9	Rheology and Mechanical Properties of Fly Ash-Based Geopolymer Mortars with Ground Granulated Blast Furnace Slag Addition [59]	FA and Slag	Siliceous sand	-	Sodium silicate solution, sodium hydroxide pellets and water	content of GGBFS in the range up to 50 wt.% did not significantly alter the rheology of geopolymer mortars within the time rage from 0 to 25 min the increase in GGBFS content was accompanied by a decrease in consistency	Tests of mechanical properties show a clear increase in strength together with an increase in the amount of GGBFS
10	Mix design and fresh properties for high-performance printing concrete [68]	Cement, Fly ash & Silica fume	Sand	Retarder, formed by amino-tris, citric acid and formaldehyde and accelerator, formed by	Water	Optimum mix corresponds to the binder content of 40% with 1 to 2 % of super plasticizer dosage.	Shear strength controlled by the usage of super plasticizer. By adding micro scale polypropylene fibers to the mix at the rate of 1.2kg/m ³ , compressive strength reached more than 100 MPa.

				sulphuric, aluminium salt and diethanolamine.			
11	Mechanical properties of layered geopolymer structures applicable in concrete 3D printing [69]	Fly ash	Sand	Steel and poly Propylene fibres	NaOH & Na ₂ SiO ₃	Addition of 1% of steel fiber reduces the workability by 4% and increases the flexural strength by 20%.	Addition of steel fiber causes bond separation issues and polypropylene fibres decreases the workability.
12	Design 3D printing cementitious materials via Fuller Thompson theory and Marson-Percy model [70]	OPC, Flyash & silica fume	Silica sand	Super plasticizer	Water	Printing with continuous sand gradation mix able to print more layers without any significant deterioration, indicates strong interfacial bond.	Mixes with continuous sand gradation possess higher yield stress and lower viscosity in comparison with uniform sand gradation
13	Fresh properties of a novel 3D printing concrete ink[15]	OPC, Fly ash and Silica fume	Sand	Nano clay, Poly carboxylate e-based high range water reducer	Water	-	Effect of small replacement of cement in concrete by fly ash and silica fume enhances the thixotropic behavior of concrete leads to improved buildability.
14	Process Development of Fly Ash-Based Geopolymer Mortars in View of the Mechanical Characteristics [7]	Fly ash (two types)	sand	-	Sodium silicate solution, sodium hydroxide pellets and water		The highest compressive strength was 60.1 MPa for the geopolymer manufactured with an Liquid/Solid of 0.2 and Na ₂ SiO ₃ /NaOH ratio of 2. The best thermal curing temperature for obtaining optimal strength characteristics was 100 °C .
15	Effect of molarity of sodium hydroxide and molar ratio of alkaline activator solution on the strength development of geopolymer concrete [6]	Fly ash (two types)	sand	-	Sodium silicate solution, sodium hydroxide pellets and water		16M NaOH yields high compressive strength when SiO ₂ /Na ₂ O in Na ₂ SiO ₃ solution is around 2.00 to 2.40 and Na ₂ SiO ₃ /NaOH=2.5.

5. Properties of Printable Geopolymer Concrete

5.1 Fresh Properties

Printing parameters such as flowability of the extrudable material, printing speed, printing time gap between the consecutive layers etc. have remarkable influence on the final printed object, [71]. To develop proper mix design for printable material extrudability, buildability and workability retention are the essential parameters. The material should possess high yield stress for buildability (high yield stress allows deposition of top layers without causing much deformation of bottom layer) and at the same time, the printable material should be below viscous nature to enable extrudability.

5.1.1 Extrudability

From the analysis of various studies among additive manufacturing extrusion technology, it is revealed that the mixes that are designed for 3D printing need to be extruded through a nozzle to attain the required shape. Extrusion is graded by [72] as full-width printing and filament printing based on layering technique, depending on the rheological properties of the material and geometric configurations of the extruder. Extrusion is so important for further performance; monitoring for real-time efficiency is suggested by [73] by a vision-based technique. 2D images are analyzed in this system, and the reliability of the system was checked by providing various materials.

[62] analyzed the extrudability of geopolymer mortar. Clogging is seen in the study. It will impart the higher yield stress developed due to friction generated between fine aggregates and the importance of further rheological study in geopolymer concrete. The high static yield stress can negatively affect the extrudability, and high pressure is needed to initiate the flow, but not always as cautioned in the study. The fly ash and ground granulated blast furnace slag (GGBS) quantity are varied in geopolymer to vary the thixotropy open time (TOT) for selecting an extrudable mix with the property of shape retention. Study reveals that further modelling is needed to understand extrusion fundamentals with different types of materials and structures.

The extrudability of printable geopolymer pastes are studied by [61] Extrudability is connected to its transition from the mixing system to the printing system. The study concludes that it is safer to decrease the Si/Na ratio of alkali activator to increase the potential of structure reconstruction.

[65] analyzed the properties of printable geopolymers and cementitious materials through his work. In this study to improve the workability and extrudability of mixes, bentonite clay is used as a rheological modifier, and alkaline solutions are used to activate the binders. Results conclude that the geopolymer mix has a higher viscosity in plastic stage than mixtures with cement.

5.1.2 Buildability

3D printable concrete buildability is defined as extruded layers' ability to maintain the printed shape and carry the weight of following layers without failure. The rheological behavior of concrete governs a large part of its buildability property, [53]. The bottom layer is subject to the most challenging load during the time of printing. To ensure the stability of construction until the open time the key factors for maintaining layer-by-layer load are yield stress and structure reconstruction [74].

Different publications on the rheology of geopolymer, [75] mentioned that geopolymer does not have colloidal contact like cement-based materials. Due to the use of the potassium silicate reagent's extremely vicious existence, the hydrodynamic effect will be there in the geopolymer material, therefore, in the analysis, [19] added some nano-clay (attapulgitite), compatible with the geopolymer material, to enhance this thixotropic property. It is noted that the internal structural built-up value increased with the addition of clay to mix, causing no problems such as clogging, discontinuity, etc. [61] observed that the interlayer force has a vital role in the buildability of

paste in printing process of geopolymer material. Study reveals that the inclusion of alkali activator significantly influenced the rebuilding potential of the paste. This will accelerate the polymerization thus the coagulation of the mixture improves and acquires a greater degree of structure recovery.

5.1.3 Open Time

Another important fresh property of concrete for 3D printing is open-time. There is an optimum time for the printed layer to get initial strength to hold subsequent layers but still wet so the layers can fuse together before final setting, [63]. The open-time is connected to the concrete's initial setting time. A sufficient open time is required to support subsequent layers [68]

[63], developed geopolymer mix with fly ash, slag silica fume and Sodium meta-silicate powder were used as the activator, research work it can be seen that higher wt.% of the activator results in considerably lower setting time because of a faster reaction, higher pH and a higher rate of dissolution of particles. Also, a higher w/s ratio causes prolonged setting time by lowering the pH and dissolution rate and reaction rate. Brief setting time (open-time), although giving the sign of getting strength quickly to support the subsequent layers, can result in less adhesion (fusion) between layers and most importantly the mixture can lose workability for printing very quickly.

In the research work, rather than adding an accelerator/retarder, [19] added various percent of fly ash with GGBS to get difference in open time, and noticed over time by adjusting the ability to structural built up for the chosen mix having extrudability and shape retention capacity. Other researchers have found that an improvement in GGBS typically reduces the setting time, [76] As per [19] observed a similar pattern of increasing the percentage of slag, increasing structural built up over time, which reversely affects the extrusion process.

5.1.4 Rheology

Rheology of the concrete mix (deformation of the flow of material) affects the material's extrudability and buildability. Study of [77] concludes that the rheological behavior of the mortar mix is affected by the relationship between shear stress and shear rate, termed as flow curve, can be analyzed with rheometers, Factors such as granular contacts (tribology), delivery and placement, which decides the pumpability and buildability are affected by the material and equipment parameters, [53]. By measuring the rheological properties of a mixture at various time intervals and comparing it with the open time test, the plastic viscosity and shear stress will provide data on the maximum time values needed for good extrudability.

Unlike Portland cement, the rheological behavior of the alkali-activated materials (geopolymer) is less well known. This is due to the complexity of the chemical environment and reactions taking place and the different physical properties of the main precursors. For example, an alkali silicate-activated slag has a too complicated solution environment with high ionic strength and alkalinity, which is a very challenging environment in understanding rheological behavior, [63] Rheology modifiers such as common superplasticizers (that improves workability without increasing w/s) in Portland-cement based materials not so good in geopolymer materials, [78]. In the research paper, [61] found that geopolymerization requires an alkali activation. The increase of Na ion can speed up the process of dissolution of aluminosilicate source, [79]. [62] noted that GGBS did not give a significant rheological change, affecting the material's time-dependent structural built-up capacity by reducing paste setting time. Therefore, who should carefully regulate the composition of the mixture, thus maintaining a reasonable final strength level but the addition of silica fume in the fresh stage has been useful in regulating the rheological parameters of the mixture. Silica fumes particles having high surface area, which allowed the blend to be smoothly extruded through the deposited filaments and hence shape retention capacity.

[65] concludes through the study that no special relationship exists among the rheological parameters of printable material. For better pumpability for the printable material, thixotropy

value should be more than 10000Nmm rpm. In geopolymer mortar design, [65] applied Acti-gel, since it has the property to provide a mixture with shape stability. It can minimize shear stress through a nozzle during the extruding process and increase the extruded mixture's buildability. By measuring the rheological properties of a mix with different time intervals, particularly the plastic viscosity, it can provide information on the maximum time values needed for good extrudability.

5.2 Hardened Properties

The mechanical properties such as compressive strength, flexural strength, and tensile bond strength must be adequate for a printed structure, in addition to the fresh properties of the geopolymer mixtures for good printing.[63] analyzed that samples with a lower percentage of the activator showed higher strength than the models with higher % of the activator. Lower alkalinity drive formation of a particular geopolymer gel which increases the mechanical performance. Also, higher w/s results typically in lower strength of geopolymers. The samples with higher % of the activator, instead of having faster reaction initiated by lower initial setting time and faster changes in workability (higher rate of increased yield stress vs time), showed lower compressive strength. [80], mentioned in their studies that compressive strength is in direct relation with the molarity of sodium hydroxide when the mortar is prepared with fly ash and slag. [65] concludes that printing parameters such as nozzle orifice shape, printed object complexity etc. influence printed specimens' mechanical properties. Through the research work, [19] reported that the printed sample shows greater compressive strength when load is applied normal to the specimen whereas in flexural test, results are less when loading in the same direction. Results imply that the force of attraction between the layer is less compared with the force along the layers. Another major parameter is the tensile bond strength which is directly influenced by the open time.

6. Conclusion

Geopolymer is a new environmentally friendly cementitious material, and its development has the potential to reduce carbon dioxide emissions caused by the growth of the cement industry. The current analysis analyzed important advancements in geopolymer technology in the construction industry, as well as recent discoveries and future research directions. This topic has piqued the interest of numerous academics over the last decade as a potentially efficient alternative to typical Portland cement-based binders in terms of both technological qualities and environmental sustainability. The increasing number of research publications by years reveals that additive manufacturing technology is a part of industry 4.0. In terms of technological innovation and applicability, significant progress was accomplished as well. One of the most noteworthy achievements achieved is the ability to change geopolymer mixes for sophisticated Additive Manufacturing techniques, which opens up new design flexibility for engineer optimization in the construction industry. In this context, more research is needed to better understand how 3D printing technology might be used to produce effective geopolymer-based applications in the building–architectural disciplines. This state of art paper gives a systematic review of Additive manufacturing techniques and the development of printable material. The effect of several parameters, the type of binders, alkaline activators, admixtures and the binder activator mix ratio on workability, flowability, extrudability, shape retention ability and the mechanical properties of printable alkaline activator mortar. In order to be used in 3D printing of alkali-activated and geopolymer materials, significant rheological development is necessary. Also investigate additive manufacturing technology and critical issues in developing AAM printable materials. For an Additive Manufacturing printed concrete structure with adequate structural and serviceable performance, proper control must be there at the time of material selection, relevant parameters in the mixture design and printing process. For the acceptance of additive manufacturing technology as a construction technology standardization and specification for materials and methods and proper structural design procedures are required.

References

- [1] Khan MS, Sanchez F, Zhou H. 3-D printing of concrete: Beyond horizons. *Cement and Concrete Research*, 2020;133:106070. <https://doi.org/10.1016/j.cemconres.2020.106070>
- [2] Gosselin C, Duballet R, Roux P, Gaudillière N, Dirrenberger J, Morel P. Large-scale 3D printing of ultra-high-performance concrete-a new processing route for architects and builders. *Materials & Design*, 2016;100:102-9. <https://doi.org/10.1016/j.matdes.2016.03.097>
- [3] Farooq F, Jin X, Javed MF, Akbar A, Shah MI, Aslam F, Alyousef R. Geopolymer concrete as sustainable material: A state of the art review. *Construction and Building Materials*, 2021;306:124762. <https://doi.org/10.1016/j.conbuildmat.2021.124762>
- [4] Youssef N, Rabenantoandro AZ, Lafhaj Z, Dakhli Z, Hage Chehade F, Ducoulombier L. A novel approach of geopolymer formulation based on clay for additive manufacturing. *Construction Robotics*, 2021;5(2):175-90. <https://doi.org/10.1007/s41693-021-00060-1>
- [5] Naghizadeh A, Ekolu SO. Method for comprehensive mix design of fly ash geopolymer mortars. *Construction and Building Materials*, 2019;202:704-17. <https://doi.org/10.1016/j.conbuildmat.2018.12.185>
- [6] Reddy VS, Karnati VK, Rao MS, Shrihari S. Effect of molarity of sodium hydroxide and molar ratio of alkaline activator solution on the strength development of geopolymer concrete. In *E3S Web of Conferences EDP Sciences*. 2021; 309. <https://doi.org/10.1051/e3sconf/202130901058>
- [7] Öz HÖ, Doğan-Sağlamtimur N, Bilgil A, Tamer A, Günaydin K. Process Development of Fly Ash-Based Geopolymer Mortars in View of the Mechanical Characteristics. *Materials*, 2021;14(11):2935. <https://doi.org/10.3390/ma14112935>
- [8] Cong P, Cheng Y. Advances in geopolymer materials: A comprehensive review. *Journal of Traffic and Transportation Engineering (English Edition)*. 2021;8(3):283-314. <https://doi.org/10.1016/j.jtte.2021.03.004>
- [9] Al-Kerttani OM, Mutar A. Studying the behavior of geopolymer concretes under repeated loadings. *Journal of Engineering and Applied Science*, 2021;68(1):1-2. <https://doi.org/10.1186/s44147-021-00013-z>
- [10] Sambucci M, Sibai A, Valente M. Recent advances in geopolymer technology. A potential eco-friendly solution in the construction materials industry: A review. *Journal of Composites Science*, 2021; 5(4):109. <https://doi.org/10.3390/jcs5040109>
- [11] Sri Harsha A, Vikram Kumar CR. Fused Deposition Modeling of an Aircraft Wing using Industrial Robot with Non-linear Tool Path Generation. *International Journal of Engineering*, 2021;34(1):272-82. <https://doi.org/10.5829/ije.2021.34.01a.30>
- [12] Wolfs RR. 3D printing of concrete structures.
- [13] Nerella VN, Mechtcherine V. Studying the printability of fresh concrete for formwork-free concrete onsite 3D printing technology (CONPrint3D). In *3D Concrete Printing Technology*, Butterworth-Heinemann 2019;333-347. <https://doi.org/10.1016/B978-0-12-815481-6.00016-6>
- [14] Van Zijl GP, Paul SC, Tan MJ. Properties of 3D printable concrete. In *Proceedings of the 2nd International Conference on Progress in Additive Manufacturing*, 2016;421-426.
- [15] Zhang Y, Zhang Y, Liu G, Yang Y, Wu M, Pang B. Fresh properties of a novel 3D printing concrete ink. *Construction and building materials*, 2018;174:263-71. <https://doi.org/10.1016/j.conbuildmat.2018.04.115>
- [16] Bhattacharjee S, Santhanam M. Enhancing buildability of 3D printable concrete by spraying of accelerating admixture on surface. In *RILEM International Conference on Concrete and Digital Fabrication*, Springer, Cham. 2020; 13-22. https://doi.org/10.1007/978-3-030-49916-7_2
- [17] Tay YW, Panda B, Paul SC, Noor Mohamed NA, Tan MJ, Leong KF. 3D printing trends in building and construction industry: a review. *Virtual and Physical Prototyping*, 2017; 12(3): 261-76. <https://doi.org/10.1080/17452759.2017.1326724>

- [18] Lim S, Buswell RA, Le TT, Austin SA, Gibb AG, Thorpe T. Developments in construction-scale additive manufacturing processes. *Automation in construction*, 2012;21:262-8. <https://doi.org/10.1016/j.autcon.2011.06.010>
- [19] Juenger MC, Winnefeld F, Provis JL, Ideker JH. Advances in alternative cementitious binders. *Cement and concrete research*, 2011;41(12):1232-43. <https://doi.org/10.1016/j.cemconres.2010.11.012>
- [20] Aldin Z, Nedeljković M, Luković M, Liu J, Blom K, Ye G. Optimization of a geopolymer mixture for a reinforced cantilever concrete bench. In 9th International Symposium on Cement and Concrete: 9th International Symposium on Cement and Concrete 2017.
- [21] McLellan BC, Williams RP, Lay J, Van Riessen A, Corder GD. Costs and carbon emissions for geopolymer pastes in comparison to ordinary portland cement. *Journal of cleaner production*, 2011;19(9-10):1080-90. <https://doi.org/10.1016/j.jclepro.2011.02.010>
- [22] Muttashar M, Lokuge W, Karunasena W. Geopolymer concrete: the green alternative with suitable structural properties. In Proceedings of the 23rd Australasian Conference on the Mechanics of Structures and Materials (ACMSM23), Southern Cross University. 2014; 101-106.
- [23] Brăduț AI, Lăzărescu AV, Hegyi A. The Possibility of Using Slag for the Production of Geopolymer Materials and Its Influence on Mechanical Performances-A Review. In The 14th International Conference Interdisciplinarity in Engineering-INTER-ENG 2020 2021; 107.
- [24] Rath B, Deo S, Ramtekkar G. Durable glass fiber reinforced concrete with supplementary cementitious materials. *International Journal of Engineering*, 2017;30(7):964-71. <https://doi.org/10.5829/ije.2017.30.07a.05>
- [25] Ghanbari M, Kohnehpooshi O, Tohidi M. Experimental study of the combined use of fiber and nano silica particles on the properties of lightweight self-compacting concrete. *International Journal of Engineering*, 2020;33(8):1499-511. <https://doi.org/10.5829/ije.2020.33.08b.08>
- [26] Doğan-Sağlamtimur N, Öz HÖ, Bilgil A, Vural T, Süzgeç E. The effect of alkali activation solutions with different water glass/NaOH solution ratios on geopolymer composite materials. In IOP Conference Series: Materials Science and Engineering 2019; 660(1) 012003. <https://doi.org/10.1088/1757-899X/660/1/012003>
- [27] Duxson P, Provis JL, Lukey GC, Van Deventer JS. The role of inorganic polymer technology in the development of 'green concrete'. *cement and concrete research*, 2007; 37(12):1590-7. <https://doi.org/10.1016/j.cemconres.2007.08.018>
- [28] Zhang Z, Provis JL, Reid A, Wang H. Mechanical, thermal insulation, thermal resistance and acoustic absorption properties of geopolymer foam concrete. *Cement and Concrete Composites*, 2015;62:97-105. <https://doi.org/10.1016/j.cemconcomp.2015.03.013>
- [29] Cheng-Yong H, Yun-Ming L, Abdullah MM, Hussin K. Thermal resistance variations of fly ash geopolymers: foaming responses. *Scientific reports*, 2017; 7(1):1-1. <https://doi.org/10.1038/srep45355>
- [30] Panda B, Paul SC, Hui LJ, Tay YW, Tan MJ. Additive manufacturing of geopolymer for sustainable built environment. *Journal of cleaner production*, 2017;167:281-8. <https://doi.org/10.1016/j.jclepro.2017.08.165>
- [31] Singh B, Ishwarya G, Gupta M, Bhattacharyya SK. Geopolymer concrete: A review of some recent developments. *Construction and building materials*, 2015;85:78-90. <https://doi.org/10.1016/j.conbuildmat.2015.03.036>
- [32] Bakharev T, Sanjayan JG, Cheng YB. Resistance of alkali-activated slag concrete to alkali-aggregate reaction. *Cement and Concrete Research*, 2001;31(2):331-4. [https://doi.org/10.1016/S0008-8846\(00\)00483-X](https://doi.org/10.1016/S0008-8846(00)00483-X)
- [33] Goriparthi MR, TD GR. Effect of fly ash and GGBS combination on mechanical and durability properties of GPC. *Advances in concrete construction*, 2017;5(4):313.
- [34] Jagtap SA, Shirsath MN, Karpe SL. Effect of metakaolin on the properties of concrete. *International Research Journal of Engineering and Technology*, 2017;4(7):643-5.

- [35] Zhang HY, Kodur V, Qi SL, Cao L, Wu B. Development of metakaolin-fly ash based geopolymers for fire resistance applications. *Construction and Building Materials*, 2014;55:38-45. <https://doi.org/10.1016/j.conbuildmat.2014.01.040>
- [36] Davidovits J. Geopolymers: inorganic polymeric new materials. *Journal of Thermal Analysis and calorimetry*, 1991;37(8):1633-56. <https://doi.org/10.1007/BF01912193>
- [37] Nedeljković M, Luković M, van Breugel K, Hordijk D, Ye G. Development and application of an environmentally friendly ductile alkali-activated composite. *Journal of Cleaner Production*, 2018;180:524-38. <https://doi.org/10.1016/j.jclepro.2018.01.162>
- [38] Glukhovskiy VD. Ancient, modern and future concretes. *Proceedings of the First International Conference on Alkaline Cements and Concretes*, Kiev, Ukraine. 1994; 1-9.
- [39] Davidovits J, editor. *Geopolymer, green chemistry and sustainable development solutions: proceedings of the world congress geopolymer 2005*, Geopolymer Institute; 2005.
- [40] Pacheco-Torgal F. Introduction to handbook of alkali-activated cements, mortars and concretes. In *Handbook of alkali-activated cements, mortars and concretes*, Woodhead Publishing; 2015; 1-16. <https://doi.org/10.1533/9781782422884.1>
- [41] Alghamdi H, Nair SA, Neithalath N. Insights into material design, extrusion rheology, and properties of 3D-printable alkali-activated fly ash-based binders. *Materials & Design*, 2019;167:107634. <https://doi.org/10.1016/j.matdes.2019.107634>
- [42] Duxson P, Fernández-Jiménez A, Provis JL, Lukey GC, Palomo A, van Deventer JS. Geopolymer technology: the current state of the art. *Journal of materials science*, 2007;42(9):2917-33. <https://doi.org/10.1007/s10853-006-0637-z>
- [43] Kurdowski W. *Cement and concrete chemistry*. Springer Science & Business; 2014. <https://doi.org/10.1007/978-94-007-7945-7>
- [44] Sikora P, Chougan M, Cuevas K, Liebscher M, Mechtcherine V, Ghaffar SH, Liard M, Lootens D, Krivenko P, Sanytsky M, Stephan D. The effects of nano- and micro-sized additives on 3D printable cementitious and alkali-activated composites: A review. *Applied Nanoscience*, 2021;1-9. <https://doi.org/10.1007/s13204-021-01738-2>
- [45] Jindal BB. Investigations on the properties of geopolymer mortar and concrete with mineral admixtures: A review. *Construction and building materials*, 2019;227:116644. <https://doi.org/10.1016/j.conbuildmat.2019.08.025>
- [46] Zhang MH, Islam J, Peethamparan S. Use of nano-silica to increase early strength and reduce setting time of concretes with high volumes of slag. *Cement and Concrete Composites*, 2012;34(5):650-62. <https://doi.org/10.1016/j.cemconcomp.2012.02.005>
- [47] Aggarwal P, Singh RP, Aggarwal Y. Use of nano-silica in cement based materials-A review. *Cogent Engineering*, 2015;2(1):1078018. <https://doi.org/10.1080/23311916.2015.1078018>
- [48] Jindal BB, Singhal D, Sharma S, Yadav A, Shekhar S, Anand A. Strength and permeation properties of alccofine activated low calcium fly ash geopolymer concrete. *Comput. Concrete*, 2017;20(6):683-8.
- [49] Jindal BB. Investigations on the properties of geopolymer mortar and concrete with mineral admixtures: A review. *Construction and building materials*, 2019 227:116644. <https://doi.org/10.1016/j.conbuildmat.2019.08.025>
- [50] Bakharev T, Sanjayan JG, Cheng YB. Effect of admixtures on properties of alkali-activated slag concrete. *Cement and Concrete Research*, 2000; 30(9): 1367-74. [https://doi.org/10.1016/S0008-8846\(00\)00349-5](https://doi.org/10.1016/S0008-8846(00)00349-5)
- [51] Chen Y, Chaves Figueiredo S, Yalçinkaya Ç, Çopuroğlu O, Veer F, Schlangen E. The effect of viscosity-modifying admixture on the extrudability of limestone and calcined clay-based cementitious material for extrusion-based 3D concrete printing. *Materials*, 2019;12(9):1374. <https://doi.org/10.3390/ma12091374>
- [52] Wangler T, Roussel N, Bos FP, Salet TA, Flatt RJ. Digital concrete: a review. *Cement and Concrete Research*, 2019;123:105780. <https://doi.org/10.1016/j.cemconres.2019.105780>
- [53] Bhattacharjee S, Rahul AV, Santhanam M. 3D Printing-Progress Worldwide. *Indian Concr. J*, 2020;94:8-25.

- [54] Pouhet R, Cyr M. Alkali-silica reaction in metakaolin-based geopolymer mortar. *Materials and Structures*, 2015;48(3):571-83. <https://doi.org/10.1617/s11527-014-0445-x>
- [55] Flatt RJ, Bowen P. Yodel: a yield stress model for suspensions. *Journal of the American Ceramic Society*, 2006;89(4):1244-56. <https://doi.org/10.1111/j.1551-2916.2005.00888.x>
- [56] Vance K, Dakhane A, Sant G, Neithalath N. Observations on the rheological response of alkali activated fly ash suspensions: the role of activator type and concentration. *Rheologica Acta*, 2014;53(10):843-55. <https://doi.org/10.1007/s00397-014-0793-z>
- [57] Nair SA, Alghamdi H, Arora A, Mehdipour I, Sant G, Neithalath N. Linking fresh paste microstructure, rheology and extrusion characteristics of cementitious binders for 3D printing. *Journal of the American Ceramic Society*, 2019;102(7):3951-64. <https://doi.org/10.1111/jace.16305>
- [58] Vance K, Arora A, Sant G, Neithalath N. Rheological evaluations of interground and blended cement-limestone suspensions. *Construction and Building Materials*, 2015;79:65-72. <https://doi.org/10.1016/j.conbuildmat.2014.12.054>
- [59] Sitarz M, Urban M, Hager I. Rheology and mechanical properties of fly ash-based geopolymer mortars with ground granulated blast furnace slag addition. *Energies*, 2020 Jan;13(10):2639. <https://doi.org/10.3390/en13102639>
- [60] Deb PS, Nath P, Sarker PK. The effects of ground granulated blast-furnace slag blending with fly ash and activator content on the workability and strength properties of geopolymer concrete cured at ambient temperature. *Materials & Design (1980-2015)*, 2014 Oct 1;62:32-9. <https://doi.org/10.1016/j.matdes.2014.05.001>
- [61] Zhang DW, Wang DM, Lin XQ, Zhang T. The study of the structure rebuilding and yield stress of 3D printing geopolymer pastes. *Construction and Building Materials*, 2018 Sep 30;184:575-80. <https://doi.org/10.1016/j.conbuildmat.2018.06.233>
- [62] Panda B, Tan MJ. Experimental study on mix proportion and fresh properties of fly ash based geopolymer for 3D concrete printing. *Ceramics International*, 2018 Jun 15;44(9):10258-65. <https://doi.org/10.1016/j.ceramint.2018.03.031>
- [63] Kashani A, Provis JL, Qiao GG, van Deventer JS. The interrelationship between surface chemistry and rheology in alkali activated slag paste. *Construction and Building Materials*, 2014;65:583-91. <https://doi.org/10.1016/j.conbuildmat.2014.04.127>
- [64] Aldin Z. 3D Printing of geopolymer concrete. Master Thesis, Delft University of Technology 2019.
- [65] Paul SC, Tay YW, Panda B, Tan MJ. Fresh and hardened properties of 3D printable cementitious materials for building and construction. *Archives of civil and mechanical engineering*, 2018;18(1):311-9. <https://doi.org/10.1016/j.acme.2017.02.008>
- [66] Panda B, Mohamed NA, Tan MJ. Effect of 3d printing on mechanical properties of fly ash-based inorganic geopolymer. *International Congress on Polymers in Concrete*, Springer, Cham. 2018; 509-515. https://doi.org/10.1007/978-3-319-78175-4_65
- [67] Bong SH, Nematollahi B, Nazari A, Xia M, Sanjayan J. Method of optimisation for ambient temperature cured sustainable geopolymers for 3D printing construction applications. *Materials*, 2019;12(6):902. <https://doi.org/10.3390/ma12060902>
- [68] Le TT, Austin SA, Lim S, Buswell RA, Gibb AG, Thorpe T. Mix design and fresh properties for high-performance printing concrete. *Materials and structures*, 2012;45(8):1221-32. <https://doi.org/10.1617/s11527-012-9828-z>
- [69] Al-Qutaifi S, Nazari A, Bagheri A. Mechanical properties of layered geopolymer structures applicable in concrete 3D-printing. *Construction and Building Materials*, 2018 Jul 10;176:690-9. <https://doi.org/10.1016/j.conbuildmat.2018.04.195>
- [70] Weng Y, Li M, Tan MJ, Qian S. Design 3D printing cementitious materials via Fuller Thompson theory and Marson-Percy model. *Construction and Building Materials*, 2018;163:600-10. <https://doi.org/10.1016/j.conbuildmat.2017.12.112>
- [71] Lewandowski JJ, Seifi M. Metal additive manufacturing: a review of mechanical properties. *Annual review of materials research*, 2016;46:151-86. <https://doi.org/10.1146/annurev-matsci-070115-032024>

- [72] Nerella VN, Krause M, Mechtcherine V. Practice-oriented buildability criteria for developing 3D-printable concretes in the context of digital construction. 2018. <https://doi.org/10.20944/preprints201808.0441.v1>
- [73] Kazemian A, Yuan X, Davtalab O, Khoshnevis B. Computer vision for real-time extrusion quality monitoring and control in robotic construction. *Automation in Construction*, 2019;101:92-8. <https://doi.org/10.1016/j.autcon.2019.01.022>
- [74] Lloret E, Shahab AR, Linus M, Flatt RJ, Gramazio F, Kohler M, Langenberg S. Complex concrete structures: Merging existing casting techniques with digital fabrication. *Computer-Aided Design*, 2015;60:40-9. <https://doi.org/10.1016/j.cad.2014.02.011>
- [75] Favier A, Hot J, Habert G, Roussel N, de Lacaillerie JB. Flow properties of MK-based geopolymer pastes. A comparative study with standard Portland cement pastes. *Soft Matter*, 2014;10(8):1134-41. <https://doi.org/10.1039/c3sm51889b>
- [76] Nath P, Sarker PK. Effect of GGBFS on setting, workability and early strength properties of fly ash geopolymer concrete cured in ambient condition. *Construction and Building materials*, 2014;66:163-71. <https://doi.org/10.1016/j.conbuildmat.2014.05.080>
- [77] Khan MA. Mix suitable for concrete 3D printing: A review. *Materials Today: Proceedings*, 2020;32:831-7. <https://doi.org/10.1016/j.matpr.2020.03.825>
- [78] Xie J, Kayali O. Effect of superplasticiser on workability enhancement of Class F and Class C fly ash-based geopolymers. *Construction and Building Materials*, 2016;122:36-42. <https://doi.org/10.1016/j.conbuildmat.2016.06.067>
- [79] Li C, Sun H, Li L. A review: The comparison between alkali-activated slag (Si+ Ca) and metakaolin (Si+ Al) cements. *Cement and concrete research*, 2010;40(9):1341-9. <https://doi.org/10.1016/j.cemconres.2010.03.020>
- [80] Jaydeep S, Chakravarthy BJ. Study on fly ash based geo-polymer concrete using admixtures. *International Journal of Engineering Trends and Technology*, 2013;4(10):4614-7.

Blank Page



Experimental assessment of recycling methods of used engine oil for sustainable environment

Afreen Nissar^{*1,a}, M. Hanief^{1,b}, Fasil Qayoom Mir^{2,c}

¹Mechanical Engineering Department, National Institute of Technology, Srinagar, J&K, India

²Chemical Engineering Department, National Institute of Technology, Srinagar, J&K, India

Article Info

Article history:

Received 13 Jan 2022

Revised 08 Apr 2022

Accepted 05 May 2022

Keywords:

Engine oil;
Environment;
FTIR;
Recycling;
Rheology;
Waste management

Abstract

Used engine oil is a high pollutant material as it contains extremely toxic contaminants accumulated during operation. These contaminants if disposed improperly can not only cause extensive damage to the environment but also affect all living organisms. To tackle this rising problem the engine oil can be recycled by recovery of its base oil and reused for various purposes. Since the cost of recycling is comparatively much lower than production from crude oil, so recycling can prove to be a preferable alternative source as crude oil reserves are getting depleted. In this research study, SAE 5W30 was collected from the vehicle where it had been used for about 3000 miles operation and the collected oil was then subjected to various recycling methods. The recycled oils obtained undergo various tests for quality check comparison by Rheometer, FTIR Spectrometer, Oil Densitometer and Flash Point Tester. From the results obtained it was clearly observed that the acid/clay treatment method fetched superlative results. The degree of viscosity reduction (%) in acid/clay treatment method was found to be 95.077% which was significantly greater than other methods. Also, different engine oil samples were analyzed and compared for contamination by FTIR spectroscopy which can assist in condition monitoring of the vehicle engine.

© 2022 MIM Research Group. All rights reserved.

1. Introduction

Engine oil, also known as lubricant or motor oil, is a class of oils which has the primary purpose of reducing friction, heat and wear between the in-contact mechanical components. Lubricant (engine oil) is an oil product that separates the metal parts of an engine, reduces friction and keeps it clean [1]. The Lubrication system of engine is intended to avoid the increase of wear, over-heating and seizure of rubbing surfaces to reduce the expenses of indicated power on overcoming mechanical losses in the engine and also to remove wear products of a machine [2]. There are two basic categories of engine lubricating oil, these being Mineral and Synthetic oil. Lubricating oils refined from naturally occurring crude oil are known as Mineral oils. On the other hand, oils that are manufactured are known as Synthetic oils. Mineral oils are currently most commonly used oil as they are extracted from crude oil at low cost. Also, the viscosity of mineral oils can be varied, thus making them useful for wide range of applications.

Lubricating oils from petroleum consists essentially of complex mixtures of hydrocarbon molecules. They are mostly composed of iso-alkanes having slightly longer branches and the mono-cycloalkanes and mono-aromatics which have several short branches on the ring [3]. Lubricating oil is extremely important for the operation of the vehicles. The main

*Corresponding author: afreenn.07@gmail.com

^a orcid.org/0000-0001-5414-1771; ^b orcid.org/0000-0001-9556-7023; ^c orcid.org/0000-0002-3211-2395

DOI: <http://dx.doi.org/10.17515/resm2022.385ma0113>

Res. Eng. Struct. Mat. Vol. 8 Iss. 3 (2022) 553-567

purpose of the properly lubrication is that the engine needs to put less effort for the movement of the pistons as they tend to glide easily. Thus, ensuring that less fuel is needed by the vehicle to operate and also enabling the car to run at a lower temperature. Hence, we can safely say that the lubricating oil not only improves the efficiency of the vehicles but also ensures reduction in the wear and tear on the moving engine parts.

The modern society is based on the use of the car, which cannot operate without lubricants. With the increase of population and the number of vehicles, the quantity of waste oils has increased. The term "waste oil" characterizes any lubricating oil, mineral or synthetic, that has become unusable for the purpose for which it was originally intended [4]. Since the lubricating oil has proven to be such a valuable resource, thus there have been many efforts to recycle the used oil. Used oil, also known as sump oil, should not be thrown away as if the oil gets dirty, it can be cleaned by removing the contaminants. Disposing the used oil in the environment or burning it as a low-grade fuel, leads to some hazardous consequences such as toxic compounds in liver or complete impairment of body functions and eventually death of organism, carcinogenicity, environmental pollution, etc.

Engine oil is made up of 98% base oil and 2% additives. It loses its properties after using it for a certain period of time as high temperature degrades the additives in lubricant and dirt and wear particles get added along the way. Degradation of lubricating oil occurs when different additives or foreign substances (metallic powders, sulfur, water, carbon, ash, etc.) impurify the oil, modifying its chemical composition and affecting its properties [5]. Recycling cleans the base oil and separates the degraded additives and new additives are added to the reclaimed base oil to return the properties of the oil to original higher quality state. The conventional recycling methods used such as distillation is a high-cost technology. Recycling method serves three purposes, that is it is economical, resource conservation and environment and health protection. For this waste engine oil can be collected in batches from vehicle maintenance garages, mechanic shops, transportation companies and industries.

Various methods can be used to recycled the oil again and again so that it can be reused for various purposes. Used engine oil is an extremely dangerous pollutant as it contains high content of heavy metals and high concentrations of PAHs which are carcinogenic compounds. PAH content of used motor oil can be 670 times greater than that of new motor oil [6]. As it is insoluble, persistent and has a high content of heavy metals and other pollutants, it is necessary to collect and recycle waste oil, in order to avoid contamination of the environment [7]. The main contaminants present in the used engine oil are water, dissolved gasoline and gas oil, polymeric and non-polymeric additives, solvents, aromatics, cleaning fluids, lead, etc.

Several recycling methods have been developed and used over the time depending on the nature of base oil and contaminants. These treatment methods include acid/clay treatment method where the process is based on treating the waste oil with different acids (sulfuric, acetic, formic) to remove pollutants and then using binders (clay or bentonite) to neutralize the resulting product [8]. Activated carbon can also be used for neutralization [9]. Another method is vacuum distillation and hydrogenation/clay treatment which is a commercially available high-cost technology where vacuum distillation is done at the temperature of 250°C and followed by hydrogenation or treatment with clay in order to remove odours and the toxic compounds of nitrogen and sulfur. Solvent extraction technology is another method used which consists of dissolving the aromatic components that affect the properties of the oils, while preserving the desired components, such as saturated hydrocarbons [10]. After treating the oil with solvent, the oil is mixed with active alumina to remove the dark colour and specific odours [11]. Solvents that can be used to treat waste oils include 1-butanol, methanol, ethanol, propane, toluene, methyl ethyl

ketone, acetone, etc. [12]. Membrane filtration technology is a very promising approach for recycling of engine oil where various types of membranes such as PAN, PES and PVDF can be used to achieve superlative results. It is a continuous operation that removes metal particles, soot and dust from used engine oil and also leads to the recovery of lubrication properties of the treated oil. Despite the benefits presented by this process, the membranes are expensive and can be damaged and soiled by large particles [13]. Pyrolysis using microwave heating is a relatively recent process, in which spent hydrocarbons are mixed with a strong microwave absorbing material, such as carbon particles, as a result of microwave heating, they are then thermally cracked in the absence of oxygen in shorter chains of hydrocarbons [14].

Different recycling methods such as hydrotreating [15], adsorption [16], extraction [17], coagulation, oxidation and vacuum-distillation [18] are used to tackle the management issues of waste engine oil. However, these techniques are high-cost, require high energy consumption and generate secondary pollution by-products [19]. Environment friendly methods need to be developed that have minimal impact on the ecosystem at low cost. The paper presents the methods that are economical and the materials are easily available. There is no requirement of big set-up or large capital investment. In future more efficient and economical methods can be discovered to produce higher quality of oil as crude oil reserves are getting depleted and there is an urgent need to find an alternate source.

2. Methodology

2.1. Analysis of Used Engine Oil Samples for Presence of Contaminants

5 samples of used engine oil were collected from 5 different vehicles having same engine specifications given in table 1 below, same car brand, but different models. Same engine oil was used in all 5 vehicles for approximately 3000 miles and then the oil was replaced and the used oil was collected from all the vehicles for FTIR analysis and then the resultant spectra of each oil was compared with the spectra of the virgin oil to detect the changes in the spectra. This also enables the condition monitoring of the vehicle engine as we identify the constituent(s) present in the used oil.

Table 1. Specification details of vehicle engine

Parameter	Details
Engine Displacement	796 cc
Fuel Type	Petrol
No. of Cylinders	3
Valves per Cylinder	4
Strokes of Engine	4 cycles
Models for oil collection	2011, 2013, 2015, 2017, 2019

Engine oil used for this experiment was SAE 5W30, where 5W30 is the viscosity grade of the oil. This oil is designed to perform at cold starting temperatures as well as the normal operation temperatures of 100°C without sacrificing performance. 5W-30 specifies that this is a multi-grade oil where two numbers are separated by W. The first number 5W shows the thickness/viscosity of the engine oil on vehicle start-up, when we start the engine. W, here stands for Winter, which indicates oil performance under colder engine temperatures when the engine has not been running.

2.2. Comparison of Various Engine Oil Recycling Methods

SAE 5W30 was used as a lubricating oil in 2011 model of 800 cc car engine and the oil was collected after using it for approximately 3000 miles. The collected used oil was then subjected to various treatment methods to recycle it and the characteristics of the recycled

oil were then compared with that of the virgin and used engine oil by performing tests to check Flash point, Specific gravity, change in viscosity with temperature using Rheometer and Fourier Transform Infrared Spectroscopy (FTIR) on all the oils from which the absorbance levels of various parameters were calculated from the transmittance obtained at their specific spectral locations and hence the absorbance levels were compared to study the changes in the oil samples. The various methods that were used to recycle the oil are Acid Treatment Method, Activated Charcoal/ Clay Treatment Method and Acid/ Clay Treatment Method.

2.2.1. Pre-Treatment

Filtration of used engine oil was done before any treatment method in order to remove impurities such as dust, metallic chips, sand, particles, micro impurities, etc. In the pre-treatment process a funnel was placed along with the Whatman filter paper grade 1 (circular sheet with particle retention 11 μm and nominal thickness 180 μm) on top of the vacuum flask and the vacuum pump was connected to the other outlet in the bottom of the flask and thus the filtered oil was collected in the flask. The vacuum pump created a negative pressure in the flask which sucked the oil inside and left the micro particles on the filter paper.

2.2.2. Acid Treatment Method

Oil was centrifuged at 1500 rpm for few minutes and then allowed to settle down for 10-15 mins. It was then heated on magnetic stirrer and stirred continuously. The content was then allowed to cool down and then treated with conc. H_2SO_4 and agitated strongly to create homogeneity. Then the mixture was allowed to settle down for 48 hours and 2 layers were detected. The sludge at the bottom was separated and the remaining oil was treated with NaOH to neutralize the acid.

2.2.3. Activated Charcoal/Clay Treatment Method

100 ml of used engine oil was treated with 50 ml ethyl acetate in a separating funnel and then left at room temperature for 24 hours. After decanting from the paste left at the bottom the separated solution was then treated with activated bentonite clay and activated charcoal.

2.2.4. Acid/Clay Treatment Method

Used engine oil was centrifuged at 1000 rpm for 20-30 mins after which decantation was done to remove liquid at the top as the suspended particles get settled at the bottom. The oil was then thermally treated. 100 ml of the oil was then treated with conc. H_2SO_4 and in the end activated bentonite clay was added.

3. Results and Discussion

3.1. Analysis of Used Engine Oil Samples for Presence of Contaminants

FTIR Spectroscopy consists of an interferometer which is used to modulate the wavelength from a broadband infrared source. The intensity of transmitted or reflected light is measured by the detector as a function of its wavelength. The interferogram obtained from the detector in form of the signal is analysed with a computer to obtain a single beam infrared spectrum by using Fourier Transform. FTIR spectra is plotted between wavenumber (cm^{-1}) and intensity which can be represented as the light transmitted or absorbed at each wavenumber. For qualitative material identification the unknown IR absorption spectrum is compared with spectrum of known material to identify the constituent(s) of the sample. Absorption bands in the range 4000-1500 are usually due to functional groups and absorption bands in the region from 1500-400 is due to

intramolecular phenomena specific to particular material. This specificity of these bands enables identification of the constituent in the sample.

Table 2. Spectral locations of various components in used engine oil (FTIR)

Component	Spectral Location (cm ⁻¹)
Moisture	3400
Soot	2000
Oxidation/ viscosity	1750
Carboxylic acid	1725-1700
Nitration	1650-1600
TBN	1170
Sulfation	1150
ZDDP	980
Aromatics and PAHs	650-850

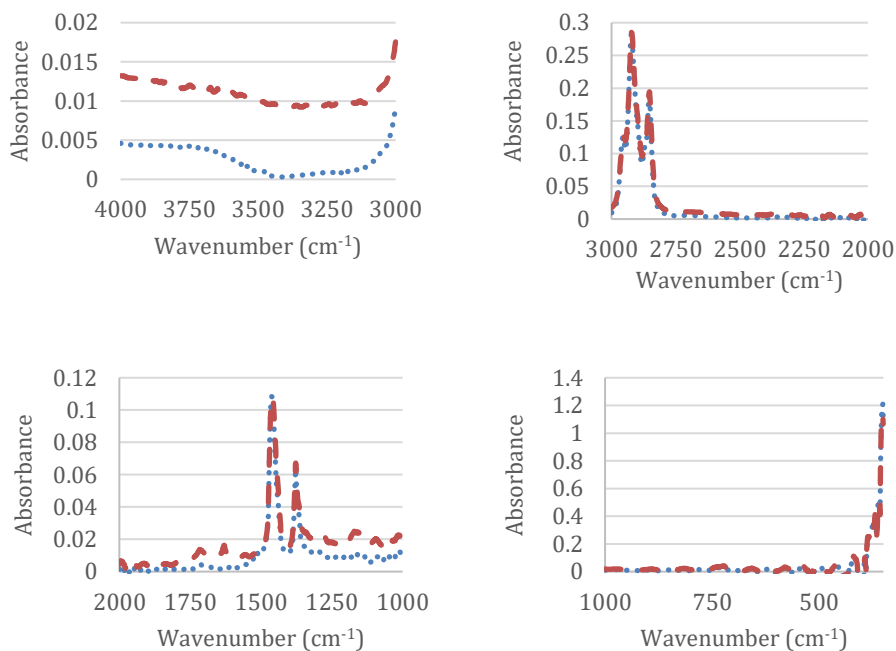


Fig. 1 FTIR of oil sample 1 from spectral locations 4000 to 300 cm⁻¹ (red-used engine oil, blue- virgin oil)

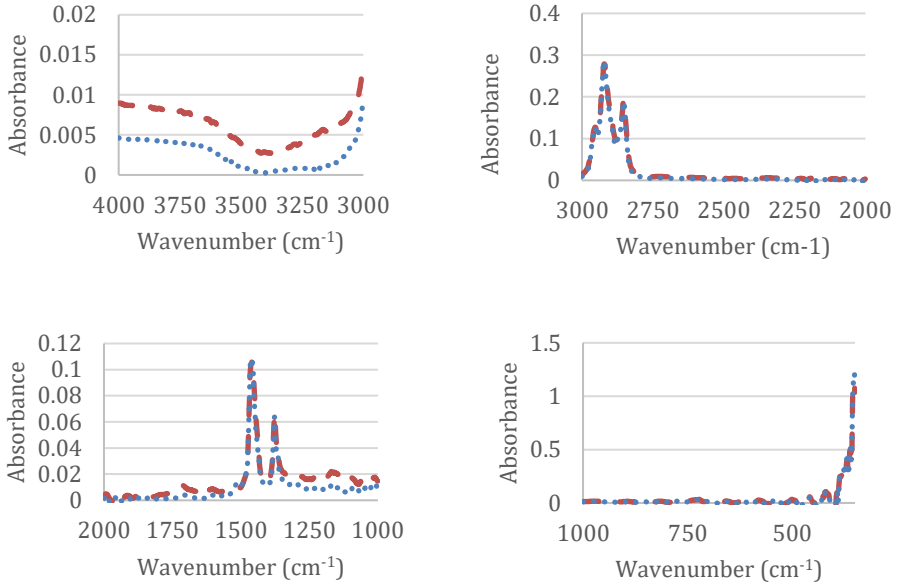


Fig. 2 FTIR of oil sample 2 from spectral location 4000 to 300 cm⁻¹ (red-used engine oil, blue- virgin oil)

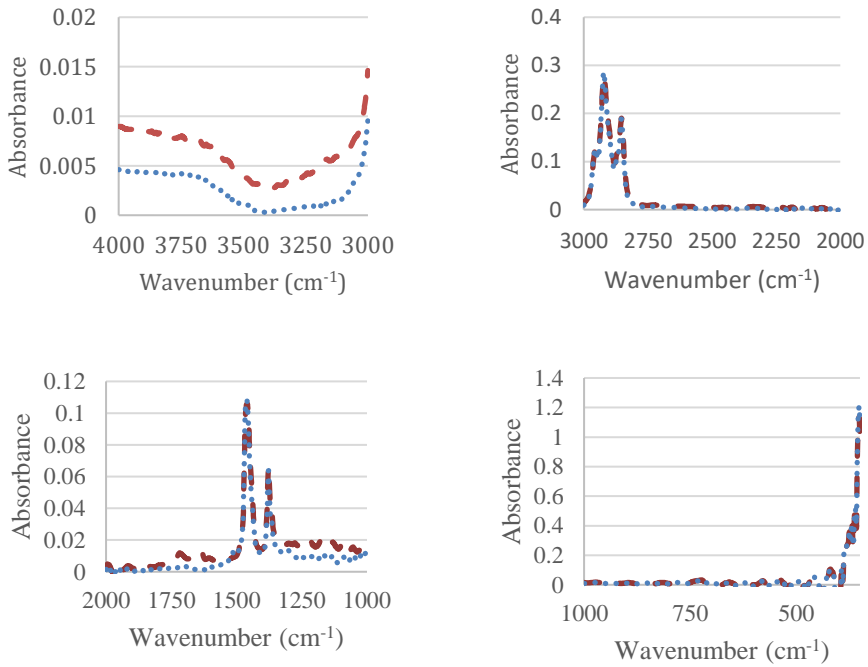


Fig. 3 FTIR of oil sample 3 from spectral location 4000 to 300 cm⁻¹ (red-used engine oil, blue- virgin oil)

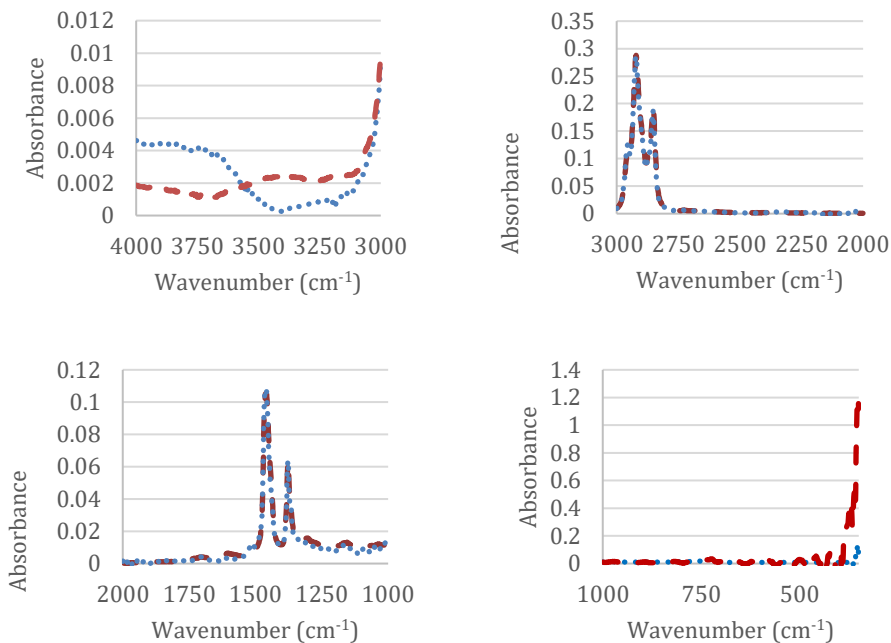


Fig. 4 FTIR of oil sample 4 from spectral location 4000 to 300 cm⁻¹ (red-used engine oil, blue- virgin oil)

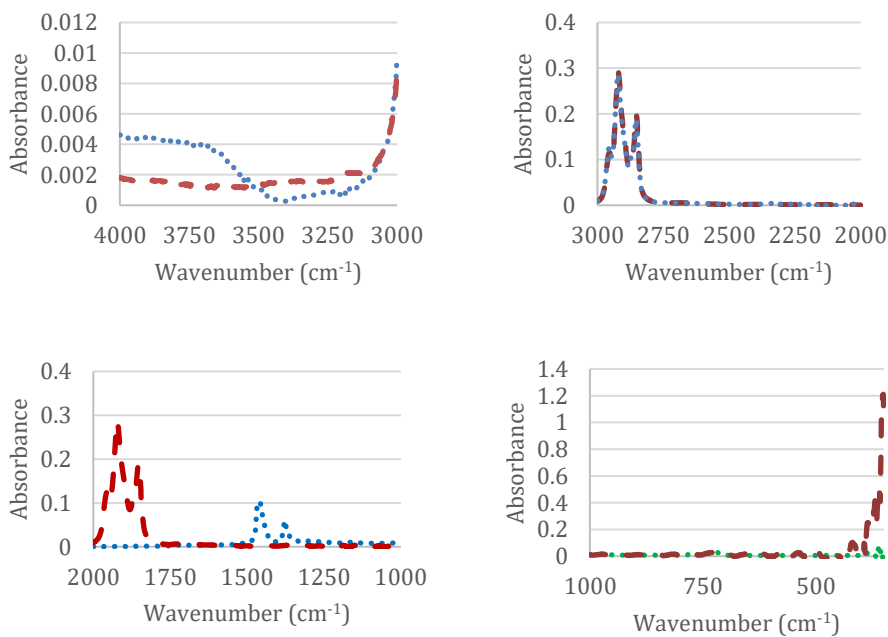


Fig. 5 FTIR of oil sample 5 from spectral location 4000 to 300 cm⁻¹ (red-used engine oil, blue- virgin oil)

Table 3. Summary of parameter comparative graphs

Contaminant	Vehicle make (year)				
	2011	2013	2015	2017	2019
Moisture	Increases	Mild Increase	Mild Increase	Mild Increase	Mild Increase
Soot	Increases	Decreases	Increases	Decreases	Decreases
Oxidation/Viscosity	Increases	Moderate Increase	Increases	Mild Increase	No change
Nitration	Increases	Moderate Increase	Moderate Increase	Mild Increase	Mild Increase
TAN	Increases	Mild Increase	Increases	Mild Increase	No change
TBN	Decreases	Mild Decrease	Decreases	Mild Decrease	No change
Sulfation	Increases	Moderate Increase	Increases	Mild Increase	Mild Increase
ZDDP	Mild Increase	Decreases	Mild Increase	Decreases	Mild Increase
Aromatics &PAHs	Mild Increase	Mild Increase	Mild Increase	Mild Increase	Mild Increase

Instrumental Error and uncertainty:

With reference standards, uncertainty level of $\pm 0.03\%$ has been observed in FTIR Spectrometer and instrumental error of almost $\pm 3\%$ in rheometer. In oil densitometer creation of bubbles in sample can cause error in readings. The oil densitometer is capable of determining the density of liquids across temperature range of -40 to 150°C , at pressures from 0.1 to 30 MPa with expanded uncertainty of 0.015% (at 95% confidence).

3.2. Comparison of Various Engine Oil Recycling Methods

3.2.1. Flash Point and Specific Gravity

Flash point is the lowest temperature at which enough vapours are developed for ignition under specified conditions. This is an important characteristic as it contributes to the scope of lubricating oil since a vehicle can achieve the temperature of 150°C , so no engine oil with flash point of 150°C or less can be used.

Specific gravity or relative density is the ratio of the mass of given volume of product and mass of equal volume of water at same temperature. Standard reference temperature to measure specific gravity is 15.6°C . It is determined by ASTM D 1298. Higher the specific gravity of the material, heavier it will be.

At flash point, oil develops enough vapors to ignite and then it continues to burn afterwards. Oil with flash point of 150°C or less cannot be used as the vehicle engine has the capability of attaining 150°C during operation and can increase fire and explosion risk. Thus, it is advisable to change the engine oil after certain period of time as it is evident from table 4 that the flash point of used engine oil has decreased considerably to 156°C due to dilution and addition of contaminants during operation. It is further observed from the readings that increase in flash point after recycling of oil is quite evident and hence deeming it safe for usage.

Specific gravity relates density of oil to that of water and is measured by oil densitometer. Since it is known that specific gravity of water is equal to 1 , so if the oil attains specific gravity of greater than 1 , then it will become heavier than water and anything lighter than water will have specific gravity of less than 1 . Since engine oil has specific gravity of less

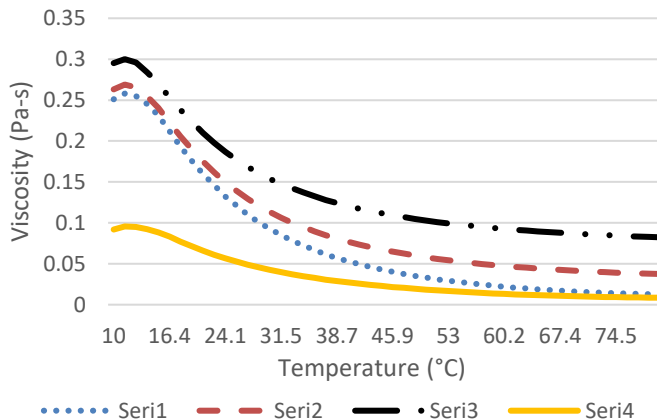
than 1, so it is less dense than water. Hence, if there is moisture problem in the vehicle engine, it will get collected and settled at the bottom of the sump, so it can be drained out first and easily. From table 4, it is observed that in used engine oil there is increase in specific gravity and it occurs when oil becomes thicker due to addition of contaminants. This will in turn cause wear particles and contaminants such as rust to settle down slowly, which can lead to failure of the system, as longer the particles are in the suspension, more cavitation and corrosion they can cause.

Table 4. Flash point and specific gravity of all oil samples

	Used Engine oil	Recycled oil (Acid Treatment Method)	Recycled oil (Activated Charcoal/ Clay Treatment Method)	Recycled oil (Acid/Clay Treatment Method)	Virgin oil
Flash Point (°C)	156	192	202	213	232
Specific Gravity @ 15.6°C	0.956	0.901	0.897	0.891	0.8818

3.2.2. Change in Viscosity with Temperature

Viscosity is inversely proportional to the temperature and can be measured by a rheometer, as when temperature increases the lubricant becomes thinner and thus its load bearing capacity is reduced. But when the temperature decreases, lubricant becomes thick which makes it difficult to pour or pump it. Increase in viscosity of engine oil can be a contribution of oxidation, polymerization, soot, other contaminants, anti-freeze, etc.



- Series 1 Recycled oil (Acid/Clay Treatment Method)
- Series 2 Recycled oil (Activated Charcoal/ Clay Treatment Method)
- Series 3 Recycled oil (Acid Treatment Method)
- Series 4 Pure/ Virgin oil

Fig. 6 Effect of temperature on viscosity (Rheometer readings)

Oil thickness, also termed as viscosity determines the film strength of engine oil and its efficiency to prevent friction and thus wear between two moving parts of the engine. If the oil has high viscosity, it is thick and vice versa. For proper operation, engine oil should have perfect viscosity so that it is neither too thick to pour at low temperatures, nor becomes too thin as the temperature increases that it will not create an appropriate film between two parts as the temperature of the vehicle engine varies from ambient temperature to 150°C during operation. For too thick oil, engine has to work harder which in turn generates more heat whereas too thin oil is not enough for friction, hence causing unnecessary wear and tear in both cases. From figure 6, it is clearly observed that acid/clay treatment method has lower viscosity at low temperature and the viscosity gets closer to that of virgin oil as the temperature increases.

The flow characteristics of the oil are mostly affected by the operating temperatures. At high temperature, since viscosity is reduced so it is easy to pump the oil. In order to evaluate the improvement in flow characteristics of obtained recycled oils, we can calculate the degree of viscosity reduction (%) from rheometer observations of viscosity as a function of temperature at constant shear rate, where;

$$DVR (\%) = \frac{\text{initial value} - \text{final value}}{\text{initial value}} \times 100$$

and, thus from table 5 we can observe that the recycled oil obtained from Acid/clay treatment method has maximum DVR % reduction and hence has better fluidity enhancement.

Table 5. Viscosity reduction of various recycled oils

Recycled oil	Initial Value Viscosity (Pa-s)	Final Value Viscosity (Pa-s)	DVR %
Acid Treatment Method	0.3	0.0823	72.56
Activated Charcoal/ Clay Treatment Method	0.269	0.0375	86.05
Acid/Clay Treatment Method	0.258	0.0127	95.077

3.2.3. Fourier Transform Infrared Spectroscopy

The oil can be analyzed by Fourier Transform InfraRed (FTIR) Spectroscopy which is a proven technique to analyze and characterize the used and recycled engine oil samples. When the engine oil is exposed to infrared radiation, the molecules absorb radiation at different wavelengths and thus the contaminants are detected by the absorbance value at particular spectral locations, the absorbance value being directly proportional to the quantity of the contaminant. Following absorbance levels were recorded by FTIR in the oil samples at specific spectral locations of various functions groups:

Since absorbance value of contaminants and functional groups is directly proportional to the quantity of contaminant present in the oil, as more the contaminant, more radiation it will absorb. So, from table 5, it is observed that there is increase in the absorbance value of used engine oil when compared to that of virgin oil due to addition of contaminants and then decrease in the absorbance values can be observed in recycled oils.

In the research study various methods were used to return the lubricating oil to its original state so that it can be reused by removing the contaminants. Analyzing the results, we can

observe that oil recycled by Acid/clay treatment method has shown maximum recovery and improvement. It was also observed that using materials such as sulfuric acid for recycling can be harmful as it produces high sulfur level by-products that are toxic.

Used engine oil is an incredibly toxic material. It does not wear out and only gets filthy by the addition of contaminants and thus can be cleaned of contaminants and recycled continuously to the point where it can be reused as fuel oil, hydraulic oil or in the manufacture of many petro-chemical based products such as plastics.

Table 6. Absorbance values of all oil samples measured by FTIR spectroscopy

Contaminant/ Functional group	Virgin oil	Used Engine Oil	Recycled oil (Acid Treatment Method)	Recycled oil (Activated Charcoal/ Clay Treatment Method)	Recycled oil (Acid/Clay Treatment Method)
Moisture	0.0002	0.00943	0.00283	0.0024	0.0015
Soot	0.00147	0.004715	0.00049	0.00049	0.000177
Oxidation/ Viscosity	0.002045	0.00753	0.00424	0.0029	0.00205
Carboxylic Acid	0.000397	0.01363	0.01188	0.01144	0.005
Nitration 1600 cm ⁻¹ (Series 1)	0.00156	0.0097	0.00679	0.00499	0.00307
Nitration 1650 cm ⁻¹ (Series 2)	0.00392	0.01148	0.00804	0.00655	0.00451
TBN	0.0109	0.0248	0.0166	0.01264	0.0102
Sulfation	0.0096	0.02305	0.0184	0.01366	0.0102
ZDDP	0.01416	0.0191	0.01365	0.01366	0.01246
Aromatics & PAHs 650 cm ⁻¹ (Series 1)	0.00828	0.0162	0.00745	0.00977	0.00853
Aromatics & PAHs 720 cm ⁻¹ (Series 2)	0.0323	0.0339	0.0304	0.0311	0.0319
Aromatics & PAHs 850 cm ⁻¹ (Series 3)	0.01068	0.0185	0.0124	0.0143	0.0122

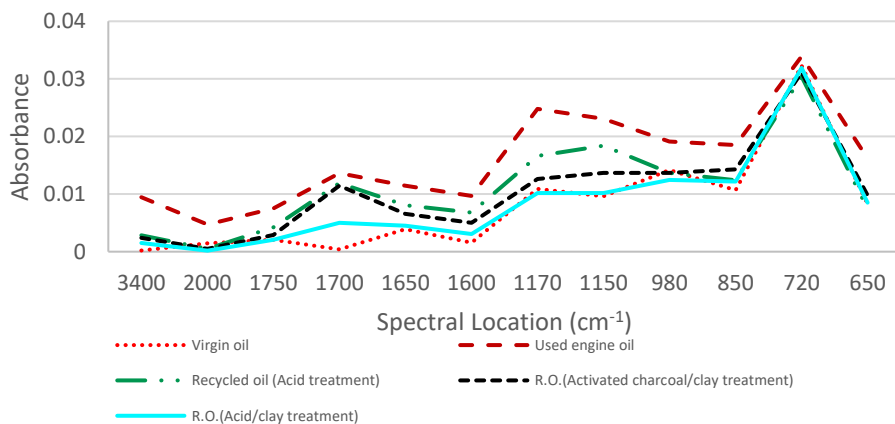


Fig. 7 FTIR Spectroscopic comparison of recycled oils

Table 7. Comparison of efficiency in reducing contaminant level by various methods

Contaminant	Acid Treatment Method	Activated Charcoal/Clay Treatment Method	Acid/Clay Treatment Method
Moisture	Minimum decrease	Median decrease	Maximum decrease
Soot	Minimum decrease	Minimum decrease	Maximum decrease
Oxidation/Viscosity	Minimum decrease	Median decrease	Maximum decrease
Carboxylic Acid	Minimum decrease	Median decrease	Maximum decrease
Nitration 1600 cm ⁻¹	Minimum decrease	Median decrease	Maximum decrease
Nitration 1650 cm ⁻¹	Minimum decrease	Median decrease	Maximum decrease
TBN	Minimum decrease	Median decrease	Maximum decrease
Sulfation	Minimum decrease	Median decrease	Maximum decrease
ZDDP	Minimum decrease	Minimum decrease	Maximum decrease
Aromatics & PAHs 650 cm ⁻¹	Maximum decrease	Minimum decrease	Median decrease
Aromatics & PAHs 720 cm ⁻¹	Maximum decrease	Median decrease	Minimum decrease
Aromatics & PAHs 850 cm ⁻¹	Median decrease	Minimum decrease	Maximum decrease

Table 8. Impact of contaminants found in used engine oil

Contaminants	Observed effect
Poly-cyclic aromatic hydrocarbons (PAHs) formed by incomplete combustion of organic matter	They are classified as human carcinogens causing various types of cancers.
Heavy metals	Cancer, anemia, skin ulcerations and cardiovascular diseases.
Particulates produced by burning of used oil	Respiratory problems such as loss of lung function, loss of ability to resist infection and death.
Sulphur dioxide and Nitrogen dioxide	Adverse respiratory effects on humans and deterioration of foliage and plant growth.
Organo-chlorine compounds such as dioxins and furans	Skin toxicity, immune-toxicity, Carcinogenicity and adverse effects on reproduction, development and endocrine functions.
Polychlorinated biphenyls (PCBs)	Liver damage, respiratory problems, cancer promotion, endocrine disruption and neurotoxicity.
Harmful metals such as arsenic, cadmium, chromium, zinc and lead formed by the decomposition of the additive lead tetraethyl	Acute toxicity in fish and tumors. Also, direct toxicity in plants.
Mercury, PCBs and Organo-chlorine Oil floating on surface of water bodies	Secondary poisoning in organisms. Prevents penetration of oxygen in water and has an adverse effect on aquatic life.

Oil sample on x-axis:

- 1- Virgin oil
- 2- Used Engine oil
- 3- Recycled oil (Acid Treatment Method)

4- Recycled oil (Activated Charcoal/ Clay Treatment Method)

5- Recycled oil (Acid/Clay Treatment Method)

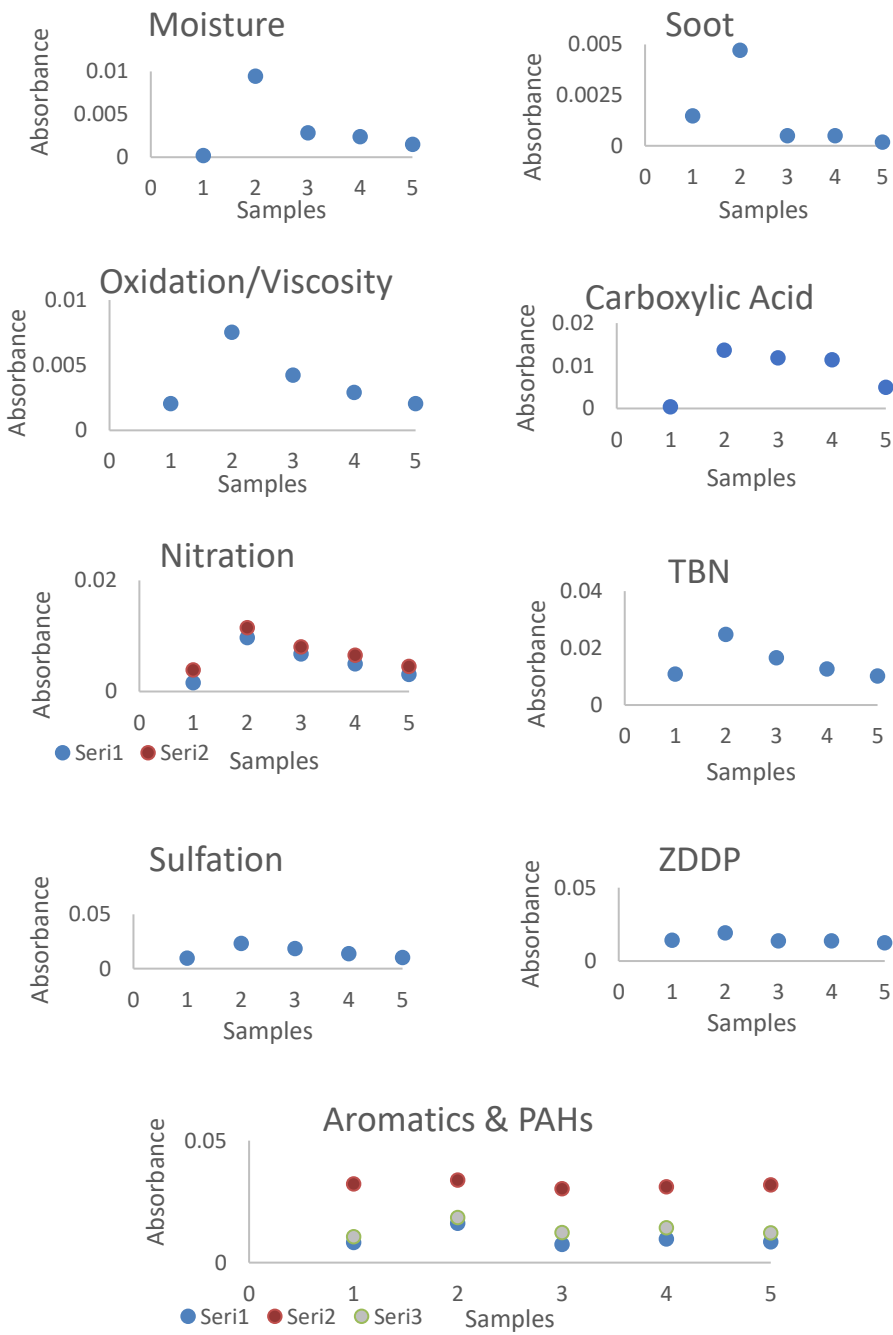


Fig. 8 Comparison graphs of contaminants in all oil samples

4. Conclusion

Million tonnes of used engine oil are spilled into the environment each year thus leading to massive damage of human health and of other living organisms including the plants. Recycling and reusing used engine oil is considered to be a preferable way rather than disposal as it can provide great environmental benefits. Recycled engine oil can be processed into fuel oils and can be used as low-grade oil. Re-refining removes the to produce new base oil and the base oil obtained can be blended with fresh additive to restore the oil to its original effectiveness. Successful recycling of this used engine oil can not only solve the environmental pollution problem but also can prove to be economical as well as the crude oil reserves are getting depleted day by day. Experimental results obtained from this research indicate that a good quality base oil can be obtained from waste engine oil at relatively very low cost when compared to production from crude oil. Further research in this field can provide additional benefits as there is a scope of converting the by-products of the experiments into valuable products. Since already existing commercially used distillation process is costly and has tendency to break down frequently, the methods used in this research can prevent that downtime and thus the loss of time, labour and money. The benefits of recycling and reusing used engine oil are three-fold:

- *Economical*: Since oil is considered to be a non-renewable resource, so it will become increasingly difficult to find new reserves in future. The price of oil rises with time as the reserves of crude oil gets depleted. Recycling will provide time to develop alternate fuels and thus reusing of the recycled oil will save lot of money.
- *Public Health*: Health sector can be seriously threatened if oil is disposed of improperly as it enters the air, water and soil. Recycling and reusing waste oil can prevent its improper disposal and thus entering into the systems of plants and animals where it can cause toxic reactions and various terminally ill diseases like cancer etc. which can eventually lead to death of organisms.
- *Environmental*: Improper disposal of waste oil can create both air and water pollution which can have various hazardous consequences. It can only be prevented by reusing the waste oil and thus saving the environment as the contaminants in the gases can even cause damage to the ozone layer.

References

- [1] Turk J. Introduction to environmental studies. 3rd edition Saunders College Publisher New York, 1993; 23-41.
- [2] Cock V R. Laboratory Handbook for Mineral oil and Organic oil analysis. Academy Press London, 1998; 111-113.
- [3] Cutler ET. Conserve Lube Oil: Re-Refine. Hydrocarbon Processing, 2009:265.
- [4] Abdalla N, Fehrenbach H. Ecological and energetic assessment of re-refining waste oils to base oils. Heidelberg, 2017.
- [5] Diphare MJ, Muzenda E, Pilusa J, Mollagee M. A Comparison of Waste Lubricating Oil Treatment Techniques. 2nd International Conference on Environment, Agriculture and Food Sciences (ICEAFS'2013), Kuala Lumpur, Malaysia, 106-109, 2013.
- [6] Vazquez- Dubalt. Environmental impact of used motor oil. The Science of the Total Environment, 1989; 1-23. [https://doi.org/10.1016/0048-9697\(89\)90049-1](https://doi.org/10.1016/0048-9697(89)90049-1)
- [7] Andrews L. Compendium of Recycling and Destruction Technologies for Waste Oils. United Nations Environment Programme, 2008.
- [8] Regional Activity Centre for Cleaner Production (RAC/CP) Mediterranean Action Plan. Possibilities for the recycling and reuse of used oils, 2000.

- [9] Ahamad MT, Chadra Sekhar BP, Mohan PN, Joshi KS, Sree TDR. Recycling and Analysis of Spent Engine Oil. *International Journal of Scientific & Engineering Research*, 2015; 6:11 711-715.
- [10] Rincon J, Canizares P. Waste oil recycling using mixtures of polar solvents. *Ind. Eng. Chem. Res.*, 2005; 7854-7859. <https://doi.org/10.1021/ie0580452>
- [11] Osman DI, Attia SI, Taman AR. Recycling of used engine oil by different solvent. *Egyptian Journal of Petroleum*, 2018; 27: 221-225. <https://doi.org/10.1016/j.ejpe.2017.05.010>
- [12] Boadu KO, Joel OF, Essumang DK, Evbuomwan BO. A Review of Methods for Removal of Contaminants in Used Lubricating Oil. *Chemical Science International Journal*. 2019; 26:4 1-11. <https://doi.org/10.9734/CSIJ/2019/v26i430101>
- [13] Henry M. Re-refining and recycling of used lubricating oil and natural resource conservation in Ghana. *ARNP Journal of Engineering and Applied Sciences*, 2015; 10: 797-801.
- [14] Lam SS, Russell AD, Chase HA. Pyrolysis Using Microwave Heating: A Sustainable Process for Recycling Used Car Engine Oil. *Ind. Eng. Chem. Res.*, 2010; 10845-10851. <https://doi.org/10.1021/ie100458f>
- [15] Ramasamy KK, Ali T., Hydrogen production from used lubricating oils, *Catal. Today* 2007; 129:3-4 365-371. <https://doi.org/10.1016/j.cattod.2006.09.037>
- [16] Miyagi A, Nakajima M. Regeneration of used frying oils using adsorption processing, *J. Am. Oil Chem. Soc.* 2003; 80:1 91-96. <https://doi.org/10.1007/s11746-003-0657-5>
- [17] Mohammed RR, Ibrahim IA, Taha AH, McKay G. Waste lubricating oil treatment by extraction and adsorption, *Chem. Eng. J.* 2013; 220: 343-351. <https://doi.org/10.1016/j.cej.2012.12.076>
- [18] Shri Kannan C, Mohan Kumar K, Sakeer Hussain M, Deepa Priya N, Saravanan K. Studies on Reuse of Re-refined used automotive lubricating oil, *Res. J. Eng. Sci.*; 2014; 3:6 8-14.
- [19] Cao Y, Yan F, Li J, Liang X, He B. Used lubricating oil recycling using a membrane filtration: analysis of efficiency, structural and composing, *Desalin. Water Treat.* 2009; 11:1-3 73-80. <https://doi.org/10.5004/dwt.2009.845>
- [20] Robinson. Monitoring oil degradation with infrared spectroscopy. 2000: <http://www.wearcheck.co.za>.
- [21] Van de Voort FR, Sedman J, Cocciardi, Juneau S. An automated FTIR method for the routine quantitative determination of moisture in lubricants: An alternative to Karl Fischer titration. *Talanta*, 2007; 72: 289-295. <https://doi.org/10.1016/j.talanta.2006.10.042>
- [22] Garry MC, Bowman J. FT-IR Analysis of Used Lubricating Oils - General Considerations. Thermo Fisher Scientific, Madison, WI, USA; 2007.
- [23] Macián V, Tormos B, Gómez YA, Salavert JM. Proposal of an FTIR Methodology to Monitor Oxidation Level in Used Engine Oils: Effects of Thermal Degradation and Fuel Dilution. *Tribology Transactions*, 2012; 55: 872-882. <https://doi.org/10.1080/10402004.2012.721921>
- [24] Guide to Measuring Oil Chemistry: Nitration, Oxidation and Sulfation. Spectro Scientific.
- [25] Willermet PA, Mahoney R, Bishop CM. Lubricant Degradation and Wear II Antioxidant Capacity and IR-Spectra in Systems Containing Zinc Dialkyl dithiophosphates. *ASLE Trans.*, 1980; 23:3 217-224. <https://doi.org/10.1080/05698198008982962>

Blank Page



Research Article

Optimal water-cement ratio and volume of superplasticizers for blended cement-bamboo leaf ash high-performance concrete

Samson Olalekan Odeyemi^{*1,a}, Michael Oluwasegun Adisa^{1,b}, Olumoyewa Dotun Atoyebi^{2,c}, Uwemedimo Nyong Wilson^{3,d}, Omolola Titilayo Odeyemi^{4,e}

¹Department of Civil & Environmental Engineering, Kwara State University Malet, Nigeria

²Department of Civil Engineering, Landmark University, Omu-Aran, Kwara State. Nigeria

³Department of Civil Engineering, Nigerian Defence Academy, Kaduna, Nigeria

⁴Department of Science Laboratory Technology, Kwara State Polytechnic, Ilorin, Nigeria

Article Info

Abstract

Article history:

Received 08 Jan 2022

Revised 11 Mar 2022

Accepted 14 Mar 2022

Keywords:

Compressive strength;

Water absorption;

Bamboo leaf ash;

High-Performance

Concrete;

Superplasticizer

Attention on the use of High-Performance Concrete (HPC) for construction works has soared considerably due to the need for large volume of concrete with high level of strength for such works. The mechanical properties of HPC with Bamboo Leaf Ash (BLA) as partial replacement of cement with varying proportions of superplasticizer and water-cement ratio was investigated in this paper. The percentage of BLA was fixed at 5%, while the proportion of superplasticizer ranged from 0 to 1.5% by weight of cement. The concrete mix was designed to attain a characteristic strength of 41 N/mm² after 28 days of curing. X-ray Fluorescence (XRF) and X-ray Diffraction (XRD) were employed in determining the chemical constituents and crystallinity of the BLA respectively. The slump of the fresh HPC was also established. Concrete cubes (for water absorption and compressive strength) were cast and immersed fully in water for 56 days. Water absorption and compressive strength were established on the fully cured HPC. The optimal combination of materials at the end of the curing period is 0.360 water-cement ratio at 0.128 % superplasticizer. This resulted in a slump height of 49 mm, compressive strength of 53.61 N/mm² and 4.77% water absorption capacity.

© 2022 MIM Research Group. All rights reserved.

1. Introduction

Büyüköztürk and Lau [1] and Odeyemi *et al.* [2] defined HPC as concrete that has high workability, strength and durability. It is made from appropriate materials combined based on a designed mix, properly and thoroughly mixed, conveyed, delivered, consolidated, and cured such that the concrete produced will provide exceptional behaviour in the structural element wherein it is used, the environment where it is placed and the loads that it is subjected to throughout its service life. Several factors affect the mix proportions for HPC. These include locally available materials, specified performance properties, personal preferences, local experience, and cost. Technology has helped to advance the use of many products in enhancing the properties of HPC. HPC has been primarily applied in structures needing prolonged service lives such as long-span bridges, oil drilling platforms, and parking structures. Büyüköztürk & Lau [1] reported that High Strength Concrete (HSC) and HPC may be regarded as synonymous. Reducing the water-cement ratio in HPC, a requirement in attaining high strength, largely enhances the properties of the concrete.

*Corresponding author: samson.odeyemi@kwasu.edu.ng

^a orcid.org/0000-0001-5217-3403; ^b orcid.org/0000-0003-0047-2262; ^c orcid.org/0000-0001-9669-3179;

^d orcid.org/0000-0002-9068-9635; ^e orcid.org/0000-0003-4832-885X

DOI: <http://dx.doi.org/10.17515/resm2022.382ma0108>

Res. Eng. Struct. Mat. Vol. 8 Iss. 3 (2022) 569-581

In Nigeria, adequate shelter remains a basic need of people which has remained unsatisfied [3]. With research findings on the suitability of bamboo as a building material for use in low-cost domestic houses, the probability of average Nigerians hoping to have their houses has increased. Akeju & Falade [4] submitted that bamboo is cheaper, locally sourced, and a better substitute to steel reinforcement in columns and beams in residential houses because it has relative advantages over steel reinforcement. It does not suffer corrosion; it contains high fibre content and high water absorption capacity.

BLA is obtained from the calcination of bamboo leaves. The resulting ash components from the calcination of the bamboo leaves contain inorganic elements, mainly, potassium, silica, manganese, calcium and magnesium [5]. At early age, it is highly reactive, and its pozzolanic properties are like silica fume [6].

Asha et al. [7] examined the effect of incorporating BLA in concrete and their findings showed that due to the amorphous nature and the high silica content in BLA, it can be considered as a pozzolanic agricultural waste. However, their work did not report the water-binder ratio adopted nor the dosage of superplasticizer used. Onikeku et al. [8] examined the mechanical, physical, and durability properties of HPC by partially substituting cement with BLA calcined at 650°C at 0, 5, 10, 15, and 20% sequentially. Their work adopted a water-cement ratio (w/c) of 0.5 while the volume of superplasticizer used was varied. Their findings were that BLA enhanced the flexural, split tensile, and compressive strengths of the concrete at a benchmark of 10% as the optimal replacement level of cement with BLA. Further increase in BLA content reduced the slump, compacting factor, consistency, setting time, water absorption, compressive, split tensile and flexural strengths of the concrete.

Olutoge and Oladunmoye [9] also used BLA as supplementary cementitious material in concrete. They adopted a w/c of 0.5 without using superplasticizers. The authors concluded that the inclusion of BLA in concrete up to 20% can aid the compressive strength and workability of concrete. Dhinakaran and Chandana [5] also used BLA in concrete. They adopted a w/c of 0.5 without superplasticizers to produce concrete with a target strength of 25.8 MPa. They opined that 15% replacement of cement with BLA is the optimum.

Hunchate et al. [10] considered HPC containing superplasticizer and silica fume. They used a w/c of 0.29 and 5.11 kg of superplasticizer per meter cube (m³) of concrete for a target strength of 69 Mpa. They observed an increase in the compressive strength of the resulting HPC as the content of the silica fume increases to 15%. Dembovska et al., [11] studied the influence of pozzolanic additives on the growth in strength of HPC. A varying water-cement ratio ranging from 0.21 – 0.38 was adopted while a superplasticizer dosage of 0.5 kg per cubic metre of concrete was used. Their findings reveal that the inclusion of 10% silica fume by weight of cement resulted in the increase of the compressive strengths and bending of the HPC at 56 days of testing.

Latha et al. [12] conducted an investigation on HPC using waste materials such as slag sand and Bagasse ash obtained from some industries at varying percentages. Bagasse ash was partially used to replace cement while sharp sand was replaced with slag in varying proportions. A water-cement ratio of 0.34 and 1% of superplasticizer by weight of cement was adopted in the research. Their findings reveal that the use of 15% slag sand and 8% bagasse ash in concrete as a fractional replacement of cement increases its compressive strength. Increasing the quantity of the additives beyond these percentages resulted in a decline in the total strength of the concrete produced.

Odeyemi et al. [2] examined the compressive, splitting tensile, and flexural strengths of HPC containing Guinea Corn Husk Ash (GCHA) as an additive. A w/c of 0.31 and a

superplasticizer dose of 1% by weight of cement was adopted in their research. They recommended up to 10% GCHA as a partial substitute for cement in the production of HPC.

Zhutovsky and Kovler [13] studied the effect that w/c has on the effectiveness of internal curing of HPC. They used differing w/c of 0.21, 0.25 and 0.33. They concluded that w/c has a substantial consequence on the cracking potential of concrete cured internally.

Some researchers such as Richard and Cheyrezy [14], Larrard and Sedran [15], Droll [16], Wen-yu et al. [17], Gao et al. [18], Wille et al. [19], and Shi et al. [20] suggested water-cement ratios ranging from 0.08 - 0.25 for use in the production of HPC. Also, a dosage of superplasticizers ranging from 1 to 8 % by weight of cement has been recommended by Schmidt et al. [21] and Wille et al. [19].

In view of the benefits of using HPC, several studies have considered the development of a rational or standardized method of concrete mix design for HPC using varying water-binder ratios and dosages of superplasticizers. However, no optimal quantity of both is currently available. Hence, there is a need to investigate the water-cement ratio and dosage of superplasticizer for blended Cement-Bamboo leaf ash HPC. Therefore, this study determined the optimal water-cement ratio and dosage of superplasticizers for cement-BLA blended HPC.

2. Research Methodology

2.1 Experimental Design

Design Expert (Version 12) was used to design the experimental setup where an RSM in a Central Composite Design (CCD) was utilized in optimizing the BLA, Superplasticizer percentage and w/c. The CCD entails that before carrying out the benchmark in the laboratory the mix combinations should be designed. Two independent variables, Superplasticizer (0-1.5%) and water Cement ratio (0.36 - 0.4) with 13 experimental runs, with 5 repeated runs for slump height, compressive strength, and water absorption were conducted in this study. The adopted mix proportion for cement, fine and coarse aggregates was 1:0.5:1. Batching was done by weight. Fig. 1 displays the design interface of the Design Expert.

Std	Run	Factor 1 A:Water cement...	Factor 2 B:Percentage of... %	Response 1 Compressive str... N/mm ²	Response 2 Workability mm	Response 3 water absorption %
1	11	0.38	0			
2	13	0.4	0			
3	1	0.36	1.5			
4	2	0.4	1.5			
5	3	0.39	0.75			
6	9	0.36	0.75			
7	4	0.375	0.375			
8	8	0.375	1.125			
9	6	0.375	0.75			
10	5	0.375	0.75			
11	7	0.375	0.75			
12	10	0.375	0.75			
13	12	0.375	0.75			

Fig. 1 Design Expert Interface

There were nine different concrete mixes from which eighty-one concrete cubes were cast for compressive strength test; eighteen cubes were cast for water absorption capacity test.

The samples were immersed fully in water for a total period of 56 days respectively with testing done at 7, 28 and 56 days.

2.2 Materials

The materials used in this study include Portland limestone cement of Dangote brand, fine aggregate (natural river sand), coarse aggregate (granite), COSTAMIX 200R Superplasticizer, water, and Bamboo Leaf Ash (BLA). The Bamboo Leaves (BA) calcinated to produce the BLA and the BLA used in the study are presented in Fig. 2 and 3.



Fig. 2 Bamboo leaves before calcination



Fig. 3 Bamboo leaf ash

2.3. Experimental Investigations

2.3.1 Properties of Materials Used

The natural river sand passed through a sieve of aperture size of 4.75 mm and had a fineness modulus of 3.76. The coarse aggregate had a maximum diameter of 10 mm and specific gravity of 2.63. Both properties conform to the standard stated in BS 12390 [22]. The Portland limestone cement was of Grade 42.5R with a specific gravity of 2.84. The potable water used in mixing the concrete had a pH of 7. The COSTAMIX 200R Superplasticizer conformed to ASTM [23] and the Bamboo leaf ash (BLA) had a specific gravity of 2.80. A summary of the materials used is presented in Table 1.

Table 1. Properties of materials used

Tests	OPC	Fine aggregates	Coarse aggregates
Fineness (%)	8.3		
Specific Gravity	3.10	2.66	2.63
Fineness Modulus		2.99	7.16
Water absorption (%)		0.4	0.3
Loose Bulk density (kg/m ³)		1446	1484

The Bamboo leaves (BL) were calcined to ashes at a temperature of 650 °C as recommended by Onikeku et al. [8], in a blast furnace at the Fabrication Workshop, Department of Mechanical Engineering, Institute of Technology, Ilorin, Kwara State. A milling machine was used to further ground the ashes into finer particles before passing them through a sieve of 90 µm aperture size.

2.3.2 Standard Consistency and Fineness of Cement

A standard consistency test was done to find the volume of water needed to yield a paste of standard consistency. This test conformed to BS EN 196-3 [24]. The fineness test of cement was carried out using British standard sieves. The weight of cement with particle size greater than 90 microns was determined after which the percentage of cement particles retained was calculated. The cement particles were placed in a sieve and unceasingly sieved by vertical and circular motion for 15 minutes. The residue retained on the sieve after the operation was weighed and recorded. The fineness of the cement was obtained from Equation 1.

$$\text{Fineness of cement (\%)} = \frac{\text{Weight of retained cement}}{\text{initial weight of cement}} \times 100 \quad (1)$$

2.3.3 Specific Gravity of Aggregates

The test to determine the specific gravity of the aggregates was performed as stipulated in BS EN 1097-2:2010. The samples were screened thoroughly on a 20 mm sieve to remove all deleterious and unwanted particles. An empty bottle was weighed and recorded as W_1 . The sample was transferred into the empty bottle, weighed, and designated as W_2 . The bottle was gradually filled with distilled water to a marked gauge. Thereafter, the bottle was shaken to remove bubbles on the surface of the sample and entrapped air and the weight was recorded as W_3 . Afterwards, the bottle was emptied, and oven-dried. It was then filled with distilled water to the marked gauge, weighed and designated as W_4 . Equation 2 was used to determine the specific gravity.

$$\text{Specific Gravity} = \frac{W_2 - W_1}{(W_4 - W_2) - (W_3 - W_2)} \quad (2)$$

2.3.4 Chemical Composition, Crystallinity, and Micrograph of Samples

The oxide composition and crystallinity of the BLA were determined at the Umaru Musa Yar'adua University Katsina, Nigeria, using an Energy Dispersive X-ray Fluorescence (XRF) Spectrometer with model number Skyray EDX 3600B, and EMPYREAN Diffractometer system EMPYREAN for X-ray Diffraction (XRD) respectively. Scanning Electron Microscopy (SEM) for pozzolanic properties was carried out at Kwara State University, Malete with the aid of a Scanning Electron Microscope with model number ASPEX 3020 at an accelerating voltage of 16.0 kV. A Blazer's sputtering device was used to coat the samples with gold before they were observed under a microscope.

2.3.5 Slump Determination (Workability)

The slump test was carried out on the fresh HPC in conformity to BS EN 12350-2 [25]. The mould was placed on a clean, smooth, horizontal, and non-porous base plate. Concrete was filled into the test mould in three layers with the base held firmly in place using the handles. Each of the layers was compacted uniformly with a rounded end 15 mm steel rod 25 times. Excess concrete at the top of the mould was removed, and the surface levelled. Afterwards, the mould was gradually lifted in the vertical direction while the unsupported concrete slumped. The slump in height at the mid-point of the concrete was measured to the nearest 5 mm.

2.3.6 Compressive Strength Determination

The compressive strength was done in line with BS EN 12390-3 [26]. After 24 hours, the concrete samples were demoulded and fully immersed in water for curing. Only in cases of concrete having a high percentage of superplasticizer were the test specimens left to harden for 48 hours before curing. The specimens were tested for their compressive

strength at 7-, 28- and 56-days of curing. The load was applied gradually at the rate of 140 kg/cm² per minute till the specimens failed. The compressive strength was determined using Equation 3.

$$\text{Compressive strength (N/mm}^2\text{)} = \frac{\text{Maximum load (kN)} \times 1000}{\text{Cross-sectional Area (mm}^2\text{)}} \quad (3)$$

2.3.7 Water Absorption Capacity

The water absorption capacity test was carried out as stipulated in ASTM C642-06 [27]. The specimen was dried in an oven at 100 °C for a period of 48 hours and weighed. The weight was designated as W_1 . Subsequently, the sample was immersed in water for another 48 hours. The samples were weighed at intervals until a constant mass was obtained which was designated as W_2 . Equation 4 was adopted in determining the water absorption capacity of the sample.

$$\text{Water absorption capacity \%} = \frac{W_2 - W_1}{W_1} \times 100 \quad (4)$$

2.3.8 Material Optimization

In optimizing the w/c and percentage of superplasticizer, the goal was to maximize the compressive strength of the concrete while keeping the variables in range. The 56th-day compressive strength results were used.

3. Results and Discussions

3.1 Material Properties

The values obtained for each of the investigations fall within the recommended values by the Standards used for this study: fineness of cement was less than 10%; specific gravity of less than 3.15 and 3.0 for cement and aggregates respectively; fineness modulus of 2.3 - 3.1 and 5.5 - 8.0 for fine and coarse aggregates respectively; and water absorption less than 3% and 0.8% for fine and coarse aggregates respectively.

3.2 Chemical Composition, Crystallinity, and Micrograph of samples

Fig. 4 shows the XRD pattern of the BLA where main Crystalline components sylvite (K_4C_{14}) peaks at 28.440 and 40.53 2θ , Quartz (Si_3O_6) peaks at 26.729 and 40.531 2θ and Calcite ($Ca_6C_6O_{18}$) peaks at 29.37 2θ . This result is similar to the one obtained by Ikumapayi [28]. Fig. 5 shows the SEM images of BLA. The BLA is closely packed, robust-like and honey-combed shaped at a magnification of 750. This is similar to the findings of Ikumapayi [28]. Table 2 shows that the addition of the oxides, Al_2O_3 , Fe_2O_3 , and SiO_2 of BLA utilized in this research, is 70.23 % with SiO_2 having the highest percentage of the oxide composition. This percentage requirement satisfies the requirement of a minimum of 70% for a supplementary cementitious material specified in ASTM C-618 [29] and BS EN 197-1 [30]. Likewise, the percentage composition of SO_3 of 0.43% and Loss of Ignition (LOI) of 6.7% are lesser than the highest limit of 4% and 10% respectively stipulated for pozzolanic additives in ASTM C-618 [29]. These corroborate that BLA is appropriate as pozzolan in concrete. These findings are also in agreement with the submissions of Olutoge and Oladunmoye [9], Adewuyi and Umoh [31], Dhinakaran and Chandana [5] and Asha et al. [7].

3.3 Workability

The 3D image of the connection between the slump height of HPC with varying w/c and varying percentage of superplasticizer is presented in Fig. 6. The slump height was highest

at 1.5% dosage of superplasticizer and declined as the percentage of superplasticizer decreased. Likewise, the slump height increased as the water–cement ratio increased. The graph further reveals that the dosage of superplasticizer has the greatest impact on slump height than the water-cement ratio, thus, improving the workability of the concrete.

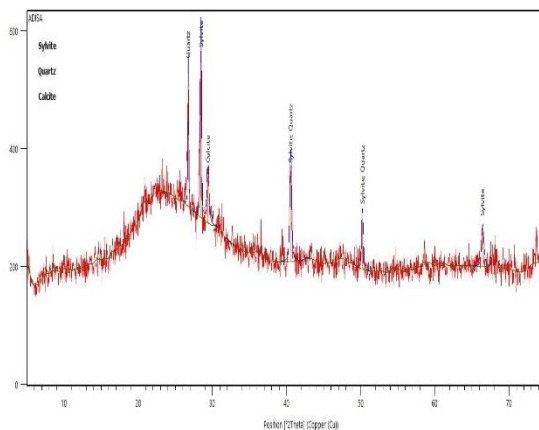


Fig. 4 XRD pattern of BLA

Table 2. Oxide composition of BLA

S/No	OXIDE	PERCENTAGE (%)
1	SiO ₂	49.438
2	Al ₂ O ₃	20.2033
3	K ₂ O	7.321
4	Cl	6.9117
5	CaO	2.598
6	MgO	1.90
7	P ₂ O ₅	1.886
8	CeO ₂	1.694
9	Fe ₂ O ₃	0.5914
10	SO ₃	0.4261
11	MnO	0.2656
12	L.O.I	6.7

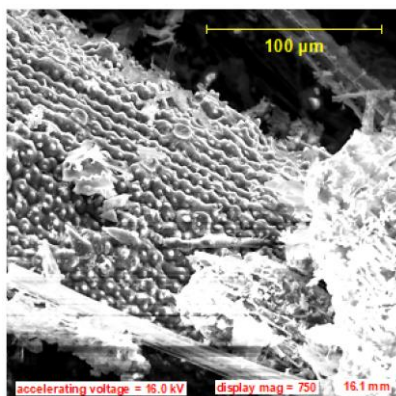


Fig. 5 SEM images of BLA

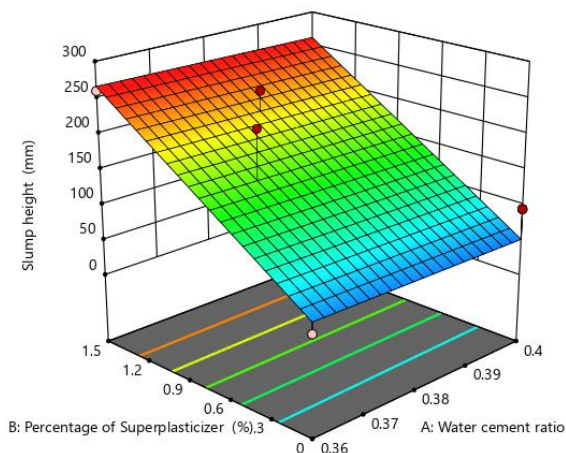


Fig. 6 3D relationship of slump height with varied percentage of superplasticizer and water-cement ratio

3.4 Compressive Strength

Fig. 7 reveals that the compressive strength of HPC after curing for 7 days declined as the measure of superplasticizer increases. Likewise, the compressive strength declined as the w/c increased from 0.36 to 0.38. A high dosage of superplasticizer and w/c had an adverse impact on the compressive strength of the BLA-HPC.

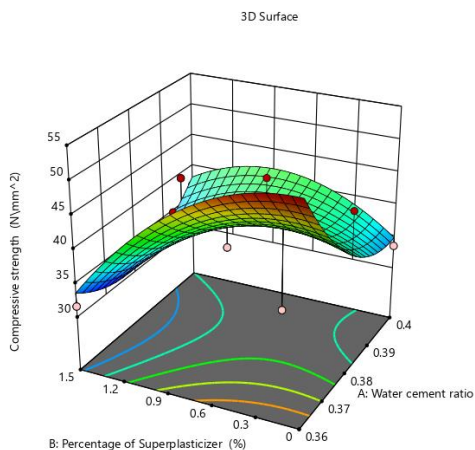


Fig. 7 Compressive strength of BLA-HPC after curing for 7 days

Fig. 8 shows the impact of w/c and percentage quantity of superplasticizer on the compressive strength of HPC after curing for 28 days. The result follows the same trend as was observed in the result obtained on the 7th day of curing.

Fig. 9 displays the 3D connection between compressive strength of HPC at 56 days with w/c and the percentage of superplasticizer. The result follows the same pattern as that of the results obtained on the 7th and 28th days of curing. Therefore, the higher the w/c and dosage of superplasticizer, the lower the strength of the BLA-HPC.

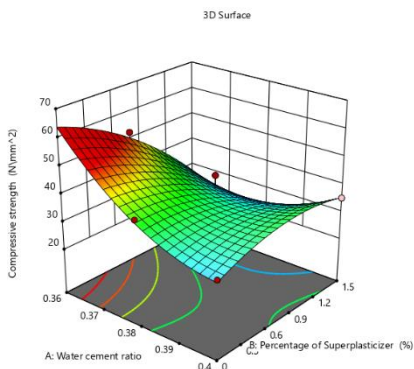


Fig. 8 Compressive strength of BLA-HPC after curing for 28 days

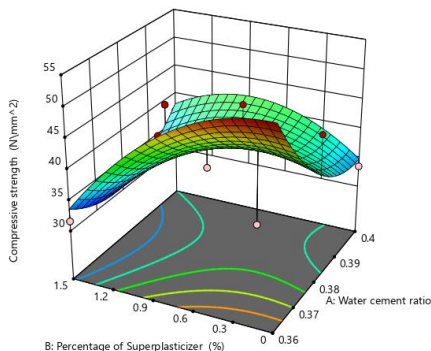


Fig. 9 Compressive strength of BLA-HPC after curing for 56 days

3.5 Water Absorption

Fig. 10 displays the relationship between the water absorption of 56 days cured HPC with the water-cement ratio and percentage of superplasticizer. The water absorption was highest at 1.5% percentage of superplasticizer, the water absorption was lowest at a water-cement ratio of 0.36 and highest at 0.4. Thus, a high dosage of superplasticizer increases the water absorption of HPC. However, the w/c has minimal influence on the water absorption of high-performance concrete.

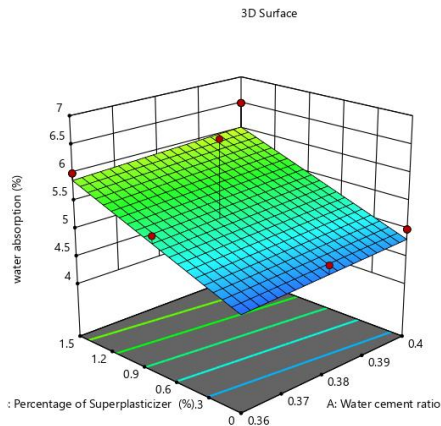


Fig. 10 Water absorption of BLA-HPC

3.6 Material Optimization

Using the test results obtained at 56 days of curing, the materials used for the HPC were optimized as shown in Fig. 11. It was discovered that to maximize the compressive strength of the concrete the optimal combination for the HPC is 0.360 w/c at 0.128 % superplasticizer. This resulted in 49 mm slump height, compressive strength of 53.61 N/mm² and 4.77% water absorption capacity. The compressive strength attained in this study is higher compared to that obtained by Onikeku et al. [8]. However, the study of Onikeku et al. (2019) did not go beyond that of normal concrete having a maximum compressive strength of 38.5 N/mm² (gained at 10% BLA) and curing age of 28 days.

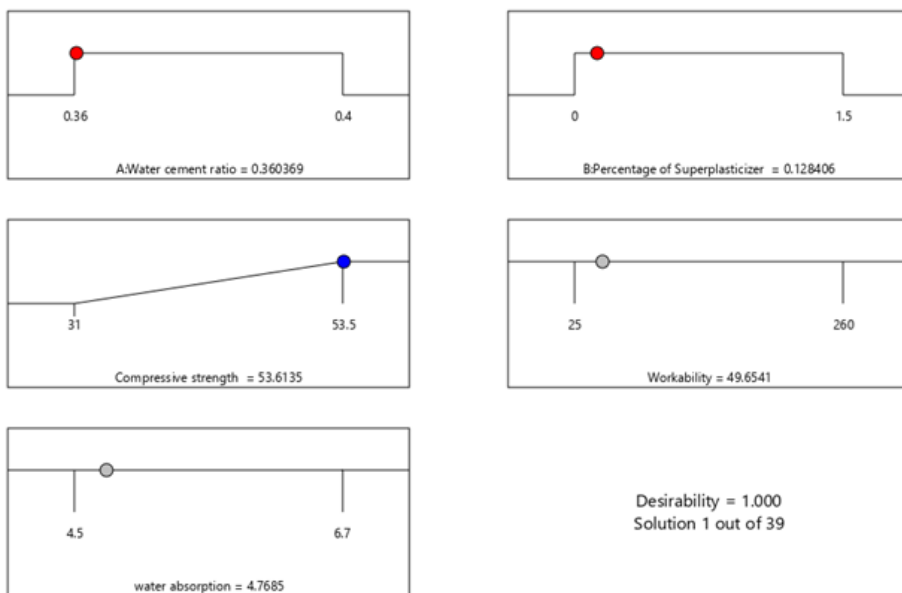


Fig. 11 Optimization of materials

3.7 Normal Probability Plot

The normal probability plot for compressive strength and workability was carried out to determine the normality of the residuals. The plots presented in Fig. 12 and 13 respectively show that normality has been satisfied since most of the plotted points are very close to the fitted line of the distribution. This implies that the normal distribution plot was able to analyze interested responses and explain the variation of the dependent variables and the effectiveness of the model [32,33].

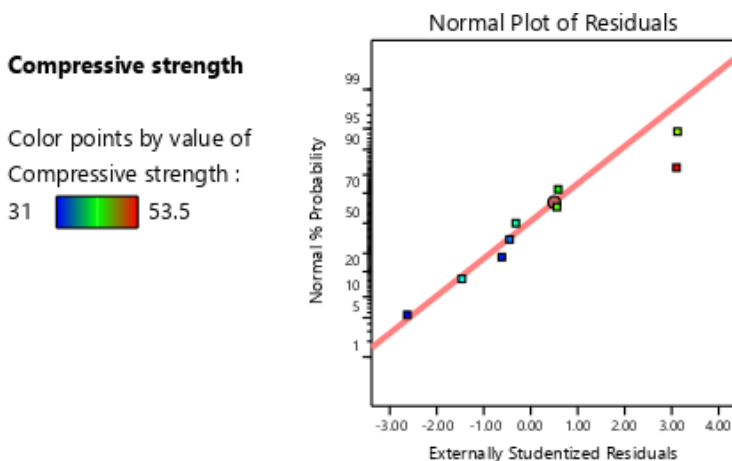


Fig. 12 Normal plot for compressive strength

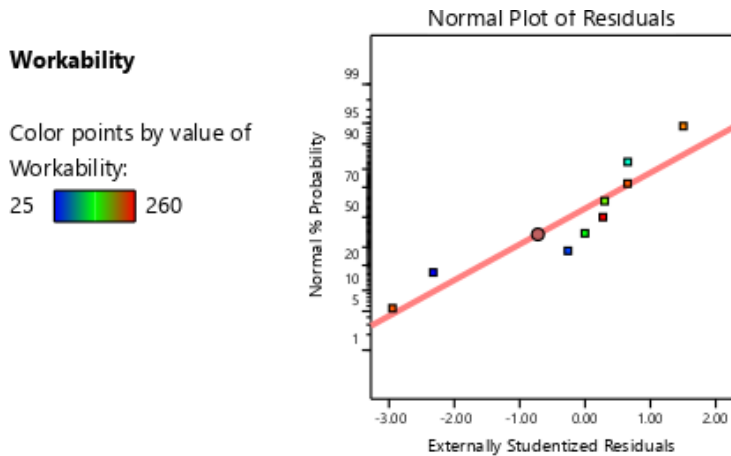


Fig. 13 Normal plot for workability

4. Conclusions

The need for High-Performance Concrete in construction works has increased in recent years. This is mainly due to the demand for large quantity of concrete with a high level of strength for such works. Lots of research have delved into the development of standardized methods of concrete mix design for HPC by adopting different water-binder ratios and dosages of superplasticizers. Nevertheless, none of these studies has reported an optimal quantity for both. Therefore, it is expedient to investigate the water-cement ratio and dosage of superplasticizers for blended Cement-Bamboo leaf ash HPC. For this reason, this study determined the optimal water-cement ratio and dosage of superplasticizers for cement-BLA blended HPC. The percentage of BLA was fixed at 5%, while the percentage of superplasticizer ranged from 0 to 1.5% by weight of cement. The mix of the concrete was designed to attain a strength of 41 N/mm² at 28 days of curing in water. XRD and XRF were employed in obtaining the crystallinity and the chemical constituents of the BLA respectively. The slump of the fresh HPC was also obtained. Concrete cubes were cast and immersed fully in water for 56 days. Water absorption and compressive strengths were established on the fully cured HPC. The inferences drawn from the study are:

- BLA is suitable as a pozzolan in HPC because the addition of the percentages of the oxides of aluminium, ferric and silicon oxides is higher than the minimum 70% stated in BS EN 197-1 [34] and ASTM C618 [29] for supplementary cementitious materials.
- A high dosage of superplasticizers improves the workability while low w/c reduces the workability of the HPC.
- Extreme dosages of superplasticizer decrease the compressive strength of the BLA-HPC while the low water-cement ratio increases its compressive strength.
- High dosages of superplasticizer increase the water absorption capacity of BLA-HPC. However, the w/c has minimal influence on the water absorption of high-performance concrete.
- An optimal combination of the constituent materials of the HPC after curing for 56 days gives 0.360 w/c at 0.128% superplasticizer. This resulted in 49 mm slump height, compressive strength of 53.61 N/mm² and 4.77% water absorption capacity.

References

- [1] Büyüköztürk O, Lau D. High Performance Concrete : Fundamentals and Application. Proc. Int. Conf. New Dev. Concr. Technol., 2002, p. 1-20.
- [2] Odeyemi SO, Anifowose MA, Abdulwahab R, Oduoye WO. Mechanical Properties of High-Performance Concrete with Guinea Corn Husk Ash as Additive. LAUTECH J Civ Environ Stud 2020; 5: 139-54. [https://doi.org/10.36108/laujoces/0202/50\(0131\)](https://doi.org/10.36108/laujoces/0202/50(0131))
- [3] Odeyemi SO, Giwa ZT, Abdulwahab R. Building Collapse in Nigeria (2009- 2019), Causes and Remedies - A Review. USEP J Sci Eng Prod 2019; 1: 123-35.
- [4] Akeju TAI, Falade F. Utilization of Bamboo as Reinforcement in Concrete for Low-Cost Housing. Proc. Int. Conf. Struct. Eng. Mech. Comput., 2001, p. 1463-70. <https://doi.org/10.1016/B978-008043948-8/50164-8>
- [5] Dhinakaran G, Chandana GH. Compressive strength and durability of bamboo leaf ash concrete. Jordan J Civ Eng 2016;10:279-89. doi:10.14525/jjce.10.3.3601. <https://doi.org/10.14525/JJCE.10.3.3601>
- [6] Villar-Cociña E, Morales EV, Santos SF, Savastano Jr. H, Frías M. Pozzolanic behavior of bamboo leaf ash: Characterization and determination of the kinetic parameters. Cem Concr Compos 2011;33:68-73. <https://doi.org/10.1016/j.cemconcomp.2010.09.003>
- [7] Asha P, Salman A, Kumar RA. Experimental Study on Concrete with Bamboo Leaf Ash. Int J Eng Adv Technol 2014;3:2249-8958.
- [8] Onikeku O, Shitote SM, Mwero J, Adedeji AA. Evaluation of Characteristics of Concrete Mixed with Bamboo Leaf Ash. Open Constr Build Technol J 2019; 13: 67-80. <https://doi.org/10.2174/1874836801913010067>
- [9] Olutoge FA, Oladunmoye OM. Bamboo Leaf Ash as Supplementary Cementitious Material. Am J Eng Res 2017; 6: 1-8.
- [10] Hunchate SR, Chandupalle S, Ghorpode VG, Venkata Reddy TC. Mix Design of High Performance Concrete Using Silica Fume and Superplasticizer. Int Journal Innov Res Sci Eng Technol 2014;3:10735-42.
- [11] Dembovska L, Bajare D, Pundiene I, Vitola L. Effect of Pozzolanic Additives on the Strength Development of High Performance Concrete. Procedia Eng 2017;1 72: 202-10. <https://doi.org/10.1016/j.proeng.2017.02.050>
- [12] Latha MS, Naveen Kumar BM, Madihalli R, Deepika R, Rudraswamy MP. Strength characteristics of high performance concrete using bagasse ash and slag sand. Int J Emerg Trends Eng Res 2020; 8: 2486-2489. <https://doi.org/10.30534/ijeter/2020/45862020>
- [13] Zhutovsky S, Kovler K. Influence of water to cement ratio on the efficiency of internal curing of high-performance concrete. Constr Build Mater 2017; 144: 311-6. <https://doi.org/10.1016/j.conbuildmat.2017.03.203>
- [14] Richard P, Cheyrezy M. Reactive powder concretes with high ductility and 200-800 MPa compressive strength. Concrete technology: Past, present, and future. Proc. V. Mohan Malhotra Symp. Am. Concr. Institute., 1994, 507-18.
- [15] Larrard F, Sedran T. Optimization of ultra-high performance concrete by the use of a packing model. Cem Concr Res 1994; 24: 997-1009. [https://doi.org/10.1016/0008-8846\(94\)90022-1](https://doi.org/10.1016/0008-8846(94)90022-1)
- [16] Droll K. Influence of additions on ultra-high performance concretes-grain size optimization. Proc. Int. Symp. UHPC, Kassel, Ger., 2004, 285-301.
- [17] Wen-yu J, Ming-zhe A, Gui-ping Y, Jun-min W. Study on reactive powder concrete used in the sidewalk system of the Qinghai-Tibet Railway bridge. Int. Work. Sustain. Dev. Concr. Technol. Beijing, China, 2004, 333-338.
- [18] Gao R, Liu Z, Zhang L, Stroeven P. Static properties of reactive powder concrete beams. Key Eng Mater 2006; 302: 521-527. <https://doi.org/10.4028/www.scientific.net/KEM.302-303.521>

- [19] Wille K, Naaman A, Montesinos G. Ultra-high performance concrete with compressive strength exceeding 150 MPa (22 ksi): a simpler way. *ACI Mater J* 2011;108:46-54. <https://doi.org/10.14359/51664215>
- [20] Shi C, Wu Z, Xiao J, Wang D, Huang Z, Fang Z. A review on ultra high performance concrete: Part 1. Raw materials and mixture design. *Constr Build Mater* 2015;101:741-751. <https://doi.org/10.1016/j.conbuildmat.2015.10.088>
- [21] Schmidt D, Dehn F, Urbonas L. Fire resistance of ultra-high performance concrete (UHPC)-testing of laboratory samples and columns under load. *Proc. Int. Symp. UHPC, Kassel, Ger., 2004*, p. 703-15.
- [22] British Standard Institution. BS EN 12390-3:2019. Test Hardened Concr Compressive Strength Test Specimens 2019.
- [23] ASTM. ASTM C494/C494M – 19: Standard Specification for Chemical Admixtures for Concrete. 2019.
- [24] BS EN 196-3 B. Methods of testing cement part 3: Determination of setting times and soundness. 2016.
- [25] BS EN 12350-2:2009. Testing fresh concrete. Slump-test. London, UK: 2009.
- [26] BS EN 12390-3. Testing hardened concrete. Compressive strength of test specimens. 2019.
- [27] ASTM International - ASTM C642-06. Standard Test Method for Density, Absorption, and Voids in Hardened Concrete. 2006.
- [28] Ikumapayi CM. Chemical and Microstructural Effects of Different Calcinating Temperatures on Selected Pozzolans. *J Mater Sci Chem Eng* 2018;06:16-31. doi:10.4236/msce.2018.612002. <https://doi.org/10.4236/msce.2018.612002>
- [29] ASTM C-618. Standard specification for testing Pozzolanas. American Society for Testing and Materials. 2001.
- [30] BS EN 197-1:2011 B. Cement composition, Specifications and conformity criteria for common cements. 2019.
- [31] Adewuyi TO, Umoh AA. Influence of Bamboo Leaf Ash Blended Cement. *J Eng Technol* 2016;7:18-29.
- [32] Bradley N. *The Response Surface Methodology*. 2007.
- [33] Atoyebi OD, Osuolale OM, Ibitogbe EM. Strength Evaluation of Cocos nucifera Fibre Reinforced Concrete. *J Eng Appl Sci* 2019;14:8061-8066. <https://doi.org/10.36478/jeasci.2019.8061.8066>
- [34] BS EN 197-1:2011. Cement-Composition, specifications and conformity criteria for common cements, British Standards. 2011.

Blank Page



Research Article

Fracture behavior of plain and fiber-reinforced high strength concrete containing high strength steel fiber

P.N. Ojha^a, Pranay Singh^b, Brijesh Singh^{*c}, Abhishek Singh^d, Piyush Mittal^e

National Council for Cement and Building Materials, India

Article Info

Article history:

Received 28 Dec 2021

Revised 18 Jan 2022

Accepted 13 Feb 2022

Keywords:

Fiber-reinforced concrete;
Fracture Energy;
High strength concrete;
Characteristic Length;
Load-Deflection;
Load-CMOD

Abstract

With the increase in strength, concrete explodes spontaneously at failure creating a serious safety hazard. Researchers are actively looking for methods to arrest the cracks in concrete and design a higher strength concrete that fails in a more ductile fashion. Fiber-reinforced concrete has emerged as one of the solutions to this problem. This paper presents findings from the experimental investigation conducted to compare the fracture behavior of plain and fiber-reinforced high strength concrete of varying compressive strength. Six different concrete mixes were prepared with w/b ratios of 0.47, 0.36, and 0.20 resulting in average compressive strength of 36, 52, and 92 MPa. Each mix consists of two variations, first without fiber and second with 1% of steel fiber by volume. The mixes were tested for their strength and fracture behavior using various standard codes and recommendations. From the Load-deflection and Load-CMOD (Crack Mouth Opening Displacement) curves obtained from the study, Fracture parameters like Fracture energy, Stress intensity factor, energy release rate, and Characteristic length is evaluated and compared for plain and Steel fiber reinforced concrete. It was found that adding steel fiber significantly improves the fracture properties of the concrete of different compressive strengths. By adding 1% of steel fiber in the high-strength concrete, the average fracture energy increased by 850%, 770%, and 450% respectively for the concrete with compressive strength of 36, 52, and 92 MPa. Other parameters also show a very significant improvement suggesting fiber reinforcement as a suitable choice to prevent brittle failure and increase the fracture performance of high strength concrete.

© 2022 MIM Research Group. All rights reserved.

1. Introduction

Concrete shows many desirable properties like good compressive strength, high durability, ability to be cast in any shape, and comparatively lower cost than other construction materials. All these qualities have made concrete a universal construction material almost integral to every construction project. But one of the major limitations of concrete is its brittle nature and low crack resistance. This limits its ability to take the flexural load and makes it extremely dangerous under extreme events like earthquakes [1, 2]. Due to this weakness, concrete structures under flexural loads are susceptible to getting cracked and fail spontaneously without warning. The strain capacity of concrete further reduces for high strength concrete. High strength concrete shows better properties in terms of compressive strength, Abrasion, toughness, and impact than normal concrete [3–5]. But its ductility and crack resistance reduce drastically with strength increase, leading to sudden failure.

One of the quantitative estimations of brittleness and ductility of concrete is its fracture properties. RILEM [6, 7] proposes a three-point bending test on a notched beam to find the

*Corresponding author: brijeshshwagi96@gmail.com

^aorcid.org/0000-0003-1754-4488; ^borcid.org/0000-0001-6169-9482; ^corcid.org/0000-0002-6512-1968;

^dorcid.org/0000-0002-2343-5934; ^eorcid.org/0000-0002-1994-0946

DOI: <http://dx.doi.org/10.17515/resm2022.377ma1228>

Res. Eng. Struct. Mat. Vol. 8 Iss. 3 (2022) 583-602

fracture parameters for concrete. Fracture energy is one of the most important fracture parameters and it can be defined as a parameter to analyze and compare the toughness and cracking resistance of the concrete. As per RILEM, Fracture energy is the amount of energy necessary to create a unit area of crack [6]. Other fracture parameters are fracture toughness, Energy release rate, and characteristic length. Fracture toughness refers to the resistance of brittle materials to the spread of cracks. The energy release rate is the rate at which the energy is transformed with the fracture propagation in the material. Characteristic length is one of the measures of the brittleness of the concrete, a concrete can be considered more brittle if it shows a lower characteristic length [8].

Various work has been done in past to measure these fracture parameters and correlate them with the ductility and crack resistance of the concrete. Trevidi et al. [9] compared three different approaches i.e., Rilem method, Bi-linear approximation, and energy release rate to investigate the size-independent fracture energy of concrete and found almost similar results suggestion any one of these can be used to calculate the size-independent fracture energy of concrete. Khalilpour et al. [10] further compared the number of available methods of determination of fracture parameters and reviews the factors affecting these parameters. Yin et al. [11] presents Four-point bending tests for the fracture properties of concrete. Murthy et al. [12] studied the fracture energy and tension softening relation for nano-modified concrete. This study compared the different methods of fracture energy determination and concluded that the notch to depth ratio has a significant impact on the specific fracture energy determined using the RILEM work-of-fracture technique. Kaya et al. [13] studied the effects of temperature and deformation rate on fracture behavior of S-2 glass/epoxy laminated composites. The study presents a Finite Element Method based approach to find the fracture parameters and compares the experimental and FEM-based results.

The effect of adding different types of fibers in the concrete on its fracture behavior has been discussed by many researchers. Almusallam et al. [14] performed an analytical and experimental investigation on fracture behavior of concrete containing steel, Kevlar, and polypropylene and found better fracture properties. Mousavi et al. [15] studied fracture properties of concrete under varying steel fiber content as well as water to cementitious content ratio and suggests that with the decrease in w/b ratio fracture energy decreases for plain concrete but increases for fiber reinforced concrete. Arslan [16] studied the fracture behavior of basalt fiber reinforced concrete (BFRC) and glass fiber reinforced concrete (GFRC). BF and GF addition considerably increase the fracture energy of test specimens compared to Reference specimens. Noaman et al. [17] studied the Fracture characteristics of plain and steel fiber reinforced rubberized concrete. Only up to a certain degree of replacement does the fracture energy of plain and steel fiber concrete rise. Because of the loss of strength in the cement matrix, the fracture energy decreases slightly after this replacement ratio. The fracture energy of plain concrete is significantly increased when rubber aggregate is combined with hooked-end steel fiber. Wtaife et al. [18] studied the Fracture Mechanism of fiber Reinforced Concrete Pavement based on a RILEM Design Approach. Despite having relatively low ultimate moment capacities, the ultimate moment capacities increase as the volume fraction of fiber increases.

Studies on the effect of silica fume and fly ash addition along with cement as a binder material in concrete and aggregate size distribution on its fracture behavior are reported by various researchers. Gil et al. [19] studied the effect of Silica Fume and Siliceous Fly Ash Addition on the Fracture Toughness of Plain Concrete. His finding suggests an optimum dose of Silica fume and Flyash for maximum strength and fracture toughness. Siregar et al. [20] studied the effects of aggregate size distribution on the fracture behavior of high-strength concrete. The ductility level of high-strength concrete is influenced by the

aggregate size distribution and w/b ratio also the maximum value of fracture energy is related to the maximum strength of the aggregate.

Fracture properties variations on concrete exposed to higher temperatures have been studied in past. Tang et al. [21] examined Fracture behavior of recycled concrete with waste crumb rubber subjected to elevated temperatures. At ambient temperature Rubber modified Recycled aggregate concrete (RRAC) shows an increasing trend in fracture energy with increasing content of recycled aggregate. After exposure to high temperature, the fracture energy of RRAC was lower than Rubber modified Natural aggregate concrete (RNAC). With the increase in temperature, a decrease in fracture energy was reported in the study. Yu et al. [22] studied the Fracture properties of high-strength/high-performance concrete (HSC/HPC) exposed to high temperatures. Concrete's characteristic lengths dropped linearly with the temperature rise, indicating a reduction in brittleness. At all temperatures, the characteristic length of lower strength concrete sample was greater than that of a higher strength sample, indicating that the brittleness of concrete increased with compressive strength.

Tran et al.[23] Fracture energy of ultra-high-performance fiber-reinforced concrete (UHPC) at high strain rates. The UHPCs' fracture strength and specific work-of-fracture values were extremely sensitive to the applied strain rates, but their softening fracture energies were not much affected. The fracture process of recycled concrete was thoroughly investigated by Guo et al. [24] and compared to that of conventional concrete of the same structural class. In recycled aggregate concrete, higher strain gradients are seen in the localized damage zone. Strong discontinuities or existing fractures in recycled aggregate aid in the identification of the primary crack. Because fracture occurs at the aggregate-mortar interface, the recycled aggregate concrete's larger strain gradient and poor stiffness suggest a weak interface between the new mortar and recycled aggregate, which is attributed to excessive porosity and existing fractures.

In the present study, six different mixes were prepared with three w/b (water to binder) ratios. The w/b ratios adopted are 0.47, 0.36 and 0.20. These three mixes represent concrete with compressive strength above 30 MPa, 50MPa, and 90 MPa. For each of these w/b ratios, two sets of concrete samples were prepared – one without steel fiber and one with 1% steel fiber by volume. Using the three-point bend test suggested by RILEM[6] and Tada et al. [25], fracture energy is calculated. Other fracture parameters like characteristic length, critical energy release rate, and stress intensity factors are evaluated using literature [7, 25–28]. The results are compared for plain and fiber reinforced concrete. Apart from these, 28-day cube and cylindrical compressive strength and split tensile strength are also evaluated for each sample using the Indian Standard code [29, 30].

2. Materials

In this study OPC cement, Coarse and Fine aggregates, Fly ash, Silica Fumes, Superplasticizer, water, and steel fiber are used for making concrete mixes. This section provides details of the materials used in the study.

2.1. Cementitious Materials

Ordinary Portland Cement of OPC 53 grade as per IS 269-2015 [32] is used along with fly ash and silica fume. 28-day compressive strength of cement was 36.0 MPa and specific gravity was 3.16. Fly ash and silica fume have the fineness of 403 and 22000 and specific gravity of 2.2 and 2.24 respectively. Detailed physical and chemical properties of cement, fly ash, and silica fume is given in Table 1.

Table 1. Physical, chemical and strength characteristics of cementitious materials

Characteristics	OPC -53 Grade	Silica Fume	Fly Ash
Physical Tests			
Fineness Blaine's (m ² /kg)	320.00	22000	403
Soundness Autoclave (%)	00.05	-	-
Soundness Le Chatelier (mm)	1.00	-	-
Setting Time Initial (min.) & (max.)	170.00 & 220.00	-	-
Specific gravity	3.16	2.24	2.2
Chemical Tests			
Loss of Ignition (LOI) (%)	1.50	1.16	0.4
Silica (SiO ₂) (%)	20.38	95.02	60.95
Iron Oxide (Fe ₂ O ₃) (%)	3.96	0.80	5.70
Aluminium Oxide (Al ₂ O ₃)	4.95	-	26.67
Calcium Oxide (CaO) (%)	60.73	-	2.08
Magnesium Oxide (MgO) (%)	4.78	-	0.69
Sulphate (SO ₃) (%)	2.07	-	0.29
Chloride (Cl) (%)	0.04	-	0.009
IR (%)	1.20	-	-
Moisture (%)	-	0.43	-

2.2. Aggregates

Crushed aggregate with a maximum nominal size of 20mm is utilized as coarse aggregate and crushed fine aggregate conforming to Zone II as per IS: 383-2016 [33] was employed as fine aggregate in the study. Fine aggregate has been shown in figure 1(a) and figure 1(b) shows the coarse aggregate. The physical properties of both coarse and fine aggregate are presented in Table-2.



Fig. 1 (a) Crushed fine aggregate (b) Granite coarse aggregate

Table 2. Properties of aggregates

Property	Granite		Fine Aggregate
	20 mm	10 mm	
Specific gravity	2.83	2.83	2.65
Water absorption (%)	0.3	0.3	0.59
Sieve Analysis Cumulative Percentage Passing (%)	20mm	98	100
	10 mm	1	68
	4.75 mm	0	2
	2.36 mm	0	0
	1.18 mm	0	0
	600 μ	0	0
	300 μ	0	0
	150 μ	0	0
	Pan	0	0
Abrasion, Crushing & Impact Value	19,19,13	-	-
Flakiness % & Elongation %	29, 25	-	-

2.3. Steel Fiber

The trough and hooked end-shaped steel fibers are used. Some of the previous studies suggest these fibers be more efficient with improved pull-out resistance and toughness compared to straight end fibers. The fibers are 0.55 mm in diameter and 35 mm in length. It has an aspect ratio of 63 which is as per ASTM A-820 [34]. The tensile strength of the fibers as per the manufacturer is 1486.99 N/mm². Figure 2 shows the steel fiber added to the concrete mix. The figure on the left shows the fibers as available from the industry and the figure on the right shows a single steel fiber.

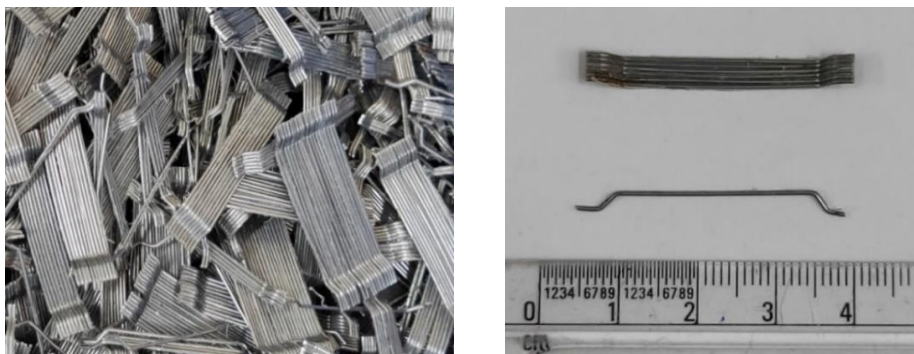


Fig. 2 Steel Fiber added to the concrete

2.4. Superplasticizer

A polycarboxylic group-based superplasticizer is used in the study for all the w/b ratios as per Indian Standard IS:9103[35].

3. Mix Design and Specimen Details

3.1. Mix Design

Six different sets of mixes were prepared with a w/b ratio of 0.47, 0.36, and 0.20. These different types of concrete mixes were prepared in two variations-(i) plain concrete and (ii) concrete with 1% steel fiber. The fresh concrete's slump was regulated between 75 and 100 mm. Based on the slump cone test as per Indian Standard, IS 1199: Part 2 [36], a pre-study was conducted to identify the best superplasticizer dose for obtaining the requisite workability. The amount of steel fiber added to the concrete was adopted based on past studies suggesting it as an economical and optimum dose for maximum improvement in overall mechanical parameters [35, 36].

Table 3 lists the concrete mix data for the sample. Water content has been decreased and cementitious content has been increased to get a higher strength concrete. Also, in the case of a mix with a w/b ratio of 0.20, silica fume has been added to obtain a much higher strength of the concrete. Silica fume was added to improve the mechanical properties, particularly the compressive strength of high-strength concrete [39].

Table 3. Mix design details

Fibers % by volume of concrete	w/b	Total Cementitious Content [Cement C + Flyash (FA) + Silica Fume (SF)] (Kg/m ³)	Ratio of silica fume to flyash (SF /FA)	Water Conten t (Kg/m ³)	Admixt ure % by weight of Cement	Fine Aggregate as % of Total Aggregate by weight
Without Fibers	0.47	362 (290+72+0)	-	170	1.00	35
	0.36	417 (334+83+0)	-	150	0.45	39
	0.20	750 (548+112+90)	0.80	150	1.75	35
1% steel fiber	0.47	362 (290+72+0)	-	170	1.00	35
	0.36	417 (334+83+0)	-	150	0.45	39
	0.20	750 (548+112+90)	0.80	150	1.75	35

As an adjustment for aggregate water absorption, a change was made to the amount of added water. The concrete mixes for the investigations were made in a pan-type concrete mixer. The molds were adequately coated with mineral oil before usage, and casting was done in three layers, each of which was compressed on a vibration table to reduce air bubbles and voids. The specimens were removed from their separate molds after 24 hours. Temperature and relative humidity were measured in the laboratory at 27^o+2^o C and relative humidity of 65 percent or greater at various ages. The specimens were removed from the tank and allowed to dry on the surface before being tested in a saturated surface dried state.

3.2. Specimen Details

Different specimens were made for different tests as per specifications in the standard codes, international recommendations, and literature.

Concrete cubes of size 150 mm x 150 mm x 150 mm are cast to find 28-day compressive strength as per IS 516[30].

Concrete cylinders of size 150 mm diameter and 300 mm height are cast to find the 28-days compressive strength of the concrete as per IS 516[30].

Concrete beams of size 100mm x 100mm x 500mm are cast for a 3-point bending test at 28-days to evaluate the fracture parameters using various proposed procedures as

discussed in the introduction section. 24 hours before testing a notch of 35mm is made in the beam. Table 4 shows specimen details and Figure 3 shows the freshly prepared concrete specimens in molds.

Table 4. Specimens details and experiments in the study

S.No.	Specimen	Dimension(mm)	Tests
1	Concrete Cubes	150 x150 x 150	28-Day compressive strength
2	Concrete Cylinders	150D x 300H	28-Day compressive strength Split Tensile strength
3	Concrete Beams	100 x 100 x 500	3 - Point bend test to evaluate fracture Parameter



Fig. 3 Concrete cubes, cylinders, and beams in molds



Fig. 4 Notched beam sample

4. Experimental Procedure

The following section details the adopted procedures for conducting the experiments. In the present study compressive strength test, split tensile strength test and 3-Point bend test on notched beams are performed. Findings and derivation of other parameters are given in the next section, i.e., the results and discussion section.

4.1. Compressive strength test and split tensile strength test

The compressive strength of cylindrical and cubical specimens was evaluated at 28-days as per IS: 516 [30]. And the split tensile strength of the cylindrical concrete specimen was evaluated as per the testing procedure of IS: 5816-1999 [31] on the cylindrical specimen at 28 days. These tests were performed on a set of three specimens and the average value has been presented in the study.

4.2. Three-point bending test to evaluate fracture parameters

For calculating the fracture parameters, a 3-point bending test based on the method proposed by RILEM [6, 7] was used. Various fracture parameters were evaluated from the tests and are discussed in the subsequent sections. Figure 5 shows a schematic diagram for the three-point bend test and figure 6 shows the laboratory arrangement for the conducted test. As presented in figure 5, a beam of dimension 100mm x 100mm x 500mm with a notch of 35mm at the mid-span was used. 400 mm of the clear span was considered and the load

was applied using a displacement control machine of capacity 300 Kn. Deflection at the mid-span of the beam was measured using LVDT and Crack Mouth Opening Displacement (CMOD) was measured using clip gauge placed at the bottom of the beam and fixed in position by two steel knife edges as shown in figure 6(b). In the present study, a total of eighteen beams has been tested which includes 3 beams for each of the mix presented in Table 3.

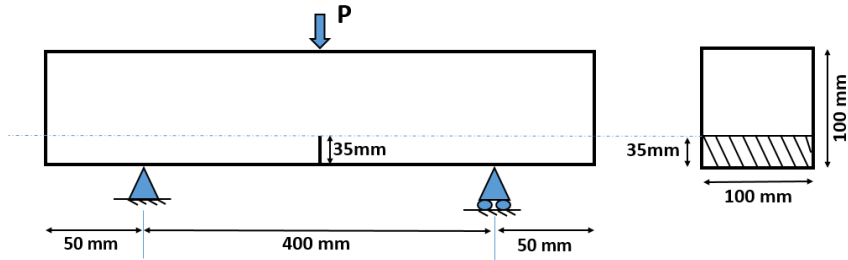


Fig. 5 Sample specification for 3-point bending test

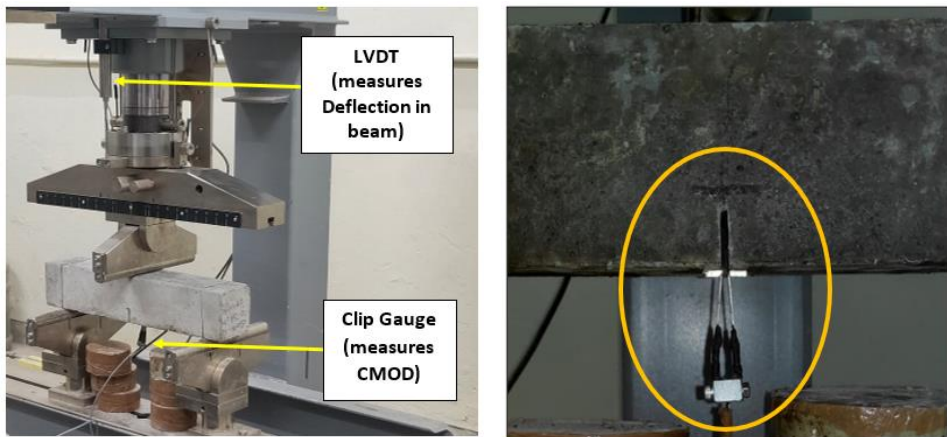


Fig. 6 (a) Test setup three-point bending test, and (b) Clip gauge measuring CMOD

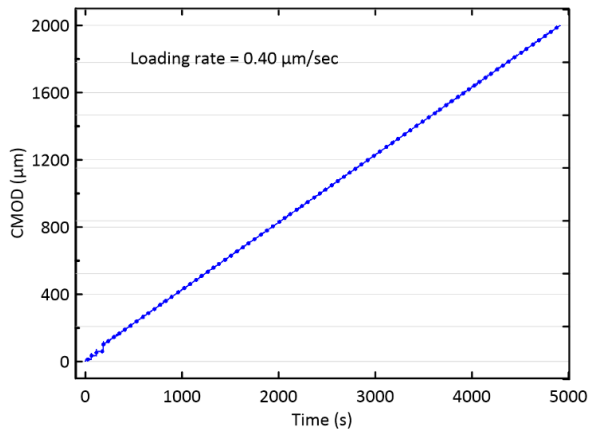


Fig. 7 CMOD vs time plot for the test

Figure 7 shows the CMOD vs time plot for the test. As described earlier the displacement-controlled test was adopted for this study and load was applied in such a manner that gives a constant increase in CMOD ($0.40\mu\text{m/s}$) with time as shown above. The test was performed till the beam failed or a maximum CMOD of $2000\mu\text{m}$ is reached.

5. Results and Discussions

5.1. Compressive strength test and split tensile strength test

The cube compressive strength of mix with w/b ratio of 0.47, 0.36, and 0.20 are 37 MPa, 53 MPa, and 92 MPa respectively. Adding steel fiber does not considerably increase the compressive strength and only a marginal increase of not more than 10% is observed for any of the mixes. A similar marginal increase is observed in the split tensile strength of the mixes with and without steel fiber. By addition of steel fiber, split tensile strength of the mix with w/b ratio 0.47, 0.36, and 0.20 increased by 2%, 2%, and 4% respectively. Table 5 shows the results of the cube and cylindrical compressive strength and split tensile strength.

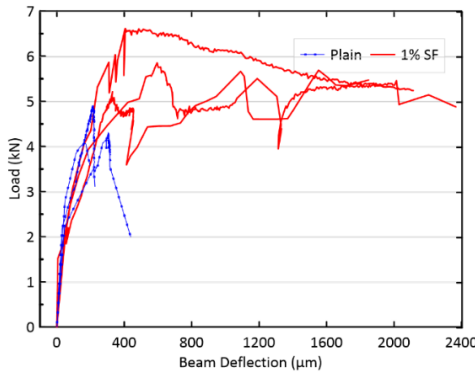
Table 5. Cube and cylindrical compressive strength and split tensile strength

W/B ratio	Type	28-day strength (MPa)		
		Cube Strength	Cylinder strength	Split Tensile Strength
0.47	Plain	36.90	27.62	3.37
0.47	Steel fiber	37.40	28.25	3.95
0.36	Plain	51.60	39.30	4.04
0.36	Steel fiber	53.20	44.87	4.73
0.2	Plain	92.20	78.29	5.35
0.2	Steel fiber	91.70	68.97	7.19

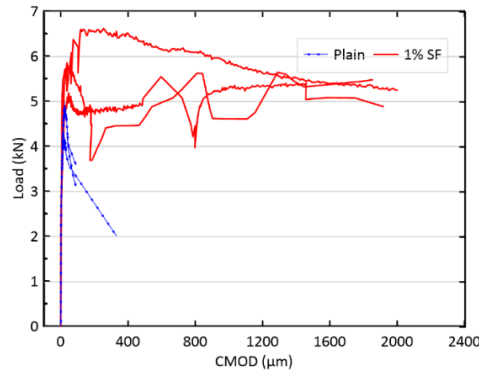
5.2 Load-Deflection and Load-CMOD Behavior

In the present section, the Load-Deflection and Load-CMOD behavior of three beams each for a w/b ratio (0.47, 0.36 and 0.20) and fiber content (0% and 1%) is presented in figure 8, 9, and 10 respectively. As can be seen from these diagrams that for the w/b ratio of 0.47, the curve is uneven for fiber-reinforced beam, and it smoothies as the strength increases. The possible cause for this behavior can be attributed to the slipping of fiber from the concrete and uneven load distribution and sudden load transfer among concrete and fibers with the increase in CMOD at a lower strength. At higher strength, fibers and concrete matrix act as a single unit resulting in a smoother curve.

Another important observation is the variability of the results for fiber-reinforced beams. As can be seen in the plots that all the three beams of normal strength concrete show almost a similar characteristic in their behavior suggesting homogeneity in all three beams. But this cannot be assured for the fiber reinforced concrete as the orientation and distribution of fibers cannot be perfectly homogenized for all three beams. With the addition of steel fiber, the strain capacity of the beam increases, and with the increase in compressive strength, Peak-load increases. Both of these factors increase the area under the load-deflection curve increasing the fracture energy as discussed in the next section.

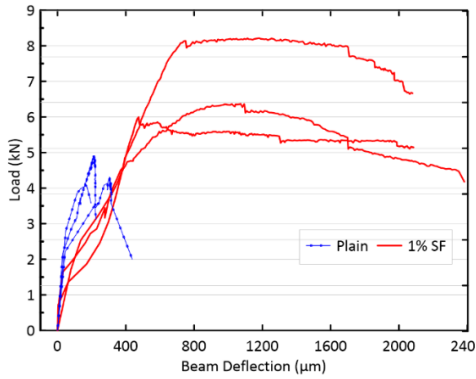


(a) Load - deflection curve

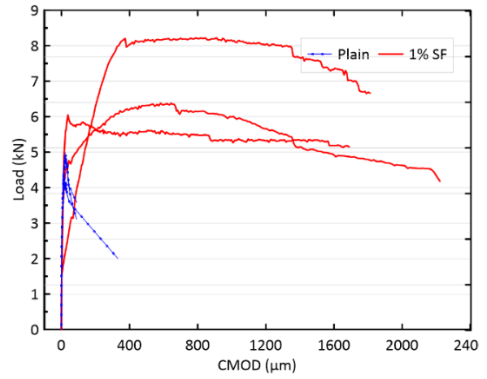


(b) Load CMOD curve

Fig. 8 W/B ratio 0.47

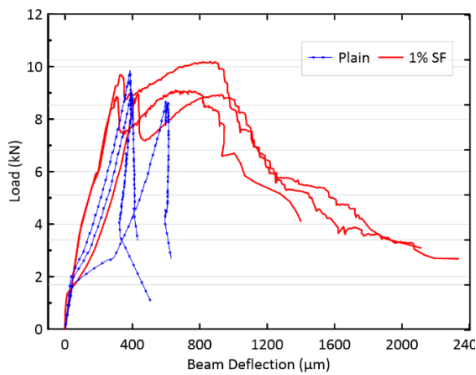


(a) Load - deflection curve

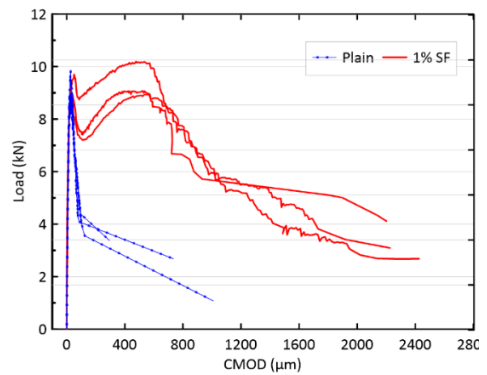


(b) Load CMOD curve

Fig. 9 W/B ratio 0.36



(a) Load - deflection curve



(b) Load CMOD curve

Fig.10 W/B ratio 0.20

5.3 Fracture Energy

Fracture energy, represented as G_f is defined as the energy required to produce a unit crack in the specimen. It is one of the basic properties of the material which can be used to analyze and determine the toughness, brittleness, and cracking resistance of the concrete. From RILEM 50-FMC [6] fracture energy can be calculated from the equation (1);

$$G_f(N/m) = (W_o + mg\delta_o)/A_{lig} \tag{1}$$

Here in equation (1) G_f refers to the fracture energy, W_o is the area under the load-deformation curve for the beam as shown in figure 7. m is the total weight of the beam between the support and weight of the part of loading arrangement which is not attached to the machine, but follows beam until failure. g is the acceleration due to gravity, i.e., 9.81 m/s^2 . δ_o is the deformation of the beam at the final stage of failure and A_{lig} is the area of the ligament which is the area of the projection of fracture zone on the plane perpendicular to the beam axis, as represented by the shaded region in Figure 11.

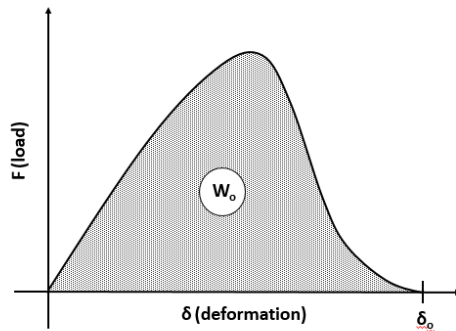


Fig. 11 Area under force and beam mid-point deflection (deformation) curve

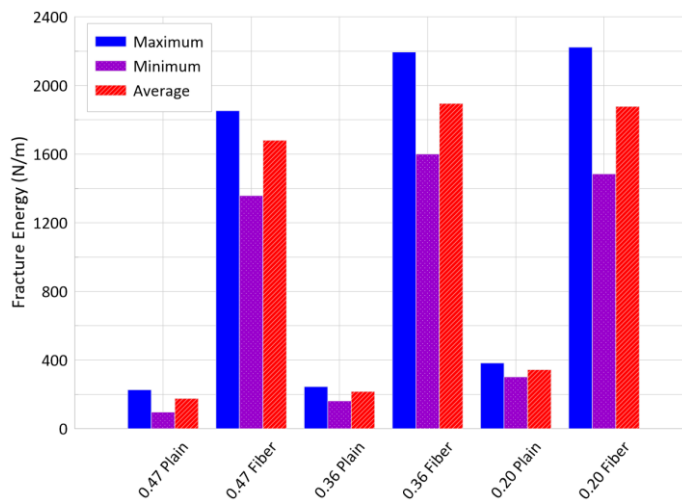


Fig. 12 Obtained fracture energy for w/b ratio of 0.47, 0.36 and 0.20

Figure 12 depicts a comparison between the obtained fracture energy for mix with different w/b ratios and fiber content. As can be observed from the figure addition of fibers significantly increases the fracture energy of the notched beam. An increasing trend in fracture energy can also be with an increase in concrete's compressive strength. An increase in fracture energy due to fiber addition is caused by a much larger strain value for the fiber-reinforced beam than the normal beam. And with the increase in compressive strength the maximum load taking capacity of the beam increases which results in higher fracture energy. The increase in fracture energy is about 9.5 times for the w/b ratio of 0.47, whereas it is only 8 times for 0.36 and 5 times for 0.20. With the increase in compressive strength relative benefit of adding fiber reduces because concrete at higher strength is itself capable of taking a higher bending load than a low strength concrete.

Previous literature [26] suggests an increase of about 8 times in fracture with the addition of steel fiber in normal concrete. The fracture energy reported for a concrete sample with compressive strength of 54 MPa was 271.4 N/m which increased to 2183.0 N/m, similar results were observed in our study also.

5.4 Initial Compliance and Modulus of Elasticity

The Modulus of Elasticity of the notched beams is calculated using equation (2) as presented by [38].

$$E \text{ (MPa)} = 6S \frac{\alpha V_1(\alpha)}{C_i db^2} \tag{2}$$

Where C_i is the initial compliance which is the inverse of the slope of the initial straight portion of the Load vs CMOD curve. Figure 13 shows the calculation of the slope of the initial straight portion of the Load-CMOD curve. $V_1(\alpha)$ is calculated using the equation (3) given by Tada et al. [25] as follow:

$$V_1(\alpha) = 0.76 - 2.28a + 3.87a^2 - 2.04a^3 + \frac{0.66}{(1 - a)^2} \tag{3}$$

Table 6. Initial compliance and modulus of elasticity

W/ B ratio and fiber	Cube compressive strength (MPa)	Initial compliance C_i (10^{-9} m/N)	Modulus of elasticity(GPa) [cmod test]	Modulus of elasticity (GPa) [Arora et al.][3]
0.47 Plain	36.90	5.26	31.08	29.52
0.47 Fiber	37.40	4.54	35.17	29.64
0.36 Plain	51.60	5.0	32.27	32.64
0.36 Fiber	53.20	4.0	40.55	32.94
0.20 Plain	92.20	2.63	60.61	38.85
0.20 Fiber	91.70	2.22	72.63	38.79

Table 6 shows the calculated values of initial compliance and Young's modulus as obtained in the test and derived from the empirical equation given by [3]. As observed from table 6 calculation of modulus of elasticity from initial compliance give a higher value than the studies conducted in the past[3, 8], therefore Load-CMOD compliance-based approach does not seem to be a highly accurate method of determining the modulus of elasticity, therefore for the subsequent calculations in the study modulus of elasticity values obtained by Arora et al. [3]. Deterministic evaluation of the absolute value of the modulus of elasticity from the three-point bend test proposed by RILEM is extremely difficult due to the required level of sensitivity of the measurement. The proposed Load-CMOD curve and initial compliance are extremely sensitive and it requires accurate measurement of the

order of 10^{-9} m in a mechanical bend test. Even a slight variation in the initial slope of the Load-CMOD curves leaves a magnified effect in the values of modulus of elasticity. Also, calculated values of modulus of elasticity were higher than established previous results. These values tend to become enormously high for higher strength concrete (for average compressive strength of 92 MPa). It can be suggested to limit this method only for comparative analysis and for absolute determination of modulus of elasticity various other well-established methods should be used.

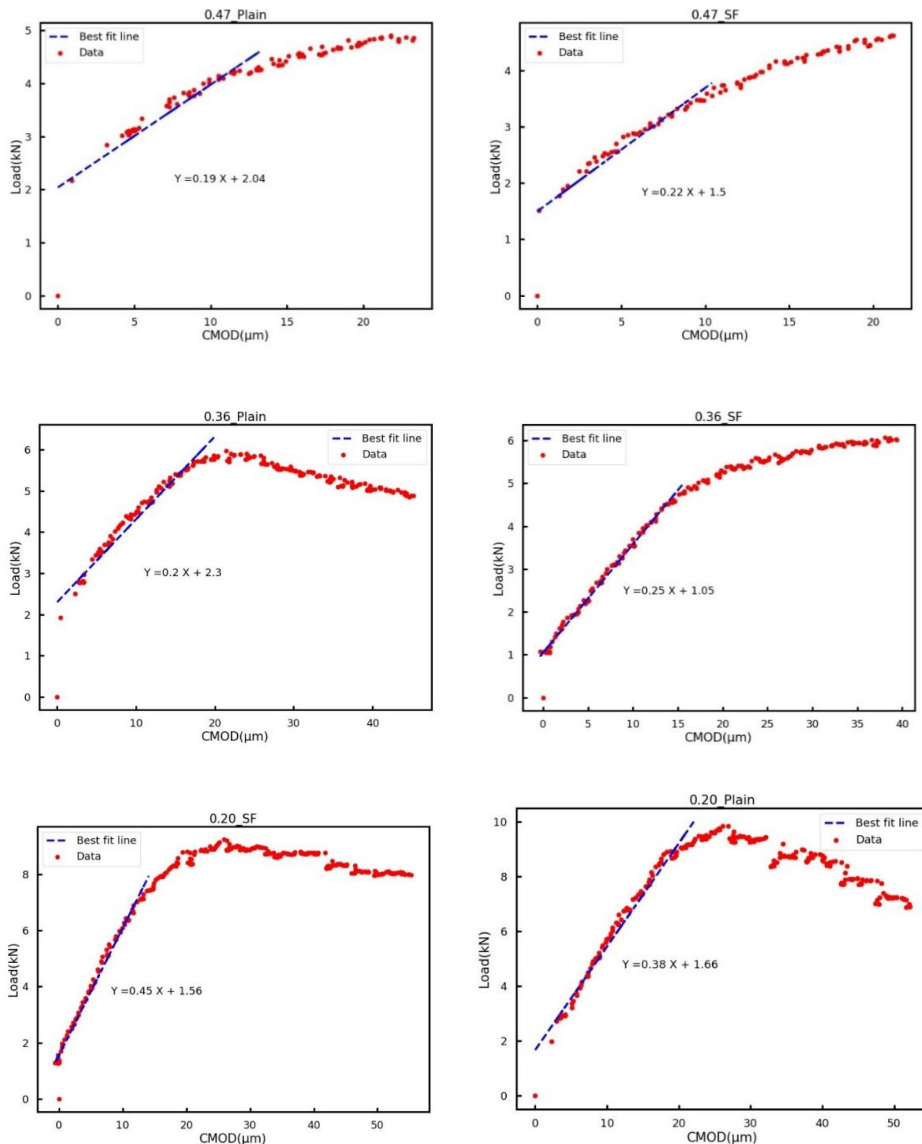


Fig. 13 Calculation of initial compliance from Load-CMOD curves

5.5 Stress Intensity Factor

The stress intensity factor (K_{Ic}) is a measure of stresses in the neighborhood of a crack. It is a measure to predict the stress intensity caused by the residual stresses near the tip of a notch or crack. It can also be used to compare the brittleness of two different materials. Higher (K_{Ic}) means that the material can allow higher stresses around the crack, suggesting a less brittle behavior.

The stress intensity factor is calculated using the equation (4), given by RILEM TC 89-FMT [7] as follow:

$$K_{Ic} (MPa \sqrt{m}) = 3(P_{Nmax} + 0.5mg) \frac{S\sqrt{\pi a}}{2d^2 b} f(\alpha) \tag{4}$$

Where P_{Nmax} is the maximum load on the notched prism in N, S is the span of the beam in m, α is the ratio of a and d, i.e., $\alpha = a/d = 0.35$ and $f(\alpha)$ is the geometry correction for bending load. A much accurate estimate of this parameter for varying specimen size, notch depth, and material property can be done using Finite Element Analysis[13]. But for simplicity and comparative analysis equation (5) is widely accepted and is used in the present study:

$$f(\alpha) = \frac{1.99 - \alpha(1-\alpha)(2.15 - 3.9\alpha + 2.7\alpha^2)}{\sqrt{\pi(1+2\alpha)(1-\alpha)^{3/2}}} \tag{5}$$

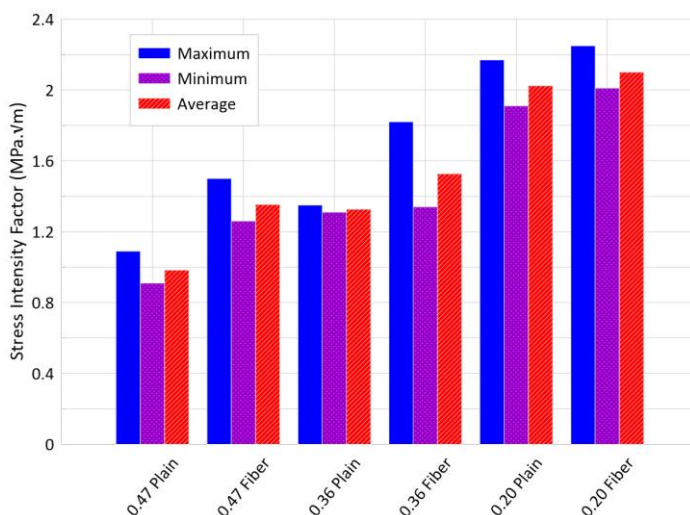


Fig. 14 Calculated stress intensity factor in the study

Figure 14 shows the values of the calculated stress intensity factor in the study. From the study, two important observations can be made. Firstly, adding steel fibers increases the stress intensity factor only marginally, this can be explained as fibers play a significant role only after a certain amount of crack has been made. Therefore, although fibers can significantly help arrest the cracks at a later stage, fiber only helps marginally in preventing initial cracks. Initial cracks formation in the beam depends on the tensile strength of the concrete which is related to the compressive strength and therefore a consistent increase in the stress intensity factor with compressive strength can be observed in the obtained result.

For a particular concrete sample, reported values of stress intensity factor in the literature [26] is about 1.14 MPa√m for normal concrete which increases to 1.48 MPa√m after the addition of steel fiber. Values, as well as the trend observed in our study, agrees with the literature.

5.6 Critical Energy Release Rate

The critical energy release rate, G_{IC} , is the rate at which energy is changed as the material gets fractured and creates a new surface. It can be mathematically defined as the decrease in total potential energy per increase in fracture surface area. For evaluating the material qualities related to fracture and fatigue, the energy release rate is a crucial factor. The equation given by Taha et al. [41] is used for calculating G_{IC} and is given in equation (6) as follow:

$$G_{IC}(N/m) = \frac{K_{IC}^2}{E} \tag{6}$$

The values of the calculated energy release rate are shown in figure 15. From the figure, a general trend can be observed that with the increase in concrete compressive strength a significant increase in energy release rate is observed. Therefore, with each new crack, a higher amount of strain energy is released for higher-strength concrete. The addition of fiber also increases the energy release rate but with the increase in concrete compressive strength, the percentage increase decreases. Similar to the stress intensity factor, this can be explained as at higher strength, the binder-aggregate mix is capable of taking a much higher load therefore the effect of fiber is slightly reduced compared to lower strength concrete.

The typical Energy release rate suggested in the literature [26] for normal concrete is 22.4 J/m², and for concrete with fiber is 100.2 J/m². Similar findings were observed for one of the samples in our analysis with a w/b ratio of 0.36.

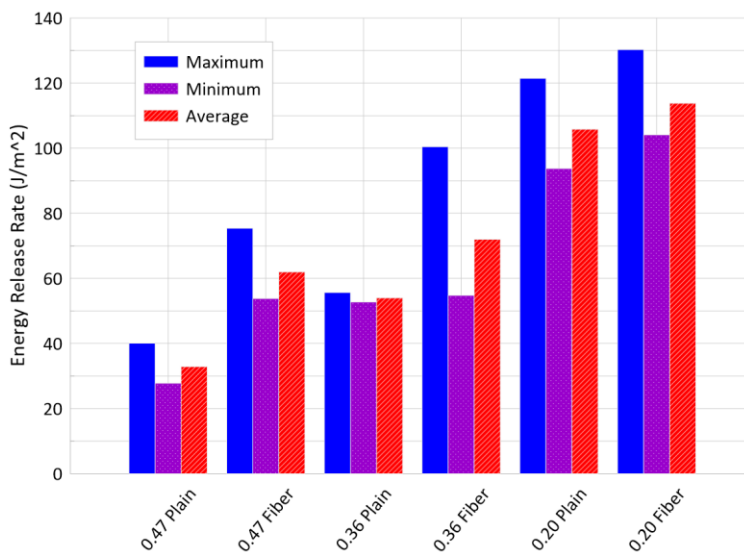


Fig. 15 Calculated energy release rate in the study

5.7 Characteristic Length

Characteristic length is a material parameter that reflects the lowest feasible breadth of a zone of strain-softening damage in nonlocal continuum formulations [42]. It can be understood as the minimum possible spacing of fractures in discrete fracture models. The principal idea behind finding the characteristic length is to compare the brittleness of two materials after the onset of initial cracks. Material with a smaller characteristic length can be considered more brittle, and crack can propagate easily in these materials. It can be calculated using the equation (7) provided by [43] as follows where E is young's modulus, G_f is fracture energy, and f_{st} is split tensile strength.

$$L_{ch}(mm) = \frac{EG_f}{f_{st}^2} \quad (7)$$

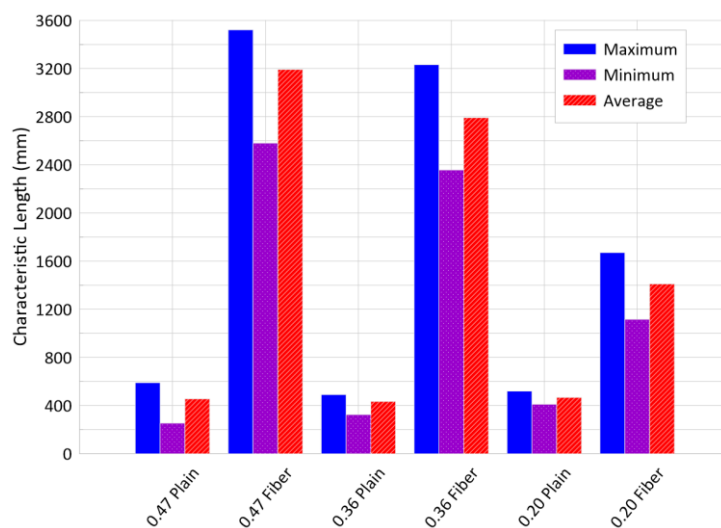


Fig. 16 Calculated Characteristic length of the study

The obtained values of the characteristic length in the study are presented in figure 16. From the figure, it can be observed that with an increase in compressive strength of concrete characteristic length decreases. Findings suggest that, for higher strength of concrete, Initial crack formation may be difficult due to higher stress intensity factor but crack propagation takes place much easily because cracks are less localized. Also, there is a large jump in the values of characteristic length after fiber addition. Therefore, it can be concluded that with the addition of fiber, concrete can have a much larger zone of strain-softening damage. This suggests that although crack may be initiated, but can be localized with the help of fiber addition. Past literature [26] also shows a massive jump in characteristic length from 806mm to 5382 mm when fiber was added to the concrete. A similar increase in the values in the characteristic strength was observed in our study.

6. Conclusions

In the present study, fracture parameters are evaluated for concrete mixes with w/b ratios of 0.47, 0.36, and 0.20 having a respective average compressive strength of 36 MPa, 52 MPa, and 92 MPa without and with 1% steel fiber by volume. The three-point bending test method with central point loading is used in the study. Based on the analysis of the results following can be concluded from the study.

- Adding steel fibers significantly increase the fracture energy. The observed increase in fracture energy was 850%, 770%, and 450% respectively for a w/b ratio of 0.47, 0.36, and 0.20. Comparing concrete with different w/b ratios, with the increase in strength of concrete a consistent increase in the fracture energy is observed. The addition of fiber increases the strain carrying capacity of concrete and with the increase in concrete compressive strength, peak load in the load-deformation curve increases.
- Deterministic evaluation of the absolute value of the modulus of elasticity from the three-point bend test proposed by RILEM is extremely difficult due to the required level of sensitivity of the measurement. The Load-CMOD curve and initial compliance value are extremely sensitive and it requires accurate measurement of the order of 10^{-9} m in a mechanical bend test. Even a slight variation in the initial slope of the Load-CMOD curves leaves a magnified effect in the values of modulus of elasticity. Also, calculated values of modulus of elasticity were higher than established previous results. These values tend to become enormously high for higher strength concrete (for average compressive strength of 92 MPa). It can be suggested to limit this method only for comparative analysis and for absolute determination of modulus of elasticity various other well-established procedures should be used.
- Stress intensity factor and energy release rate shows a similar trend and these two parameters improve with the addition of steel fiber but the observed increase is less when compared to increase in fracture energy. Results suggest that the compressive strength of concrete is an equally important factor for the increase in the values of these parameters along with the addition of fiber.
- Characteristic length of concrete shows an opposite trend from other parameters when concrete with different strengths is compared. For higher-strength concrete characteristic length is less. Comparing normal concrete with fiber reinforced concrete for a particular w/b ratio, a significant increase in characteristic length of the order of increase in fracture energy was observed.
- From the study it can be concluded that adding steel fiber tremendously increases the amount of energy needed for fracture of the beam. It also helps in arresting the cracks by increasing the characteristic length. But the formation of the initial crack is much closely related to the grade of concrete as fiber action can only be observed after the onset of initial cracks.

References

- [1] Ojha P, Singh B, Singh A, Patel V, Arora VV. Experimental study on creep and shrinkage behaviour of high strength concrete for application in high rise buildings. *Indian Concrete Journal*, 2021; 95:2 30-42.
- [2] Singh B, Arora VV, Patel V. Study on stress strain characteristics of high strength concrete. *Indian Concrete Journal* 2018; 92:6 37-43.
- [3] Arora V.V., Singh Brijesh, Patel Vikas, Trivedi Amit. Evaluation of modulus of elasticity for normal and high strength concrete with granite and calc-granulite aggregate. *Structural Concrete*, 2021; 22:S1. <https://doi.org/10.1002/suco.202000023>
- [4] Arora VV, Singh B, Jain S. Effect of indigenous aggregate type on mechanical properties of high strength concrete. *Indian Concrete Journal* 2017; 91:1 34-44.
- [5] Arora VV, Singh B, Jain S. Experimental studies on short term mechanical properties of high strength concrete. *Indian Concrete Journal* 2016; 90:10 65-75.
- [6] RILEM TC-50 FMC (Draft Recommendation). Determination of the fracture energy of mortar and concrete by means of three-point bend tests on notched beams. *Mater Struct.*, 1985; 18:106 285-290. <https://doi.org/10.1007/BF02472918>

- [7] Shah SP. Determination of fracture parameters (K_{Ic}s and CTOD_c) of plain concrete using three-point bend tests. *Materials and Structures*, 1990; 23:6 457-460. <https://doi.org/10.1007/BF02472029>
- [8] Patel V., Singh B., Arora V.V. Study on fracture behaviour of high strength concrete including effect of steel fiber. *Indian Concrete Journal*, 2020; 94:4 1-9.
- [9] Trivedi N, Singh RK, Chattopadhyay J. A comparative study on three approaches to investigate the size independent fracture energy of concrete. *Engineering Fracture Mechanics.*, 2015; 138: 49-62. <https://doi.org/10.1016/j.engfracmech.2015.03.021>
- [10] Khalilpour S, BaniAsad E, Dehestani M. A review on concrete fracture energy and effective parameters, 2019. <https://doi.org/10.1016/j.cemconres.2019.03.013>
- [11] Yin Y, Qiao Y, Hu S. Four-point bending tests for the fracture properties of concrete. *Engineering Fracture Mechanics*, 2019; 211: 371-381. <https://doi.org/10.1016/j.engfracmech.2019.03.004>
- [12] Murthy AR, Ganesh P, Kumar SS, Iyerc NR. Fracture energy and tension softening relation for nano-modified concrete. *Structural Engineering and Mechanics*, 2015; 54:6 1201-1216. <https://doi.org/10.12989/sem.2015.54.6.1201>
- [13] Kaya Z, Balcioglu HE, Gün H. The effects of temperature and deformation rate on fracture behavior of S-2 glass/epoxy laminated composites. *Polymer Composites*, 2020; 41:11 4799-4810. <https://doi.org/10.1002/pc.25753>
- [14] Almusallam T, Ibrahim SM, Al-Salloum Y, Abadel A, Abbas H. Analytical and experimental investigations on the fracture behavior of hybrid fiber reinforced concrete. *Cement and Concrete Composites*, 2016; 74: 201-217. <https://doi.org/10.1016/j.cemconcomp.2016.10.002>
- [15] Mousavi SM, Ranjbar MM, Madandoust R. Combined effects of steel fibers and water to cementitious materials ratio on the fracture behavior and brittleness of high strength concrete. *Engineering Fracture Mechanics*, 2019; 216. <https://doi.org/10.1016/j.engfracmech.2019.106517>
- [16] Arslan ME. Effects of basalt and glass chopped fibers addition on fracture energy and mechanical properties of ordinary concrete: CMOD measurement. *Construction and Building Materials*, 2016; 114: 383-391. <https://doi.org/10.1016/j.conbuildmat.2016.03.176>
- [17] Noaman AT, Abu Bakar BH, Akil HM, Alani AH. Fracture characteristics of plain and steel fibre reinforced rubberized concrete. *Construction and Building Materials*, 2017; 152: 414-423. <https://doi.org/10.1016/j.conbuildmat.2017.06.127>
- [18] Wtaife S, Alsabbagh A, Shaban AM, Suksawang N. Fracture Mechanism of Fibre Reinforced Concrete Pavement Based on a RILEM Design Approach. In *IOP Conference Series: Materials Science and Engineering*. Institute of Physics Publishing (2020). <https://doi.org/10.1088/1757-899X/671/1/012087>
- [19] Gil DM, Golewski GL. Effect of Silica Fume and Siliceous Fly Ash Addition on the Fracture Toughness of Plain Concrete in Mode I. In *IOP Conference Series: Materials Science and Engineering*. Institute of Physics Publishing (2018). <https://doi.org/10.1088/1757-899X/416/1/012065>
- [20] Siregar APN, Rafiq MI, Mulheron M. Experimental investigation of the effects of aggregate size distribution on the fracture behaviour of high strength concrete. *Construction and Building Materials*, 2017; 150: 252-259. <https://doi.org/10.1016/j.conbuildmat.2017.05.142>
- [21] Tang Y, Feng W, Chen Z, Nong Y, Guan S, Sun J. Fracture behavior of a sustainable material: Recycled concrete with waste crumb rubber subjected to elevated temperatures. *Journal of Cleaner Production*, 318 (2021). <https://doi.org/10.1016/j.jclepro.2021.128553>
- [22] Yu K, Yu J, Lu Z, Chen Q. Fracture properties of high-strength/high-performance concrete (HSC/HPC) exposed to high temperature. *Materials and Structures/Materiaux*

- et Constructions, 2016; 49:11 4517-4532. <https://doi.org/10.1617/s11527-016-0804-x>
- [23] Tran NT, Tran TK, Jeon JK, Park JK, Kim DJ. Fracture energy of ultra-high-performance fiber-reinforced concrete at high strain rates. *Cement and Concrete Research*, 2016; 79: 169-184. <https://doi.org/10.1016/j.cemconres.2015.09.011>
- [24] Guo M, Alam SY, Bendimerad AZ, Grondin F, Rozière E, Loukili A. Fracture process zone characteristics and identification of the micro-fracture phases in recycled concrete. *Engineering Fracture Mechanics*, 2017; 181: 101-115. <https://doi.org/10.1016/j.engfracmech.2017.07.004>
- [25] Arora VV, Singh B. Use of Fly Ash Concrete and Recycled Concrete Aggregates-A Cost Effective Solution and Durable Option for Construction of Concrete Roads. *Indian Concrete Journal*, 2017; 91:1
- [26] Alwesabi EAH, Bakar BHA, Alshaikh IMH, Zeyad AM, Altheeb A, Alghamdi H. Experimental investigation on fracture characteristics of plain and rubberized concrete containing hybrid steel-polypropylene fiber. *Structures*, 33 (2021). <https://doi.org/10.1016/j.istruc.2021.07.011>
- [27] Al-Tayeb MM, Abu Bakar BH, Akil HM, Ismail H. Effect of Partial Replacements of Sand and Cement by Waste Rubber on the Fracture Characteristics of Concrete. *Polymer - Plastics Technology and Engineering*, 2012; 51:6. <https://doi.org/10.1080/03602559.2012.659307>
- [28] Srawley JE. Wide range stress intensity factor expressions for ASTM E 399 standard fracture toughness specimens. *International Journal of Fracture*, 1976; 12:3. <https://doi.org/10.1007/BF00032844>
- [29] Noaman AT, Abu Bakar BH, Akil HM, Alani AH. Fracture characteristics of plain and steel fibre reinforced rubberized concrete. *Construction and Building Materials*, 2017; 152: 414-423. <https://doi.org/10.1016/j.conbuildmat.2017.06.127>
- [30] IS 516:2014. Method of Tests for Strength of Concrete. IS : 516 - 1959 (Reaffirmed 2004). (2004).
- [31] Bureau of Indian Standards. Method of Test Splitting Tensile Strength of Concrete. IS 5816: 1999. (2018).
- [32] Bureau of Indian Standards. Ordinary Portland Cement - Specification (Sixth Revision). (2015).
- [33] Bureau of Indian Standards. Coarse and Fine Aggregate for Concrete - Specification (Third Revision). (2016).
- [34] ASTM. Standard Specification for Steel Fibers for Fiber-Reinforced Concrete. A820/A820M.
- [35] Bureau of Indian Standards. Specification for Concrete Admixtures. IS 9103-1999. (2018).
- [36] Bureau of Indian Standards. Fresh Concrete: Methods of Sampling, Testing and Analysis Part 2 Determination of Consistency of Fresh Concrete (First Revision). IS 1199 (Part 2): 2018. (2018).
- [37] Ojha PN, Trivedi A, Singh B, N S AK, Patel V, Gupta RK. High performance fiber reinforced concrete - for repair in spillways of concrete dams. *Research on Engineering Structures and Materials*, 2021. <https://doi.org/10.17515/resm2021.252ma0128>
- [38] Singh B., Arora VV, Patel V. Experimental study on stress strain behaviour of normal and high strength unconfined concrete. *Indian Concrete Journal*, 2020; 94:4 10-19.
- [39] Smarzewski P. Influence of silica fume on mechanical and fracture properties of high performance concrete. *Procedia Structural Integrity*, 2019; 17: 5-12. <https://doi.org/10.1016/j.prostr.2019.08.002>
- [40] Javier Malvar L, Warren GE. Fracture energy for three point bend tests on single edge notched beams: Proposed evaluation. *Materials and Structures*, 1987; 20:6. <https://doi.org/10.1007/BF02472495>

- [41] Reda Taha MM, El-Dieb AS, Abd El-Wahab MA, Abdel-Hameed ME. Mechanical, Fracture, and Microstructural Investigations of Rubber Concrete. *Journal of Materials in Civil Engineering*, 2008; 20:10. [https://doi.org/10.1061/\(ASCE\)0899-1561\(2008\)20:10\(640\)](https://doi.org/10.1061/(ASCE)0899-1561(2008)20:10(640))
- [42] Bažant ZP, Pijaudier-Cabot G. Measurement of Characteristic Length of Nonlocal Continuum. *Journal of Engineering Mechanics*, 1989; 115:4. [https://doi.org/10.1061/\(ASCE\)0733-9399\(1989\)115:4\(755\)](https://doi.org/10.1061/(ASCE)0733-9399(1989)115:4(755))
- [43] Şahin Y, Köksal F. The influences of matrix and steel fibre tensile strengths on the fracture energy of high-strength concrete. *Construction and Building Materials*, 2011; 25:4. <https://doi.org/10.1016/j.conbuildmat.2010.11.084>



Research Article

Effect of metakaolin and steel slag on performance of binary blended concrete

Moulshree Dubey^{*a}, Shirish V Deo^b, Gangadhar Ramtekkar^c

Department of Civil Engineering, National Institute of Technology, Raipur-492010

Article Info

Abstract

Article history:

Received 20 Jan 2022

Revised 13 Mar 2022

Accepted 5 Apr 2022

Keywords:

Metakaolin;

Steel Slag;

Strength;

Durability;

Regression Analysis

In this study the effect of steel slag and metakaolin as replacement material to cement on strength and durability of binary blended concrete has been investigated. In concrete cement is the very significant material and serves as a binder. The combined effect metakaolin and steel slag as replacement to cement on concrete performance has been studied. The cement has been replaced with metakaolin and steel slag by 30% by weight of cement. For obtaining optimum dosage of metakaolin and steel slag different proportions are added as substitutionary material of cement. The compressive strength, flexural strength, electrical resistivity, and water absorptions tests are conducted to study the effect of replacement on strength and durability of concrete. There is a maximum of 25% enhancement in compressive strength of concrete has been observed in binary concrete containing 15% of steel slag and 15% of metakaolin in comparison with control concrete. Results confirm that the addition of steel slag and metakaolin in binary blended concrete enhances the concrete performance. Also, regression analysis has been performed to predict the compressive strength of concrete. The developed model will predict the compressive strength results accurately with minimum error.

© 2022 MIM Research Group. All rights reserved.

1. Introduction

Concrete is the most highly consumable material in the world due to its high strength and durability. In concrete mix cement works as a binder. The manufacturing of cement releases huge amounts of global warming gasses into the atmosphere [1]. The greenhouse effect is today's most significant environmental concern, because it is inextricably linked to global warming. Global warming is now developing at a pace that might have severe and permanent implications if prompt actions to ameliorate the situation are not done [2]. There is a one ton of CO₂ is releasing into the atmosphere for every one ton of cement manufacturing [3]. As a result, the use of supplementary cementitious materials (SCMs) as substitute for cement becomes an option for developing low carbon footprint binder systems [4][5][6]. The supplementary binder materials like steel slag, metakaolin, fly-ash, rice husk ash, and ground granulated blast furnace slag (GGBS) are extensively utilized in concrete as a partial alternative to cement [7][8]. The steel slag and GGBS are by-products from the steel industries. GGBS is the slag formed at a blast furnace during the pig iron production process. Steel slag is the slag generated at a steel melting shop. In recent years, SCMs and their application in blended concrete have attracted the curiosity of people all over the globe to reduce carbon emissions while also improving the overall performance of concrete [9][1]. The addition of SCMs to concrete mixture to generate blended concrete mixes may increase the

^{*}Corresponding author: moulshreedubey1189@gmail.com

^a orcid.org/0000-0003-2089-9474; ^b orcid.org/0000-0003-3371-2082; ^c orcid.org/0000-0002-3063-4480

DOI: <http://dx.doi.org/10.17515/resm2022.389ma0120>

Res. Eng. Struct. Mat. Vol. 8 Iss. 3 (2022) 603-614

concrete characteristics. The addition 10% of metakaolin substitutionary material to cement improves the compressive strength by 21% as comparison to control mix [10]. The addition of steel slag also enhances the performance concrete [11]. Similarly, the addition of GGBS, silica fume, fly ash, and rice husk ash also improves the strength and durability of concrete [12][13][14]. The addition fly-ash and metakaolin as substitutionary material to cement enhances the performance of concrete [15]. The addition of 10% of fly-ash and 10% of rice husk ash as substitutionary material to cement shows optimum enhancement in strength of concrete as compared to control mix [16]. However, the utilization of these SCMs in concrete has negative effects also. The addition fly-ash or steel slag in concrete shows lower early strength results. The addition of metakaolin more than 30% reduces the strength of concrete [17]. In this research an endeavour has been made to examine the performance of binary mixed concrete including steel slag and metakaolin. The steel slag shows low early strength results and metakaolin is a highly reactive material and provides high early strength to concrete [18][19]. The main aim of the study is to achieve best binary mix by combining steel slag and metakaolin. The response surface method has been utilized to predict and optimize the compressive strength results of binary blended concrete. The response surface method shows there is a good agreement between experimental and predicted compressive strength results. The blending of these two materials as replacement to cement improves the concrete performance in initial and final stage.

2. Materials and Methods

2.1. Materials

Ordinary Portland cement (43 Grade) has been utilized in this study having a specific gravity of 3.1, and cement has been tested as for Indian Standards IS: 4031-1988. The coarse aggregate with a size smaller than 20 mm and fine aggregate conforming to Zone II were employed, with specific gravity values of 2.78 and 2.65 respectively, in accordance with IS: 383-1970. Normal portable water available in the lab has been used for preparation of concrete. Metakaolin used in this study was procured from the ASTRRA chemicals, chennai and used in this study. The procured metakaolin has a specific gravity of 2.5 and used in its current form. The steel slag used in this was procured from the emami cement limited and has a specific gravity of 2.9. The elemental composition of metakaolin and steel slag are listed in Table 1.

Table 1. Elemental composition of Metakaolin and steel slag using EDX analysis

Elements	Metakaolin (Weight %)	Steel Slag (Weight %)
Si	61.47	24.28
Mg	0.05	3.67
Al	17.55	4.49
Ca	0.15	2.46
Fe	0.32	14.52
O	20.46	50.58

2.2. Concrete Mix Design

Concrete mix design has been done according IS 10262-2009 [11]. The detailed mix proportions per cubic meter are given in Table 2. The word C100 refers to control mix. The aggregates, lime, fly-ash, steel slag, and sand are added into the pan mixer and mixed for 2 minutes. For proper mixing, half quantity water and chemical admixture were added to concrete and it was mixed thoroughly for 2 minutes. The remaining quantity of water and chemical admixture were added and concrete was mixed for 2 to 4 minutes up to getting uniform colour and homogeneous mix. The fly-ash and steel slag are

pozzolanic materials they can react with $\text{Ca}(\text{OH})_2$ during hydration process of cement and liberates C-S-H gel. This improves the strength and durability of concrete. To avail the sufficient amount of $\text{Ca}(\text{OH})_2$ in concrete matrix the dosage of alternative materials are limited to 30%.

Table 2. Mix details of concrete per cubic meter

Mix Details	Metakaol in (%)	Steel slag (%)	Cement (kg/m^3)	Metakaolin (kg/m^3)	Steel slag (kg/m^3)
C100	0	0	507	0	0
MK5SS25	5	25	354	26	127
MK10SS20	10	20	354	51	102
MK15SS15	15	15	354	76	76
MK20SS10	20	10	354	102	51
MK25SS5	25	5	354	127	26

Table 2(Con). Mix details of concrete per cubic meter

Mix Details	Sand (kg/m^3)	20mm (kg/m^3)	10mm (kg/m^3)	Water (kg/m^3)	Super Plasticizer (kg/m^3)
C100	607.28	732	487	152.1	6.08
MK5SS25	603	726	484	152.1	6.08
MK10SS20	601	736	490	152.1	6.08
MK15SS15	601	724	482	152.1	6.08
MK20SS10	604	727	484	152.1	6.08
MK25SS5	598	721	488	152.1	6.08

2.3. Testing Methods

The fresh concrete property such as workability of concrete has been measured using slump cone test. The slump cone test has been performed immediately after mixing of concrete as per IS: 1199 – 2004 [20]. The cube specimens having size of 100 x 100 x 100 mm are casted after testing of the slump cone test and these cubes are used for compressive strength test. The test has been performed to 7 days and 28 days water cured samples on triplicate as per IS: 516-1959 standards [21]. The testing arrangement for compressive strength test is shown in Fig. 1.

The concrete beam specimens of size 100 x 100 x 500 mm was used for evaluate the flexural strength of concrete. The beams are tested on 7 days and 28 days curing on triplicate. The test has been performed as per the IS: 516-1959 standards [21]. The arrangement for flexural strength set up is shown in Fig. 2.



Fig.1 Testing arrangement for compressive strength test for concrete



Fig. 2 Arrangement for flexural strength test for concrete beams

A Leader RCONTM Concrete Electrical Resistivity Meter was used for measuring the concrete electrical resistance. For this study, 100 x 100 x 100 mm cubes were used. The test has been performed on 7 and 28 days cured samples on triplicate. The test has been performed as per ASTM C 1202 standards [22]. The test was performed on saturated cube in these the pores of concrete are filled with water. The testing arrangement of electrical resistivity meter as shown in Fig. 3.

One of the primary aspects of concrete durability is permeability. Concrete with decreased permeability exhibited better protection against chemical attacks. Generally the high durable concrete has lower permeability test results [23]. In this investigation, a water absorption test was carried out to know the durability of concrete. The test was carried out in triplicate on 28-day-cured concrete cubes measuring 100 x 100 x 100 mm in accordance with ASTM C 642-13 criteria [24].

3. Results and Discussion

3.1. Workability

The Fig. 4 depicts the slump cone test results. From Fig.4 it is noticed that the addition of 15% of metakaolin and 15% of steel slag considerably improves the workability in

comparison with control mix. There is a maximum of 27% improvement in slump values has been observed in concrete mix MK15SS15 in comparison with control mix. The addition of 5% metakaolin and 25% of steel slag shows 6% improvement in the slump values in comparison with control mix. The addition of 10% of metakaolin and 20% of steel slag shows 13.5% improvement in slump values of concrete as compared to control mix. Similarly, the concrete mix with 25% of metakaolin and 5% of steel slag shows 8% improvement in slump values of concrete in comparison with control mix. The addition of higher dosages of steel slag diminishes the workability. As the dosages of steel slag reduces the workability of concrete increases. On the other side the addition of metakaolin up to 15% enhances the workability of concrete. The binary concrete mix containing 15% of metakaolin and 15% of steel slag are optimum for improving the workability. The addition of steel slag improves cohesiveness and reduces the water demand in concrete thus the workability of concrete enhances [25]. While the increase in the dosage of metakaolin reduces the workability of concrete due to smaller particle size increases the water demand in concrete.



Fig. 3 Set up for measuring electrical resistivity of concrete

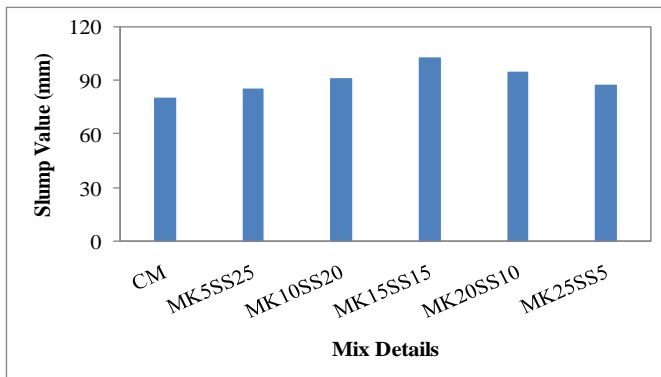


Fig. 4 Slump cone test results of various concrete mixes

3.2. Compressive Strength

The Fig. 5 depicts the compressive strength test results of various concrete mixes. From the Fig.5 it is observed that the addition of 15% of metakaolin and 15% of steel slag shows optimum improvement in compressive strength in comparison with control concrete. A 25.5% optimum enhancement in compressive strength has been noticed in mix MK15SS15 in comparison with control mix. The addition of higher dosages of steel

slag diminishes the strength. The addition of metakaolin up to 15% enhances the strength in comparison with control concrete. The metakaolin is a high reactive pozzolanic material due to its higher surface area. As a result, the strength of concrete improves. From the mix MK20SS10 and MK25SS5 it is noticed that the addition of metakaolin more than 15% slightly diminishes the compressive strength. At higher dosages of metakaolin weakness the interfacial transition zone (ITZ) of concrete by forming micro-cracks due to availability of high specific surface area [26]. From the Fig.5 it is also observed that the addition of steel slag at higher concentrations reduces the compressive strength. From the mix MK5SS25, MK10SS20, and MK15SS15 it is noticed that the reduction in the dosages of steel slag increases the compressive strength. The addition of steel slag in concrete shows very little pozzolanic activity thus strength improvement is very little by the addition of steel as substitutionary material to cement [27]. The addition of steel slag up to 10.5% as replacement to cement did not negatively effect the its properties [28]. The binary concrete mixes have an advantage of higher utilization of steel slag in concrete. The mix MK5SS25 shows higher strength results than control mix. The addition of steel slag in concrete causes the reduction in cement content in concrete which is an effective to minimize environmental impacts without increasing the cost.

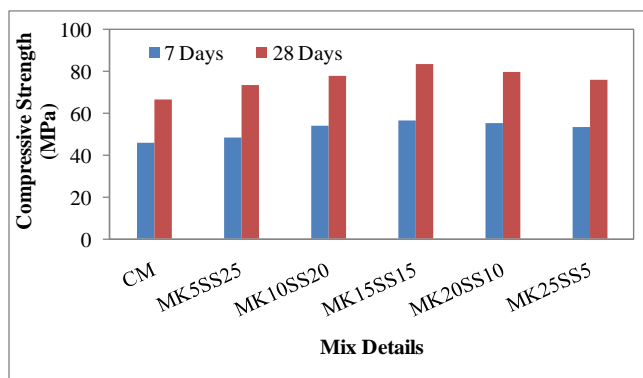


Fig. 5 Compressive strength test results of various concrete mixes

3.3. Flexural Strength

The Fig. 6 depicts the flexural strength test results of various concrete mixtures. The mix containing 15% of metakaolin and 15% of steel slag shows optimum percentage enhancement in flexural strength. An optimum improvement of 25% enhancement in flexural strength is observed for the mix MK15SS15 in comparison to control mix at an age of 28 days. The mix MK5SS25 shows 6% and 9% enhancement in flexural strength in comparison to control mix at an age of 7 and 28 days. The mix MK10SS20 shows 13.6% and 16.9% enhancement in flexural strength in comparison to control mix for 7 and 18 days cured samples. The mix MK20SS10 and MK25SS5 shows reduction in strength as compared to the mix MK15SS15. The addition of higher dosages of metakaolin reduces the flexural strength. In the same lines the addition of higher dosages of steel slag also diminishes the flexural strength. The binary mix containing 15% of steel slag and 15% of metakaolin shows optimum strength improvement in 7 and 28 days respectively. The metakaolin has high pozzolanic reactivity and thus enhances the strength of concrete. Steel slag has lower pozzolanic reactivity due to this very less improvement has been noticed in flexural strength of concrete.

3.4. Electrical Resistivity of Concrete

The Fig. 7 depicts the electrical resistivity test results of various concrete mixes. From the Fig. 7 it is seen that the inclusion of steel slag and metakaolin in concrete as replacement material to cement raises the electrical resistivity. The mix MK15SS15 shows the optimum improvement in electrical resistivity. The mix MK15SS15 shows an electrical resistivity of 18.5 k Ω -cm and 29 k Ω -cm at an age of 7 and 28 days. While the control mix shows an electrical resistivity of 11.9 k Ω -cm and 13.9 k Ω -cm at an age of 7 and 28 days. The mix MK20SS10 and MK25SS5 shows enhanced electrical resistivity test results than control mix. The mix MK20SS10 and MK25SS5 shows reduction in electrical resistivity in comparison to the mix MK15SS15. The electrical resistivity of concrete is influenced by its micro-structure characteristics, pores, and micro-cracks. The inclusion of metakaolin to concrete promotes the development of secondary C-S-H. It improves the micro-structure of concrete as a result increases its electrical resistance. Parande et al. [29] shown that inclusion of metakaolin up to 15% in concrete enhances the electrical resistivity. The steel slag has low pozzolanic reactivity and shows reduction in electrical resistivity as dosages of steel slag increases. The steel slag works as a filler material and minimizes the pores in concrete if we add minimum amount. The binary blend containing 15% of steel slag and 15% of metakaolin shows optimum improvement in electrical resistivity. The 15% of metakaolin and 15% of steel slag provides sufficient amount of secondary C-S-H also improves the denseness of concrete by minimizing the pores in concrete matrix. The SEM test results also confirm the dense structure in mix MK15SS15. Due to having dense structure and less micro-cracks the electrical resistivity of the mix MK15SS15 is very high as compared to other mixes.

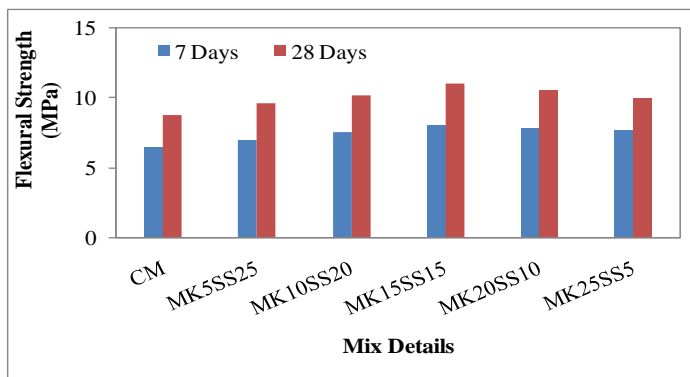


Fig. 6 Flexural strength test results of various concrete mixes

3.5. Water Absorption

The Fig. 8 displays the test results of several concrete mixes. From the Fig.8 it is observed that the mix MK15SS15 shows optimum reduction in water absorption. There is a 43.4% diminution in water absorption is noticed for the mix MK15SS15 in comparison with control concrete. The mix MK5SS25 and MK10SS20 shows decrease in water absorption test results in comparison to control concrete. The mixes MMK20SS10 and MK25SS5 shows less reduction in water absorption as compared to the mix MK15SS15. The test results confirm that the mix MK15SS15 is a high durable concrete mix as compared to other concrete mixes. The mix MK15SS15 shows better compressive and flexural strength test results. It confirms that the mix MK15SS15 is having very dense structure and less voids and pores. Because of this the water absorption is very less in the mix MK15SS15.

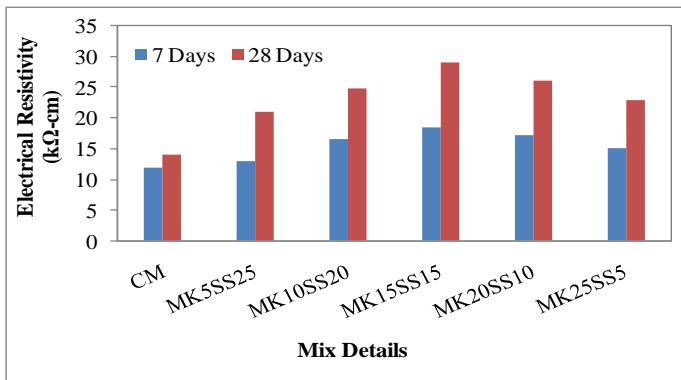


Fig. 7 Electrical resistivity test results of various concrete mixes

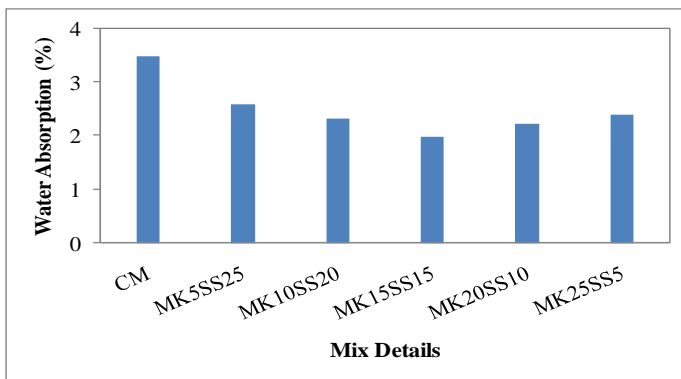


Fig. 8 Water absorption test results of different concrete mixes

3.6. Scanning Electron Microscope

A high-resolution scanning electron microscope (SEM) was utilised to examine the sample's micro-structure. The 28 days cured concrete samples are utilized for this study. The cubes of size 10 x 10 x 10 mm were prepared from the broken pieces. These samples were coated with gold in a sputter coater for SEM observation in order to produce good SEM images. The testing was done on ZEISS SEM machine. The Fig.9 shows the SEM images of control concrete and the mix MK15SS15 for 28 days cured samples. The micro-structure of MK15SS15 seems to be more homogeneous and compact than the control mix in Fig.9. The presence needle type crystal ettringite is observed in control mix. The inclusion of 15% metakaolin and 15% steel slag as a cement replacement resulted in the decrease of needle-like crystals of ettringite and the formation of fibrous calcium silicate hydrates and calcium alumina silicate hydrates. As a result strength and durability of concrete enhances.

3.7. Regression Analysis

The Multi-variable regression analysis may be used to determine the optimal amount of cement replacement in binary blended mixtures [30]. A multi-variable regression analysis was used in this work to investigate the effect of substituting cement with varying quantities of steel slag and metakaolin on the compressive strength of concrete, and a model was constructed for it. The dosage of metakaolin (x_1), dosage of steel slag (x_2), and age of the concrete (x_3) are considered as the input parameters and the

compressive strength is being the output parameter. Regression analysis yielded the following first-order multi-linear response surface model:

$$Y = 2027 - 66x_1 - 66x_2 + 1.427x_3 \tag{1}$$

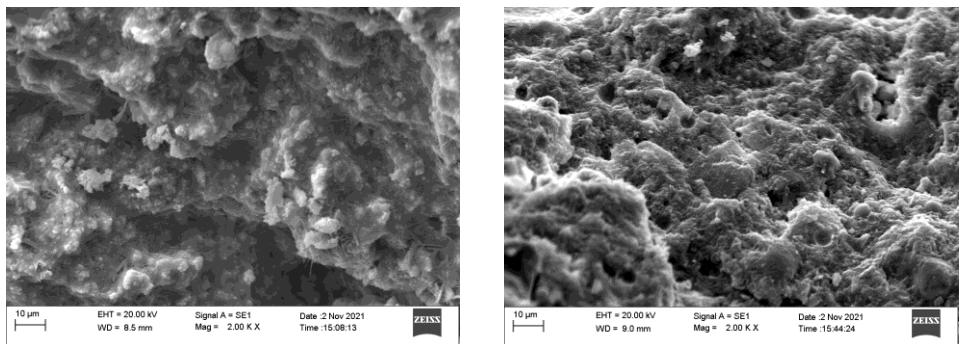
where;

Y = Compressive strength of concrete (MPa)

x₁ = Dosage of metakaolin (%)

x₂ = Dosage of steel slag (%)

x₃ = Age of concrete (Days)



(a)

(b)

Fig.9 SEM test results of (a) Control mix (b) MK15SS15 mix

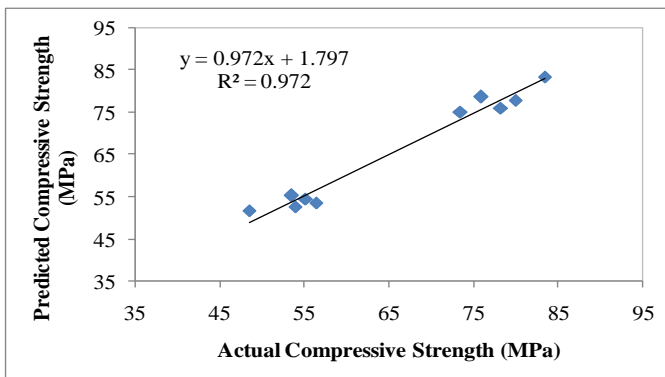


Fig. 10 The actual and predicted compressive strength results

The Fig. 10 depicts the actual and predicted compressive strength values. The smaller the magnitude of error between anticipated and experimental values, the more often the normality assumption is met. It should be emphasised, however, that regression equations are particular to the variables and their features, and so cannot be generalised, but are highly effective in predicting the outcome from a given response. From Fig.10 the disparity in total variance is just 0.028 percent, the created model's coefficient of determination ($R^2 = 0.972$) demonstrates that it falls within a permissible error range. Considering the R^2 value of the developed model it is a good fit model.

4. Conclusions

The effect of steel slag and metakaolin on concrete performance has been studied. The increase in the dosage of steel slag increases the workability of concrete. While the increase in the dosage of metakaolin diminishes the workability of concrete. The combination of 15% of metakaolin and 15% of steel slag shows optimum workability results. The addition 15% of steel slag and 15% metakaolin shows optimum development in strength and durability of concrete also. There is a maximum of 25% enhancement in compressive strength of concrete has been noticed in the mix MK15SS15 in comparison to control mix. The durability of concrete also considerably improved. This was confirmed by the electrical resistivity and water absorption tests. The SEM test results also confirm the improvement in micro-structure of concrete. The addition of 20% of metakaolin and 10% of steel slag diminishes the strength of concrete as compared to the mix MK15SS15. Similar trend has been followed in the mix MK25SS5 also. The addition of higher dosages of metakaolin weakness the ITZ of the matrix and diminishes the strength of concrete. The higher dosage of steel slag also diminishes the strength of concrete due to its less pozzolanic activity. The electrical resistivity and water absorption test results also confirm that the mixes MK20SS10 and MK25SS5 are less durable as compared to the mix MK15SS15. Regression analysis has been used to develop a model for predicting the compressive strength. The model's coefficient of determination $R^2 = 0.972$ value confirms it is a good fit model. The results confirm that the developed regression equation will predict the compressive strength results accurately with minimum error. The test results suggest that the addition of 15% of metakaolin and 15% of steel slag as substitutionary material to cement are optimum for enhancing the workability, strength, and durability of concrete.

References

- [1] Palod R, Deo SV, Ramtekkar GD. Effect on mechanical performance, early age shrinkage and electrical resistivity of ternary blended concrete containing blast furnace slag and steel slag. *Mater. Today Proc.*, 2020; 32:4 917-922. <https://doi.org/10.1016/j.matpr.2020.04.747>
- [2] Padavala AB, Potharaju M, Kode VR. Mechanical properties of ternary blended mix concrete of fly ash and silica fume. *Mater. Today Proc.*, 2021; 43: 2198-2202. <https://doi.org/10.1016/j.matpr.2020.12.127>
- [3] Chee C, Kok C, Ramli M, Gin L. The engineering properties and microstructure development of cement mortar containing high volume of inter-grinded GGBS and PFA cured at ambient temperature. *Constr. Build. Mater.*, 2016; 122: 683-693. <https://doi.org/10.1016/j.conbuildmat.2016.06.105>
- [4] Ouldkaoua Y, Benabed B, Abousnina R, Kadri E, Khatib J. Effect of using metakaolin as supplementary cementitious material and recycled CRT funnel glass as fine aggregate on the durability of green self-compacting concrete. *Constr. Build. Mater.*, 2020; 235: 117802. <https://doi.org/10.1016/j.conbuildmat.2019.117802>
- [5] Vijay K, Babu KH, Indrasena YV. Effect of Wood-Ash as Partial Replacement to Cement on Performance of Concrete Effect of Wood-Ash as Partial Replacement to Cement on Performance of Concrete. *IOP Conf. Ser. Earth Environ. Sci. Pap.*, 2021; 796:1 1-6. <https://doi.org/10.1088/1755-1315/796/1/012020>
- [6] Gencil O, Karadag O, Hulusi O, Bilir T. Steel slag and its applications in cement and concrete technology: A review. *Constr. Build. Mater.*, 2021; 283: 122783. <https://doi.org/10.1016/j.conbuildmat.2021.122783>
- [7] Duchesne J. Alternative supplementary cementitious materials for sustainable concrete structures: a review on characterization and properties. *Waste and Biomass Valorization*, 2021; 12:3 1219-1236. <https://doi.org/10.1007/s12649-020-01068-4>

- [8] Pacewska B, Wilińska I. Usage of supplementary cementitious materials: advantages and limitations. *J. Therm. Anal. Calorim.*, 2020; 142:1 371-393. <https://doi.org/10.1007/s10973-020-09907-1>
- [9] Sern LJ, Cheah CB, Ramli MB. The setting behavior, mechanical properties and drying shrinkage of ternary blended concrete containing granite quarry dust and processed steel slag aggregate. *Constr. Build. Mater.*, 2019; 215: 447-461. <https://doi.org/10.1016/j.conbuildmat.2019.04.162>
- [10] Poon CS, Kou SC, Lam L. Compressive strength, chloride diffusivity and pore structure of high performance metakaolin and silica fume concrete. *Constr. Build. Mater.*, 2006; 20: 858-865. <https://doi.org/10.1016/j.conbuildmat.2005.07.001>
- [11] Jiang Y, Ling T, Shi C, Pan S. Characteristics of steel slags and their use in cement and concrete - A review. *Resour. Conserv. Recycl.*, 2018; 136: 187-197. <https://doi.org/10.1016/j.resconrec.2018.04.023>
- [12] Ofuyatan OM, Adeniyi AG, Joshua O. Evaluation of fresh and hardened properties of blended silica fume self-compacting concrete (SCC). *Res. Eng. Struct. Mater.*, 2021; 7:2 211-223. <https://doi.org/10.17515/resm2020.228ma1023>
- [13] Li G, Tan H, He X, Zhang J, Deng X, Zheng Z, Guo Y. G. Li et al., The influence of wet ground fly ash on the performance of foamed concrete. *Constr. Build. Mater.*, 2021; 304: 124676. <https://doi.org/10.1016/j.conbuildmat.2021.124676>
- [14] Vishvanath N, Deo SV, Murmu M. Effect of Fly Ash and Rice Husk Ash as Partial Replacement of Cement on Packing Density and Properties of Cement. *Int. J. Innov. Technol. Explor. Eng.*, 2019; 8:7 1940-1945.
- [15] Moser RD, Jayapalan AR, Garas VY, Kurtis KE. Cement and Concrete Research Assessment of binary and ternary blends of metakaolin and Class C fly ash for alkali-silica reaction mitigation in concrete. *Cem. Concr. Res.*, 2010; 40:12 1664-1672. <https://doi.org/10.1016/j.cemconres.2010.08.006>
- [16] Kanthe VN, Deo SV, Murmu M. Effect of fly ash and rice husk ash on strength and durability of binary and ternary blend cement mortar. *Asian J. Civ. Eng.*, 2018; 6: 1-8. <https://doi.org/10.1007/s42107-018-0076-6>
- [17] Homayoonmehr R, Akbar A, Mirdarsoltany M. Influence of metakaolin on fresh properties, mechanical properties and corrosion resistance of concrete and its sustainability issues: A review. *J. Build. Eng.*, 2021; 44: vol. 44, 103011. <https://doi.org/10.1016/j.jobe.2021.103011>
- [18] Mohan C, Goyal R. Analysing mechanical properties of concrete with nano silica, silica fume and steel slag. *Mater. Today Proc.*, 2021; 45:6 4520-4525. <https://doi.org/10.1016/j.matpr.2020.12.1032>
- [19] Badogiannis E, Kakali G, Tsvivilis S. Metakaolin as Supplementary Cementitious Material Optimization of kaolin to metakaolin conversion. *J. Therm. Anal. Calorim.*, 2005; 81: 457-462, 2005. <https://doi.org/10.1007/s10973-005-0806-3>
- [20] IS: 1199 -1959, "Methods of Sampling and Analysis of Concrete," Bur. Indian Stand., no. 11, pp. 1-49, 2004.
- [21] IS: 516 - 1959, "Methods of Test for Strength of Concrete," Bur. Indian Stand., no. 18, pp. 1-30, 1959.
- [22] ASTM C1202, "Standard Test Method for Electrical Indication of Concrete's Ability to Resist Chloride Ion Penetration," Am. Soc. Test. Mater., no. C, pp. 1-8, 2012.
- [23] Ramezaniapour AA, Pilvar A, Mahdikhani M, Moodi F. Practical evaluation of relationship between concrete resistivity, water penetration, rapid chloride penetration and compressive strength. *Constr. Build. Mater.*, 2011; 25:5 2472-2479. <https://doi.org/10.1016/j.conbuildmat.2010.11.069>
- [24] ASTM C 642-13, "Standard Test Method for Density, Absorption, and Voids in Hardened Concrete," Am. Soc. Test. Mater., pp. 11-13, 2008.

- [25] Xiaolu GUO, Huisheng SHI, Kai WU. Effects of Steel Slag Powder on Workability and Durability of Concrete. *J. Wuhan Univ. Technol. Sci. Ed.*, 2014; 733-739. <https://doi.org/10.1007/s11595-014-0988-2>
- [26] Abdelmelek N, Lubloy E. Evaluation of the mechanical properties of high strength cement paste at elevated temperatures using metakaolin. *J. Therm. Anal. Calorim.*, 2020; 1:2 1-16.
- [27] Rosales J, Cabrera M, Agrela F. Effect of stainless steel slag waste as a replacement for cement in mortars. Mechanical and statistical study. *Constr. Build. Mater.*, 2017; 142: 444-458. <https://doi.org/10.1016/j.conbuildmat.2017.03.082>
- [28] Tsakiridis PE, Papadimitriou GD, Tsivilis S, Koroneos C. Utilization of steel slag for Portland cement clinker production. *J. Hazard. Mater.*, 2008; 152: 805-811. <https://doi.org/10.1016/j.jhazmat.2007.07.093>
- [29] Parande AK, Babu BR, Karthik MA, Kumar KKD, Palaniswamy N. Study on strength and corrosion performance for steel embedded in metakaolin blended concrete/mortar. *Constr. Build. Mater.*, 2008; 22: 127-134. <https://doi.org/10.1016/j.conbuildmat.2006.10.003>
- [30] Palod R, Ramtekkar SVDGD, Utilization of waste from steel and iron industry as replacement of cement in mortars. *J. Mater. Cycles Waste Manag.*, 2019; 1-15. <https://doi.org/10.1007/s10163-019-00889-3>



Research Article

Effect of asphalt pavement construction on the environment of Ethiopia

Badrinarayan Rath

Civil Engineering Department, Wollega University, Nekemte, Ethiopia.

Article Info

Article history:

Received 10 Oct 2021

Revised 06 Feb 2022

Accepted 22 Feb 2022

Keywords:

*Asphalt Pavement;
Environmental Impact;
Life Cycle Impact
Assessment;
Biodiesel*

Abstract

Nowadays road construction is rapidly increasing on-demand to meet several medium and long terms development programs. A huge amount of natural resources, types of machinery and fuels are used in road construction. Using material resources and fuel an efficient manner, reducing in emission of greenhouse gases and controlling various impacts on the environment are important tasks in the road construction industry. In the present research, several environmental impacts related to the construction of asphalt paved highways in Ethiopia have been determined using the Life Cycle Assessment Approach for common pavement materials and construction activities. A deep focus has been given towards the extraction and processing of sand and gravel for preparation of base and sub-base; transportation of these input raw materials; consumption of fuels by various road construction machinery; direct or indirect emissions of carbon dioxide and other pollutants to atmosphere etc. Various suitable methods have been used to calculate the impacts of raw materials, fuel and machinery on various categories such as global warming potential, ozone depletion potential, terrestrial acidification potential, freshwater eutrophication, freshwater ecotoxicity etc. From the investigation, it has been suggested to use recycled materials for substituting gravel as base or sub-base materials and biodiesel for substituting diesel in the transportation trucks and dumpers. These types of new recycled materials may greatly help in assisting the evaluation of sustainable pavement construction. The present case study may help for potential changes in asphalt pavement construction to improve environmental sustainability.

© 2022 MIM Research Group. All rights reserved.

1. Introduction

Roads are the arteries of the country, deeply associated with its socio-economic development. It is the only infrastructure, by which society can access the resources, consumer goods and various services easily at a low cost. As the population of the world is increasing, the demand for road infrastructure is increasing in that proportion. It is found that a total of forty-three million km length of paved road has been spread throughout the world till 2010 and has targeted to construct additional fourteen million km up to 2030 [1]. Any construction (particularly road construction) inside the country causes many environmental impacts such as consumption of natural resources, deforestation, disturbances of natural habitats, a huge amount of greenhouse gas emission, the transformation of land etc [2]. Cement and aggregates are the main ingredients are used for the preparation of concrete by consuming a huge amount of natural resources. Due to the continuous consumption of a natural resource, our environment and ecosystem are badly affected. Hence geopolymer concrete can be suggested for road construction instead of cement concrete.

*Corresponding author: rath_rcpit@rediffmail.com

^a orcid.org/0000-0001-9675-9684

DOI: <http://dx.doi.org/10.17515/resm2022.352ma1010>

Res. Eng. Struct. Mat. Vol. 8 Iss. 3 (2022) 615-632

In Ethiopia, National highways and expressways have been constructed radiating from its capital city to several regional state capitals in all directions. Ethiopian Roads Authority has set a target to complete the expansion of roads up to two lakhs kilometres at the end of the current year 2021. All these proposed roads are asphalt roads and the life cycle assessment approach is best accomplished for quantifying the environmental impact of those road pavements. The Ethiopian roads can be classified based on three categories as shown in Table 1. They are Technical Classification, Functional Classification and Political Classification. The detailed road classification of Ethiopia is given below. During the most recent periods, various studies have been done on the environmental impact of road infrastructure. Among those studies, it has been focused on the environmental impact of asphalt pavement [3], it has been studied to compare the environmental impact of different pavements [4, 5], it has been explanted about the traffic fuel consumption on a different surface of the layers during the use phase or on maintenance strategies [6] and it has been studied about a review on existing of life cycle assessment [7]. Several researchers have studied the life cycle of road pavement and divided it into five categories [8, 9]. They are extraction of raw materials, construction of road, using of road and end of its life [10]. Now a days people are focusing on the exploration of various sustainable options for the construction of asphalt pavement such as its reusing, extending its lifetime [11], using recyclable materials in road construction [12], reducing of friction in between pavement and wheels of the vehicle [13]. Now a days reclaimed asphalt pavement is considered as standard asphalt pavement practice. In this process, the combined materials of asphalt and aggregates collected from old damaged asphalt road are feeding to the hot recycling of asphalt paving mixtures. In the early days recycling of pavement, process had been practiced. This type of sustainable effort was conducted in Nevada and Texas during 1974, by recovering and reusing the old asphalt paving materials [14]. The life of pavement can be extended by using a geosynthetic insulation layer with low heat conductivity [15]. Now a days various recyclable materials are used in road construction. It was found that replacing recycled polymers with coarse aggregate up to 15% in road construction increased its strength and performance with attaining sustainability and reducing the negative effect on the environment [16]. Also, it was noticed that various rejuvenators such as waste engine oil, waste cooking oil virgin olive oil can restore the aged asphalt binder to a penetration grade of 60/70 [17]. The friction resistance can be reduced by improving the flexible pavements using above rejuvenators in asphalt. As a result, vehicle energy, as well as greenhouse gas emission, will be reduced significantly. To reduce the friction and improve the asphalt mix stability performance HDPE plastic seeds can be added to asphalt at 5.5% as optimum value [18]. Due to the addition of HDPE plastic seeds into oil asphalt, the penetration value reaches 60/70. However, people are focusing on construction and maintenance phases. Various activities such as raw material extraction and its transportation, production of materials, application of pavement materials is often incorporating in the construction phase. Many studies such as Pavement Embodied Carbon Tool (PECT), Intergovernmental Panel on Climate Change (IPCC), Functional Unit (FU) have highlighted various difficulties for obtaining various data during the life cycle assessment of roads [19].

A huge amount of raw materials such as gravel, sand, bitumen, cement and water is required for the construction of road pavements. To optimize the road pavement design, several types of impacts such as environmental, economic and social on the materials should be quantified and monitored. At present condition, no such type of protocol has been applied in Ethiopia. This type of quantification is required to develop a holistic life cycle assessment model on design and technology of construction, maintenance and rehabilitation. Hence the first step for the development of such a holistic life cycle assessment model is an analysis of life cycle inventories. The life cycle assessment process consists of tracking resources, energy, input materials, outputs of waste, coproducts etc to

provide a proper indicator to the system against various environmental impacts [20]. Moreover, due to local construction techniques and context-dependent aspects, the road section has been analyzed for the designed traffic load and its life span. The production of various road materials highly influences the lifecycle environmental impact [21]. Particularly production of bitumen influences asphalt pavement and the production of cement influences concrete pavement [22]. Besides the production of road materials, road maintenance also plays a significant role in the lifecycle environmental impact [23]. From the literature review, it is found that near about one-third of life cycle environmental impact are caused by the various operations for maintenance such as asphalt overlay, reconstruction, thin hot-mix asphalt (HMA) overlay, chip seal, crack seal and cold in-place recycling (CIR) with foamed asphalt etc. Traffic fuel consumption is another environmental impact that is much higher than the environmental impact due to the production of road construction material and road maintenance [13]. The consumption of energy from construction, maintenance and operation of the road is only 9.9% whereas the consumption of energy due to traffic is near about 11.8% [21]. Also, several authors have recommended that for the analysis of traffic fuel consumption, the texture of road surface should be included [6] [24], [25]. If one compares to the environmental impacts between concrete pavement and asphalt pavement, it can be concluded that global warming potential and human health impacts are more contributed by construction and maintenance of concrete pavement while acidification, photochemical smog and eutrophication are more contributed by construction and maintenance of asphalt pavement [7]. Besides the lifecycle environmental impact, lifecycle costing is also increasing in the transportation sector. Various countries like the USA, Europe and Canada are using lifecycle cost at a state-of-the-practice [26]. Comparing concrete pavement and asphalt pavement it is found that concrete pavement is more expensive but suitable for a higher traffic intensity. Because concrete pavement requires lower maintenance frequencies and a less amount of thickness of concrete is required for higher traffic intensities [27].

The environmental licensing monitors the various socio-environmental impacts, which depends on the elaboration of environmental impact studies such as climate change, ozone depletion, ecotoxicity, acidification, Eutrophication etc. [28]. These studies always require several types of impacts caused by the activity, which include an order of magnitude estimation of indirect and direct impacts. But the life cycle approach is not followed by these studies, whether the road built will reduce the habit disruption and deforestation or not. In other words, the various impacts related to road construction are not assessed. Thus, the objective of this study is to determine the environmental impacts associated with the construction of the road in Ethiopia using the life cycle assessment method.

In the present research, a deep level study has been done by the two road projects of Ethiopia (Addis Ababa- Ambo and Addis Ababa-Adama) and found that a huge amount of natural resources has been deployed for the construction of those road pavements. Various types of environmental impacts have been quantified. It is found that the major reason for the pollution of environment (i.e. air, water and soil) is due to the consumption of huge amount petroleum fuel on various activities of road construction such as mining of hills for natural aggregates, transportation of the materials from mines to crushing centre and crushing centre to the construction site, operation of various types of machinery, refining of petroleum products for getting bitumen etc. To reduce this environmental pollution due to a huge amount of fuel consumption, using biodiesel is suggested in vehicles and types of machinery used for road construction. A comparison has been shown between using of petroleum fuel and biodiesel in various types of construction machinery on various environmental impacts.

Table 1. Classification of Ethiopian roads [29]

Technical Classification				Functional Classification			Political Classification												
DS	Traffic (ADT)	Width (m)	Type of Surface				Ownership												
DS-1	10K-15K	7.2	Asphalt	Feeder	Collector	Main	Link	Trunk	ERA (Federal Roads)										
DS-2	5K-10K	7.2																	
DS-3	1K-5K	7.0																	
DS-4	200-1K	6.7																	
DS-5	100-200	7.0	Gravel						Feeder	Collector	Main	Link	Trunk	RRAs (Regional Roads)					
DS-6	50-100	6.0																	
DS-7	30-75	4.0																	
DS-8	25-50	4.0	Earth											Feeder	Collector	Main	Link	Trunk	Woreda Rural Road Office
DS-9	0-25	4.0																	
DS-10	0-15	3.3																	

2. Research Significance

The pavement construction process of the country passes through several phases such as the production of raw materials, transportation of raw materials, construction of pavement, use and maintenance of pavement, and its end life. All these processes possess a unique burden on the local environment [30]. Hence evaluation of the environmental impact of the country's pavement by using lifecycle assessment is the best solution for getting a future warning to society and the construction industry. Lifecycle assessment can assess a product from cradle to grave, explore everything from each and every supply chain process to recycling or disposal after reaching of product at its ultimate end life. In the present condition, no lifecycle data on environmental impact are available in the ordinance of the Ethiopian Road Authority (ERA). The aim of this study is to evaluate various environmental impacts which are associated with the construction of asphalt pavement in Ethiopia by using a life cycle assessment approach.

The life cycle assessment process includes the various construction activities such as extraction of gravel, sand and asphalt and their process; transportation of these materials to the construction site; use and operations of various types of machinery; emissions of greenhouse gases directly or indirectly from materials, transportations and types of machinery fuel. The required input data have been collected from two road projects of Ethiopia. Various impacts are calculated by the ReCiPe method for each category and verified by a suitable alternate method. After analysis of environmental impact, an alternative scenario has been proposed to replace petroleum diesel with biodiesel in diesel-operated machinery and transportation trucks. The innovative part of the present research is the finding of different factors which affect the local environment badly during the road construction process of Ethiopia and finding out the solution for reducing the environmental pollution. A limited amount of research has been found on how the local environment has been badly affected due to the various construction process in Ethiopia. For this reason, two case studies (Addis Ababa-Ambo and Addis Ababa-Adama highway) on the asphalt road project have been deeply studied. It is found that the air is polluting due to the emission of greenhouse gasses from various types of construction machinery, vehicles used for transportation of construction materials, hot mix plant, crushers, petroleum refineries plant etc, whereas the local watersheds and soils are polluted from petroleum refineries plant, washing of various types of construction machinery and materials. Since the major factor of pollution is the emission of greenhouse gasses, biodiesel is suggested to use in various types of machinery and vehicles for the

construction process. It is also found that by using of biodiesel in construction machinery then air pollution can be reduced more than 50%.

3. Methodology

3.1. Method for Life Cycle Assessment

The Life Cycle Assessment (LCA) is divided into four different parts. They are the definition of aim and scope, life cycle inventory, assessment of impact, interpretation of results [31]. The present study aims to determine the environmental impacts of the construction of flexible asphalt pavement in Ethiopia. The observation sample has been taken as 1 km of the two-lane highway for a total road width of 7.3 m. The following activities have been encompassed in the present system. They are extraction or production of road construction materials such as sand, gravel and asphalt; transportation of those road construction materials to and within the construction site; production of asphalt from hot mix concrete plant near to the site; preparation of land for pavement construction by excavation and compaction and application of pavement materials. Energy, road construction materials and fuels needed for all activities are taken as input. Emission of all types of greenhouse gases to the atmosphere directly or indirectly during the above activities is considered as output. The direct emission may be from the construction of the pavement and the indirect emissions are those emissions from the different processes before pavement construction such as raw material extraction, asphalt production, during transportation of raw materials to the site etc. Two factors such as intensity of usage and frequency of maintenance may vary on the lifetime of the road. But the frequency of maintenance may be in between 10 to 15 years. The financial expenses during the different lifecycle stages are considered within the Life Cycle Cost approach. They are investment costs such as expensive for materials, labour and indirect costs for initial construction, maintenance, cleaning, energy cost at the time of use phase and demolition cost and treatment of waste at the time of the end-of-life stage. The life cycle financial cost is the sum of all expenditure occurring during the period of the life cycle of the road infrastructure. This research is following an attributional approach, to determine the environmental impacts that stem from the flow of energy to and from the system boundary. All activities are linked from activity producing waste to the process of waste treatment by the allocation method, which is used at the point of substitution. The whole system considered in the study is shown in Figure 1. Since all the transportation trucks in Ethiopia are using diesel as a fuel, this research also considered the environmental impacts when biodiesel will be filled in the truck instead of petro-diesel for transportation of raw materials to the construction site.

3.2. Life-Cycle Inventory

The amount of materials required for road pavement construction and using of inventories for extraction or production of those materials are described in this section. It also consists of the consumption of fuel and greenhouse gas emissions at the time of freight transportation and machinery operation.

3.2.1. Materials Used in Ethiopian Roads

The width of the road and the depth of the layers is directly related to the environmental impacts. In most parts of Ethiopia, the width of the road is 7.2 m. Most of the pavement in this country possesses the following layers. They are (i) Natural Subgrade, (ii) Compacted Subgrade, (iii) Sub Base Course, (iv) Base Course, (v) Binder Course (vi) Finishing Coat. Since the surface coat is thin layers, they are calculated based on the area of application. The construction depth for each layer and the ratio between thick layer density to the utilized area for thin layers are showing in Table 3. There is no specific rule for road construction products in Ethiopia, hence it was not required to follow any product category

rule. The technical specification for various road construction material such as gravel, binders, asphalt, sand etc has been followed as per Ethiopian standards [32].

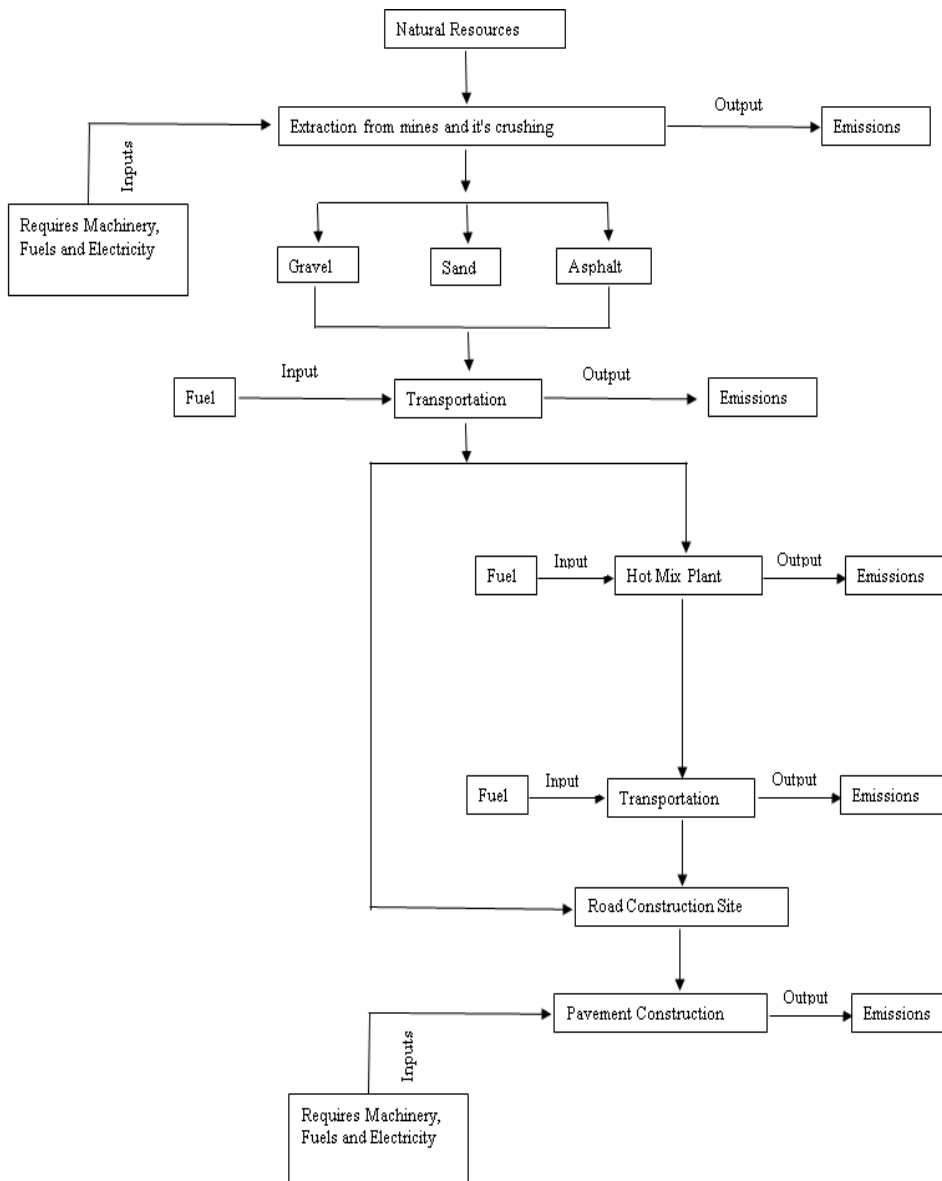


Fig. 1 System diagram for energy consumption and green house gas emission during pavement construction

Table 2. Depth of pavement layer and quantity of materials applied in 1 km road

Layers	Depth (m)	Ratio of Application	Quantity (Metric Ton)
Sub-Base Course	0.35	2150 kg/m ³	5423
Base Course	0.15	2150 kg/m ³	2324
Binder Course	0.05	2400kg/m ³	864
Finishing Coat	0.04	2200 kg/m ³	634

Table 3. Pavement layer composition (kg)

Layers	Gravel	Sand	Asphalt
Sub-Base Course	1	0	0
Base Course	1	0	0
Binder Course	0.81	0.25	0.05
Finishing Coat	0	0.11	0.07

Table 4. Total quantity of materials for the construction of 1 km road with 7.2 m width

Particulars	Quantity	Unit
Gravel	8500	Metric Ton
Sand	300	Metric Ton
Asphalt	100	Metric Ton
Material transportation to the construction site	695000	Tkm
Material transportation within the construction site	190000	Tkm
Excavator (Poclairn or JCB)	4307	M ³
Diesel used in construction machine and hot mix plant	7200	Litre
Diesel operating machinaries	15	Operating hours
Electricity used for crushing of stones	2000	kwh

Both the sub-base and base course are filled by gravel only. Both binder course and finishing coat are assumed as filled by asphalt. The filler in the binder course is sand. Due to the thin section of the binder course and finishing coat, the amount of materials has been calculated on the basis of surface area. Two different bitumen mixes have been prepared for both binder course and finishing coat depending upon the percentage of aggregate materials (i.e sand and gravel). The Binder course has larger aggregate materials as compared to the finishing coat.

3.2.2. Classification of Road Construction Materials for Extraction and Production

Based on the total quantity of materials of each layer and the composition of each layer, the quantities of gravel, sand and asphalt required for the construction of pavement for 1 km length and 7.2 m width is possible. The detailed quantity of materials for above is shown in Table 4 for the corresponding depth shown in Table 2. In Table 2 the depth of different layers has been taken according to Ethiopian Building Code. The density of local materials required for each layer has been determined in the laboratory. The width of the road is taken as 7.2 m. The mass of materials for each layer has been determined by the multiplication of the volume of each layer with the corresponding density of materials. The required quantity of materials may vary depending upon the width of the lane and the depth of the layers.

Three extraction and production types of materials (Sand, Gravel and Asphalt) are described here. The sands are extracted from the river bed. The process includes dredging

of slurry (i.e. mixture of sand, water, silt and clay) from the river, washing of sand to separate clay and silt and transportation of the separated sand to the site. This process considers the energy for loading on the trucks but does not consider the separation of sand from silt and clay. All equipment is considered as diesel running equipment. The gravels are collected from an open granite quarry. The extraction process includes drilling and blasting of stones in open pits, transportation of mined big stone blocks to crushers, crushing of big stone blocks into gravels of different sizes by electric operated crusher, loading and unloading of crushed stones into delivery trucks. The production process of asphalt was developed in such a way that the end products obtained with some specific impacts because it should be followed some specific allocation rules to confirm the impacts for asphalt product were correctly determined. The whole extraction process of asphalt passes through the various process such as the construction of refinery infrastructure, storage of crude oil in refinery ground, feeding of crude oil into the refinery, supplying of freshwater from nature for refinery process, wastewater treatment process exhausted from refinery plant and use of energy.

3.2.3. Detailed Process of Transportation of Materials

The distance for transportation of road construction material to the construction site or within the construction site depends upon the geographical locations and ease of connectivity of road construction projects with other service roads. In this study, the transportation distance has been recorded as the average distance of two road construction projects of Ethiopia. The detailed distance for transportation of different materials is shown in Table 5 has been recovered from Final Project Report, Ethiopian Road Authority 2019 [33]. The total quantity of materials for 1 km road construction to the construction site or within the construction site (Table 4) is calculated based on total transportation distance (Table 5) and quantity of composition materials used in each pavement layer (Table 3). It is assumed that the transportation of all materials is carried to the construction site or with in construction site by trucks of a capacity of 23 metric tons. The inventory for transportation of material includes all activities such as production maintenance of the truck, production of diesel, construction and maintenance of road. A small modification has been done such as low sulfur diesel production in Ethiopia has suggested instead of petroleum diesel.

3.2.4. Various Machinery Operation

For base preparation and soil excavation, excavators like poclain and JCB are used. Various types of machinery are used for each layer of pavement as follows. For sub-base course sheep foot compactor, for base course sheep foot compactor followed by a smooth wheel roller, for binder course asphalt spray truck, paver, pneumatic roller and for finishing coat paver, smooth wheel roller have been used. Electricity has used for rotating the mixture drum, running the pumps, compressors, fans, elevators, driving the belt etc while diesel has used for the operation of the hot mix plant for heating the mixtures. The total operating hours, volume for excavation, consumptions of electricity and diesel are summarized in Table 6. From the Ecoinvent database [34] machinery operation inventories are obtained. The capacity of all machinery is assumed as above 75kW and high load factor, operated by diesel and the mode of operation has considered as operating hours. It is based on calculations performed by US EPA's Motor Vehicle Emissions Simulator (MOVES) [35]. The inventory for the excavator has based on excavated volume.

The hot mix plant operation has been divided into two categories. The first one is the heating process running on diesel and the second one is building machine running on electricity. All inventories are used for local geography with incorporating necessity modification to Ethiopian electricity production mix [36].

Table 5. Transportation distance to the construction site or within construction site for present research

Materials	From	To	Total Distance (km)
Sand	River bed	Hot mix plant/Storage site	150
	Storage site	Application on pavement	10
Gravel	Mines	Hotmix Plant/ Storage site	100
	Storage site	Application on pavement	10
Asphalt	Petroleum Refinery	Hotmix plant	600
Hot mixed bituminous mixture	Hotmix plant	Application on pavement	10

3.2.5. Production of Bio-Diesel and its use in Transportation Trucks

In the present research, an alternative scenario has been suggested that to use biodiesel instead of petroleum diesel in transportation trucks as a fuel [37]. The biodiesel can be formed from various African oil bean seeds [38]. It will give a positive impact on the environment and cost during transportation of materials to the construction site. For the production of biodiesel and transport trucks running on this biodiesel, a separate inventory is required.

The African oil bean seeds are consuming at a limited amount by local people as a vegetable and can be categorized as an underutilized crop. Though this crop has a good yield in present condition, a few numbers of local farmers are cultivating these types of crops. Due to lower demand in the market, farmers are not getting a good sum. If these oil bean seeds will be used for extraction of edible oil and made the conversion of oil to other product, then its value will be added and a higher financial turnover can be yield.

3.2.6. Life Cycle Impact Assessment

To determine the impacts on various categories such as Global Warming Potential, Ozone Depletion Potential, Terrestrial Acidification Potential, Freshwater Eutrophication Potential and Freshwater Ecotoxicity Potential. To calculate the impacts, two types of approaches have followed. The first one is ReCiPe 2016 [39] and the second one is different methods for evaluating impact from the ILCD handbook. For the Global Warming Potential category, the IPCC 2013 method [40], for Ozone Depletion Potential and Terrestrial Acidification Potential category the CML 2001 method [41], for Freshwater Eutrophication Potential category USEtox v1.0 method and Freshwater Ecotoxicity Potential category EDIP 2003 method [42] has been used. To evaluate the impacts of each system of production, open Life Cycle Assessment software version 1.10.2 has been used [43].

Table 6. Specifications for various machineries operated in pavement construction

Layer	Type of Machinery	Specification
Excavation	Excavator (Poclairn or JCB)	Based on the excavated volume
Sub Base Course	Sheep-foot Compactor	No of passing per lane: 8 Power of Compactor: 100 kW Avg. speed of Compactor: 5.5km/h Compactor width: 2.1m
Base Course	Sheep-foot Compactor	No of passing per lane: 6 Power of Compactor: 100 kW Avg. speed of Compactor: 5.5km/h Compactor width: 2.1 m
	Smooth Wheeled Roller	No of passing per lane: 10 Power of Compactor: 100 kW Avg. speed of Compactor: 5.5 km/h Compactor width: 2.1m
Binder Course	Asphalt Spray Truck	Power: 205 kW Average Speed: 4 km/h No of passing per lane: 2
	Paver	Power: 200 kW Paver width: 2.5m Avg. Speed: 4 km/h No of passing per lane :8
	Pneumatic Roller	Power: 100 kW Avg. speed: 10 km /h Roller width: 2.1m
Finishing Coat	Paver	No of passing per lane: 2 Power: 195 kW Paver width: 2.5m Avg. Speed: 4 km/h
	Smooth-wheeled Roller	No of passing per lane: 6 Power: 195 kW Paver width: 3m Avg. Speed: 4 km/h
Mixer	Hotmix plant	Plant capacity: 130 t/h Power: 240 kW Fuel Consumption: 7.2 L/t of asphalt mix

4. Results and its Interpretation

Figure 2 and Figure 3 show the impacts on various categories that have been considered in the present research. The impact of each process within the road pavement construction has been shown in Figure 4 and Figure 5 as a percentage contribution and following notations have been given for different processes. The notation for "Sand", "Gravel" and "Asphalt" shows the extraction of these materials; Transport refers to the transportation of all above material; and the word "Machinery" indicates use and operation machinery for the building of the pavement. Notation C1 represents the condition for the present situation i.e. all transport vehicles are fueling by petroleum diesel whereas notation C2 represents the alternative condition i.e. all transport vehicles are fueling by biodiesel.

4.1. Total Impact

The total impact of both conditions i.e. C1 and C2 are analyzed in Table 7. For condition C1, two types of life cycle impact assessment approaches have been implemented. They are ReCiPe and combined methods. For condition C2, only ReCiPe has been used. Figure 2 and Figure 3 are showing the total impact for conditions C1 and C2 by using the ReCiPe method. From Figure 2 and Table 7 it can be seen that the transportation truck fueled by biodiesel (C2) has lower environmental impacts than the transportation truck fueled by petroleum diesel (C1). By comparing two conditions C1 and C2 it has been found that values of C1 are 41.6%, 11.1%, 20%, 50% and 60% more than w.r.t the values of C2 for different types of impacts such as GWP, ODP, TAP, FWEP and FWECF respectively. Again, from Figure 3, it has been found that there is a close relationship between methods used for various categories of life cycle impact assessment except for FWECF. The normalized value was calculated by ReCiPe method and IPCC method for GWP, ReCiPe method and CML method for both ODP and TAP categories, ReCiPe and EDP method for FWEP category. But there is a large difference between ReCiPe and USEtox for the FWECF category.

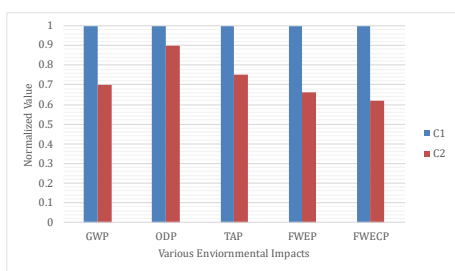


Fig. 2 Total impact for both conditions C1 and C2 calculated by ReCiPe method

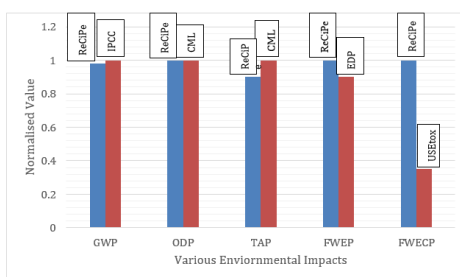


Fig. 3 Comparison between ReCiPe and combined methods for calculation of total impacts

Table 7. Total impacts for conditions C1 and C2 by using life cycle impact assessment approaches

Types of Impact	ReCiPe 2016		Combined Methods	Unit
	C1	C2	C1	
GWP	2.45E+5	1.85E+5	2.48E+5	kg CO ₂
ODP	8.5E-2	7.65E-2	8.5E-2	kg CFC
TAP	2.3E+3	1.9E+3	2.53E+3	kg SO ₂
FWEP	1.75E+1	1.6E+1	1.61E+1	kg P
FWECF	2.5E+3	1.9E+3	2.53E+3	kg 1,4-DCB

4.2. Role of Each Process to the Total Impact

There is a various process who plays an important role to the impacts for the condition C1 based on the ReCiPe method are gravel, asphalt and transport. The maximum contributions of machinery are near about 15%, while sand has a very negligible contribution to all impacts. Various contributions of materials and process in percentage on total impact by ReCiPe method has shown in Figure 4. It is found that the gravel impacts on TAP at the highest percentage and on ODP at the lowest percentage by both methods. Asphalt contributes near about 50% on ODP as highest and 10% on FWECF as the lowest percentage. The contribution of sand to total impact is very negligible. Machinery contributes at an equal level to all categories impacts ranges in between (10% to 13%).

Transport contributes near about to 52% on GWP as of the highest percentage and 15.5% on TAP as the lowest percentage of contribution. Again, from Figure 5, it can be seen that when biodiesel (C2) is used instead of petroleum diesel (C1) there is an increase in the transportation process for all categories except ODP. The transportation process decreased from 28.7% to 18.4%.

5. Brief Discussions of Results

Based on an interpretation of results impact from the various parameters such as sand, gravel, asphalt, machinery and transportation, a brief discussion with its scientific causes has been quoted after analyzing the results. In this analysis, every process has been a break down into various subprocesses and their impacts resulting from each of them. From the contribution tree of open life cycle analysis software, the contribution of each sub-process to the total impacts has been obtained and discussed briefly as follows.

5.1. Global Warming Potential (GWP)

From Figure 5, one can notice that the Global Warming Potential category has been influenced by mainly the transportation process which is analyzed for conditions C1 and C2 (above 50% contribution). Also, by ReCePi and IPCC method, Global Warming Potential has been influenced by the transportation process showing its contribution percentage as above 50% for condition C1. This highest value is showing due to the emission of carbon dioxide into the atmosphere directly during transportation. The production and utilization of diesel fuel to other machinery are showing 13% and 12% by ReCiPe and IPCC method respectively. Seeing the more contribution of transportation process to Global Warming Potential due to using petroleum diesel in transportation truck and other machinery, biodiesel is used as an alternative fuel. Vegetable oil is the main source of biodiesel for the African country. Though biodiesel is eco-friendly, the transportation process showing higher contribution towards Global Warming Potential. This is due to the transportation of vegetables to the oil mill for grinding and preparation of biodiesel. Near about 70% contribution is giving to Global Warming Potential for transportation of raw materials. Hence it is recommended that more biodiesel plants should be established near the firm land of Ethiopia. Again, it can be seen that the transport category only impacts near about 4.5% caused by the emission of carbon dioxide during transport itself since 95.5% of these emissions of carbon dioxide are non-fossil [44].

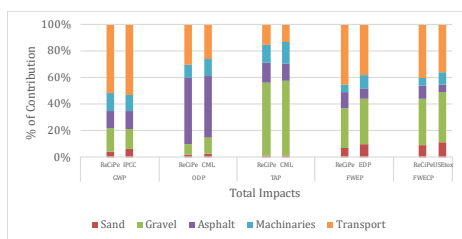


Fig. 4 Contribution of different categories to the total impacts by various methods for condition C1

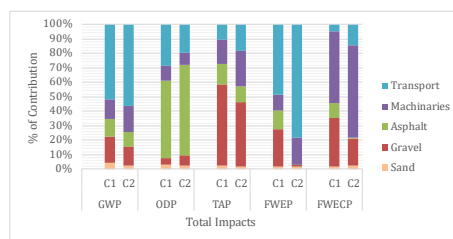


Fig. 5 Contribution of different categories to the total impacts by both conditions C1 and C2

Since the transportation of vegetable seeds to the oil mill and production of fuel has been considered in condition C2, the biodiesel impacts more than petroleum diesel on Global Warming Potential though it has been replaced to the petroleum diesel to a transportation truck. But for the extraction of sand, gravel and asphalt the biodiesel (condition C2) impacts less than petroleum diesel (condition C1). For condition C1, the process of gravel

is showing an 18% contribution to Global Warming Potential, from which near about 40% contributes from direct emissions from machinery fueled by petroleum diesel for production of gravel and the remaining 38% contributes from explosives used in quarry for blasting purposes. The asphalt contributes 18% to Global Warming Potential impact, out of which 65% contributes emissions from oil refinery plants and the remaining 35% from direct emissions during transportation and heating before application to the pavement. Again, the contribution of machinery is showing 14% on Global Warming Potential impact, out of which only 15% contributes at the time of petroleum diesel production and the remaining 85% contributes at construction activities such as excavation, hot mix plant and road construction types of equipment. On average there is no significant variation between two life cycle impact assessment methods. The difference between total Global Warming Potential impacts differ between the two methods is only 1.5% due to the absence of some factors such as CO in the ReCiPe method. The impact factor of carbon dioxide for both methods is showing the same.

5.2. Ozone Depletion Potential (ODP)

Among the various categories of life cycle assessment, the production of asphalt is showing the highest contribution i.e. 53.2 and 60.1 for conditions C1 and C2 respectively. This is because of the direct emission of the halogenated compound such as Halon-1211, Halon-1301 and CFC-114 from petroleum refinery [45]. The emission of halogenated compounds depletes the ozone layer. The production of diesel plays the main contributor to the Ozone Depletion Potential impact among all processes. But for condition C2, biodiesel has been replaced with petroleum diesel and reduced the impact due to transportation near about 10.3% for the total Ozone Depletion Potential impact. Again, the impact value due to the transportation process is near about to same for both ReCiPe and CML methods.

5.3. Terrestrial Acidification Potential (TAP)

The Terrestrial Acidification Potential category for condition C2 has impacted 8% more than Condition C1. This is because of the higher emission of NO_x during the combustion of biodiesel. The oxygen inside the biodiesel helps to increase the percentage of NO_x due to an increase in temperature during the combustion process [46]. Under the transportation process, both petroleum diesel and bio-diesel contribute near about 30% in the process of fuel production. It is seen that the transportation of petroleum diesel impacts 37%, whereas transportation of bio-diesel impacts 53%.

From condition C1 it is found that TAP is already affected by gravel only, which contributes near about to 50% by both ReCiPe and CML method with very good agreement. Both methods are indicating that the cause behind contributing a higher percentage of gravel is the blasting of mineral mines. The blasting process contributes near about to 80% and rest of 20% are contributed by diesel-fueled truck for transportation of gravel. Again, it is found from the ReCiPe method that the most contributing substance to Terrestrial Acidification Potential by gravel process is NO_x. It contributes near about 60% along with 40% NH₃. But in the CML method, the contribution of NO_x is 75% along with 25% of NH₃. Now it is verified with the previous literature that the ReCiPe method contributes a higher value of NH₃ and a lower value of NO_x as compared to the CML method [40]. Next to gravel the second most category which contributes to TAP is the transport process and production of asphalt. Though the values by both ReCiPe and CML methods are near about equal, the ReCiPe method is slightly higher than CML due to the emission of NO_x.

5.4. Freshwater Eutrophication Potential (FWEP)

From various literature, it is found that phosphorous and nitrogen are used as a reference compound for aquatic eutrophication potential [40]. Generally phosphorous is using for fresh lake water and nitrogen for saline marine water. From Figure 4 it is found that the

EDIP method shows higher value than the ReCiPe method for sand, gravel and machinery categories and lower value for asphalt and transport categories. The lower value (i.e 4% for asphalt and 7% for transportation) for the EDIP method is due to the emission of P-containing to the freshwater source [44]. The main contribution of phosphate to impact freshwater from the treatment of residues emitted from construction, machinery and production of raw materials. For the processing of gravel, the freshwater is impacted near about 90% due to direct emission during blasting and consumption of diesel by the ReCiPe method. No seashore is near to Ethiopia country; hence Merine Eutrophication Potential has not found here. In condition C2, using bio-diesel in transport trucks shows a large eutrophication impact than petroleum diesel because of the emission of phosphate during utilization of chemical fertilizer to the bean plants. Hence it is recommended that organic fertilizer has to be used for the cultivation of vegetable seeds for the production of bio-diesel.

5.5. Freshwater Ecotoxicity Potential (FWECP)

From Figure 4 it is found that the USEtox method is showing more impacts on Freshwater Ecotoxicity Potential by the categories of gravel, transport and machinery and lower impacts by the categories of asphalt and transport as compared to the ReCiPe method. Figure 3 shows a larger difference between ReCiPe and USEtox method, but it may be significant and acceptable. The USEtox model does not show absolute comparison with others [47]. The higher uncertainties in the parameters of both models give more differences because 10 to 20 numbers of most contributing substances make both models ideal rather than predicting the actual value. Both models are influenced by gravel and transportation at a higher percentage. The transport category is influenced more by the USEtox method (48%) than the ReCiPe method (40%). The higher percentage is due to residue treatment during the truck production process and tire and brake wear emissions. The impact on Freshwater Ecotoxicity Potential by gravel is showing more due to the use of explosive materials in mines and the treatment of residues during the process of explosive production. The substances which cause more impact to Freshwater Ecotoxicity Potential are copper than other influenced materials such as zinc, nickel, silver and vanadium. By replacing petroleum diesel with biodiesel in condition C2, the Freshwater Ecotoxicity Potential is impacting 2.8 times than condition C1. This is because of the esterification of vegetable oils, treatment of various residues such as phosphoric acid, chemical fertilizer, methanol etc from the raw materials used for the production of biodiesel.

6. Conclusions

This work belongs to an inventory for the asphalt paved road construction based on collected data from Ethiopian Road Authority. By using different methods various environmental impacts like Global Warming Potential, Terrestrial Acidification Potential, Ozone Depletion Potential, Freshwater Eutrophication Potential and Freshwater Ecotoxicity Potential have been analyzed by taking various factors such as road construction materials, machinery and transport. Also, the environmental impacts have been evaluated by replacing petroleum diesel with biodiesel in transportation and machinery. From the evaluation process following conclusions are drawn.

- Among all impact categories, gravel and transport are two main processes, who are playing an important contributor to each environmental impact categories.
- Asphalt influences more to Ozone Depletion Potential category than other categories.

- The improvements in the production process of road construction materials such as sand, gravel, asphalt and transportation should be required to reduce their impacts on the environment and improve the quality of construction.
- The environmental impact from transport may vary on the location of the construction site and the availability of the distribution network.
- Each category of environmental mental impact evaluated by different methods are showing a similar percentage of contribution and the same substances and sub-process are showing as the most impactful.
- The replacement of petroleum diesel by biodiesel derived from the vegetable oils is showing lower environmental impacts than petroleum diesel and proved beneficial. Hence it is recommended that the production of biodiesel should be encouraged by Govt. of Ethiopia.
- Since the production process of gravel plays one important role in environmental impacts, it is suggested that construction waste may be a substitute for gravel. So that the natural resources of the country may be saved as well as our environment may be kept green.

Acknowledgement

Our grateful acknowledgment goes to Wollega University for its extensive support. No funding was received.

References

- [1] Chandra S. Highway capacity research on inter-urban highways in india, *Transp Dev Econ*, 2015;1(1):20-4. <https://doi.org/10.1007/s40890-015-0003-4>
- [2] Rath B, Debnath R, Paul A, Velusamy P, Balamoorthy D. Performance of natural rubber latex on calcined clay-based glass fiber-reinforced geopolymer concrete, *Asian J Civ Eng*, 2020;21(6): 1-16. <https://doi.org/10.1007/s42107-020-00261-z>
- [3] Mazumder M, Sriraman V, Kim HH, Lee S-J. Quantifying the environmental impacts of crack sealing and filling treatment in hot mix asphalt pavement, *Innovative Infrastructure Solution*, 2018;3(1):1-12. <https://doi.org/10.1007/s41062-018-0161-4>
- [4] Lu G, Wang Y, Li H, Wang D, Oeser M. The environmental impact evaluation on the application of permeable pavement based on life cycle analysis, *Int J Transp Sci Technol*, 2019; 8(4):351-357. <https://doi.org/10.1016/j.ijst.2019.05.006>
- [5] Jocelyn Ivel, Rachel Watson, Bassim Abbassi, Ziad Salem Abu-Hamatteh. Life cycle analysis of concrete and asphalt used in road pavements, *Environmental Engineering Research*, 2020; 25(1): 52-61. <https://doi.org/10.4491/eer.2018.399>
- [6] Trupia L, Parry T, Neves LC, Presti D Lo. Rolling resistance contribution to a road pavement life cycle carbon footprint analysis, *Int J Life Cycle Assess*, 2017;22(6):972-985. <https://doi.org/10.1007/s11367-016-1203-9>
- [7] Santero NJ, Masanet E, Horvath A. Life-cycle assessment of pavements. Part I: Critical review, *Resour Conserv Recycl*, 2011;55(9-10):801-809. <https://doi.org/10.1016/j.resconrec.2011.03.010>
- [8] Trunzo G, Moretti L, D'Andrea A. Life cycle analysis of road construction and use, *Sustainability*, 2019; 11: 1-13. <https://doi.org/10.3390/su11020377>
- [9] Shtayat A, Moridpour S, Best B, Rumi S. An overview of pavement degradation prediction models, *Journal of Advanced Transportation*, 2022:1-15. <https://doi.org/10.1155/2022/7783588>
- [10] Santero NJ, Masanet E, Horvath A. Life-cycle assessment of pavements Part II: Filling the research gaps, *Resour Conserv Recycl*, 2011;55(9-10):810-818. <https://doi.org/10.1016/j.resconrec.2011.03.009>

- [11] Alaye QEA, Ling X, Dong Z, Bambou G. Evaluation of mixture performance recycled asphalt pavement materials as base layer with or without Rejuvenator into the asphalt, *J Wuhan Univ Technol Sci Ed*, 2020;35(3):579-597. <https://doi.org/10.1007/s11595-020-2295-4>
- [12] Appiah JK, Berko-Boateng VN, Tagbor TA. Use of waste plastic materials for road construction in Ghana, *Case Stud Constr Mater*, 2017; 6:1-7. <https://doi.org/10.1016/j.cscm.2016.11.001>
- [13] Yu M, You Z, Wu G, Kong L, Liu C, Gao J. Measurement and modeling of skid resistance of asphalt pavement: A review, *Constr Build Mater*, 2020;260:1-15. <https://doi.org/10.1016/j.conbuildmat.2020.119878>
- [14] Lang AS. recycling materials from highways. National cooperative highway research program synthesis of highway, Practice No. 54, Transportation Research Board, Washington, DC, 1978.
- [15] Mallick RB, Singh D, Veeraragavan A. Extension of asphalt pavement life by reduction of temperature, *Transp. in Dev. Econ*, 2016; 2(7): 1-7. <https://doi.org/10.1007/s40890-016-0013-x>
- [16] Al-Hasan SJA, Balamuralikrishnan R, Altarawneh M. Eco-friendly asphalt approach for the development of sustainable roads, *Journal of Human, Earth and Future*, 2020; 1(3): 97-111. <https://doi.org/10.28991/HEF-2020-01-03-01>
- [17] Bilema M, Bin Aman Y, Hassan NA, Al-Saffar Z, Ahmad K, Rogo K. Performance of aged asphalt binder treated with various types of rejuvenators, *Civil Engineering Journal*, 2021; 7(3): 502-517. <https://doi.org/10.28991/cej-2021-03091669>
- [18] Nawir D, Mansur AZ. The impact of hdpe plastic seeds on the performance of asphalt mixtures, *Civil Engineering Journal*, 2021; 7(9): 1569-1581. <https://doi.org/10.28991/cej-2021-03091744>
- [19] Hoxhaa E, Vignisdottirb HR, Barbieric DM, Wangcd F, Bohnec RA, Kristensenb T, Passera A. Life cycle assessment of roads: Exploring research trends and harmonization challenges, *Science of The Total Environment*, 2021;759:1-16. <https://doi.org/10.1016/j.scitotenv.2020.143506>
- [20] Singh A, Pant D, Olsen SI. Life cycle assessment of renewable energy sources. Springer; 2013. <https://doi.org/10.1007/978-1-4471-5364-1>
- [21] Trigaux D, Wijnants L, De Troyer F, Allacker K. Life cycle assessment and life cycle costing of road infrastructure in residential neighbourhoods, *Int J Life Cycle Assess*, 2017;22(6):938-51. <https://doi.org/10.1007/s11367-016-1190-x>
- [22] Szymański P, Pikos M, Nowotarski P. Concrete road surface with the use of cement concrete-selected results, *Procedia Eng*, 2017;208:166-73. <https://doi.org/10.1016/j.proeng.2017.11.035>
- [23] Giustozzi F, Crispino M, Flintsch G. Multi-attribute life cycle assessment of preventive maintenance treatments on road pavements for achieving environmental sustainability, *Int J Life Cycle Assess*, 2012;17(4):409-19. <https://doi.org/10.1007/s11367-011-0375-6>
- [24] Nguyen T, Lechner B, Wong YD. Response-based methods to measure road surface irregularity: a state-of-the-art review, *Eur. Transp. Res. Rev*, 2019;11: 1-18. <https://doi.org/10.1186/s12544-019-0380-6>
- [25] Fontaras G, Zacharof NG, Ciuffo B. Fuel consumption and CO2 emissions from passenger cars in Europe - Laboratory versus real-world emissions, *Progress in Energy and Combustion Science*, 2017; 60: 97-131. <https://doi.org/10.1016/j.pecs.2016.12.004>
- [26] Sala S, Amadei AM, Beylot A, Ardente F. The evolution of life cycle assessment in European policies over three decades, *Int J Life Cycle Assess*, 2021;1-20. <https://doi.org/10.1007/s11367-021-01893-2>

- [27] Hassouna F, Jung YW. Developing a higher performance and less thickness concrete pavement: using a nonconventional concrete mixture, *Adv Civ Eng*, 2020; 1-8. <https://doi.org/10.1155/2020/8822994>
- [28] Hauschild M. Environmental impact. In: the international academy for production engineering, Laperrière L., Reinhart G. (eds) *CIRP Encyclopedia of Production Engineering*. Springer, Berlin, Heidelberg, (2014).
- [29] Emmenegger R. *The Roads of Decentralization: the history of rural road construction in Ethiopia*. 2012.
- [30] Lima MSS, Hajibabaei M, Hesarkazzazi S, Sitzenfrei R, Buttgereit A, Queiroz C, Haritonovs V, Gschösser F. Determining the environmental potentials of urban pavements by applying the cradle-to-cradle lca approach for a road network of a midscale german city, *Sustainability*, 2021; 13(22): 1-14. <https://doi.org/10.3390/su132212487>
- [31] Salah M, Haggag El. Rural and developing country solutions, *Environmental Solutions*, 2005: 313-400. <https://doi.org/10.1016/B978-012088441-4/50015-0>
- [32] ERA. *The Federal Democratic Republic Of Ethiopia Ethiopian Roads Authority Pavement Design Manual Volume I: Flexible Pavements*. Pavement Des. 2013; I(March):281.
- [33] Final project report, Training Program for Improved Performance of Surface Treatments in Ethiopia, Ethiopian Roads Authority. 2019: 1-84.
- [34] Wernet G, Bauer C, Steubing B, Reinhard J, Moreno-Ruiz E, Weidema B. The ecoinvent database version 3 (part I): overview and methodology, *Int J Life Cycle Assess*, 2016;21(9):1218-30. <https://doi.org/10.1007/s11367-016-1087-8>
- [35] Wernet G, Bauer C, Steubing B, Reinhard J, Moreno-Ruiz E, Weidema B. The ecoinvent database version 3 (part I): overview and methodology, *Int J Life Cycle Assess*, 2016;21(9):1218-30. <https://doi.org/10.1007/s11367-016-1087-8>
- [36] Mondal MAH, Bryan E, Ringler C, Mekonnen D, Rosegrant M. Ethiopian energy status and demand scenarios: prospects to improve energy efficiency and mitigate GHG emissions, *Energy*, 2018;149:161-72. <https://doi.org/10.1016/j.energy.2018.02.067>
- [37] Praveenkumar T. R, Velusamy P, Balamoorthy D. Pyrolysis oil for diesel engines from plastic solid waste: a performance, combustion and emission study, *Int J Ambient Energy*, 2020;1-5. <https://doi.org/10.1080/01430750.2020.1818124>
- [38] Ndukwu MC, Onyeoziri CI. African oil bean seed as feedstock for bio-oil and biodiesel production and on the effects of thermal pre-treatments on the quality of the bio-oil, *Biomass Convers Biorefinery*, 2020;1-12. <https://doi.org/10.1007/s13399-020-00754-6>
- [39] Kousis I, Fabiani C, Ercolanoni L, Pisello AL. Using bio-oils for improving environmental performance of an advanced resinous binder for pavement applications with heat and noise island mitigation potential, *Sustain Energy Technol Assessments*, 2020;39:1-13. <https://doi.org/10.1016/j.seta.2020.100706>
- [40] Hope AP, Canty TP, Salawitch RJ, Tribett WR, Bennett BF. Forecasting global warming. In: *Paris climate agreement: Beacon of hope*. Springer, Cham; 2017: 51-113. https://doi.org/10.1007/978-3-319-46939-3_2
- [41] Nunez P, Jones S. Cradle to gate: life cycle impact of primary aluminium production. *Int J Life Cycle Assess*. 2016;21(11):1594-1604. <https://doi.org/10.1007/s11367-015-1003-7>
- [42] Pettersen JB, Song X. Life cycle impact assessment in the arctic: challenges and research needs. *Sustainability*. 2017;9(9):1-20. <https://doi.org/10.3390/su9091605>
- [43] Ciroth, A. ICT for environment in life cycle applications open LCA - a new open source software for life cycle assessment, *Int. J. Life Cycle Assess*, 2007; 12: 209-210. <https://doi.org/10.1065/lca2007.06.337>
- [44] Thalmann P, Vielle M. Lowering CO2 emissions in the Swiss transport sector. *Swiss J Econ Stat*. 2019;155(1):1-12. <https://doi.org/10.1186/s41937-019-0037-3>

- [45] Barletta B, Meinardi S, Simpson IJ, Rowland FS, Chan C-Y, Wang X, et al. Ambient halocarbon mixing ratios in 45 Chinese cities, *Atmos Environ*, 2006;40(40):7706-19. <https://doi.org/10.1016/j.atmosenv.2006.08.039>
- [46] Özener O, Yüksek L, Ergenç AT, Özkan M. Effects of soybean biodiesel on a DI diesel engine performance, emission and combustion characteristics, *Fuel*, 2014;115:875-83. <https://doi.org/10.1016/j.fuel.2012.10.081>
- [47] Rosenbaum RK, Bachmann TM, Gold LS, Huijbregts MAJ, Jolliet O, Juraske R, et al. USEtox-the UNEP-SETAC toxicity model: recommended characterisation factors for human toxicity and freshwater ecotoxicity in life cycle impact assessment, *Int J Life Cycle Assess*, 2008;13(7):532-46. <https://doi.org/10.1007/s11367-008-0038-4>



Technical Note

Self - compacting concrete made with partial replacement of lime stone and quarry dust powder

Deepan Rajendran^a, Chella Gifta Christopher^{*b}, Malaiappan Sindhu Muthu^c

Faculty of Civil Engineering, National Engineering College, KR Nagar, Kovilpatti, Tamilnadu, India

Article Info

Abstract

Article history:

Received 01 Oct 2021

Revised 22 Jan 2022

Accepted 07 Feb 2022

Keywords:

Quarry dust;

Lime stone powder;

Self compactability;

Compressive strength;

Density

Self-compacting concrete is very popular in the field of concrete technology and it plays a significant role while placing the concrete in congested reinforcements. Self-compacting concrete could be produced with high fluidity and good cohesiveness, and it gets compacted by its gravitational force. This paper attempts to understand the influence of filler materials such as lime stone powder and quarry dust as a partial replacement of cement material. Self-compacting concrete was produced by partially replacing the cement by 10%, 20%, 30% Lime stone and Quarry dust powder, and their influence on fresh properties such as passing and filling ability, flowability are examined as per European Federation of National Associations Representing for Concrete (EFNARC) guidelines. Results of fresh and hardened properties exhibited replacement up to 10% lime stone and quarry dust is the optimum level, and other replacement levels produced satisfactory results. Compressive strength, water sorptivity, and density values are marginally affected by the addition of 20% and 30% replacement of these filler materials.

© 2022 MIM Research Group. All rights reserved.

1. Introduction

Concrete is a primary construction material and construction industry has a greater demand for achieving a strong and durable concrete. Cement, aggregates, water, mineral and chemical admixture are the raw materials used in the manufacture of conventional concrete. According to the Cement Industry 2019 report, India is the second largest cement producer in the world and the per capita cement consumption is estimated to be 239kg [1]. Cement manufacturing industries are the major sources of carbon di oxide emission and they produces 310 million tonnes of cement clinkers and they are the major pollutants to the environment [2]. Report says about 12% -15% of total industrial energy emission is contributed by the cement manufacturing industry. It causes a major threat to living hood and endangers the human respiratory systems by producing huge quantity of particulate matters in the production stage. Hence it is necessary to search for an alternative material to replace the cement in the production of concrete in order to save the energy as well as the environment. Nowadays cement is partially replaced with wide variety of supplementary cementitious materials (SCM) and high quality SCM produces strong and durable concrete. However, the extensive use of these SCM's also leads to the depletion of natural resources and hence some initiatives are necessary to identify a suitable substitute for replacing the cement with similar morphological properties [3].

Lime stone and Granite quarries are considerably increasing in number and they produces large amount of Lime stone and Quarry dust in powder form during their crushing process. Handling becomes a challenge for these quarries, because the land filling and disposal of

*Corresponding author: erchellac@gmail.com

^a orcid.org/0000-0002-2399-3338; ^b orcid.org/0000-0002-4956-9332; ^c orcid.org/0000-0001-7420-8523

DOI: <http://dx.doi.org/10.17515/resm2022.346ma1001tn>

Res. Eng. Struct. Mat. Vol. 8 Iss. 3 (2022) 633-642

this powder creates serious environmental problems like water, land pollutions and cause determinantal effects to the human health. Both powdered materials are very fine in nature and they contaminate the air during summer and spring seasons [4]. However these finer materials could be successfully utilized as a binder medium to enhance the flowability and viscosity in the production of special concrete like self- compacting concrete (SCC). Self-compacting concrete is a new composite developed in recent years, producing concrete of high fluidity, self compactability, high strength and better serviceability during their exposure conditions. SCC mix designs are different from traditional one in which the rheology of the mortar is adjusted to achieve the concrete with high level of workability. Mineral admixtures and plasticizers are used to achieve the fluidity of concrete and the particle size distribution is the best approach to optimize the fluidity of self-compacting concrete. Inter particle separation combined with particles packing density is the main rheological parameter governing the design of self-compacting concrete. The addition of mineral additives or powders in addition to the cement content is used to achieve the appropriate viscosity of self-compacting characteristics. In SCC, aggregate – cement interface zone is the weakest one and it depends on the fineness of the mineral admixture [4]. Hence the advantages of SCC are numerous and it is described as a most revolutionary material in the construction industry. It offers some economic benefits such as faster construction, reduced man power, good surface finishes, thinner concrete sections, reduced noise level and no vibrations etc. In spite of these merits there are few bottle necks in the application of SCC. Lack of Indian standard codes describing the testing procedures, mix design, high cost, high quality control and need of special form works are few, which may limit the application of self-compacting concrete. Several authors have already explored the behaviour of self-compacting concrete with the incorporation of basalt, granite, marble powders in cement paste, cement mortar and concrete [5 - 7]. Burak Felekoglu produced SCC with quarry lime stone powder as partial replacement of cement reported the substitution of materials reduced the strength when lime stone powder content is increased [8]. Demone et al. analyzed the SCC fresh properties with 16mm and 20mm size coarse aggregates along with the lime stone fillers concluded the robustness of SCC could be improved by the addition of viscous modifying agents [9]. Dehwah summarized relatively better mechanical properties of SCC incorporated with quarry dust powder than its combination with silica fume [10]. Khaleel et al. reported the usage of uncrushed gravel improves the flowability, passing ability, and segregation resistance when compared with crushed gravel [11]. Schankoski et al. concluded the SCC produced with diabase and gneiss quarry powders slightly increased the fresh and hardened properties in comparison with lime stone as filler in concrete production [12]. Self-compacting concrete has become a sustainable development in the field of concrete technology and it could be used in many civil engineering applications [13]. Hence this paper mainly focus on characterizing the self-compacting concrete produced with the incorporation of quarry dust and lime stone powder as a partial replacement of cement. Their impacts on fresh properties and few hardened properties were determined and reported.

2. Experimental Procedure

To understand the behaviour of self-compacting concrete manufactured with the addition of fillers, the following materials were used: Ordinary Portland Cement, Lime stone and Quarry dust powder, Aggregate and Super plasticizers.

2.1. Material and Mixture Proportions

In this experimental study Ordinary Portland Cement 53 grade conforming to IS 12269: 2013 specification was used as an important binder [14]. Physical properties of the cement used in this study are given in Table 1. Cement is replaced with Lime stone powder

particles of size less than 0.125 mm and its specific gravity is 2.53. Crushed quarry dust powder smaller than 150 μ m is also used as a partial replacement material and its specific gravity was measured to be 2.30. Lime stone powder and Crushed quarry dust powder used in this study are shown in Fig. 1 and Fig. 2. Angular shaped aggregates of maximum size 12 mm and specific gravity 2.78 are used as a coarse aggregate. Bulk density and fineness modulus of coarse aggregate are 1486 kg/m³ and 7.48 respectively. Locally available river sand passing through 4.75mm with specific gravity 2.64 conforming to zone II of IS 383: 1970 specifications were used in the study [15]. Bulk density and fineness modulus are measured to be 1720 kg/m³ and 2.85 respectively. CONPLAST SP 430 lignosulphonate based aqueous solution compatible with most of the pozzolanic materials are used as a super plasticizer (SP) in this investigation and its properties are shown in Table 2. Effective dispersion of cement is essential for the production of SCC and electro static dispersion of lateral chains and their linked polymer backbones are capable of producing flowable concrete with reduced water cement ratio.

Eco- friendly SCC mix proportion was done by the detailed mix design procedure suggested by Nan su et al [16].M30 grade concrete is chosen and volume ratio of aggregate is assumed to be in the range of 59% to 68% in this study. Packing factor is an another important parameter in SCC mix design and it is assumed as 1.18 by trial-and-error procedure. Water cement ratio of 0.44 is considered and mixture proportion for the reference concrete is obtained for this testing programme. All the ingredients of concrete are mixed together in a Pan mixer of 40 litres capacity shown in Fig. 3. The details of control mixture are presented in Table 3.



Fig. 1 Lime stone powder



Fig. 2 Quarry dust powder

Table 1. Properties of OPC 53 grade

Properties	Range of values
Specific gravity	3.13
Normal consistency	33%
Initial setting time	105 min
Final setting time	185 min

Table 2. Properties of CONPLAST SP 430

Properties	Range of values
Colour	Colourless
Relative density	1.01 \pm 0.01
pH	8 \pm 1

Seven series of mixtures were prepared to examine the fresh properties of SCC made with different proportions of Lime stone (LS) and Quarry dust powder (QD) and their replacement is made on weight basis. Fresh concrete mixture used for SCC testing is shown

in Fig. 4. Trial mixtures with various replacement level and their designations are mentioned below.

- Control concrete without any replacement (CC series)
- Cement replaced by 10%, 20% and 30% lime stone powder. (LS series)
- Cement replaced by 10% ,20% and 30% Quarry dust (QD series)

Table 3. Control concrete mixture proportions per cubic meter

Materials	Quantity
Cement	3.13
Fine aggregate	33%
Coarse aggregate	105 min
Water	185 min
Super Plasticizer	4.8% of binder content

2.2. Testing on Fresh properties of Self - Compacting Concrete

The main characteristic of self-compacting concrete is the ability to spread and consolidate by its own weight. Fresh properties are assessed as per the EFNARC guidelines and to measure the filling ability Slump flow, T 500 mm slump flow and V Funnel test were conducted [17]. In order to check the flowing and passing ability L box test is conducted and it is shown in Fig. 5. U box test are done to measure the packing ability of the concrete. The difference in filling height ($h_2 - h_1$) gives the U box test results. The test set up is shown in Fig. 6. The segregation resistance is measured by V funnel and the test is conducted for 5 minutes time duration. Test set up is shown in Fig. 7. In addition to that fresh state stability is measured by visual examination to ascertain the segregation and bleeding. Fig. 8 shows the slump flow obtained in this experimental programme.

2.3. Hardened Properties of Self-Compacting Concrete

Immediately after the fresh concrete testing, the seven series of specimens were made to understand the influence of filler materials on their hardened properties. Compressive strength test is conducted in a 2000kN capacity compression testing machine as per IS 516 -1959 guidelines on 100mm x 100mm x 100mm size cube specimens after 28, 60, 90, 120 days curing [18]. Dry density values are measured in all the test specimens and their values are compared to observe the influence of limestone and quarry dust in the hardened concrete composites. For each series, three specimens were tested and the average compressive strength and dry density values are considered. Water sorptivity test also conducted to evaluate the potential durability properties of concrete on hardened stage.



Fig. 3 Pan mixer



Fig. 4 Fresh concrete mix



Fig. 5 L box test

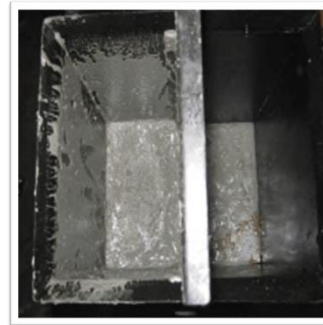


Fig. 6 U box test



Fig. 7 V funnel test



Fig. 8 Slump flow test

3. Results and Discussion

European Federation of National Association Representing for Concrete (EFNARC) has given the typical range of values for ascertaining the flow properties and passing ability of SCC and it is given in Table 4. Tests were conducted as per standard testing procedure and the fresh properties of self-compacting concrete are given in Table 5. The influence of Lime stone filler and quarry dust on compressive strength and water absorption at different curing ages are described in Fig. 9 to Fig. 11.

3.1. Fresh Properties Results of SCC

The influence of lime stone and quarry dust powder on the fresh properties of self – compacting concrete was studied and the results of slump flow, V funnel, L box and U box test are given in Table 5. From the test results, it is observed that the flow properties of 10% lime stone powder was quite high when compared to control concrete and its passing ability as well as the filling ability are increased. The slump flow value is 741mm for CC series and whereas it is 748 mm for LS10 but LS20 and LS 30 shows lower workability than reference concrete. However they are within the EFNARC guidelines mentioned in Table 4, and said to be a self-compacting concrete. Besides it is found that for the same level of replacement with quarry dust powder, the flowability in all the three-replacement found decreased when compared to Lime stone series. Hence the self-compacting concrete designed with lime stone powder is more flowable than SCC produced with quarry dust material. The evidence of flow of mortar and its bleeding characteristics in QD series are

observed by its slump flow T500 test . Lime stone powders indicate better shape when compared to quarry dust and the friction between the particles leads to the high flowability characteristics [19]. In V funnel test all the SCC composites satisfies the acceptance criteria of EFNARC specifications. However, in lime stone series the 20% and 30% replacement levels reduced the filling and passing ability which gets altered with the replacement of 30% quarry dust in the fresh composite. L box test results (h_2/h_1) are typically in the range of 0.811 – 0.986, which satisfies the SCC acceptance criteria. U box test results corresponding to the difference in height of concrete between the two sections are presented in Table 5. U box results of control concrete is 8 seconds and the passing ability of 10LS series is only 5 seconds and it indicates lime stone powder 10% replacement level increased the passing ability, while the higher replacement shows the opposite trend. U box results of 30QD series are closer to the maximum limit of EFNARC acceptance. This represents the flow is significantly affected by the inclusion of quarry dust powder in SCC concrete.

Table 4. EFNARC guidelines for SCC

Method of testing	Unit	Typical range of values	
		min	max
L-Box Test	-	0.8	1.0
U-Box Test	mm	0	30
V-Funnel Test	sec	6	12
Slump flow test	mm	650	800
J-Ring test	mm	0	10

Table 5. Fresh properties of SCC

Series	Slump flow	T500mm (sec)	Vfunnel (sec)	L box (h_2/h_1)	U box (mm)
CC	741	1.08	6.83	0.986	8
10LS	748	1.02	6.78	0.994	5
20LS	716	1.24	7.10	0.917	12
30LS	695	1.43	8.64	0.849	18
10QD	720	1.41	7.38	0.884	17
20QD	698	1.67	7.65	0.852	22.5
30QD	672	1.86	11.41	0.811	27

3.2. Compressive Strength of SCC

Fig. 9 shows the variation of compressive strength of cube specimen water cured after 28 days, 60 days, 90 days and 120 days. Compressive strength of cube specimens increases up to 4.38 % with the addition of 10% lime stone powder at 28 days. This lime stone particles act as a nucleation for CH crystals and thereby increase the strength marginally at lower replacement level. The same strength got reduced by up to 12 % particularly in 30LS series [20]. In addition, the strength development does not increase with the increase in curing age in all the test series. Except 30% lime stone replacement all other series produces compressive strength more than 30MPa and maximum value was reported as 34.67 MPa in control concrete and 36.36 MPa in 10% replacement level.

Fig. 10 represents compressive strength results of cubes tested at 28, 60, 90 and 120 days with the partial replacement of cement with quarry dust. The decrease in compressive strength is continuous when the immersion period increases and also the rate of fall increases with the increase in replacement of quarry dust in self-compacting concrete.

When compared to the control concrete at 90 days, the compressive strength of 10 QD, 20 QD and 30 QD series decreases by 5.30%, 7.15% and 27.37% respectively. It implies that the presence of SiO₂ phases existing in the quarry dust becomes inactive and pozzolanic activity does not promote any improvement in compressive strength [21].

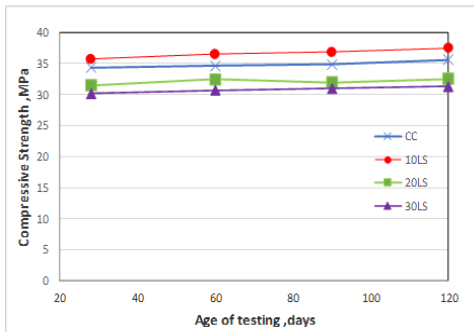


Fig. 9 Compressive strength results of Lime stone series

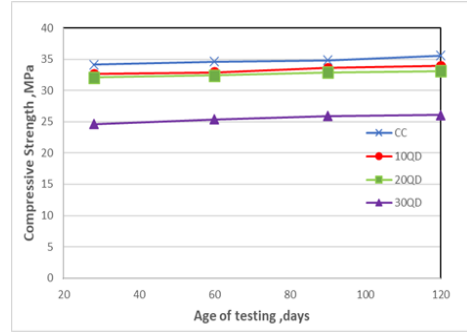


Fig. 10 Compressive strength results of quarry dust series

3.3. Density Values of SCC

Table 6 shows the density variation among control concrete, Lime stone series and Quarry dust series of self-compacting concrete. From the Table 6 it is understood that the density values are not much affected due to inclusion of fillers in the concrete composites. Maximum drop of 2.40 % was observed at 120 days cured specimens and at 30% Lime stone replacement level. This drop is less in Quarry dust replaced series. This is attributed to the dilution effect caused by the addition of crystalline mineral particles which acts as the nucleation sites of heat dissipations and reduces the compressive strength when substitution levels are increased.

Table 6. Density values in kg/m³

Series	28days	56days	90days	120days
CC	2453	2486	2490	2496
10LS	2453	2480	2486	2490
20LS	2536	2566	2566	2573
30LS	2470	2503	2506	2513
10QD	2493	2520	2516	2523
20QD	2526	2540	2553	2561
30QD	2400	2416	2436	2441

3.4. Water Sorptivity Values of SCC

Sorptivity tests results on lime stone series cube specimens are shown in Fig. 11. Based on the test results it is understood that the changes seems to be negligible in 28 days and 60 days cured specimens. Beyond this age, there is no change in water sorptivity, which implies the reduction in permeation of water as the time goes on increasing in both the filler materials.

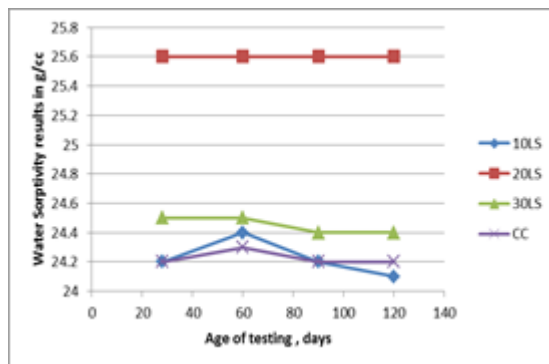


Fig. 11 Water sorptivity results of Lime stone series

4. Conclusions

Based on the experimental investigation the following conclusions can be made:

- Results indicate the feasibility of producing SCC with the inclusion of lime stone and quarry dust powder as cement replacement materials and their dilution effect enhances the flow properties at all replacement levels, satisfying the values recommended by EFNARC guidelines.
- Fresh properties of self-compacting concrete were found to be good up to 10 % lime stone replacement and beyond that they were slightly affected with the increase in replacement levels. Lime stone powder shows better performance when compared to quarry dust. Lime stone powders are more reactive in the presence of cement rather than they act as fillers. Both can be successfully used in the production of self-compacting concrete.
- Compressive strength of Lime stone 10% replacement level is slightly higher than the control specimens and reduction in density was 1.5 % due to the increased shear when compared with other filler materials. Similarly, the reduction in replacement of 10% quarry dust was 1 % less than control concrete. Sorptivity test results reduced by 1% when compared to control concrete in lime stone series.
- Overall test results indicate the replacement of cement with 10 % lime stone improves the strength and flow properties of self-compacting concrete and also, they reduce the environmental risk of solid waste disposal problems.
- Micro fine lime stone powders fills the coarser voids of cement particles in the concrete and thus increases the density. Loss in mass ratio was found to be negligible in tested specimens and hence they found as appropriate replacement material to produce clean and sustainable products in future.
- Cost effective SCC is feasible with the incorporation of limestone powders as a replacement material.

This study gives some new reasons to use Lime stone powder as fillers and its effect on cement hydration process.

Acknowledgement

The author wishes to express the thanks to Department of Civil Engineering, National Engineering College, Kovilpatti Tamilnadu for providing laboratory facilities to carry out this investigation.

References

- [1] India Brand Equity Foundation Report on Cement Industry (June 2020) Science, <https://www.ibef.org/download/Cement-June-2020.pdf>
- [2] Worrell E, Price L, Martin N, Hendriks C, Ozawa Meida L. Carbon dioxide emissions from the global cement industry. Annual Review of Energy and Environment. 2001; 26:303-329. <https://doi.org/10.1146/annurev.energy.26.1.303>
- [3] Yang R, Yu R, Shui Z, Gao X, Han J, Lin G, Qian D, Liu Z, Yongji H . Environmental and economical friendly ultra-high-performance concrete incorporating appropriate quarry-stone powders. Journal of Cleaner Production. 2020:121112. <https://doi.org/10.1016/j.jclepro.2020.121112>
- [4] Felekoglu B. Utilization of high volumes of lime stone quarry wastes in concrete industry (Self-compactingconcretecase). ResourcesConservationRecycling. 2007; 51:4 770-791. <https://doi.org/10.1016/j.resconrec.2006.12.004>
- [5] Sadek DM, El-Attar MM, Ali HA, Felekoglu B. Reusing of marble and granite powders in self-compacting concrete for sustainable development. Journal of Clean Production.2016; 121:10 19-32. <https://doi.org/10.1016/j.jclepro.2016.02.044>
- [6] Medina G, Sáez del Bosque IF, Frías M, Sánchez de Rojas MI, Medina Granite quarry waste as a future eco-efficient supplementary cementitious material (SCM): scientific and technical considerations. Journal of Cleaner Production. 2017; 148:1 467-476. <https://doi.org/10.1016/j.jclepro.2017.02.048>
- [7] Ho DWS, Sheinn AMM, Ng CC, Tam CT. The use of quarry dust for SCC applications. Cement Concrete Research. 2002; 32:4 505-511. [https://doi.org/10.1016/S0008-8846\(01\)00726-8](https://doi.org/10.1016/S0008-8846(01)00726-8)
- [8] Felekoğlu B, Türkel S, Baradan B. Effect of water/cement ratio on the fresh and hardened properties of self-compacting concrete. Building and Environment. 2007; 242:4 1795 -1802. <https://doi.org/10.1016/j.buildenv.2006.01.012>
- [9] Demone PL. Self -compacting Concrete: An analysis of 11 years of case studies. Cement and Concrete Composites. 2006; 28:2 197-208. <https://doi.org/10.1016/j.cemconcomp.2005.10.003>
- [10] Dehwah HAF. Mechanical properties of self-compacting concrete incorporating quarry dust powder, silica fume or fly ash. Construction and Building Materials. 2012; 26(1): 547-551. <https://doi.org/10.1016/j.conbuildmat.2011.06.056>
- [11] Khaleell OR, Al-Mishhadan SA, Abdul Razak H. The Effect of Coarse Aggregate on Fresh and Hardened Properties of Self- Compacting Concrete (SCC). Procedia Engineering. 2011; 14: 805-813. <https://doi.org/10.1016/j.proeng.2011.07.102>
- [12] Schankoski RA, Pilar R Ricardo de Matos P, Roberto Prudêncio L, Douglas Ferron R. Fresh and hardened properties of self-compacting concretes produced with diabase and gneiss quarry by product powders as alternative filler. Construction and Building Materials. 2019; 224:10 659-670. <https://doi.org/10.1016/j.conbuildmat.2019.07.095>
- [13] Gupta N, Siddique R, Belarbi R., Sustainable and Greener Self-Compacting Concrete incorporating Industrial By-Products: A Review, Journal of Cleaner Production. 2020. <https://doi.org/10.1016/j.jclepro.2020.124803>
- [14] IS 12269 -2013, Indian Standard Ordinary Portland Cement 53 Grade specifications. BIS India.
- [15] IS 383 -2016, Indian Standard Coarse and Fine aggregate specifications. BIS India.
- [16] NanSu, Hsu KC, Chai HW. A simple mix design method for self-compacting concrete. Cement and Concrete Research 2001; 31:12 1799-1807. [https://doi.org/10.1016/S0008-8846\(01\)00566-X](https://doi.org/10.1016/S0008-8846(01)00566-X)
- [17] EFNARC Specification and Guidelines for Self-Compacting Concrete, February 2002.
- [18] IS 516 -1959, Indian Standard Methods of Tests for strength of concrete, BIS India.

- [19] Meko B, Ighalo JO, Ofuyatan M. Enhancement of self-compactability of fresh self-compacting concrete: A review Cleaner Materials. 2021; 100019 -16. <https://doi.org/10.1016/j.clema.2021.100019>
- [20] Berodier E, Scrivener K. Understanding the Filler Effect on the Nucleation and Growth of C-S-H. Journal of the American Ceramic Society 2014; 97:12 3764-3773. <https://doi.org/10.1111/jace.13177>
- [21] Abdellahi M, Karafshani MK, Rizi AS. Modeling effect of SiO₂ nanoparticles on the mechanical properties of the concretes. Journal of Building Rehabilitations.2017; 2:8. <https://doi.org/10.1007/s41024-017-0027-8>

Content

- Research Article
431 KR Yellu Kumar, Adnan Qayoum, Shahid Saleem, Fasil Qayoom Mir
Effect of blowing ratio on adiabatic effectiveness for effusion cooling in gas turbine combustor liners
- Research Article
447 Bisma Ali, Adnan Qayoum, Shahid Saleem, Fasil Qayoom Mir
Synthesis and characterization of high-quality multi layered graphene by electrochemical exfoliation of graphite
- Research Article
463 Nitin Kumar, Michele Barbato, Erika L. Rengifo-López, Fabio Matta
Capabilities and limitations of existing finite element simplified micro-modeling techniques for unreinforced masonry
- Review Article
491 Ali İhsan Çelik
Evaluation of energy retention capacity of composite CFRP and GFRP in RC beam strength
- Research Article
519 Megha Bhatt, Sandip A. Vasanwala
Moment-curvature relationships for RC chimney sections
- Review Article
535 T. V. Sheeja, S. V. S. Jebadurai, D. Tensing
Additive manufacturing techniques in construction
- Research Article
553 Afreen Nissar, M. Hanief, Fasil Qayoom Mir
Experimental assessment of recycling methods of used engine oil for sustainable environment
- Research Article
569 Samson Olalekan Odeyemi, Michael Oluwasegun Adisa, Olumoyewa Dotun Atoyebi, Uwemedimo Nyong Wilson³, Omolola Titilayo Odeyemi
Optimal water-cement ratio and volume of superplasticizers for blended cement-bamboo leaf ash high-performance concrete
- Research Article
583 P.N. Ojha, Pranay Singh, Brijesh Singh, Abhishek Singh, Piyush Mittal
Fracture behavior of plain and fiber-reinforced high strength concrete containing high strength steel fiber
- Research Article
603 Moulshree Dubey, Shirish V Deo, Gangadhar Ramtekkar
Effect of metakaolin and steel slag on performance of binary blended concrete
- Research Article
615 Badrinarayan Rath
Effect of asphalt pavement construction on the environment of Ethiopia
- Technical Note
633 Deepan Rajendran, Chella Gifta Christopher, Malaiappan Sindhu Muthu
Self - compacting concrete made with partial replacement of lime stone and quarry dust